ELECTROCHEMICAL AND CHEMICAL INVESTIGATIONS OF VARIOUS SUBSTITUTED PORPHYRINS, CHLORINS AND PORPHYRAZINES

by
Lei Cong

A dissertation submitted to the Department of Chemistry,
College of Natural Sciences and Mathematics
in partial fulfillment of the requirements for the degree of

Doctor of Philosophy

in Chemistry

Chair of Committee: Karl M. Kadish

Committee Member: Thomas S. Teets

Committee Member: Ogenjen Miljanic

Committee Member: Melissa L. Zastrow

Committee Member: Eric Van Caemelbecke

University of Houston
December 2019

Dedication

This dissertation is dedicated to

My parents

Lixin Cong and Heqin Shi

My husband

Yibo Wang

Acknowledgements

My deep gratitude goes first to my supervisor Dr. Karl M. Kadish who expertly guided me through my PhD career, who offered the support and shared the excitement of four years of discovery, who inspired me for his patience, motivation, and immense knowledge, which I believe will be a life-long treasure for me.

I would like to thank my committee members, Dr. Karl M Kadish, Dr. Thomas S. Teets, Dr. Ogenjen Miljanic, Dr. Melissa L. Zastrow and Dr. Eric Van Caemelbecke for their brilliant comments and suggestions.

I also would like to thank you my collaborators, Dr. Sankar Muniappan from the Indian Institute of Technology Roorkee and Dr. Maria Pia Donzello as well as Dr. Claudio Ercolani from the Sapienza University of Rome for providing the compounds which are investigated in the current thesis and also for their contribution to the projects that I have finished.

In spite of this, I would like to express my gratitude to all of you my colleagues and friends I have met during my years at the University of Houston for offering me countless helpful advice and kindly sharing their valuable knowledge.

Finally, I would like to express my greatest gratitude to my parents and other family members being so supportive all the time. Words cannot express how grateful I am for all of the sacrifices that you've made.

Abstract

In this dissertation, by studying the electrochemistry and spectroelectrochemistry of three types of macrocycles: *β*-substituted, *meso*-substituted and/or fused porphyrins, chlorins and porphyrazines derivatives in a variety of non-aqueous media, the substituent, macrocycle, metal center, solvent condition, temperature and supporting electrolyte effects on the electrochemical and chemical behavior of these three types of macrocycles are investigated. Electrochemically or chemically synthesized products are also detected with different added anions, bases, or acids. Here are the key findings described in this dissertation: the electrochemically and chemically driven interconversion between the Ni(II) hydroxyphenylporphyrin and a reduced porphodimethene or oxidized porphyrin-like product, porpho-5,15-bis-paraquinone methide is seen; up to four facile reversible ring-centered reductions generating chlorin tetraanions are observed for the difused chlorins for the first time; strong hydrogen bonded dimers which exhibit mutiple reductions due to electronic communication between the two porphyrin π-ring systems are observed; by changing the size of π-ring systems, adding electron withdrawing/donating substituents or ligating metal centers with different ligands, the redox potentials can be tuned accordingly.

Table of Contents

List of Tables

List of Charts

List of Figures

List of Schemes

Chapter One

Introduction

1.1 Outline of Dissertation

This dissertation is divided into seven chapters in which a variety of different porphyrins and porphyrin-like compounds are investigated for their electrochemical and chemical properties. Basically, three types of structures are investigated in this thesis, which are porphyrins, chlorins, and porphyrazines, repectively. A brief description of each chapter is given in the following text. Chapter one is a background introduction of different types of investigated macrocycles discussed in this thesis. Chapter two describes experimental methods utilized in this dissertation. Chapter three describes the electrochemical and chemical reactivity of nickel(II) octahalogenated *meso*-tetrakis(3, 5-di-*tert*-butyl-4-hydroxyphenyl) porphyrins. Chapter four introduces the electrochemical properties of acetylacetone (acac) and ethyl acetate (EA) appended *β*-trisubstituted push-pull porphyrins and the formation of hydrogen-bonded porphyrin dimers under certain experimental conditions. Chapter five studies the electrochemical and chemical properties of porphyrazines derivatives with different metal centers and substituents. Chapter six focuses on the electrochemical characterization of a series of differently substituted di-fused porphyrins and chlorins. Chapter seven introduces the electrochemical and spectral behavior of a group of meso- and β-substituted porphyrins.

1.2 Electrochemistry

Electrochemistry is chemical processes that involves the moving of electrons. The electrochemical properties of a variety of porphyrins and related macrocycles has long been investigated.[1, 2] Cyclic voltammetry is one of the methods utilized to study the electrochemical potentials and reversibility of these compounds.

Generally, almost all known metalloporphyrins are electroactive and exhibit four or more redox reactions. Most metalloporphyrins with electroinactive central metal ions (such as Cu^{II} and Zn^{II}) are known to undergo at least two ring-centered oxidations and reductions in nonaqueous media.[1-3] However, for porphyrins with some β-substituted highly electron-withdrawing groups, facile and reversible electrogenerations of porphyrin trianion and tetraanion were seen and reported[4] as shown in Equations 1-1 to 1-4 in which [MP] represents metalloporphyrin. Equations 1-5 and 1-6 shows the typically observed two ring-centered oxidations of different metalloporphyrins while a third metal-centered oxidation is sometimes observed for nickel centered porphyrin under certain circumstances.[5]

Reductions

$$[MP] + e^- \rightleftharpoons [MP]^- \quad (1\text{-}1)$$

$$[MP]^- + e^- \rightleftharpoons [MP]^{2-} \quad (1\text{-}2)$$

$$[MP]^{2-} + e^- \rightleftharpoons [MP]^{3-} \quad (1\text{-}3)$$

$$[MP]^{3-} + e^- \rightleftharpoons [MP]^{4-} \quad (1\text{-}4)$$

Oxidations

$$[MP] - e^- \rightleftharpoons [MP]^+ \quad (1\text{-}5)$$

$$[MP]^- - e^- \rightleftharpoons [MP]^{2+} \quad (1\text{-}6)$$

The reversibility and potentials for these redox reactions will depend upon the type of central metal ion, the ligation state, the macrocycle, and the type and number of electron-donating or electron-withdrawing substituents on the macrocycle.[1, 2, 6, 7] It also depends on the properties of the solvent, supporting electrolyte, and temperature. Each generated cationic or anionic metalloporphyrin will have different stability leading in some cases to an irreversibility of the overall electron transfer reactions.[8-11]

Thus, on the routine cyclic voltammetry timescale, irreversible redox reactions are sometimes observed which maybe due to several reasons such as the product of the electron transfer reacts with the solvent or a component in the solution and the occurrence of radical coupling.[8-11]

Metalloporphyrins with electroactive central metal ions such as the Fe, Co, Mn, Cr and Ni [5, 7, 12-17] maybe also involve redox reactions that occur in the metal center. The oxidation state of the central metal ion typically varies between +1 to +6 while higher and lower oxidations are also possible.[1]

1.3 Spectroelectrochemistry

Spectroelectrochemistry is an experimental method utilized to elucidate the electron transfer mechanisms for a variety of porphyrin or porphyrin-like derivatives under different solution conditions. This technique is a combination of electrochemical measurement with *in-situ* spectroscopic measurements such as UV-visible, FTIR, and ESR (in this dissertation, we only use UV-visible spectroelectrochemistry). By applying a given reduction or oxidation potential to the working electrode (depending on the $E_{1/2}$ of the redox reaction), the corresponding redox reaction takes place and is monitored by UV-visible spectroscopy by recording the spectral changes during the redox reaction. Studies of the spectral changes which occur as a function of time or applied potential during a certain redox reaction have often been utilized to distinguish between ring-centered reactions and metal-centered reactions in metalloporphyrins.[4, 12, 18]

In most cases, a porphyrin metal-centered redox reaction will lead to a red or blue shift in the wavelength of the most intense UV-visible band (known as Soret band) located between 350 and 450 nm.[18] However, when an electron transfer process occurs at the conjugated π-ring system

of a porphyrin, or porphyrin-like molecule, a significant decrease in intensity of the Soret band is often observed as well as the appearance of new, broad visible or near-IR bands located between 600-900 nm.[4, 18, 19] These types of spectral changes indicate the probable location of the electron abstraction or addition process. When redox reaction includes more than one steps, correspondingly, more than one trend of spectral changes will be observed during this reaction.

1.4 Porphyrins

Porphyrins are well-known aromatic molecules composed of four pyrrole rings linked via methine bridges. Because of the conjugated macrocycle as well as the coordination ability of the central metal ions which can exist in a variety of different oxidation states (from M^{I} to M^{VI}), porphyrins have been used in a wide range of biological applications such as oxygen transport, electron transfer, energy conversion, and biological oxidation.[20-23] One of the best-known families of porphyrin complexes is heme, the pigment in red blood cells.[20, 22]

The parent porphyrin is porphine with structure shown in Figure 1-1. Substituted porphines are called porphyrins. As seen in the figure, there are two kinds of substitution positions on a porphine ring, one is at the four methine bridges of the macrocycle defined as the *meso* position and the other at the eight β-pyrrole positions of the macrocycle. With a total of 26 π-electrons, 18 π-electrons of the macrocycle are involved in the delocalization pathway. According to Huckel's rule ($4n+2$ electrons where $n \geq 2$), porphyrins have a highly conjugated π-ring system and aromatic properties.[24] Thus, they exhibit a typical spectrum showing very intense absorption bands in the visible region and may be deeply colored.[25]

Basically, the porphyrin compound can be substituted by both electron-withdrawing and electron-donating groups which will both affect the electron density on the π-ring system of the

macrocycle. Consequently, the energy level of both the HOMO and LUMO will be changed accordingly, which will result in the shift of the redox potentials for redox reactions, and could lead to changes in the HOMO-LUMO gap and absorption Soret bands (intense peak located in the blue wavelength region of the visible spectrum) of the complex.

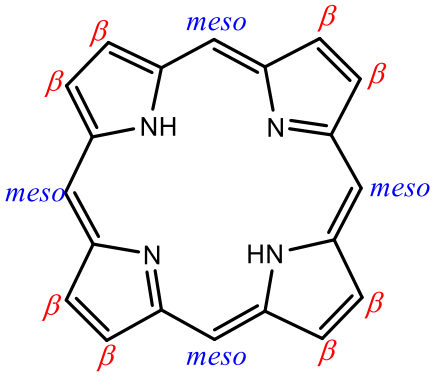

Porphine

Figure 1-1. Structure of porphine.

In this thesis, a variety of differently substituted and fused porphyrins are studied. The structures of the investigated porphyrins are shown in Figure 1-2b and their reference porphyrin compounds are shown in Figure 1-2a.

Four types of porphyrin macrocycles: tetraphenylporphyrin, octaphenylporphyrin, tetrakis(3,5-di-tert-butyl-4-hydroxyphenyl)porphyrin, and octahalogenated tetraphenylporphyrin are utilized as the reference compounds for comparison (structures shown in Figure 1-2a). The investigated compounds (structures shown in Figure 1-2b) were synthesized by Dr. Sankar Muniappan from the Indian Institute of Technology Roorkee and Dr. Maria Pia Donzello as well as Dr. Claudio Ercolani from Sapienza University of Rome and sent to us for electrochemical and spectral investigation. By adding different electron-withdrawing or electron-donating groups to

the β-pyrrole positions of the reference porphyrin macrocycles, the electrochemical and spectral properties of these compounds can thus be tuned. Up to five metal centered porphyrins (M = Cu^{II}, Zn^{II}, Co^{II}, Ni^{II} and 2H) are studied. The effect of the metal center on the electrochemical and spectral behavior is also investigated.

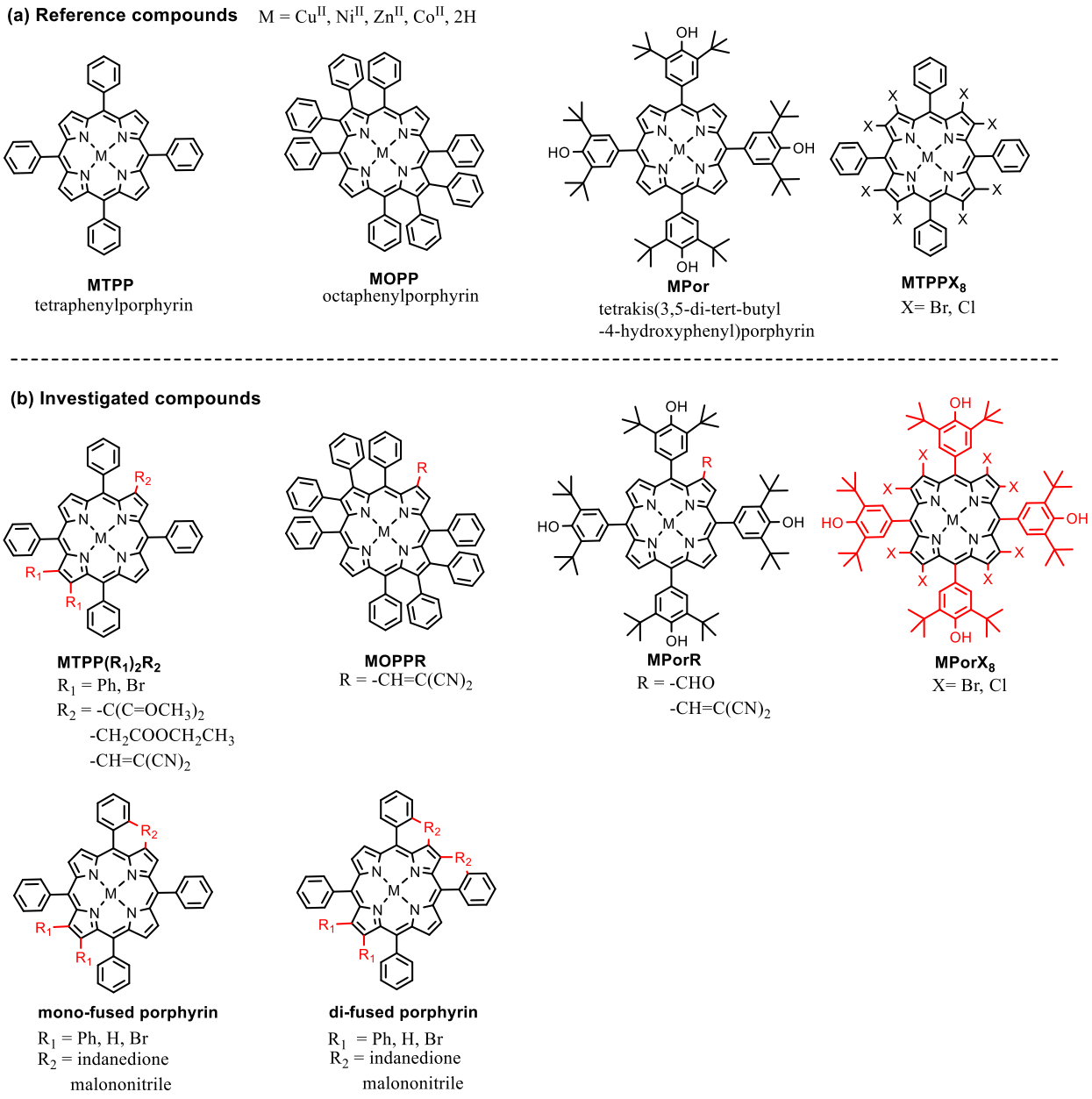

Figure 1-2. Structures of (b) investigated porphyrins and their (a) reference compounds.

Chapter three describes the electrochemistry and reversible interconversion between perhalogenated hydroxyphenyl Ni(II) porphyrins $NiPorX_8$ (structures shown in Figure 1-2b), porphodimethenes and porpho-5,15-bis-paraquinone methide. This chapter has focused on elucidating spectroscopic properties and electrochemistry of both the initial porphyrins and the porphyrin products in neutral, basic, and acidic CH_2Cl_2 solutions. The axial ligand binding of the nickel center is also investigated through a UV-vis study. The electrochemically and chemically driven interconversion between the Ni(II) hydroxyphenylporphyrin and a reduced porphodimethene or oxidized porphyrin-like product, porpho-5,15-bis-paraquinone methide, is described.

Chapter four describes the electrochemical characterization of acetylacetone (acac) and ethyl acetate (EA) appended β-trisubstituted push-pull porphyrins $MTPP(R_1)_2R_2$ (structures shown in Figure 1-2b) and the formation of electronically communicating porphyrin dimers.[26] The $MTPP(R)_2EA$ derivatives behave like MTPPs but the $MTPP(R)_2acac$ porphyrins with Cu^{II}, Ni^{II}, or Zn^{II} central metal ions form strong hydrogen bonded dimers and exhibit multiple reductions due to electronic communication between the two porphyrin π-ring systems. The first four reductions of $MTPP(Br)_2acac$ generate dimers in four different oxidation states, i.e. $[MTPP(Br)_2acac]_2^{n-}$ where n = 1, 2, 3 or 4. The dimers are stable not only in CH_2Cl_2 but also in pyridine.

Chapter six introduces the electrochemical behavior of two groups of di-fused porphyrins (structures shown in Figure 1-2b) $MDFP(MN)_2R_2$ and $MDFP(IND)_2R_2$, where M = 2H, Ni, Zn, Cu, and Co, DFP = di-fused porphyrin, MN = malononitrile and IND = indanedione. The substituent effect and metal center effect on electrochemistry of these compounds is reported. The

electrogenerated anionic forms of the porphyrins are highly reactive, thus leading to cyclic voltammograms having reduction peaks not only of the synthesized compound added to solution but also of one or more new redox active species formed at the electrode surface in a homogenous chemical reaction following electron transfer.

Chapter seven describes the electrochemical and spectral behavior of a group of meso or β-substituted porphyrins having the formula MOPPR, MPorR and MTPP$(R_1)_2R_2$ where OPP = octaphenylporphyrin, Por = tetrakis(3,5-di-tert-butyl-4-hydroxyphenyl)porphyrin, R = different substituent groups (structures shown in Figure 1-2b). Substituent effects on the potentials, reversibility and the sites of electron transfer will be studied in detail in this chapter.

1.5 Chlorins

Chlorins are a class of tetrapyrrolic pigments that consist of one partially reduced pyrrole ring as compared to the porphyrins.[27] The structure of the core macrocycle is shown in Figure 1-3. Chlorophylls known as the core of photosynthetic pigments are magnesium centered chlorin derivatives which are responsible for light harvesting on earth.[27, 28]

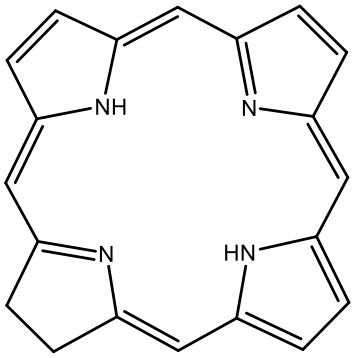

20 π-electron macrocycle
Chlorin

Figure 1-3. Structure of chlorin.

As compared to porphyrins, chlorins are less planar and less symmetric due to the one partially reduced pyrrole ring on the macrocycle. These features thus result in a blue-shifted Soret band and a more allowed and red-shifted Q band in the UV-visible spectra as well as the observation of easier oxidations in the cyclic voltammetry as compared to porphyrins.[29-32]

The electrochemical properties of chlorins are similar to what were observed for porphyrins as undergoing two ring-centered oxidations and two ring-centered reductions in most cases. Chapter six studies two different types of difused chlorins whose structures are shown in Figure 1-4.[33, 34] The fusion of the indanedione and malononitrile groups to the chlorin ring makes easier oxidations as compared to non-fused chlorins.[33] Also, with the two fused indanedione (IND) groups, four well-defined reductions are observed for $H_2DFC(IND)_2R_2$ while only two reversible reductions are observed for $H_2DFC(MN)_2R_2$. Detailed electrochemical studies on these di-fused chlorin derivatives are discussed later in Chapter six.

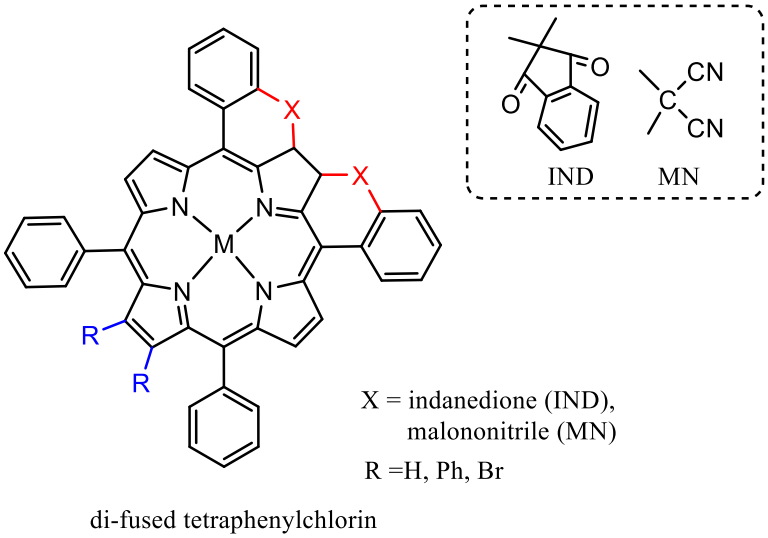

Figure 1-4. Structures of investigated di-fused chlorins.

1.6 Porphyrazines

Porphyrazines (tetraazaporphyrins; name including their metal derivatives) are characterized by a central tetrapyrrolic macrocycle in which the N atoms bridging the pyrrole rings replace the isosteric and isolelectronic ≡C-H groups present in the porphyrin analogs.[35] Porphyrazine is an aromatic tetrapyrrolic macrocycle, the structure of which is that of a *meso*-tetraaza-substituted porphine.[35, 36] This definition includes porphyrazine itself PzH_2, and its β-substituted R_8PzH_2, and β, β-annulated $(Het)_4PzH_2$ derivatives as shown in Figure 1-5.

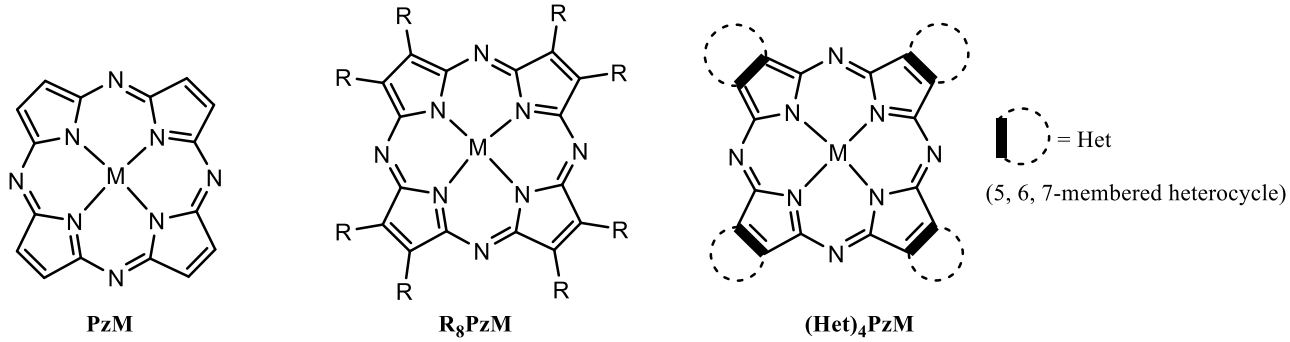

Figure 1-5. Structures of porphyrazine, its β-substituted and β,β-annulated derivatives.

A summary of the investigated porphyrazine derivatives in this dissertation and their corresponding reference compounds cited for comparison is shown in Figure 1-6. A variety of different metal centered porphyrazines are studied: metal centers with +2 oxidation state including Mg^{II}, Zn^{II}, Co^{II}, Cu^{II}, Pd^{II}, and 2H and metal centers with +3 oxidation state including Al^{III} and Ga^{III}. Basically, four types of macrocycles PzM, PcM, TTDPzM, and TPyzPzM are utilized for comparison. Structures of these compounds are shown in Figure 1-6. Adding eight pyridyl groups to TPyzPz greatly improved the solubility of TPyzPz compounds as low solubility strongly limits solution studies of the electrochemical behavior of unsubstituted TPyzPz compounds.[37]

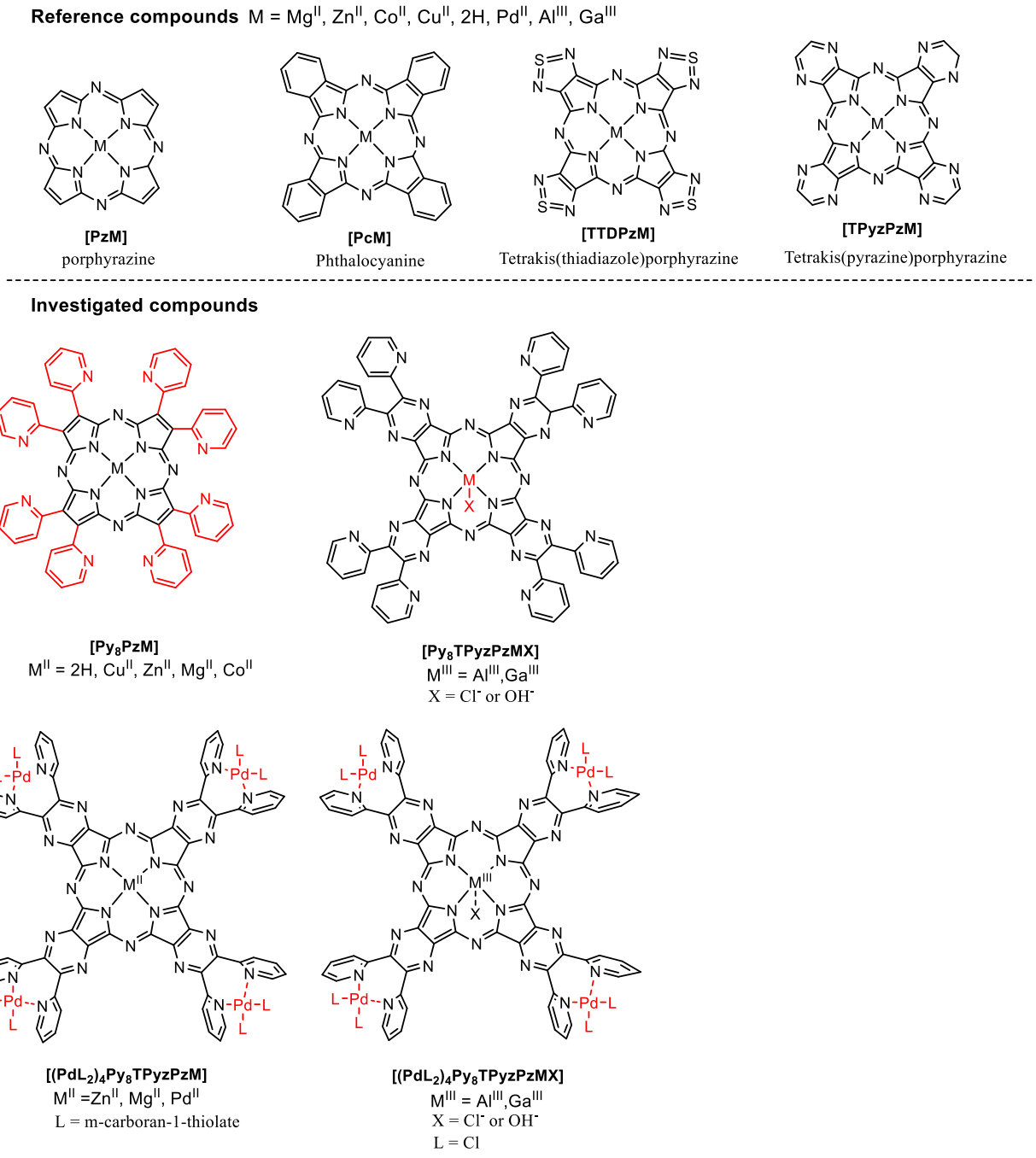

Figure 1-6. Structures of investigated porphyrazine derivatives and their reference compounds

Up to four easy ring-centered reductions are observed for porphyrazine derivatives generating $[MPz]^{4-}$ while for Co porphyrazine, one extra metal-centered reduction is also observed. A positive potential shift of up to 600 mV is observed for the octapyridinated porphyrazine derivatives as compared to their parent phalocyanine compounds.[38-41] With a ligated M^{III} metal center, the $E_{1/2}$ values for the first and following reductions of the $[Py_8TPyzPzMX]$ complexes are positively shifted by 200-300 mV as compared to the reduction potentials for the related M^{II} species $[Py_8TPyzPzM]$ in the same solvent which also matches earlier results seen for the thiadiazole analogs [TTDPzMX].[42] When every two of the right pyridyl groups are ligated with a PdL_2 group where L = Cl^- and m-carboran-1-thiolate group, even more facile reductions by 200-300 mV are observed as compared to the unligated compounds. A detailed study on the electrochemistry of these porphyrazine derivatives has been published and is described in Chapter five.[43-45]

Chapter Two

Experimental Methods

2.1 Electrochemical Methods

2.1.1 Cyclic voltammetry

Cyclic voltammetry is one of the many electrochemical methods used to determine the eletrochemical properties of different compounds. By applying the cycled potential at the working eletrode, the resulting current will be measured accordingly. A cyclic voltammogram is a plot of the current measured at the working electrode surface versus the applied voltage. Figure 2-1 is an example of a well-defined cyclic voltammogram showing a single cathodic process coupled with its anodic process and a one-electron reoxidation process. The cathodic (reduction) peak potential and the anodic (oxidation) peak potential is represented as E_{pc} and E_{pa}. The reduction (cathodic) peak current and the reoxidation peak current are labeled as i_{pc} and i_{pa}, respectively as seen in Figure 2-1. The half-wave potential for this one-electron addition step is represented as $E_{1/2}$ which equals to $(E_{pc} + E_{pa})/2$.

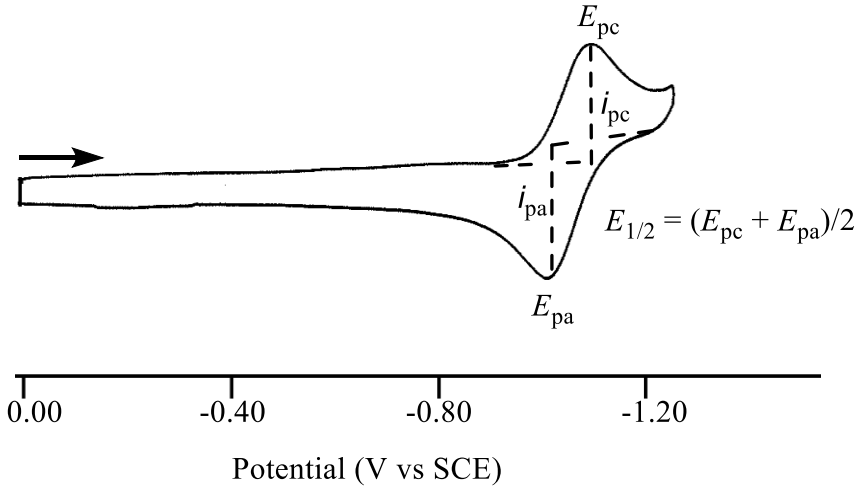

Figure 2-1. Schematic illustration of cyclic voltammogram.

The magnitude of the current i_p can be described by Ransdles-Sevcik equation,[46] which is given in Equation 2-1. At 25 ^oC, it can be simplified as shown in Equation 2-2, where i_p is the peak

current in *uA*, n is the number of electrons transferred, A is the electrode area in cm^2, F = Faraday constant in C mol^{-1}, D is the diffusion coefficient of the species in cm^2/s and *C* is the bulk concentration of the species in mol/cm^3, ν is the scan rate in V/s, R is the gas constant in J K^{-1} mol^{-1} and T is the temperature in K.

$$i_p = 0.4463nFAC\,(nF\nu D/RT)^{1/2} \quad (2\text{-}1)$$

$$i_p = (2.69 \times 10^5)n^{3/2}ACD^{1/2}\nu^{1/2} \quad (2\text{-}2)$$

For the compounds described in this dissertation, *n* was almost always 1, while the value of D was about 10^{-6} cm^2/s.

Cyclic voltammetry (CV) is one of the mostly commonly used electrochemical measurement. The regular cyclic voltammetry measurement carried out by our lab utilizes an EG&G Princeton Applied Research (PAR) 173 Potentiostat linked to an EG&GPAR Model 175 Universal Programmer and was carried out at room temperature (22±1 ºC). Cyclic voltammograms are sometimes measured at low temperature using an acetone and dry ice mixture to obtain temperatures from 20 ºC to -60 ºC. A mercury/achohol thermometer is immersed in the acetone/dry ice bath to monitor the temperature at the same time.

A home-made glass cell was used to conduct the cyclic voltammetric measurement in our laboratory. A three-electrode system consisting of a 3 mm diameter glassy carbon working electrode (WE), a platinum counter electrode (CE) and a homemade saturated calomel reference electrode (SCE) was used to carry out the cyclic voltammetry measurements. The measured potential, *E*, of the SCE is + 0.241 V SHE (standard hydrogen electrode) at 298 K. The homemade saturated calomel reference electrode is a 10-20 cm 'H' shape of glass tube container consists of a saturated water solution of potassium chloride (KCl) in contact with the mercury and the mercury chloride. The saturated calomel reference electrode was soaked in the saturated KCl

solution to maintain the concentration of chloride anion when not in use. During the measurement, in order to prevent the SEC from being 'contaminated' by the compound solution, it was inserted into a low porosity fritted glass bridge filled with the solvent/supporting electrolyte mixture. Ferrocene was utilized to check the potentials for reference electrode as an internal standard with a measured half-wave potential $E_{1/2}$ = 0.47 V vs SCE in CH_2Cl_2 containing 0.1M TBAP (tetrabutylammonium perchlorate) at room temperature.

A desired potential was set at the beginning for one cyclic voltammetry scan. The potential at the working electrode was measured against a reference electrode which increases linearly with time during the measurement. After reaching the desired potential set at the beginning, the potential applied on the working electrode was scanned in the reverse direction until the initial value was reached. One forward and reverse scan is known as 'a cycle'. The cycles of potential scan can be repeated as many times as desired. At least three cycles of potential scan were repeated for every measurement. The scan rate can also be adjusted varying from 20 mV to 200 mV/s. However, unless otherwise noted, a scan rate of 100 mV/s was used for the cyclic voltammograms in this thesis.

2.2 Spectroscopic Methods

2.2.1 Thin-layer UV-Visible Spectroelectrochemistry

UV-Visible spectroelectrochemical measurements in our laboratory were performed using a commercial spectroelectrochemical cell purchased from Pine Research Instrumentation in Durham, NC. Potentials were applied and monitored with an EG&G PAR Model 173 Potentiostat. Time-resolved UV-visible spectra were recorded with a Hewlett-Packard Model 8453 diode array

spectrophotometer. By applying a given redox potential to the working electrode, the spectral changes were monitored and recorded by this instrument during the redox reaction.

The UV-Vis spectroelectrochemical cell (thin-layer quartz cuvette) utilized in our laboratory was commercially purchased from Pine Research Instrumentation, Inc (product number AKSTCKIT3). A spectroelectrochemical cell package includes 1 quartz cuvette, 1 cell cap, 1 platinum honeycomb electrode, 2 gold honeycomb electrodes, and a low profile Ag/AgCl reference electrode. The working electrode is perforated with a honeycomb pattern of holes which allow light to pass through the electrode. A cuvette cap securely holds the honeycomb electrode card and a separate Ag/AgCl reference electrode in the proper position within the cuvette. The effective path length of light is 1.7 mm and the volume of the cell is 1.5 mL.

2.3 Titration Methods

Spectral and electrochemical titration methods are used in determining the equilibrium constants for the axial ligand binding to porphyrin. Stock solutions (ligands or reactants like base or acid) were prepared before the titration. By quantitatively adding the ligand/reactant solutions to the porphyrin solution, they will react with the porphyrin resulting in spectral and electrochemical changes. These changes were recorded as a function of the ligand concentration added to the solution using methods described in the following section to obtain equilibrium constants and the coordination number.

2.3.2 Spectroelectrochemical Titration Method

The ligand binding reaction is given by Equation 2-3. [M] and [ML_p] are the concentration of the unligated and ligated metalloporphyrin species, [L] is the free-ligand concentration in solution and p is the number of ligands axially bound to the central metal ion of the porphyrin.

$$M + pL = ML_p \quad (2\text{-}3)$$

The relationship describes the concentration of the species in solution and the equilibrium constant K, and log K as given by Equations 2-4 and 2-5.[47, 48]

$$K = [ML_P]/([M][L]^p) \quad (2\text{-}4)$$

$$\log([ML_p]/[M]) = \log K + p \log[L] \quad (2\text{-}5)$$

Assuming M and ML_p have different spectra with different absorbance, according to Beer-Lambert law[49] then we have:

$A_0 = \varepsilon_M\, b\, [M]$

$A_f = \varepsilon_{MLp}\, b\, [MLp]$

$A_i = \varepsilon_M\, b\, [M] + \varepsilon_{MLp}\, b\, [ML_p]$

[M] and $[ML_p]$ are the total concentration of M and ML_p in solution, ε is the molar absorptivity, b is the path length, A_0 and A_f are the initial and final absorbance at a given wavelength (λ_{max}) for the species M and ML_p and A_i is the absorbance at λ_{max} at any point during the titration.

According to the mass balance equation[50]: $C_M \approx C_{MLp} = [M] + [ML_p]$ (C_M is the original concentration of M and C_{MLp} is the final concentration of ML_p), we have:

$$\begin{aligned} A_i &= \varepsilon_M\, b\, [M] + \varepsilon_{MLp}\, b\, [ML_p] \\ &= \varepsilon_M\, b\, (C_M - [ML_p]) + \varepsilon_{MLp}\, b\, [ML_p] \\ &= A_0 + (\varepsilon_{MLp}\, b - \varepsilon_M\, b)\, [ML_p] \end{aligned}$$

$$[ML_p] = (A_i - A_0)/(\varepsilon_{MLp}\, b - \varepsilon_M\, b)$$

and

$$\begin{aligned} A_i &= \varepsilon_M\, b\, [M] + \varepsilon_{MLp}\, b\, [ML_p] \\ &= \varepsilon_M\, b\, [M] + \varepsilon_{MLp}\, b\, (C_{MLp} - [M]) \end{aligned}$$

$[M] = (A_f - A_i)/(\varepsilon_{MLp}\, b - \varepsilon_M\, b)$

Substituting the values of [M] and $[ML_p]$ into Equation 2-4 gives the result shown in Equation 2-6[19, 51]:

$$\log ((A_i - A_0)/ (A_f - A_i)) = \log K + p \log [L] \qquad (2\text{-}6)$$

An example of the spectral titration of pyridine for Ni centered porphyrin $NiPorCl_8$ is shown in Figure 2-2. As shown in the figure, A_0 and A_f is the initial and final absorbance at 667nm while A_i is the absorbance during the spectral changes at 667 nm. By plotting $\log ((A_i - A_0)/ (A_f - A_i))$ versus log[py], a linear relashionship with a slope of p = 2.0 is seen which is the number of ligand (pyridine) bound to the nickel center. The value of the equilibrium constant K can also be calculated at the equilibrium point as shown in the plot.

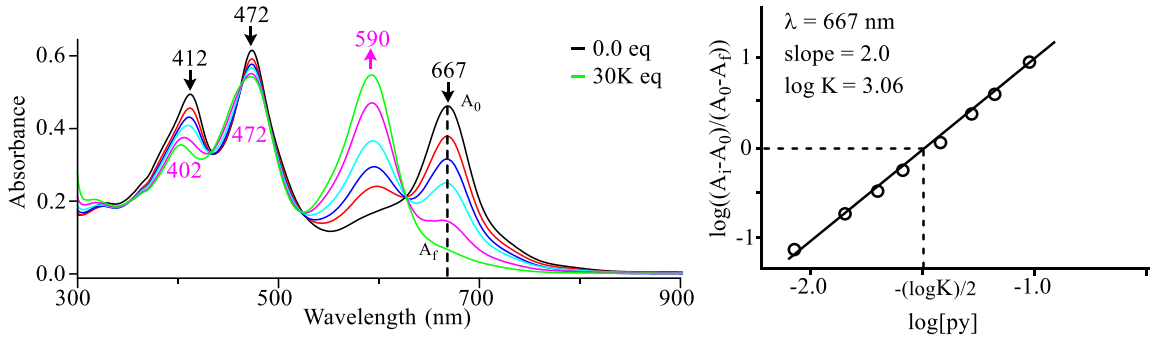

Figure 2-2. Illustration of UV-vis spectral changes of $NiPorCl_8$ during the titration of pyridine.

2.3.3 Electrochemical Titration Method

The electrochemical titration is another tiration method utilized to determine the equilibrium constants for the axial ligand binding to porphyrin.

For a cell reaction: $aA + bB \rightarrow cC + dD$, according to Nernst Equation[52] we have:

$$E = E^0 - (RT/nF)\, \ln[a_C{}^c a_D{}^d/(a_A{}^a a_B{}^b)] \qquad (2\text{-}7)$$

where E is the potential, E^0 is the standard potential, R is the universal gas constant in $JK^{-1}mol^{-1}$, T is the temperature in K, F is the faraday constant in $Cmol^{-1}$, n is the number of electrons transferred, and a is the reactivity of relevant species (in solustion conditions usually substituted by C, concentration).

At T = 298 K, the Nernst equation can be rewritten as shown in Equation 2-9:

$$E = E^0 - (0.0592V/n)\ \ln[a_C^c a_D^d/(a_A^a a_B^b)] \qquad (2\text{-}9)$$

An example of the ligation reaction and reduction reaction of ligated and unligated metalloporphyrin species are shown in Equations 2-10 and 2-11:

$$M + pL = ML_p \qquad (2\text{-}10)$$

$$ML_p + ne^- = M^{n-} + pL \qquad (2\text{-}11)$$

Based on Nernst equation, then we have the results shown in Equation 2-12[53]

$$(E_{1/2})_M - (E_{1/2})_{MLp} = -(0.0592V/n)\log K - p\,(0.0592V/n)\log [L] \qquad (2\text{-}12)$$

By plotting the $[(E_{1/2})_M - (E_{1/2})_{(MLp)}]$ versus log [L], we can get the slope, p, which equals to the number of ligands bound to the metalloporphyrin species. The y-intercept is when log [L] = 0 which gives the result shown in Equation 2-13. Thus, the equilibrium constant K can be calculated.

$$\log K = [(E_{1/2})_{MLp} - (E_{1/2})_M]/0.0592 \qquad (2\text{-}13)$$

When the reduction reaction involves a change of ligand binding number as shown in Equation 2-14:

$$ML_p + ne^- = MLq^{n-} + (p\text{-}q)\ L \qquad (2\text{-}14)$$

Based on Nernst equation, then we have the results shown in Equations 2-12[54]

$$(E_{1/2})_{MLq} - (E_{1/2})_{MLp} = -(0.0592V/n)\log K - (p\text{-}q)\,(0.0592V/n)\log [L] \qquad (2\text{-}12)$$

By plotting the [$(E_{1/2})_{(MLq)}$ - $(E_{1/2})_{(MLp)}$] versus log [L], we can get the slope (p-q) which equals to the number of ligand change during the redox reaction.

2.4 Chemicals

2.4.1 Compounds Studied

All the compounds characterized in this dissertation (Chapters three to six) were obtained from Dr. Sankar Muniappan from the Indian Institute of Technology Roorkee and Dr. Maria Pia Donzello as well as Dr. Claudio Ercolani from the Sapienza University of Rome. Their purity was verified by UV-vis spectroscopy in our lab before conducting the electrochemical experiments and our spectral data were compared to that provided by our collaborators or published in the literature. Once the compounds were received in Houston, they were sealed with parafilm and stored in the dark, or in some cases, under vacuum.

2.4.2 Other Chemicals

Solvents used in our laboratory for electrochemistry measurements were: dichloromethane (CH_2Cl_2, anhydrous, ≥ 99.8%, EMD Chemicals Inc.); pyridine (Py, biotech. grade, ≥ 99%, Sigma-Aldrich); benzonitrile (PhCN, reagent Plus, 99%, Sigma-Aldrich), freshly distilled over P_2O_5 before use; tetrahydrofuran (THF, for HPLC, ≥ 99.9%, Sigma-Aldrich) and freshly distilled using a Solvent System PS-MD-5-13-495 from Innovative Technology; iodomethane (CH_3I, reagent Plus, 99.5%, Sigma-Aldrich). Supporting electrolytes tetra-*n*-butylammonium perchlorate (TBAP) and tetra-*n*-butylammonium hexafluorophosphate ($TBAPF_6$) were purchased from Sigma-Aldrich. Before each electrochemical measurement, high purity N_2 from Trigas was used to deoxygenate the solution.

Chapter Three

Electrochemistry and Reversible Interconversion Between Perhalogenated Hydroxyphenyl Ni(II) Porphyrins, Porphodimethenes, and Porpho-5,15-bis-Paraquinone Methide

Reproduced in part with permission from [*Inorg. Chem.* **2019,** *58,* 14361-14376], American Chemical Society.

3.1 Introduction

The introduction of halogens to the β-pyrrole positions of a porphyrin leads to a distortion of the macrocycle,[55-58] a red shift of the Soret band transition energy,[6, 59-61] and pronounced shifts in the reduction potentials making the β-halogenated porphyrins much easier to reduce as compared to the unhalogenated parent compounds.[7, 62] Halogenated porphyrins are considered as remarkably active and robust catalysts for olefin epoxidation and alkane hydroxylation reactions[63] and a great deal of effort has gone into the synthesis, characterization, and reactivity of different meso-substituted octahalogenated tetraphenylporphyrins.

Although a number of different meso-phenyl substituted porphyrins with β-halogen substituents have been synthesized and characterized as to their structural, spectroscopic and electrochemical properties,[1, 13, 19, 64-66] early attempts to β-functionalize metalloporphyrins containing the meso-tetrakis(3,5-di-tert-butyl-4-hydroxyphenyl)porphyrin macrocycle (TDtBHPP) using known literature methods had been unsuccessful, giving not the desired porphyrin product, but instead an oxidized porphyrinogen derivative.

We have now followed up on earlier studies involving β-functionalization of TDtBHPP[67, 68] and in the present manuscript, describe the first successful synthesis of a β-octahalogenated derivative of this macrocycle. The spectroscopic and electrochemical properties of these newly synthesized octahalogenated porphyrins are also described along with their chemical reactivity under different solution conditions. The investigated compounds are shown in Chart 3-1a and are represented as $NiPorCl_8$ and $NiPorBr_8$ where Por = the dianion of TDtBHPP. Comparisons are made with both the parent unhalogenated porphyrin NiPor and related porphyrins in the TPP series of Chart 3-1b, namely NiTPP, $NiTPPCl_8$, and $NiTPPBr_8$.

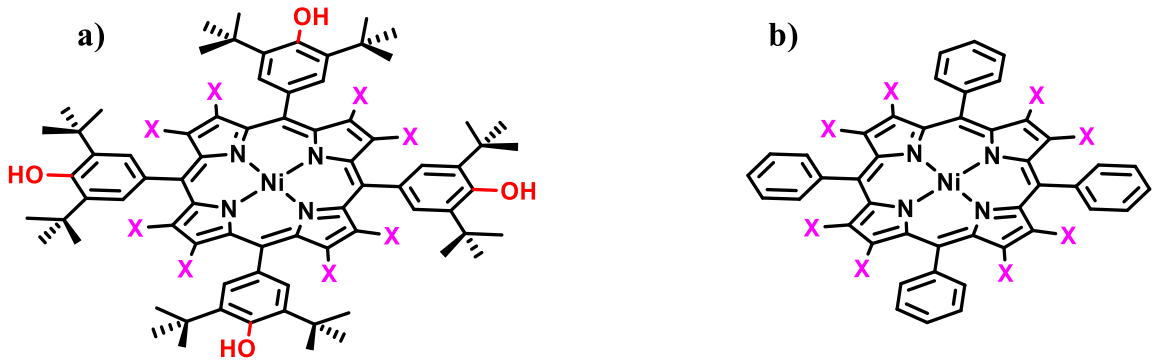

X = H; NiPor
X = Cl; $NiPorCl_8$
X = Br; $NiPorBr_8$

X = H; NiTPP
X = Cl; $NiTPPCl_8$
X = Br; $NiTPPBr_8$

Chart 3-1. Structures of (a) investigated porphyrins where Por = TDtBHPP and (b) reference tetraphenylporphyrin (TPP) derivatives.

Each Ni(II) porphyrin was spectroscopically characterized in 15 different nonaqueous solvents and electrochemically characterized in CH_2Cl_2 or pyridine containing 0.1 M tetrabutylammonium hexafluorophosphate ($TBAPF_6$) as well as in CH_2Cl_2 containing acid in the form of trifluoroacetic acid (TFA) or base in the form of TBA^+OH^-, TBA^+CN^- or TBA^+OAc^- where TBA^+ = tetrabutylammonium cation.

The UV-vis spectra of $NiPorCl_8$ and $NiPorBr_8$ vary with solvent and degree of axial coordination but are almost identical to each other in a given solvent. These spectra are also substantially different from that of the unhalogenated NiPor parent porphyrin (which resembles nickel tetraphenylporphyrin, NiTPP), and they also differ from the spectra of *β*-octahalogenated $NiTPPCl_8$ and $NiTPPBr_8$ under the same solution conditions. The $NiPorX_8$ spectra are stable with time and interpreted in terms of four or six-coordinated derivatives in 13 different nonaqueous solvents. This is not the case, however, in DMF or DMSO where a transient 6-coordinate complex

is initially formed upon dissolving the $NiPorCl_8$ followed by the formation of an air oxidized porphodimethene-like product formation called porpho-5,15-bis-paraquinone methide was observed, the time of this chemical transformation depending upon the concentration of the porphyrin in solution. The initial species formed from $NiPorCl_8$ and $NiPorBr_8$ after the first one electron addition in CH_2Cl_2 is stable for short times at -60 °C, but this is not the case at room temperature where a rapid homogeneous chemical reaction occurs. Four additional redox reactions are also observed in CH_2Cl_2 and UV-visible spectra of several in-situ generated electroreduction products are compared with that of chemically synthesized porphodimethenes formed in neutral, acidic and basic solutions of CH_2Cl_2 containing acid in the form of TFA or base in the form of TBA^+X^- where X = OAc^-, CN^-, OH^-.

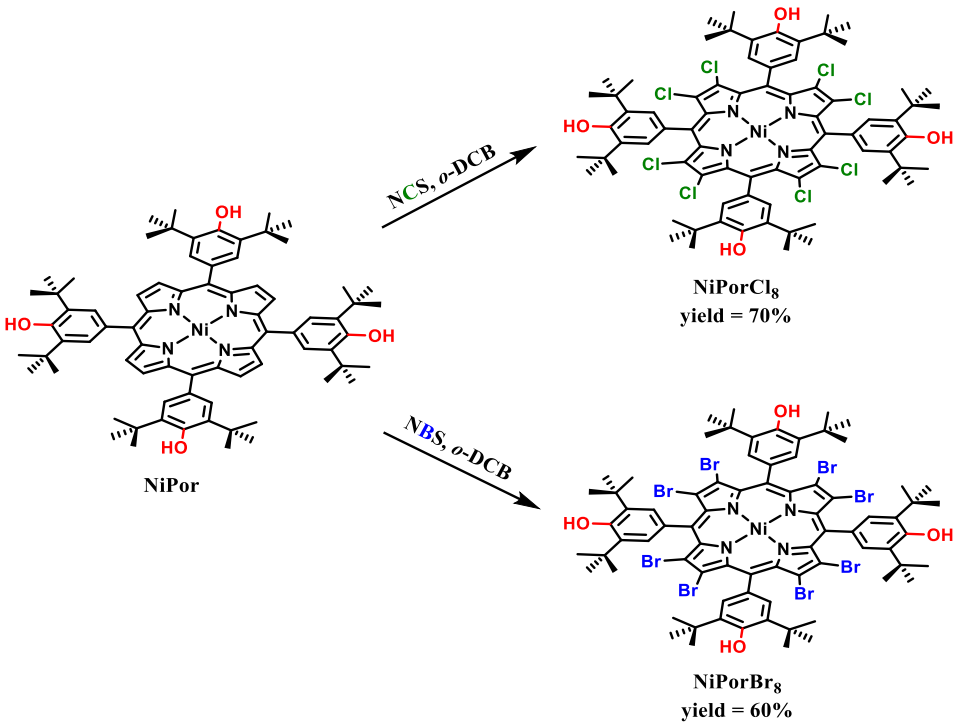

Scheme 3-1. Synthesis of halogenated porphyrins $NiPorCl_8$ and $NiPorBr_8$ (reproduced in part with permission from [*Inorg. Chem.* **2019,** *58*, 14361-14376], American Chemical Society).[11]

Finally, a reversible electrochemically driven conversion between the Ni(II) hydroxyphenylporphyrin and a reduced porphodimethene or oxidized porphyrin-like product, porpho-5,15-bis-paraquinone methide, is described.

3.2 Results and Discussion

3.2.1 Synthesis

The desired perhalogenated porphyrin products, *β*-octachloro-*meso*-tetrakis(3′,5′-di-*tert*-butyl-4′-hydroxyphenyl)-porphyrinatonickel(II) $NiPorCl_8$, and *β*-octabromo-*meso*-tetrakis(3′,5′-di-*tert*-butyl-4′-hydroxyphenyl)porphyrinatonickel(II) $NiPorBr_8$ were synthesized by Dr. Muniappan Sankar's laboratory in IIT Roorkee, India using NCS or NBS as halogenating reagents on NiPor in *o*-dichlorobenzene. The synthetic procedure, shown in Scheme 3-1 is described in the literature.[11] The synthesis and characterization of NiPor is given in the literature.[69]

3.2.2 UV-Visible Characterization of NiPor, $NiPorCl_8$ and $NiPorBr_8$

UV-visible spectra of compounds NiPor, $NiPorCl_8$ and $NiPorBr_8$ in CH_2Cl_2 are shown in Figure 3-1 and the data is summarized in Table 3-1. The octahalogenated porphyrins $NiPorCl_8$ and $NiPorBr_8$ have almost identical electronic absorption spectra in CH_2Cl_2 and are characterized by equally intense split Soret bands at 412/413 and 472/477 nm and a highly allowed $Q_x(0,0)$ band at 667/661 nm having approximately the same molar absorptivity (ε) as the Soret bands. Similar spectral patterns are also seen for the two porphyrins in hexane, $CHCl_3$, 1,4-dioxane, ethyl acetate, diethyl ether and THF as shown in Figure 3-1 and Tables 3-2 and 3-3.

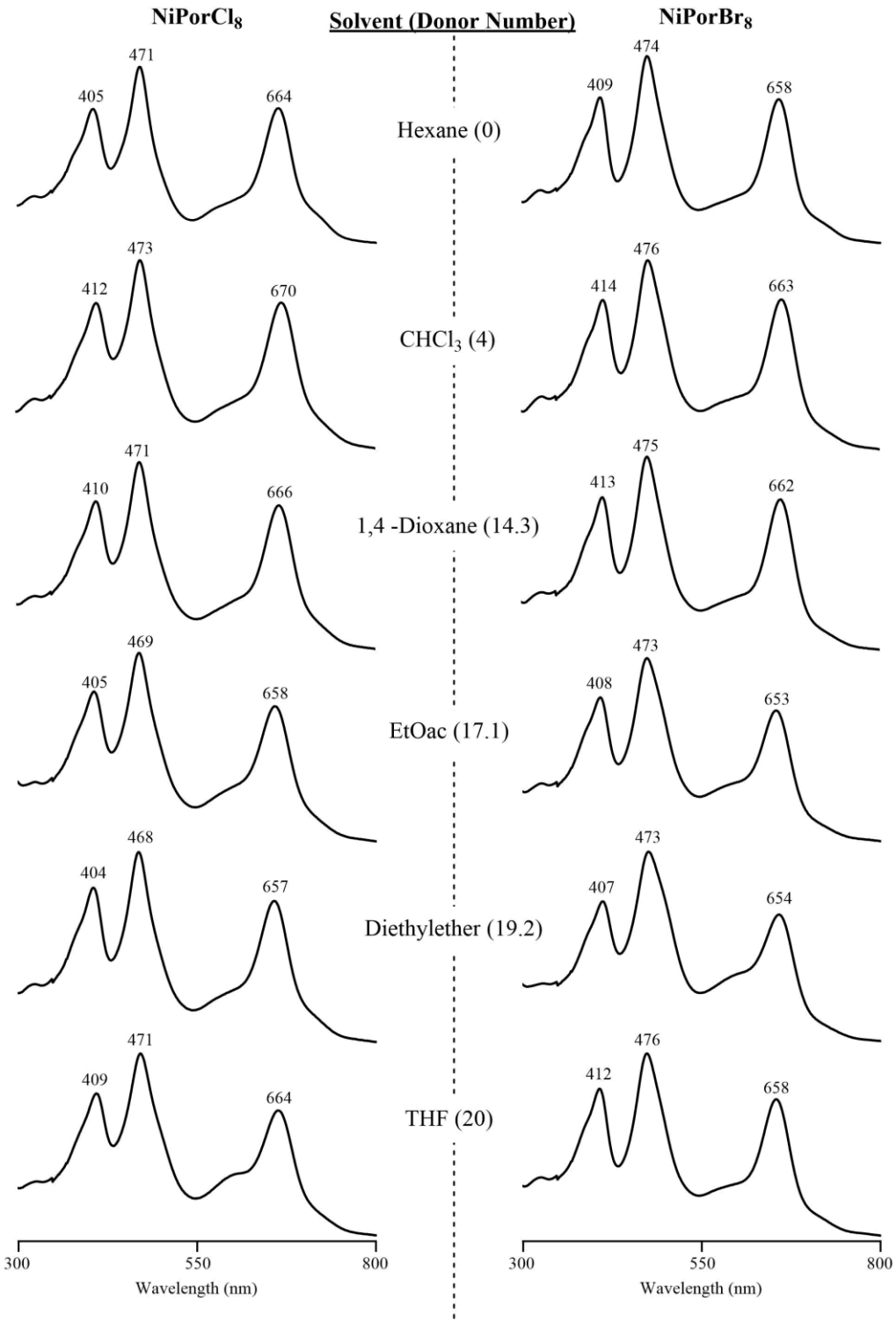

Figure 3-1. UV-vis spectra of $NiPorCl_8$ and $NiPorBr_8$ under solvent conditions which favor four-coordinate species. The donor numbers (DN) are given in Tables 3-2 and 3-3.

The increased intensity of the $Q_x(0,0)$ band and the similar intensity of the two peaks in the split Soret bands of $NiPorCl_8$ and $NiPorBr_8$ are highly pronounced in CH_2Cl_2 whereas this is not seen for the parent porphyrin, NiPor, or NiTPP and its halogenated derivatives $NiTPPX_8$ (X = Cl, Br) which contains four *meso*-phenyl groups as shown in Figure 3-2 and Table 3-1.

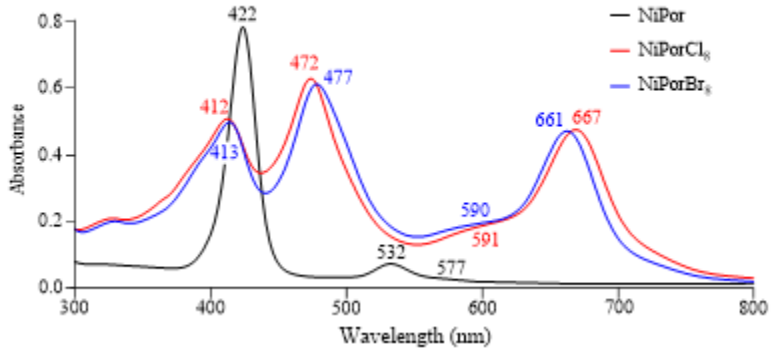

Figure 3-2. UV-visible spectra of NiPor (black curve, 5×10^{-6} M), $NiPorCl_8$ (red curve, 10^{-5} M) and $NiPorBr_8$ (blue curve, 10^{-5} M) in CH_2Cl_2.

Table 3-1. UV-visible data of synthesized porphyrins and related reference compounds in CH_2Cl_2

	λ_{max}, nm ($\varepsilon \times 10^{-4}$ $M^{-1}cm^{-1}$)				
Porphyrin	**Soret band(s)**		**Q band(s)**		**ref**
NiPor		422 (16.22)	532 (2.34)	577 (0.29)	tw
$NiPorCl_8$	412 (4.57)	472 (5.62)	591 (0.62)	667 (4.90)	tw
$NiPorBr_8$	413 (4.27)	477 (5.13)	590 (0.36)	661 (4.79)	tw
NiTPP		414 (20.89)	525 (1.35)		70
$NiTPPCl_8$		439 (19.05)	554 (1.51)	591^{sh}	70
$NiTPPBr_8$		448 (24.55)	561 (1.91)	592^{sh}	70

tw = this work; ^{sh} shoulder band.

The addition of 8 Br or Cl groups to the *β*-pyrrole positions of a tetraphenylporphyrin (TPP) or substituted tetraarylporphyrin macrocycle has been examined for a number of different metal derivatives, and leads to a 25-40 nm red shift of all absorption bands[70] with the magnitude of the

shift being smaller for chlorination as compared to bromination. An example of this is given for the Ni(II) complexes of TPP in Table 3-1 where the Soret band shifts from 414 nm in the case of the unhalogenated NiTPP to 439 nm for $NiTPPCl_8$ and 448 nm for $NiTPPBr_8$, while the most intense Q band also red shifts from 525 to 553 and then to 561 nm.[70]

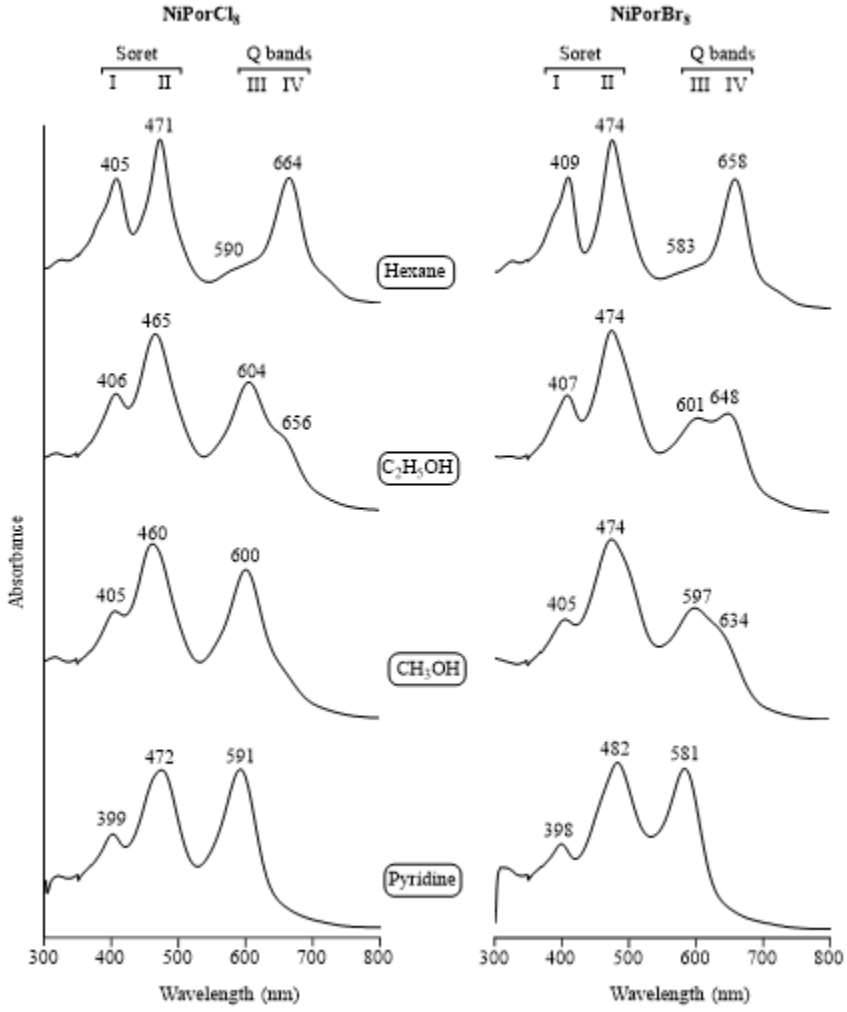

Figure 3-3. UV-vis spectra of $NiPorCl_8$ and $NiPorBr_8$ in hexane, ethanol, methanol, and pyridine.

Although the spectral envelopes of NiTPP, $NiTPPCl_8$, or $NiTPPBr_8$ are quite similar to each other in CH_2Cl_2, differing only in the position of the peak wavelengths, this is not the case for

$NiPorCl_8$ and $NiPorBr_8$ whose spectra differed substantially from that of the parent compound as shown in Figure 3-2. Other examples of UV-vis spectra for the two octahalogenated porphyrins are illustrated in Figure 3-3 when measured in hexane, C_2H_5OH, CH_3OH, and pyridine and a summary of the data in all of the investigated solvents is given in Tables 3-2 and 3-3

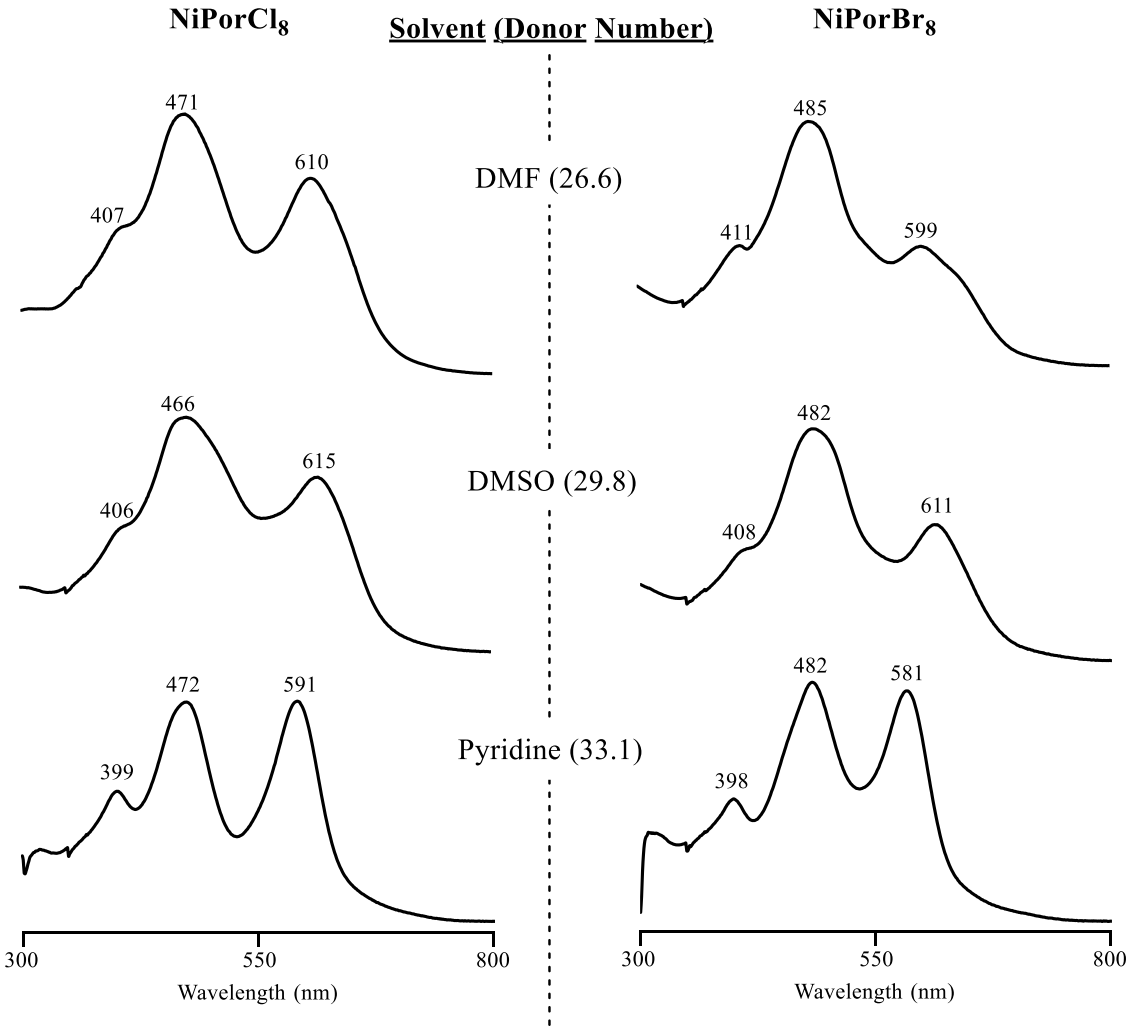

Figure 3-4. UV-vis spectra of $NiPorCl_8$ and $NiPorBr_8$ under solvent conditions which favor six-coordinate species. The donor numbers (DN) are given in Tables 3-2 and 3-3.

The spectra of $NiPorCl_8$ and $NiPorBr_8$ in hexane (top of Figure 3-3) are assigned to the four-coordinate Ni(II) complexes, while the two spectra in pyridine (bottom of Figure 3-3) are assigned

to six-coordinate bis-solvated $(py)_2NiPorCl_8$ and $(py)_2NiPorBr_8$. Similar spectra assigned to the six-coordinate Ni(II) complexes are also seen in DMF and DMSO (Figure 3-5).

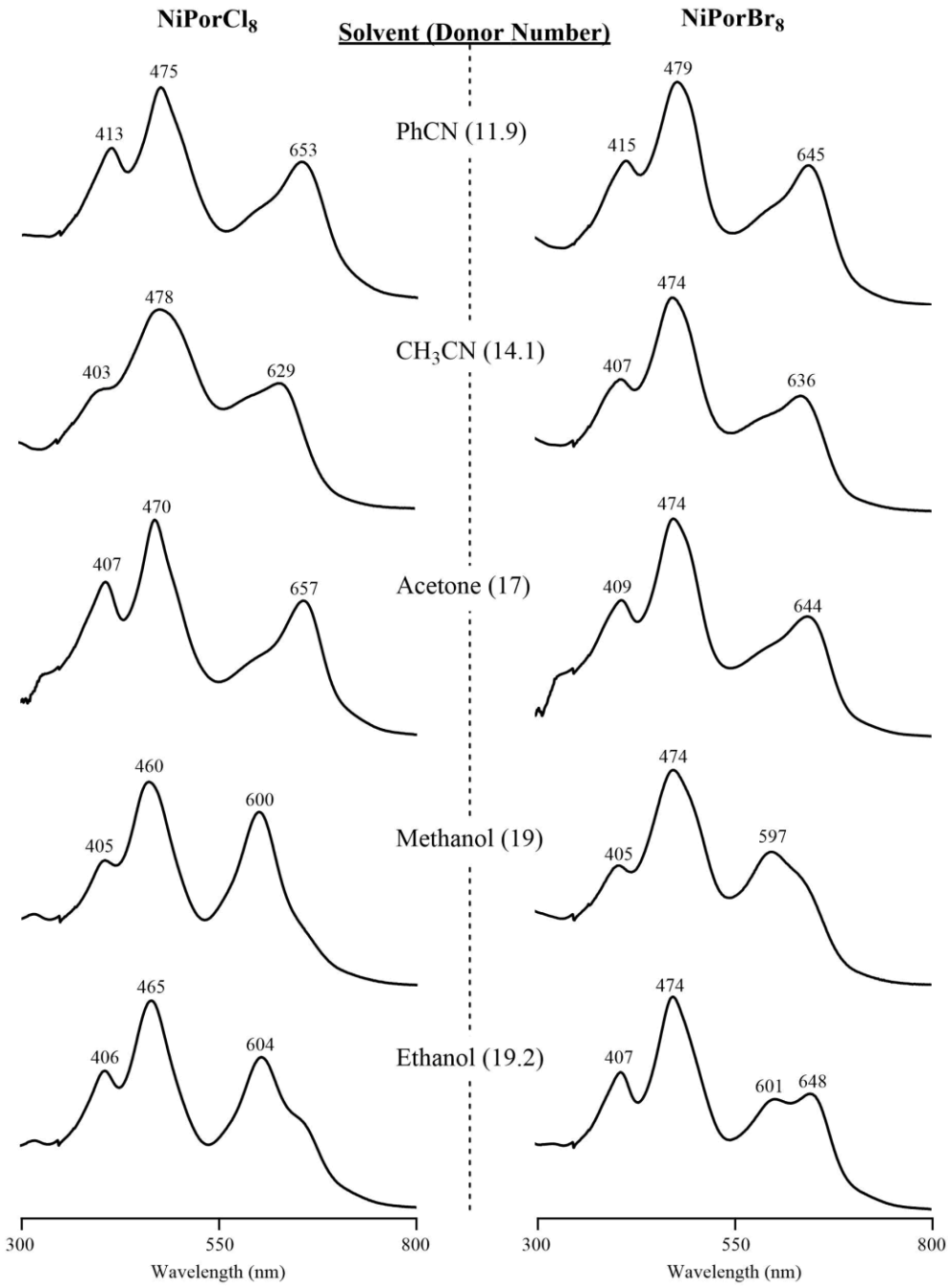

Figure 3-5. UV-vis spectra of $NiPorCl_8$ and $NiPorBr_8$ under solvent conditions which show a mixture of four and six-coordinate species. The donor numbers (DN) are given in Tables 3-2 and 3-3.

No five-coordinate Ni(II) complexes were detected in any of the solvents but a mixture of the four- and six-coordinate forms of the porphyrin is seen in a number of the neat solvents. Examples of spectra for this mixture are given in Figure 3-2 for $NiPorCl_8$ and $NiPorBr_8$ in C_2H_5OH and $NiPorBr_8$ in CH_3OH where the four-coordinate forms of the porphyrin have an intense Q band at 634-654 nm and the six-coordinate complexes have a strong Q band at 597-604 nm.

Table 3-2. UV-visible data for $NiPorCl_8$ in different solvents

			λ_{max}, nm ($\varepsilon \times 10^{-4}$, $M^{-1}\cdot cm^{-1}$)				
			Soret band(s)			**Q band(s)**	
Coordination	**Donor Number**[a]	**Solvent**	**I**	**II**	**$\varepsilon_I/\varepsilon_{II}$**	**III**	**IV**
4	0	Hexane	405 (5.49)	471 (7.24)	0.76	590 (1.58)	664 (5.50)
4	0	CH_2Cl_2	412 (4.57)	472 (5.62)	0.81	591 (0.62)	667 (4.90)
4	4	$CHCl_3$	412 (5.01)	473 (6.46)	0.78	589 (1.51)	670 (5.01)
4	14.3	1,4-Dioxane	410 (5.62)	471 (7.08)	0.79	596 (1.78)	666 (5.50)
4	17.1	Ethyl acetate	405 (5.13)	469 (6.46)	0.79	588 (1.74)	658 (4.68)
4	19.2	Diethylether	404 (5.25)	468 (6.46)	0.81	585 (1.62)	657 (4.79)
4	20	THF	409 (4.90)	471 (6.31)	0.77	598 (2.14)	664 (4.37)
4/6	11.9	Benzonitrile	413 (4.17)	475 (5.75)	0.72	598 (2.45)	653 (3.80)
4/6	14.1	CH_3CN	403 (3.72)	478 (6.17)	0.60	589 (3.39)	629 (3.89)
4/6	17	Acetone	407 (5.37)	470 (7.41)	0.72	594 (2.63)	657 (4.68)
4/6	19	CH_3OH	405 (3.47)	460 (5.62)	0.62	600 (4.79)	
4/6	19.2	C_2H_5OH	406 (4.27)	465 (6.46)	0.66	604 (4.68)	656 (2.75)
6	26.6	DMF[b]	407 (1.91)	471 (3.39)	0.56	610 (2.57)	
6	29.8	DMSO[b]	406 (3.09)	466 (6.03)	0.52	615 (4.47)	
6	33.1	Pyridine	399 (3.39)	472 (5.62)	0.60	591 (5.75)	

[a] Donor Number values obtained from the literature[71]

[b] Obtained at a concentration of 10^{-3} M before oxidation to porpho-5,15-bis-paraquinone methide (see text)

Table 3-3. UV-visible data for $NiPorBr_8$ in different solvents

			λ_{max}, nm ($\varepsilon \times 10^{-4}$, $M^{-1} \cdot cm^{-1}$)				
			Soret band(s)			**Q band(s)**	
Coordination	**Donor Number**[a]	**Solvent**	**I**	**II**	**$\varepsilon_I/\varepsilon_{II}$**	**III**	**IV**
4	0	Hexane	409 (5.13)	474 (6.61)	0.77	583 (1.48)	658 (5.01)
4	0	CH_2Cl_2	413 (4.27)	477 (5.13)	0.83	590 (0.36)	661 (4.79)
4	4	$CHCl_3$	414 (4.79)	476 (6.03)	0.79	589 (1.62)	663 (4.79)
4	14.3	1,4-Dioxane	413 (4.90)	475 (6.17)	0.79	584 (1.58)	662 (4.79)
4	17.1	Ethyl acetate	408 (4.68)	473 (5.89)	0.79	583 (1.82)	653 (4.27)
4	19.2	Diethylether	407 (4.68)	473 (5.89)	0.79	582 (1.70)	654 (4.37)
4	20	THF	412 (4.47)	476 (6.03)	0.74	591 (2.09)	658 (4.07)
4/6	11.9	Benzonitrile	415 (3.24)	479 (5.01)	0.64	594 (2.09)	645 (3.09)
4/6	14.1	CH_3CN	407 (3.02)	474 (4.79)	0.63	587 (2.14)	636 (2.63)
4/6	17	Acetone	409 (3.55)	474 (5.62)	0.63	592 (2.29)	644 (3.09)
4/6	19	CH_3OH	405 (2.40)	474 (4.37)	0.54	597 (2.69)	634 (2.09)
4/6	19.2	C_2H_5OH	407 (3.98)	474 (6.17)	0.64	601 (3.24)	648 (3.39)
6	26.6	DMF	411 (2.82)	485 (5.89)	0.48	599(2.95)	
6	29.8	DMSO	408 (2.34)	482 (5.01)	0.47	611 (3.02)	
6	33.1	Pyridine	398 (2.95)	482 (5.75)	0.51	581 (5.62)	

[a] Donor Number values obtained from the literature[71]

Other examples of the 4- and 6-coordinate porphyrin mixtures are given in Figure 3-6 for the two octahalogenated porphyrins in PhCN, CH_3CN, acetone, methanol, and ethanol. Q-band transitions are mainly forbidden in porphyrin spectra, whereas in the case of $NiPorCl_8$ and $NiPorBr_8$, these transitions become as fully allowed as that of the Soret band transitions and are quite intense as seen in Figure 3-2. Ring deformations as well as inductive effects of the *β*-chloro and *β*-bromo substituents result in a lowering of energy for the LUMO, thereby leading to a red

shift of all bands as compared to the parent compound. This also leads to a much easier than expected macrocycle reduction as compared to the unhalogenated parent porphyrin as described in later sections of this dissertation.

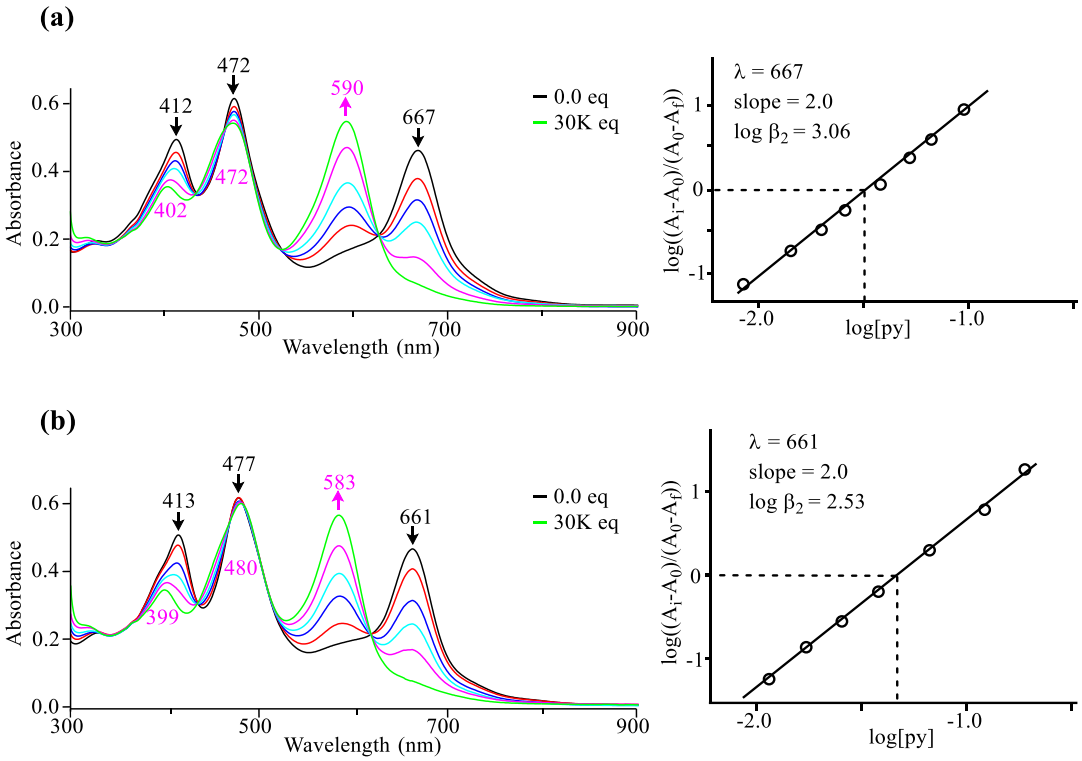

Figure 3-6. UV-vis spectral changes of (a) $NiPorCl_8$ (10^{-5} M) and (b) $NiPorBr_8$ (10^{-5} M) in CH_2Cl_2 during a titration with pyridine.

Evidence for the above assignment of four- and six-coordination is given by the results of a spectroscopically-monitored titration with pyridine which was carried out in CH_2Cl_2, the results of which are shown in Figure 3-6.

The UV-vis spectra of $NiPorCl_8$ and $NiPorBr_8$ in CH_2Cl_2 are virtually identical to the spectra in hexane and $CHCl_3$ (see Tables 3-2 and 3-3) and in these non-coordinating solvents the porphyrins are assigned to 4-coordinate complexes. The three major absorption bands labelled as

I, II, and IV in the table are located at 412, 472, and 667 nm for $NiPorCl_8$ and at 413, 477, and 661 nm for $NiPorBr_8$ in CH_2Cl_2 before the titration. The most red-shifted band IV at 667 nm (X = Cl) or 661 nm (X = Br) is assigned as being a diagnostic absorption band for the 4-coordinate complex in solution. An absorption band IV is not present when these porphyrins are dissolved in pyridine (see bottom two spectra in Figures 3-3 and 3-4) but there is instead an intense band III at 590 nm for $NiPorCl_8$ and 583 nm for $NiPorBr_8$. This band is assigned as being diagnostic of the 6-coordinate complexes in the CH_2Cl_2/pyridine mixture.

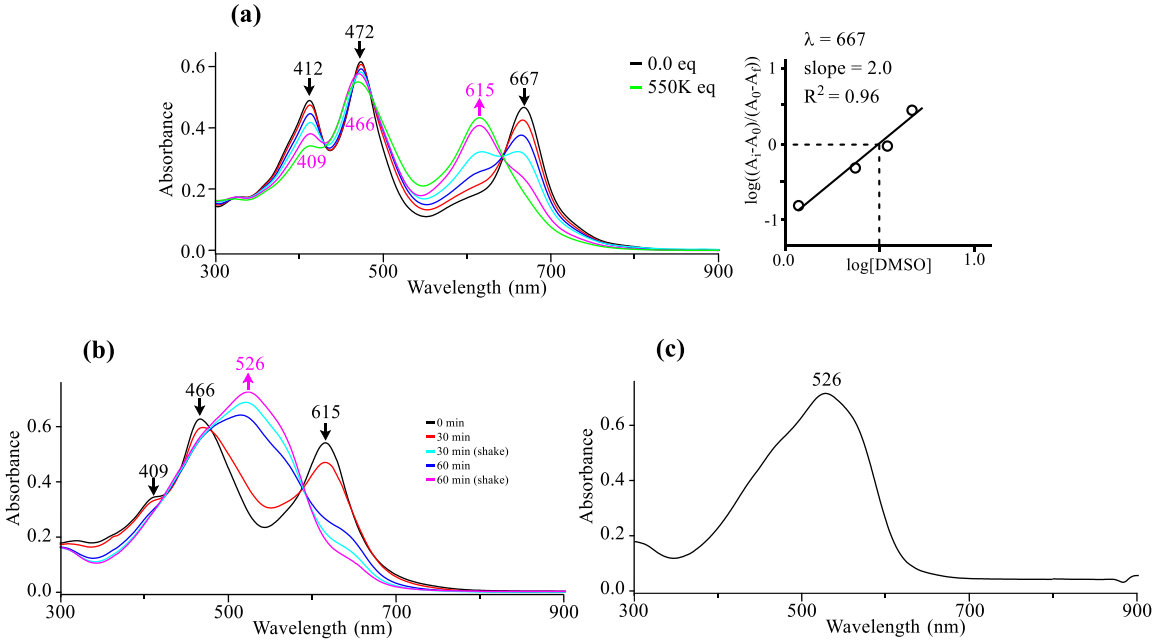

Figure 3-7. UV-visible spectral changes during (a) titration of 10^{-5} M $NiPorCl_8$ with DMSO to give $(DMSO)_2NiPorCl_8$ in CH_2Cl_2, (b) slow spectral changes of 10^{-3} M $(DMSO)_2NiPorCl_8$ to give a porpho-5,15-bis-paraquinone methide product in neat DMSO and (c) rapid (instantaneous) conversion of 10^{-5} M $(DMSO)_2NiPorCl_8$ to porpho-5,15-bis-paraquinone methide product in neat DMSO.

Well-defined isosbestic points are observed at 432, 463, 522, and 626 nm during the titration of $NiPorCl_8$ with pyridine (Figure 3-6a) while isosbestic points are seen at 434, 469, 482, and 618

nm during a similar titration of $NiPorBr_8$ (Figure 3-7b), these results are consistent with the presence of only two spectroscopically detectable forms of the porphyrin in solution. This fact, when combined with the slope of 2.0 in the diagnostic log-log plots, can only be consistent with the binding of two pyridine ligands to the uncomplexed porphyrins as shown in Equation 3-2.

Additional evidence for the addition of two pyridine axial ligands is given by comparing the number of unpaired electrons on the Ni(II) center of the porphyrin before and after axial coordination. Four-coordinate Ni(II) porphyrins have been characterized as low spin while the six-coordinate derivatives of the same macrocycle are characterized as high spin.[72, 73] Thus, it was anticipated that a spin state conversion might be observed upon complexation of the $NiPorX_8$ derivative with pyridine and this is exactly what was observed when the magnetic properties were evaluated utilizing the Evans method.[74, 75] The central metal ion of $NiPorCl_8$ and $NiPorBr_8$ are low spin with zero unpaired electrons but in solutions of pyridine the calculated number of unpaired electrons was 1.85 and 2.04 unpaired electrons for the octachloro and octabromoporphyrins, respectively, both values being consistent with the formation of a high spin Ni(II) complex after axial coordination.[72, 73]

The excellent fit of the titration data to the log-log plots in Figure 3-7 also clearly rule out the presence of a spectroscopically detectable 5-coordinate intermediate in the reaction. The measured binding constants for addition of the two pyridine ligands according to Equation 3-2 are log β_2 = 3.06 for $NiPorCl_8$ and log β_2 = 2.53 for $NiPorBr_8$.

$$NiPorX_8 + 2py \rightleftharpoons (py)_2NiPorX_8 \qquad (3\text{-}2)$$

Two DMSO molecules will also weakly bind to the octahalogenated porphyrins in CH_2Cl_2/DMSO mixtures. The log β_2 values for DMSO addition is less than 1.0 as evidenced by

the fact that spectral changes are only observed after a very high concentration of DMSO (>2.0 molar) has been added to the CH_2Cl_2 solution containing 10^{-5} M of the porphyrin (see Figure 3-7a). However, there are again well-defined isosbestic points during the spectral transition between the uncomplexed and DMSO-complexed porphyrin and the slope of the log-log plot is 2.0 (using limited data), again suggesting the presence of only 4- and 6-coordinate Ni(II) porphyrins in the CH_2Cl_2/DMSO mixture. Similar spectral changes are seen for $NiPorBr_8$ during a titration with DMSO (Figure 3-8). The paramagnetic nature of the two 6-coordinate Ni(II) porphyrins was also investigated in DMSO solutions using the Evans method where the magnetic susceptibilities were found to be 2.671 for $NiPorCl_8$ and 2.765 for $NiPorBr_8$ corresponding to 1.85 and 1.94 unpaired electrons, respectively.

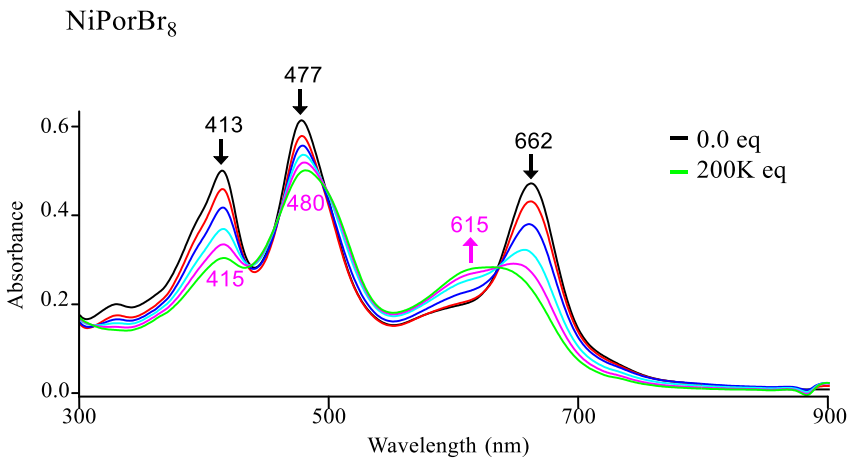

Figure 3-8. UV-vis spectral changes of $NiPorBr_8$ during a titration with DMSO.

The spectrum of the bis-DMSO adduct in Figure 3-7a is stable under N_2 (Figure 3-7a) but when O_2 is allowed into the cell, all bands of $(DMSO)_2NiPorCl_8$ disappear and are replaced by a single broad absorption band ranging from 350 to 650 nm and centered at 526 nm. The time of this change varies with the porphyrin concentration, taking up to 60 minutes for a porphyrin

concentration of 10^{-3} M (Figure 3-7b) but it is almost instantaneous when the porphyrin concentration is 10^{-5} M in DMSO (Figure 3-7c). A similar set of spectral changes occurred for $NiPorCl_8$ in DMF (Figure 3-9) and the spectral pattern of the final product formed in DMSO or DMF is identical to that of a species formed after addition of OAc^-, CN^- or OH^- to $NiPorCl_8$ in CH_2Cl_2. Also in the case of OAc^-, this reaction is proceeded by a complexation of two OAc^- ligands at the Ni(II) center with no change in oxidation state at metal center as shown in Figure 3-10 where $[(OAc)_2Ni(II)PorCl_8]^{2-}$ is characterized by bands at 505 and 637 nm.

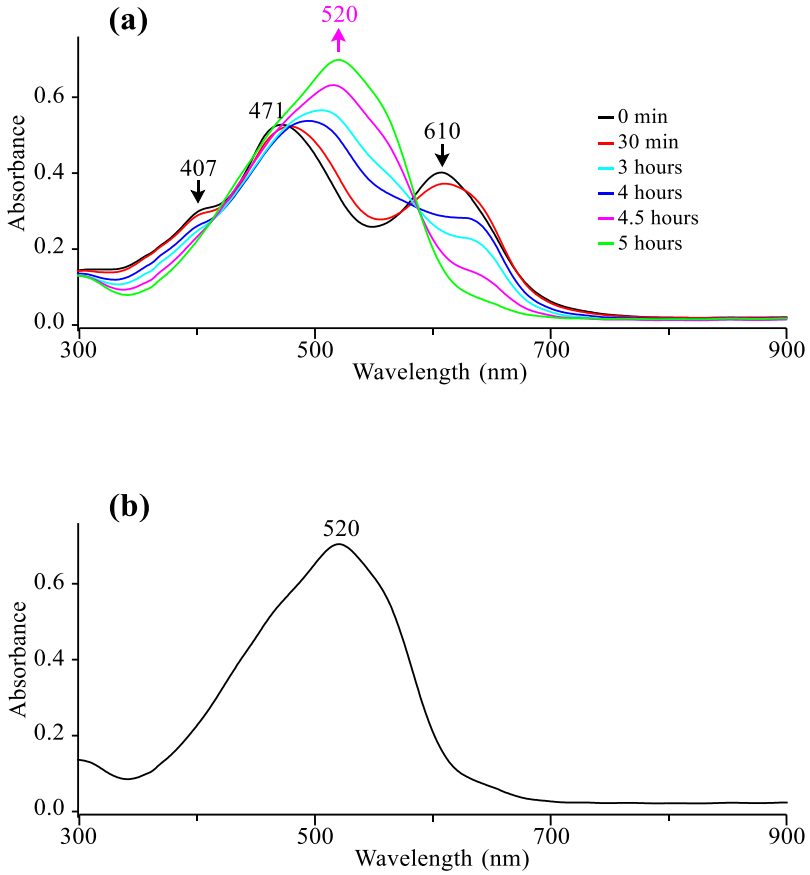

Figure 3-9. $NiPorCl_8$ in DMF where (a) is time dependent UV-vis spectral changes of $NiPorCl_8$ at 10^{-3} M DMF and (b) is the spectrum at 10^{-5} M in neat DMF.

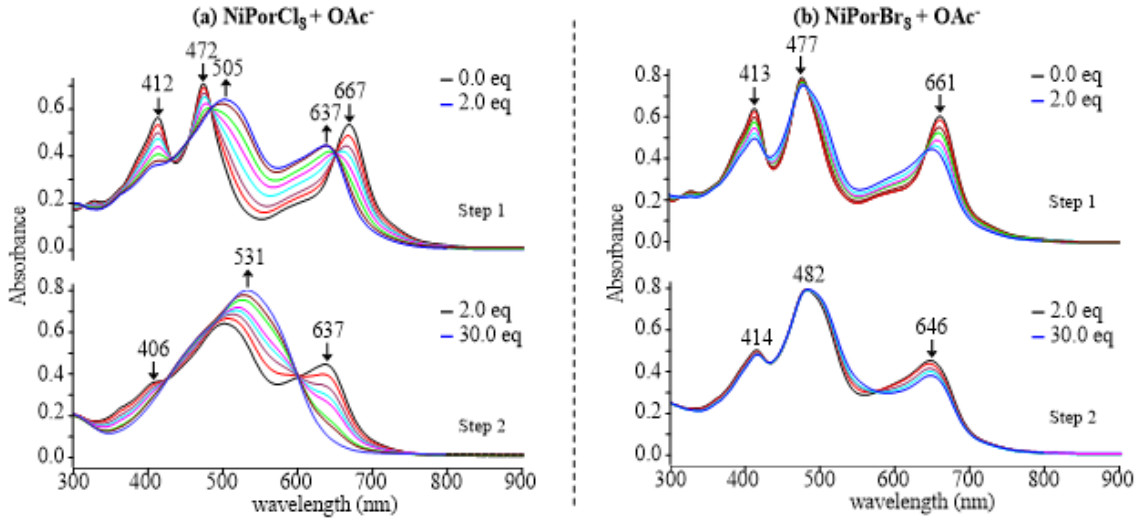

Figure 3-10. UV-vis spectral changes of (a) $NiPorCl_8$ (10^{-5} M) and (b) $NiPorBr_8$ (10^{-5} M) in CH_2Cl_2 upon incremental addition of OAc^- ions in the form of TBA^+OAc^-.

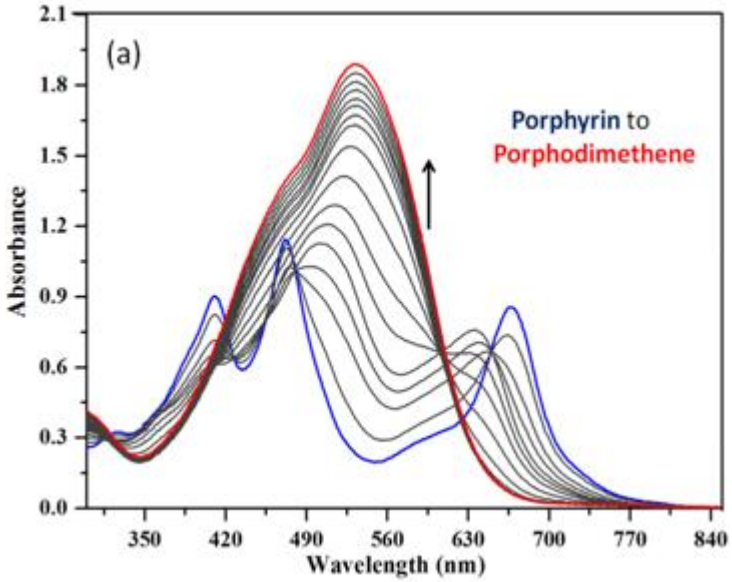

Figure 3-11. UV-Vis spectral response of $NiPorCl_8$ (2.0×10^{-5} M) upon incremental addition of CN^- ions (9.6×10^{-5} M, 4.8 equiv.) in CH_2Cl_2.

This chemically generated product with a 526 nm band in Figures 3-10b and 3-10c is assigned as a Ni(II) porpho-5,15-bis-paraquinone methide and the same final product is proposed during a titration of $NiPorCl_8$ with OAc^- (Fig 3-10a) or CN^- (Figure 3-11) with a proposed mechanism as shown in Scheme 3-2. The first step in the reaction of $NiPorCl_8$ with OAc^- is formation of the bis-ligated complex (505 and 637 nm) and this is then followed by formation of the final product having a band at 531 nm, as shown in Figure 3-10a for $NiPorCl_8$ where isosbestic points are located at 430, 484, 649 nm for the first step and at 424, 600 nm for the second.

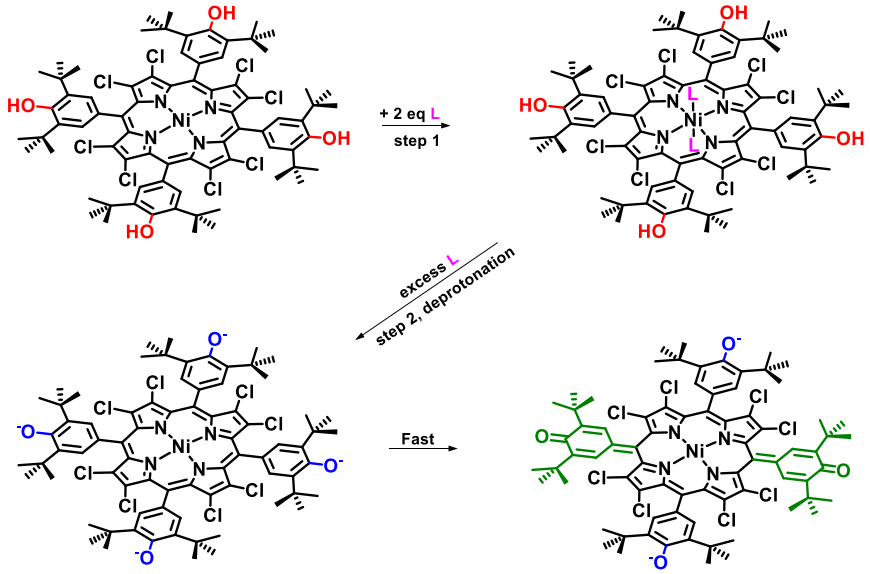

Scheme 3-2. Proposed mechanism for the formation of chemically generated porpho-5,15-bis-paraquinone methide from $NiPorCl_8$ in DMSO or DMF where L = a solvent molecule and in CH_2Cl_2 where L = OAc^- or CN^- added in the form of TBA^+OAc^- or TBA^+CN^-.

Much smaller spectral changes are observed during the titration of $NiPorBr_8$ with OAc^- (Figure 3-10b) and there is no spectral evidence for the formation of a bis-paraquinone oxidation product under these solution conditions. $(OAc)_2NiPorBr_8$ is air stable in its porphyrinic form even after addition of excess ligand to solution and is proposed to hydrogen bond with the base as shown

in Scheme 3-3. Isosbestic points during the first set of spectral changes in Figure 3-10a are located at 429, 484, 641 nm, and an isosbestic point is also located at 572 nm for the second set of spectra in Figure 3-10b.

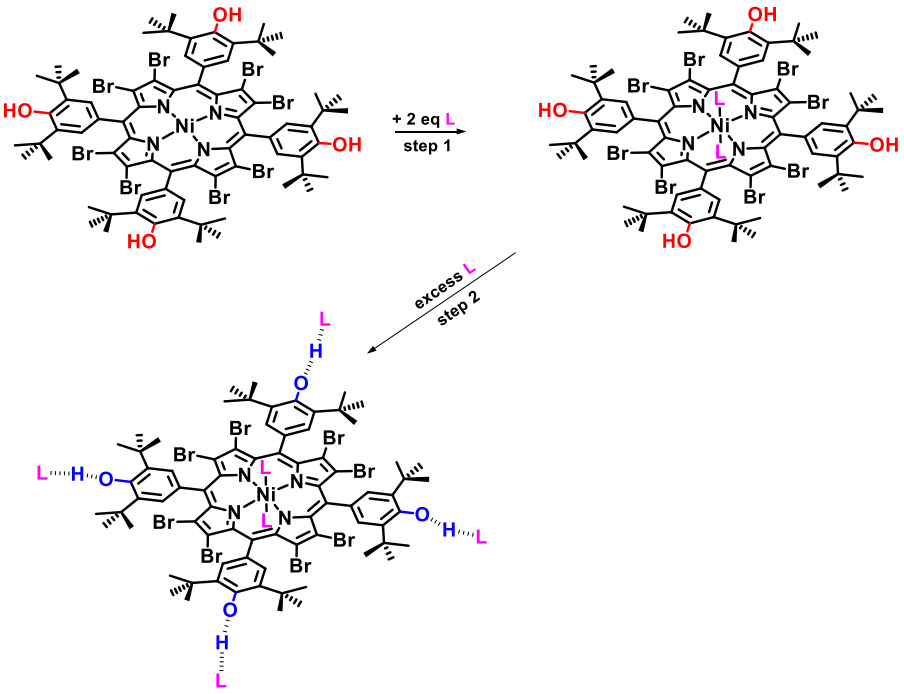

Scheme 3-3. Proposed interaction of $NiPorBr_8$ with DMSO or DMF where L = a solvent molecule or with acetate or cyanide ions in CH_2Cl_2 where L = OAc^- or CN^-.

Additional spectral evidence supporting the lack of bis-paraquinone oxidation product formation in the case of $NiPorBr_8$ is shown in Figure 3-12, where titrations of CN^- or F^- to CH_2Cl_2 solutions containing $NiPorBr_8$ yield a final product with a similar spectrum to the final spectra of the OAc^- titration shown in Figure 3-10b.

In summary, distinctly differed types of spectral patterns are observed for the two $NiPorX_8$ derivatives, depending upon the solution conditions, porphyrin concentration and electron-withdrawing β-halogen groups (Br or Cl) on the compound.

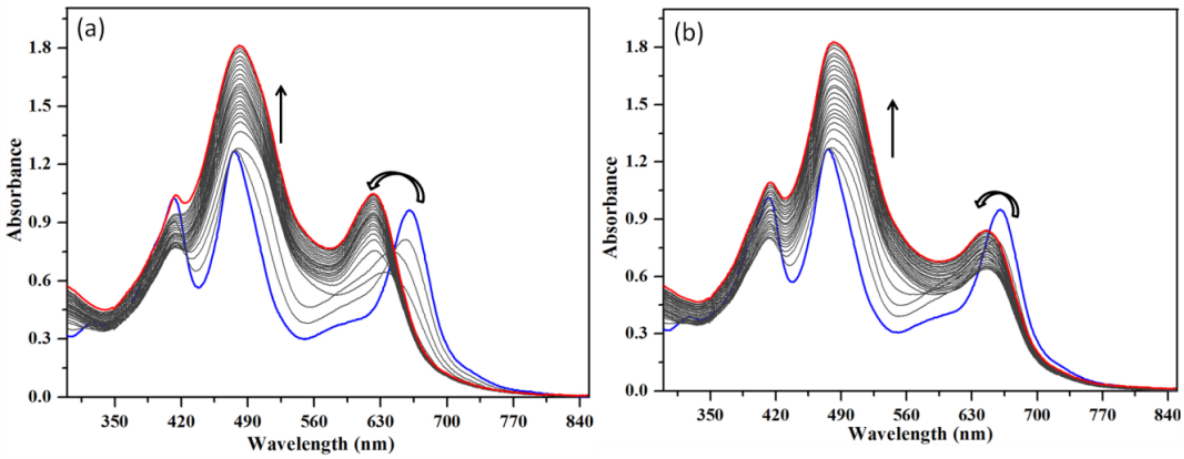

Figure 3-12. UV/Vis spectral response of $NiPorBr_8$ (2.0×10^{-5} M) upon incremental addition of (a) CN^- ions (0-5.02×10^{-4} M, 25 equiv.) in CH_2Cl_2; (b) F^- ions (0-4.99×10^{-4} M, 25 equiv.) in CH_2Cl_2.

These are (i): in neat DMF, neat DMSO or in CH_2Cl_2 containing acetate or cyanide ions where transient six-coordinate $(L)_2NiPorCl_8$ complexes are formed prior to conversion to a porpho-5,15-bis-paraquinone methide when exposed to oxygen, (ii) in neat pyridine, where both porphyrins are characterized by relatively stable six-coordinate complexes, (iii) in non-bonding or weakly bonding solvents where both porphyrins form stable four-coordinate complexes and (iv) in more strongly bonding solvents where there is a mixture of the four and six-coordinate Ni(II) porphyrins at a 10^{-5} M concentration of the compound. Examples of the latter three spectral patterns are given in Figures 3-1, 3-3 and 3-4 and a summary of the spectral data for all of the porphyrins in the different solvents is given in Tables 3-2 and 3-3.

As mentioned above, the wavelength of the absorption bands III and IV can be used as a diagnostic criterion for identifying the coordination number of the octahalogenated porphyrins in a given solvent. This band varies from 653-657 in ten of the investigated solvents where $NiPorX_8$ is assigned as pure four-coordinate and from 581-615 nm in the three solvents where the octahalogenated porphyrins are assigned as pure six-coordinate species.

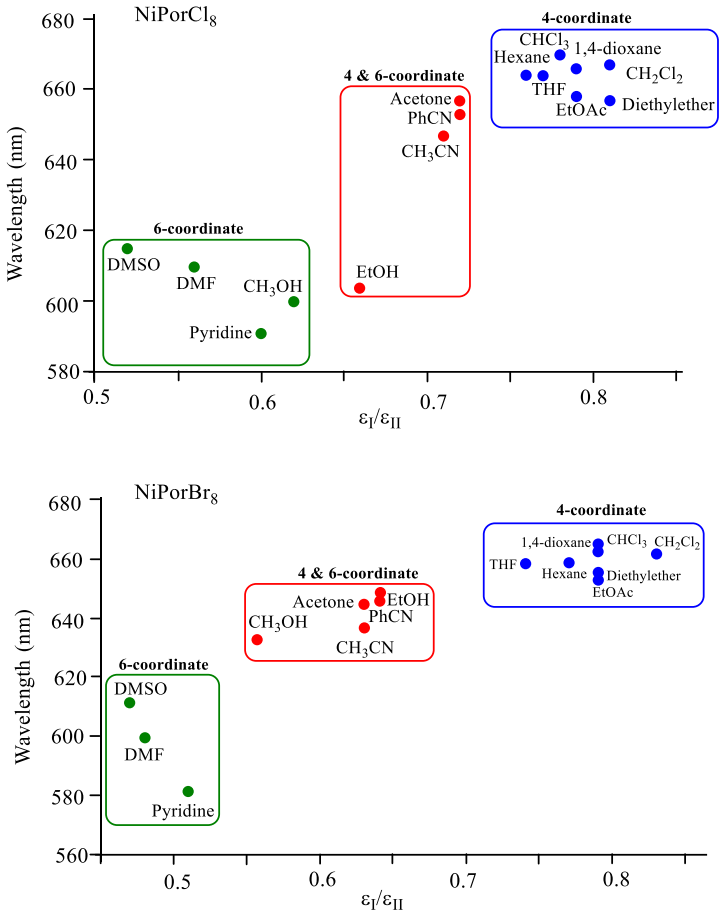

Figure 3-13. Wavelength of most intense Q band for $NiPorCl_8$ and $NiPorBr_8$ vs. the molar absorptivity ratio between the two Soret bands in a given solvent (labeled as I and II in Tables 3-2 and 3-3). Solvents where the porphyrins are 4-coordinate (in blue), 6-coordinate (in green) and a mixture of 4 and 6-coordinate (in red). Values of λmax and DN are given in Tables 3-2 and 3-3.

Another distinction between the 4 and 6 coordinate Ni(II) porphyrins is given by the ratio of absorbances for the two Soret bands of the compounds. This ratio ranges from 0.47-0.60 for the 6-coordinate complexes and from 0.74-0.83 in solvents where the porphyrin is assigned as purely 4-coordinate (see Tables 3-2 and 3-3 and Figures 3-1, 3-3 and 3-4). A plot of the most intense Q band wavelength vs. the intensity ratio of the two Soret bands for both $NiPorCl_8$ and $NiPorBr_8$ illustrated in Figure 3-13 for both octahalogenated porphyrins and shows three distinct groupings,

i.e., solvents where the porphyrins are 4-coordinate (shown in blue), 6-coordinate (shown in green) and solvents which show a mixture of 4- and 6-coordinate complexes which are shown in red.

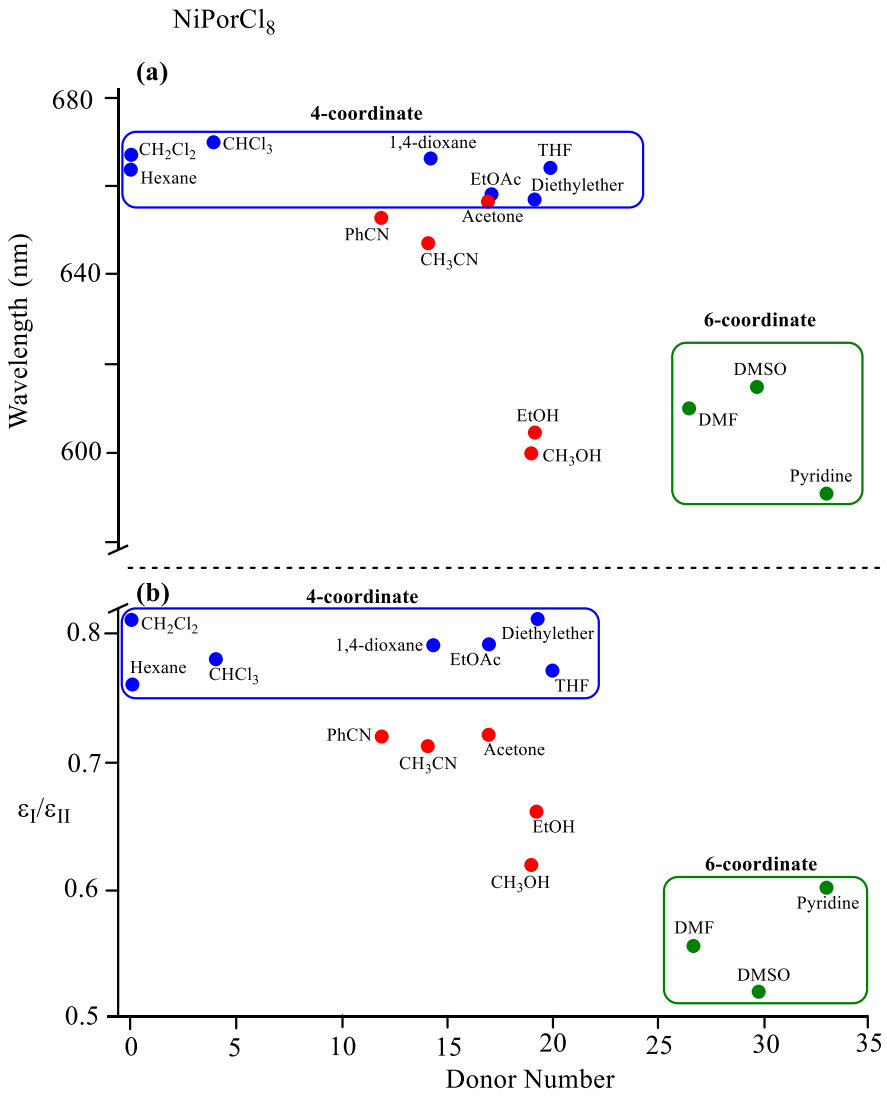

Figure 3-14. Plots of (a) the wavelength of most intense Q band and (b) the molar absorptivity ratio between the two b bands for $NiPorCl_8$ vs. the Gutman Donor Number (DN) of the solvent. (Solvents for the 4-coordinate porphyrins are in blue, those for the 6-coordinate porphyrins are in green and solvents which show a mixture of 4 and 6-coordinate porphyrins are in red. Values of λ_{max} and DN are given in Tables 3-2 and 3-3).

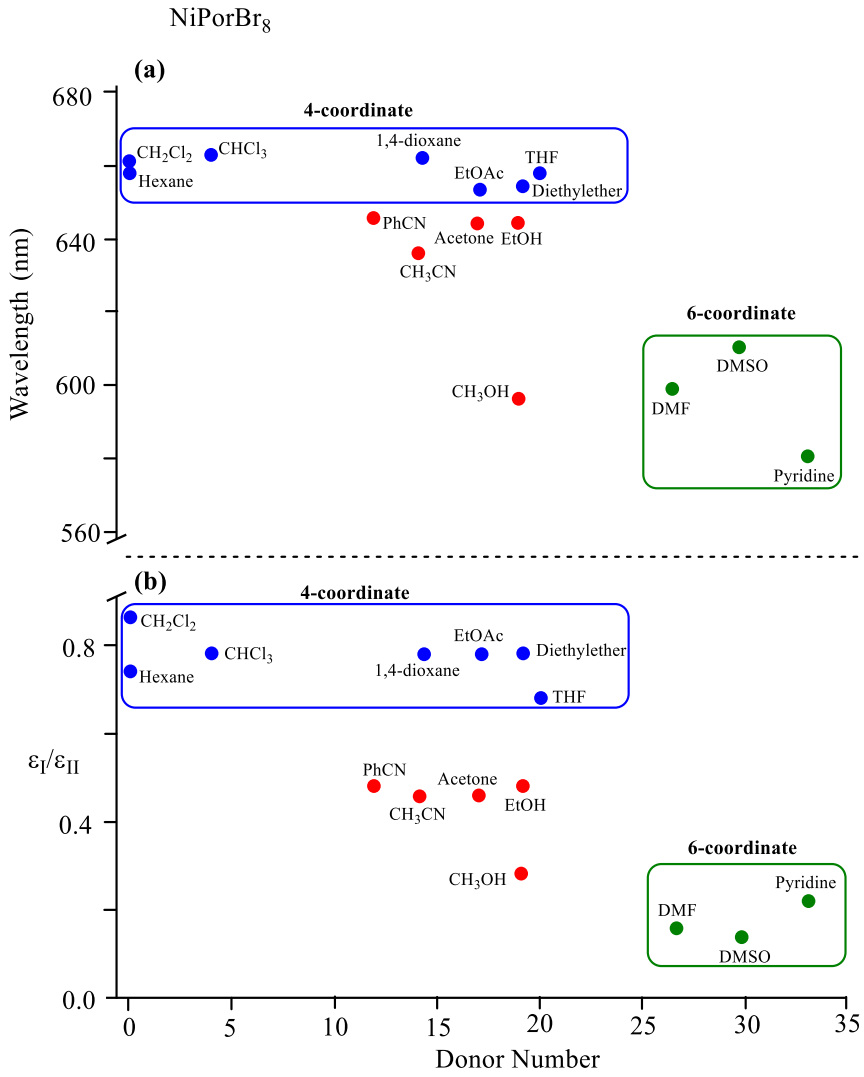

Figure 3-15. Plots of (a) the wavelength of most intense Q band and (b) the molar absorptivity ratio between the two b bands for $NiPorBr_8$ vs. the Gutman Donor Number (DN) of the solvent. (Solvents for the 4-coordinate porphyrins are in blue, those for the 6-coordinate porphyrins are in green and solvents which show a mixture of 4 and 6-coordinate porphyrins are in red. Values of λ_{max} and DN are given in Tables 3-2 and 3-3).

Correlations are also possible between the wavelengths of the most intense Q band and the Gutman donor number (DN) of the solvent.[71] These plots are shown in Figures 3-14 and 3-15 and suggest that six-coordinate Ni(II) complexes are formed in the high donor number solvents, pyridine, DMSO and DMF (where the DN = 33.1, 29.8, and 26.6, respectively). Surprisingly, the

bis-pyridine adduct of $NiPorCl_8$ is relatively stable in this solvent as shown quantitatively by the lack of change in the UV-visible spectrum over time and also qualitatively by the color of solution which remains green as compared to a red color when a bis-paraquinone oxidation product is generated (see later section of this chapter and reference [67] where the oxidized product is called a porphodimethene).

3.2.3 Electrochemistry

The effect of specific *β*-pyrrole substituents (Cl or Br) and axial coordination on the electrochemistry and porphodimethene or porpho-5,15-bis-paraquinone methide formation was investigated by cyclic voltammetry and spectroelectrochemistry under three solution conditions. These were: (1) in CH_2Cl_2 or pyridine containing 0.1 M $TBAPF_6$, (2) in CH_2Cl_2 containing 0.1 M $TBAPF_6$ and added protons in the form of trifluoroacetic acid (TFA) and (3) in CH_2Cl_2 containing 0.1 M $TBAPF_6$ and added base in the form of TBAX where X = OAc^-, CN^- or OH^-.

The effect of adding Br or Cl groups to the eight β-pyrrole positions of a *meso*-substituted tetraphenylporphyrin is to positively shift the reduction potentials, with the magnitude of the potential shift for the first electron addition generally ranging from 400-500 mV, the exact value depending upon the solvent, type of central metal ion and presence or absence of axial ligand binding.[1]

A good example of the β-halogen substituent effect on reduction is given by a comparison of potentials for three NiTPP derivatives in Chart 3-1b. The first reduction of the parent NiTPP compound is located at $E_{1/2}$ = -1.26 V[76] while $NiTPPCl_8$ and $NiTPPBr_8$ are both reduced at $E_{1/2}$ = -0.82 V,[76] a positive shift of 440 mV. The second reversible reduction of $NiTPPCl_8$ and $NiTPPBr_8$ is located at $E_{1/2}$ = -1.14 and -1.17 V, respectively,[76] and the 320-350 mV potential separation

between the two one-electron additions to the $MTPPX_8$ complexes is within the range of values generally observed between $E_{1/2}$ values for formation of a tetraphenylporphyrin π-anion radical and dianion.

The first one-electron reduction of the parent porphyrin NiPor in CH_2Cl_2 is located at $E_{1/2}$ = -1.34 V (see Figure 3-16) and $E_{1/2}$ values between -0.83 and -0.93 V might be predicted for the first reduction of $NiPorCl_8$ and $NiPorBr_8$ based on the known electron-withdrawing effect of the eight β-halogen groups as described above for NiTPP, $NiTPPCl_8$, and $NiTPPBr_8$. This prediction is clearly not borne out as shown in Figure 3-17 where extremely facile reductions are observed, these processes occurring at $E_{1/2}$ = -0.25 for $NiPorCl_8$ and -0.32 V for $NiPorBr_8$ at -60 °C and E_p = -0.28 and -0.34 V when measured for the same two porphyrins at room temperature for a scan rate of 0.1 V/s.

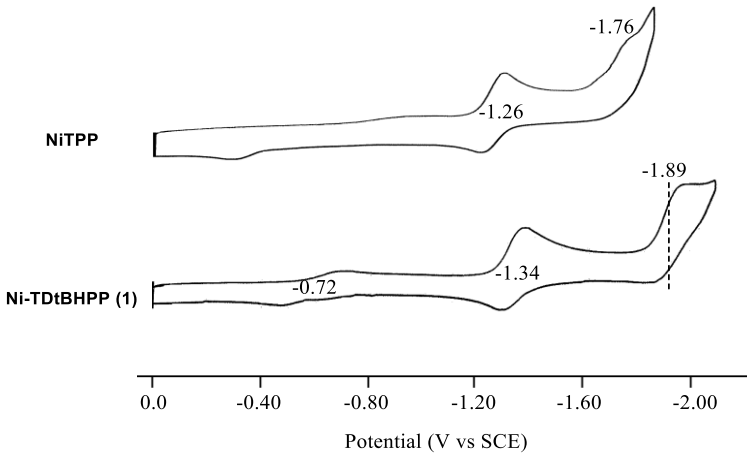

Figure 3-16. Cyclic voltammograms of NiTPP and NiPor in CH_2Cl_2, containing 0.1M TBAP. Scan rate = 100 mV/s.

The second and third reductions of $NiPorX_8$ are not reversible under any conditions and are located at E_p = -0.62 V and E_p = -1.04 V for $NiPorCl_8$ and E_p = -0.80 V and E_p = -1.06 V for

$NiPorBr_8$ at a scan rate of 0.1 V/s. These processes are then followed by one or two additional reductions as shown in Figure 3-17.

A different voltammetric pattern is seen for $NiPorCl_8$ in pyridine (Figure 3-17a) where currents for the second irreversible peak have been reduced to almost zero and the potential for the first irreversible reduction is shifted negatively by 160 mV as compared to what is observed in CH_2Cl_2, the value of the peak potential being measured as E_p = -0.44 V for a scan rate of 0.1 V/s.

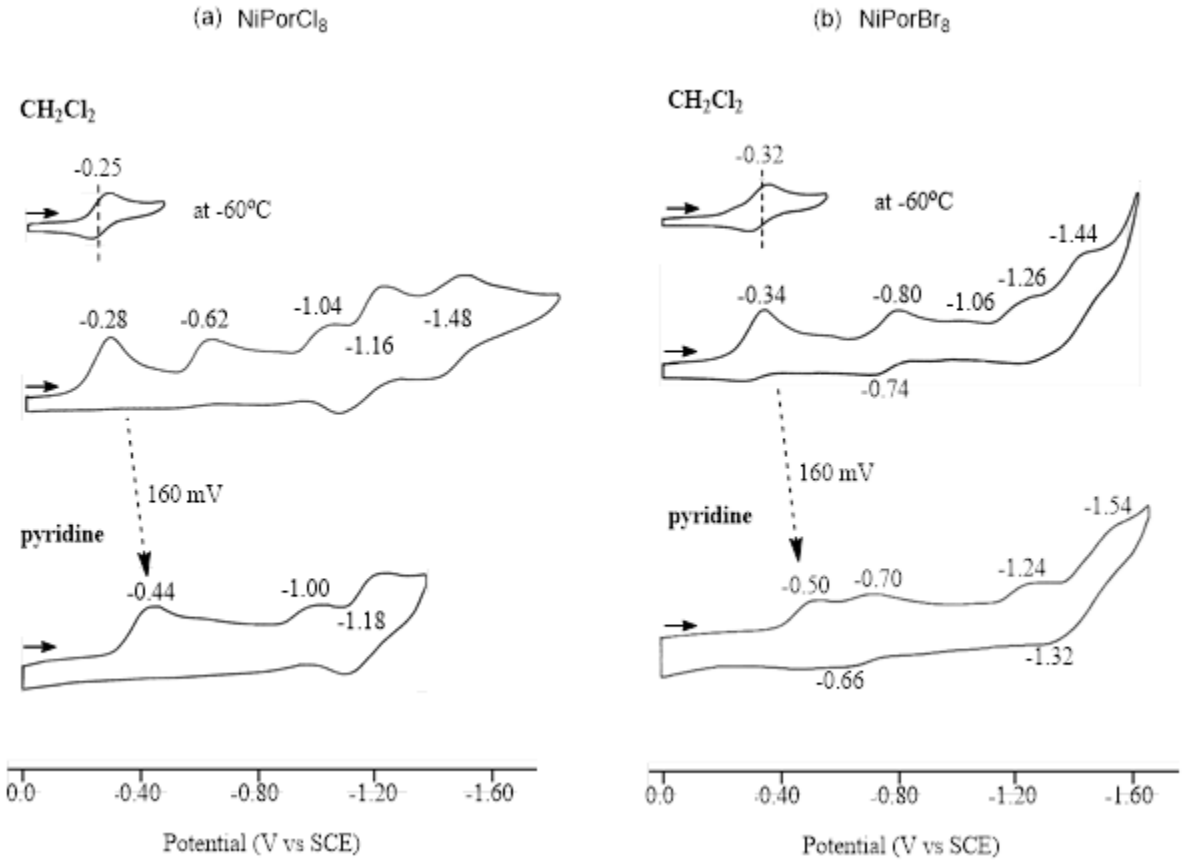

Figure 3-17. Cyclic voltammograms of (a) $NiPorCl_8$ and (b) $NiPorBr_8$ in CH_2Cl_2 and pyridine containing 0.1M $TBAPF_6$. Scan rate = 100 mV/s.

A different voltammetric pattern is also seen for $NiPorBr_8$ in pyridine (Figure 3-17b) where the first reduction is again shifted negatively by 160 mV as compared to what is seen in CH_2Cl_2

and the second has shifted towards an easier reduction. The 160 mV negative shift of the first reduction potential for both porphyrins in pyridine can be explained by the effect of axial coordination to the neutral compound (log β_2 = 2.5 to 3.0, see Figure 3-6) but could also be related to the relative differences in basicity of the two solvents.

In order to investigate this latter possibility, the electrochemistry of $NiPorCl_8$ and $NiPorBr_8$ was examined in CH_2Cl_2 containing added acid in the form of TFA or added base in the form of TBA^+OAc^-, TBA^+CN^-, or TBA^+OH^-. As will be demonstrated, two extremes of well-defined voltammetric patterns are observed for $NiPorCl_8$ and $NiPorBr_8$, depending upon the specific β-halogen substituent and the type of cation or anion added to solution.

One extreme is given by the two $NiPorX_8$ complexes in CH_2Cl_2 containing added acid, an example of which is given by the cyclic voltammograms in Figure 3-18 where the concentration of TFA in the CH_2Cl_2 solution ranged from 0.40 to 2 equivalents. As seen in the figure, the addition of 2 eq. H^+ leads to a loss of current for all but the first electron addition which remains irreversible and is located at E_p = -0.18 V for $NiPorCl_8$ and -0.26 V for $NiPorBr_8$ in CH_2Cl_2 containing 2.0 eq. H^+. The irreversible first reduction is interpreted in terms of two overlapping one-electron transfers and one or more following chemical reactions which lead to an overall irreversible redox process. More importantly, however, is the presence of two well-defined one-electron transfers at $E_{1/2}$ = -0.88 and -1.22 V for $NiPorCl_8$ and -0.94 and -1.32 V for $NiPorBr_8$ in the CH_2Cl_2 solutions containing 2 eq H^+. The first of these processes is well-defined and reversible but the second has an increased cathodic peak current and decreased anodic peak current on the return scan at higher acid concentrations, thus indicating a chemical reaction involving the electrogenerated product of the second reversible reduction. The nature of this chemical reaction was not investigated further

but is most likely related to proton attack at one or more *meso*-positions of the macrocycle leading, perhaps, to a porphomethene where three *meso*-bridges have been saturated.

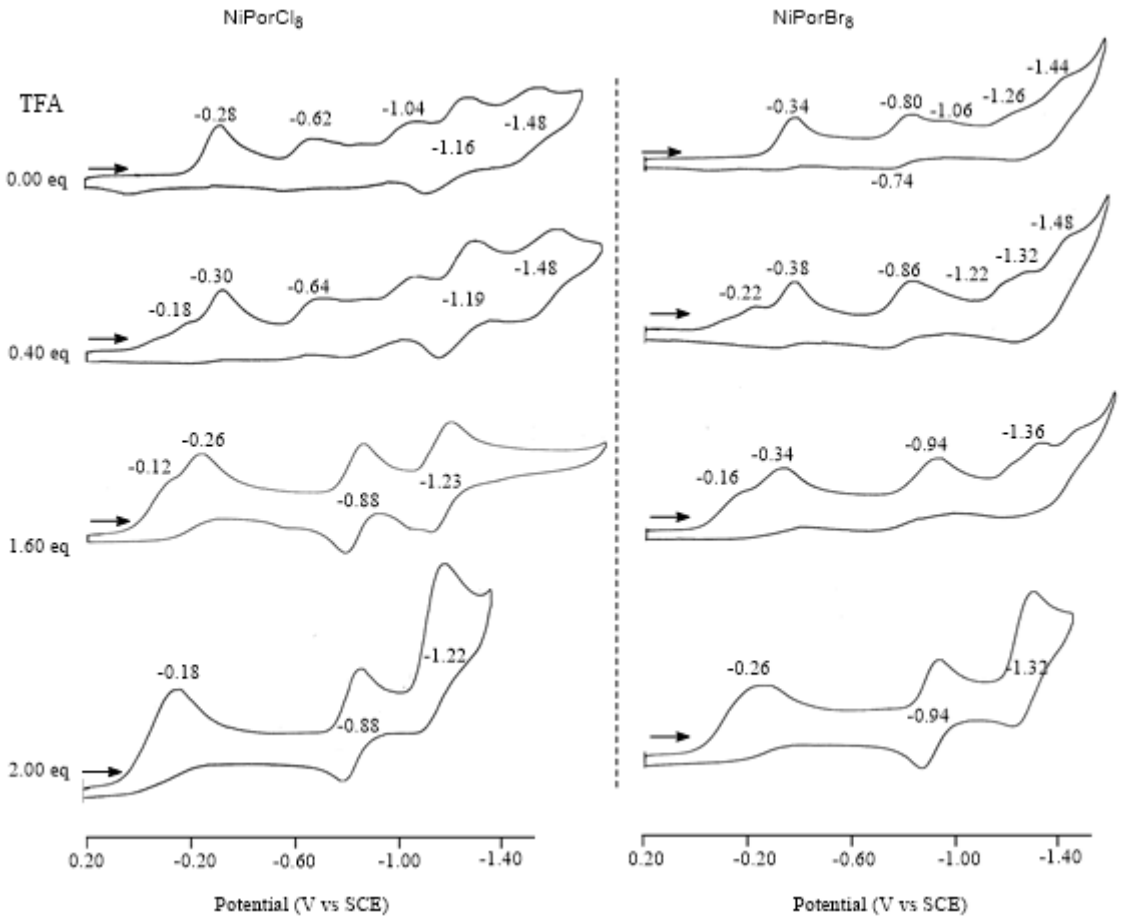

Figure 3-18. Cyclic voltammograms of $NiPorCl_8$ and $NiPorBr_8$ containing added TFA in CH_2Cl_2 and containing 0.1 M $TBAPF_6$. Scan rate = 100 mV/s.

The two reductions of $NiPorX_8$ ($E_{1/2}$ = -0.88 and -1.22 V for $NiPorCl_8$ and -0.94 and -1.32 V for $NiPorBr_8$) in the CH_2Cl_2 solutions with added acid can be interpreted in terms of electron additions to an intact conjugated macrocycle and the absence of coupled chemical reactions following electron transfer. Moreover, the 330 to 380 mV separation in $E_{1/2}$ values between the two reversible reductions of $NiPorCl_8$ and $NiPorBr_8$ in acidic CH_2Cl_2 is quite similar to the

observed potential separation of 320-350 mV between the two reversible one-electron reductions of $NiTPPCl_8$ and $NiTPPBr_8$ (See Table 3-4).

Table 3-4. Potentials (V vs SCE) for reduction of the Ni(II) TPP complexes in CH_2Cl_2 containing 0.1 M TBAP and the NiPor derivatives in CH_2Cl_2 containing $TBAPF_6$ and added H^+ in the form of TFA. Scan rate = 100 mV/s

		Reductions (V vs SCE)				
Compounds	Solvent	Irrev [b]	Reversible[c]		$\Delta E_{1/2}$	reference
NiTPP	CH_2Cl_2		-1.26	-1.76[a]	0.50 [d]	36
$NiTPPCl_8$	CH_2Cl_2		-0.82	-1.14	0.32	36
$NiTPPBr_8$	CH_2Cl_2		-0.82	-1.17	0.35	36
NiPor	CH_2Cl_2		-1.33	-1.89	0.56	tw
$NiPorCl_8$	CH_2Cl_2 + 2eq. H^+	-0.18[a]	-0.88	-1.22	0.33	tw
$NiPorBr_8$	CH_2Cl_2 + 2eq. H^+	-0.26[a]	-0.94	-1.32	0.38	tw

tw = this work; [a] E_{pc} values ; [b] Irrev = irreversible reductions: [c] Assigned as reversible ring-centered reductions
[d] $\Delta E_{1/2} = |E_{1/2} - E_{pc}|$ for NiTPP.

The first reduction of the $NiPorCl_8$ and $NiPorBr_8$ in CH_2Cl_2 with increasing H^+ concentration was further investigated by plotting the measured peak potential in the CH_2Cl_2/TFA mixtures as a function of increasing acid concentration in solution, which varied from 10^{-3} to 10^{-1} M. These plots are shown in Figure 3-19 where E_p vs. log[H^+] is linear with a slope close to the theoretical Nernstian value of -60 mV expected for a rate determining step involving the addition of one electron and one proton or two electrons and two protons.[77] This result, and the known chemistry which occurs during the reduction of porphyrins in acidic nonaqueous media[78] strongly suggests an overall 2- electron, 2 proton transfer and the formation of porphodimethenes as probable products of the electron transfer reactions.

In order to distinguish between the two porphyrin reduction products, the reactions were monitored in a spectroelectrochemical cell, first in CH_2Cl_2 containing 0.1M $TBAPF_6$ with no added acid and then in CH_2Cl_2 containing 0.1M $TBAPF_6$ with $NiPorCl_8$ and 50 eq. of added H^+. The spectral changes under these conditions are illustrated in Figure 3-20 where the final product of the first electroreduction in CH_2Cl_2, 0.1 M $TBA^+PF_6^-$ (Figure 3-20a) is characterized by a broad band at 527 nm and is almost identical to the spectrum formed after addition of OAc^- or CN^- to $NiPorCl_8$ in CH_2Cl_2 (Figures 3-10 and 3-11). It is also identical to the spectrum formed when the same porphyrin is dissolved in DMSO or DMF (Figures 3-7 and 3-9). In each case, the chemically generated spectra are assigned to a porpho-5,15-bis-paraquinone methide oxidation product whose structure is shown in Scheme 3-2.

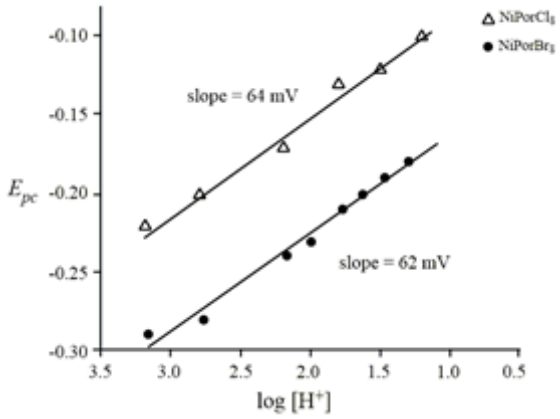

Figure 3-19. Plot of peak potential *E*pc for the first reduction of $NiPorCl_8$ and $NiPorBr_8$ vs. log $[H^+]$ in CH_2Cl_2 containing 0.1 M $TBAPF_6$ and varying concentrations of added TFA.

A spectral product with a band at 527 nm is also seen during the thin-layer reduction of $NiPorCl_8$ at -0.60 V in CH_2Cl_2 containing 2 eq. of added H^+ (Figure 3-20b) but under these solution conditions, a porphyrin-like spectrum having a Soret band at 458 nm is first formed in the thin-

layer cell followed at longer timescales by a spectrum with a broad band centered at 527 nm. Well-defined isosbestic points are seen in both sets of spectral transitions of Figure 3-20b.

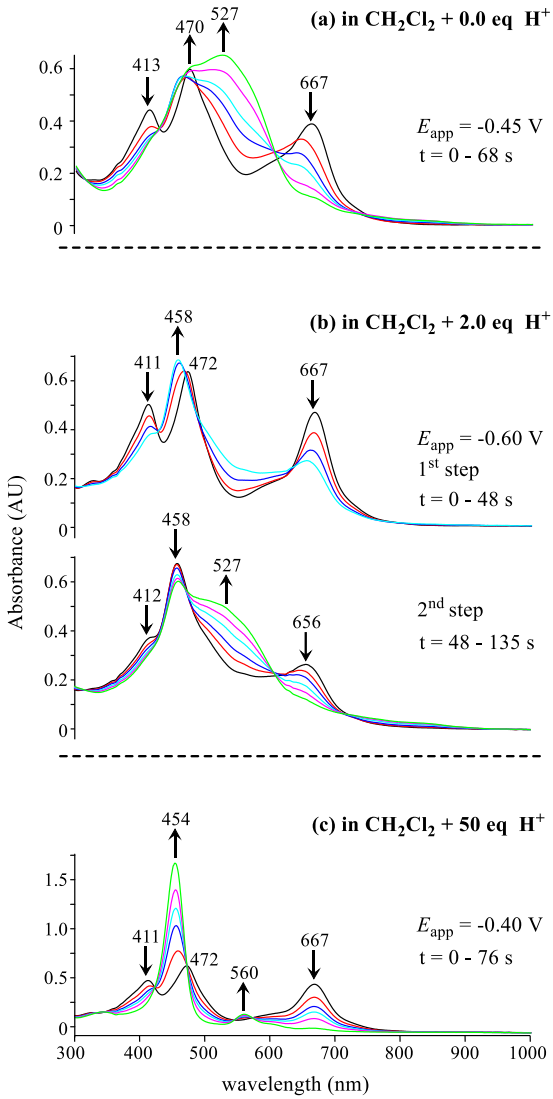

Figure 3-20. Spectral changes during first reduction of $NiPorCl_8$ in CH_2Cl_2 containing 0.1 M $TBAPF_6$ solutions and varying amounts of TFA where (a) no added TFA, (b) 2.0 eq. of H^+ and (c) 50 eq. of H^+.

Finally, when the controlled potential reduction of $NiPorCl_8$ was carried out at -0.40 V in CH_2Cl_2 containing 50 eq. H^+, only a single spectral product is generated which closely resembled

the initial product of reduction in CH_2Cl_2 containing 2 eq. H^+. The final spectrum of the reduction is characterized by well-defined Soret and Q bands at 454 and 560 nm, respectively (Figure 3-20c).

The final product formed after the reduction of $NiPorCl_8$ in highly acidic CH_2Cl_2 solutions is assigned as a porphodimethene having the structure shown in Scheme 3-4 and it should be noted that no demetallation occurs in CH_2Cl_2 solutions containing at least 0.1 M TFA (see Figure 3-21). The well-defined Soret and Q bands at 454 and 560 nm are both red-shifted from the corresponding bands of $NiTPPCl_8$ in CH_2Cl_2 (439 and 554 nm) but the reversible reduction potentials ($E_{1/2}$ = -0.88 and -1.23 V) in the CH_2Cl_2 solution with 2 eq H^+ (Figure 3-18) are not so different than the $E_{1/2}$ values of -0.82 and -1.14 V for the stepwise reductions of $NiTPPCl_8$ in CH_2Cl_2 containing only TBAP. The same can be said for the $\Delta E_{1/2}$ values between the two processes of the TPP and Por derivatives; these separations in $E_{1/2}$ are 320 mV for $NiTPPCl_8$ and 330 mV for $NiPorCl_8$.

This similarity between potentials for the one-electron reduction of $NiTPPCl_8$ at $E_{1/2}$ = -0.82 V and the proposed electrogenerated porphodimethene product generated from $NiPorCl_8$ ($E_{1/2}$ = -0.88 V) is not unexpected based on data in the literature showing almost identical reduction potentials for free-base dodecaphenylporphyrin ($E_{1/2}$ = -1.28 V) and its dodecaphenylporphodimethene product ($E_{1/2}$ = -1.30 V) in CH_2Cl_2[78] or between the first one-electron reduction of NiOEP in CH_2Cl_2 ($E_{1/2}$ = -1.46 V) and the *meso*-dimethyl Ni(II) porphodimethene product in the same solvent ($E_{1/2}$ = -1.52 V).[79]

In summary, the spectral changes in Figure 3-20a coupled with the lack of isosbestic points can be interpreted as an initial generation of the deprotonated porphyrin followed by a chemical or photooxidation[80] of the tetraanionic porphyrin to give the porpho-5,15-bis-paraquinone methide

product. Two forms of the porphyrin are also seen in Figure 3-20b where porphodimethene and porpho-5,15-bis-paraquinone are both electrochemically generated in the thin-layer cell, but this does not occur under the conditions of Figure 3-20c where only the fully protonated porphodimethene can be spectroscopically detected.

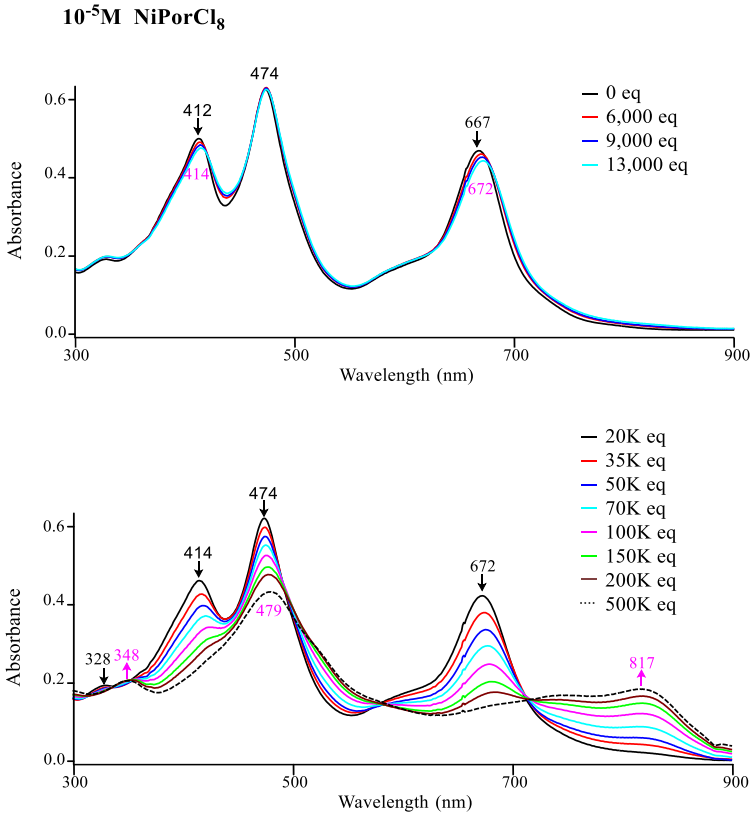

Figure 3-21. UV-Vis spectral changes of $NiPorCl_8$ at 10^{-5} M in CH_2Cl_2 upon titration of TFA.

Additional evidence in support of a porpho-5,15-bis-paraquinone methide product in the electrochemical reduction is given by the relative currents for the first three redox processes during a titration of $NiPorCl_8$ with base in CH_2Cl_2. As seen in Figure 3-22, the stepwise addition of CN^- or OAc^- to a CH_2Cl_2 solution of $NiPorCl_8$ shows the progressive loss of current for the first and

second reductions with a concomitant increase in the current for the third reduction (see boxed portion of voltammograms in Figure 3-22). Under each solution condition, this irreversible process at E_{pc} = -1.01 to -1.04 V is assigned to an electrode reaction of the chemically or electrochemically generated porpho-5,15-bis-paraquinone methide product in solution.

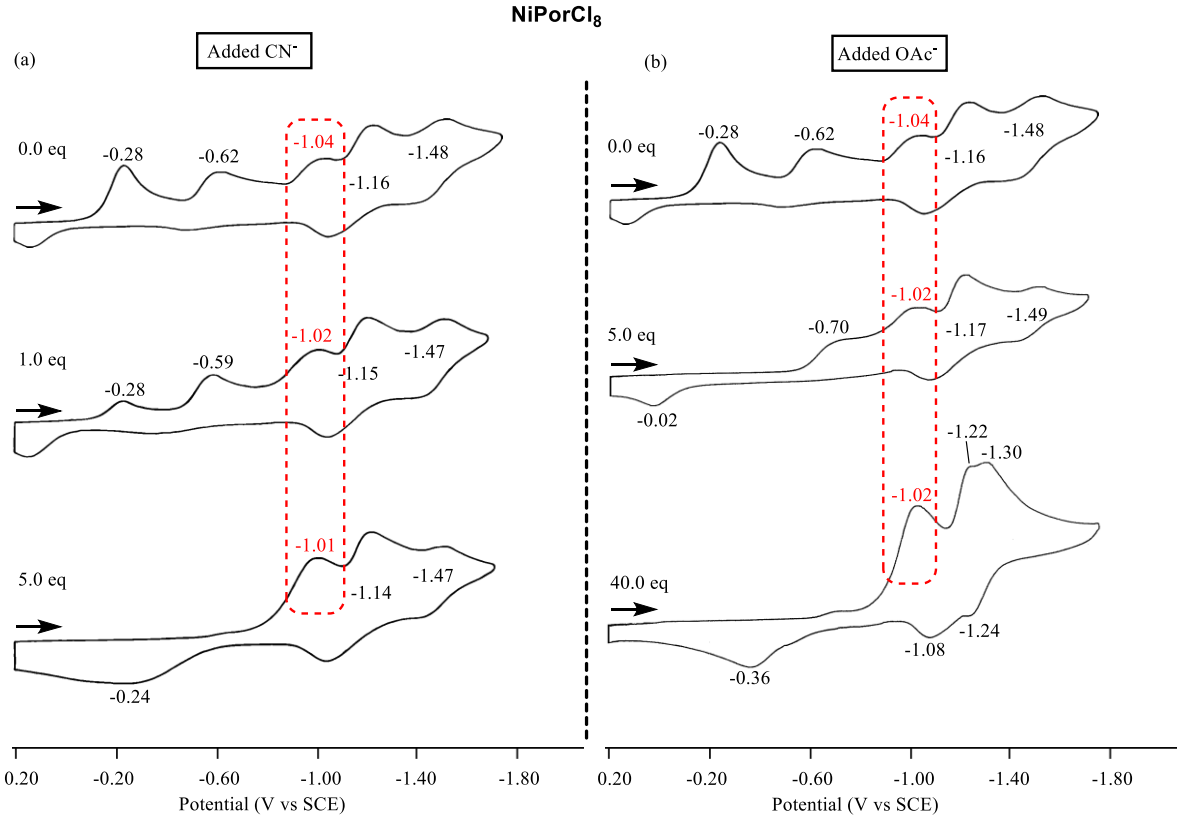

Figure 3-22. Cyclic voltammograms showing the reduction of $NiPorCl_8$ in CH_2Cl_2 with different equivalents of added (a) TBA^+CN^- or (b) TBA^+OAc^- (Scan Rate = 100 mV/s).

The best evidence for the same product being chemically or electrochemically generated is given in Figure 3-22a where $NiPorCl_8$ has reductions at E_{pc} = -1.04 V and $E_{1/2}$ = -1.16 and -1.48 V in CH_2Cl_2 containing TBAP and these three reductions remain (at E_{pc} = -1.01 V and $E_{1/2}$ = -1.14 and -1.47 V) after addition of 5 eq. of TBA^+CN^- to solution. As mentioned previously the UV-vis

spectrum after addition of 4.8 eq TBA^+CN^- to $NiPorCl_8$ (Figure 3-11) is almost identical to the final spectrum in Figure 3-20a after reduction at -0.45 V in a thin layer cell. The equivalence of TBA^+CN^- needed in each titration coupled with the identical spectra and redox potentials of the chemically and electrochemically generated product implies a removal of four protons in the electrochemical reduction with formation of the same porpho-5,15-bis-paraquinone methide product. As will be described on the following pages, the two reversible reductions following the irreversible process at $E_{pc} \approx$ -1.0 V are assigned to the stepwise addition of electrons to the π ring system of a tetraanionic porphyrin.

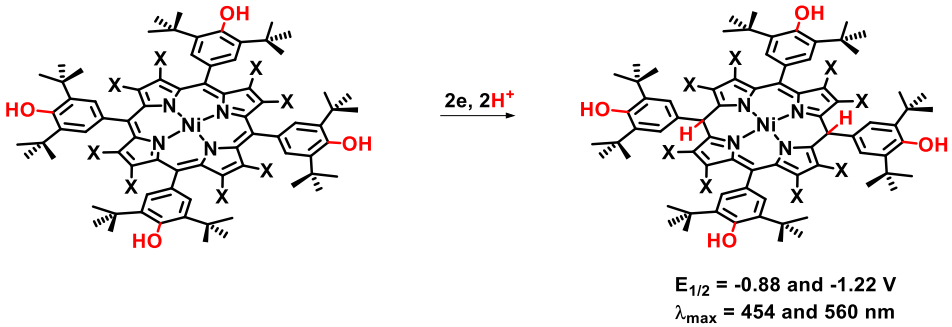

Scheme 3-4. Proposed mechanism for formation of electrochemically generated porphodimethene from $NiPorCl_8$ after the first two electron reduction in acidic CH_2Cl_2. A similar process occurs for $NiPorBr_8$ in acidic CH_2Cl_2 solutions where the first reduction peak potentials are given in Figure 3-19 as a function of H^+ concentration.

3.2.4 Reversible Interconversion Between the Neutral Porphyrin and a bis-Paraquinone Product.

The chemical conversion of fully protonated $NiPorX_8$ in CH_2Cl_2 (λ = 412, 472, 667 nm) to the porpho-5,15-bis-paraquinone methide in basic CH_2Cl_2 (λ = 535 nm) is reversible and the original porphyrin could be quantitatively regenerated by addition of ascorbic acid which serves as a reducing agent and a source of protons. An example of this reversibility is shown in Figure 3-23 for the case of $NiPorCl_8$.

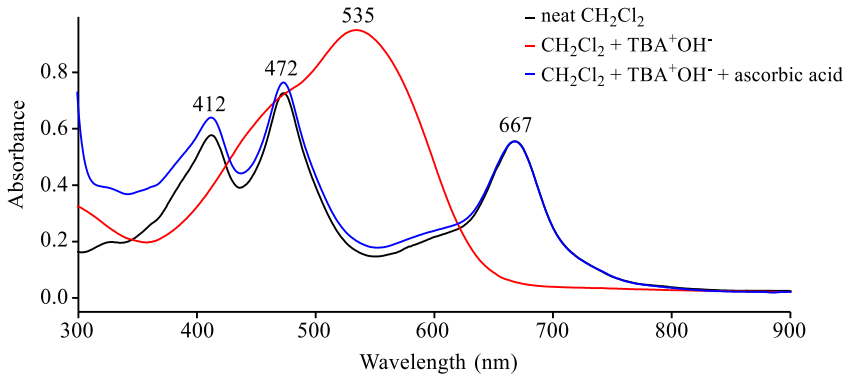

Figure 3-23. $NiPorCl_8$ in neat CH_2Cl_2 and with added TBA^+OH^- and then washed back with added ascorbic acid.

A chemical and/or photochemical 'porphyrin to a porphyrin-like oxidation product' interconversion was previously demonstrated for a related free-base porphyrin containing two meso-t-butylhydroxophenyl groups and two meso-t-butylphenyl groups.[81] An electrochemically driven interconversion between a porphyrin and porphyrin-like oxidation product was also shown for free-base and Cu(II) or Zn(II) bis-meso-carboxynaphthalene derivatives[82] but the electrochemical data described on the following pages provides the first example for an electrochemically generated interconversion between octahalogenated Ni(II) tetraanionic porphyrins and the corresponding Ni(II) dianionic porpho-5,15-bis-paraquinone methide derivatives.

The bis-paraquinone methide product which is chemically generated from $NiPorCl_8$ in CH_2Cl_2 solutions containing excess OAc^- or CN^- (Figures 3-10 and 3-11) is characterized by an initial irreversible reduction located at Epc ~ -1.01 V (Figure 3-22) to generate what is proposed to be the fully deprotonated porphyrin as a product which can then be reduced to its anion radical and dianionic forms at more negative potentials. The electrogenerated porphyrin can also

reoxidized back to the original porpho-5,15-bis-paraquinone methide on the return scan. This later process is located at *E*pa = -0.24 V in CH_2Cl_2 solutions containing excess TBA^+CN^- and at *E*pa = -0.36 V in solutions containing excess TBA^+OAc^-.

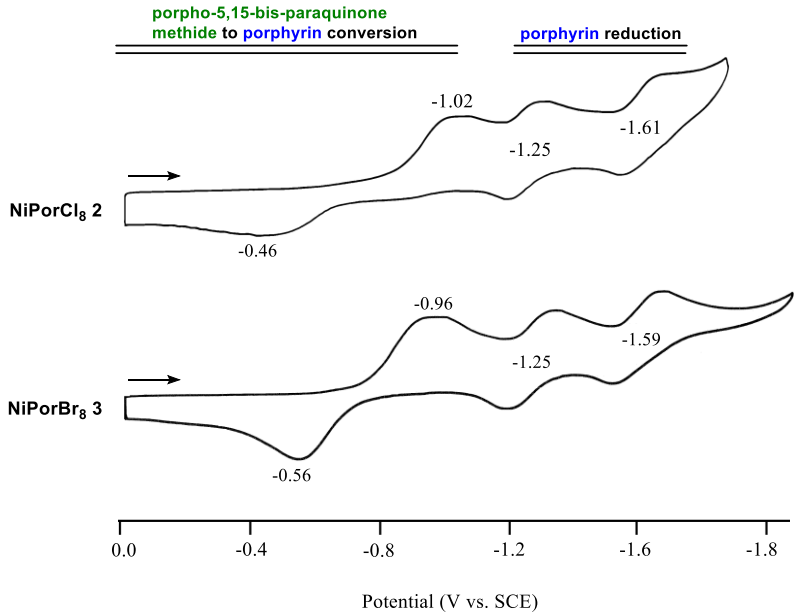

Figure 3-24. Cyclic voltammetry of $NiPorCl_8$ and $NiPorBr_8$ in CH_2Cl_2 with 100 equivalence of added TBA^+OH^-. Scan rate = 100 mV/s.

A porpho-5,15-bis-paraquinone methide to porphyrin interconversion also occurs in CH_2Cl_2 solutions containing excess TBA^+OH^- and in the presence of this strong base a similar electrochemical reactivity is seen for $NiPorCl_8$ and $NiPorBr_8$. The first reduction and reoxidation of both $NiPorX_8$ complexes are located at *E*pc = -1.02 V and *E*pa = -0.46 V for $NiPorCl_8$ and at *E*pc = -0.96 V and *E*pa = -0.56 V for $NiPorBr_8$ at a scan rate of 100 mV/s (Figure 3-24). The irreversible first reductions are then followed by two reversible one electron transfers of the electrogenerated porphyrin at $E_{1/2}$ = -1.25 and ~ -1.60 V as seen in the figure.

The first electroreduction of $NiPorCl_8$ and $NiPorBr_8$ in CH_2Cl_2 containing added OH^- involves an electrochemical EC mechanism (a chemical reaction following electron transfer) and generates a porphyrin with an intact π ring system and four *t*-butyl phenolate groups as shown in Scheme 3-5. These reductions are again coupled to reoxidations (E_{pa} = -0.46 V for $NiPorCl_8$ and -0.56 V for $NiPorBr_8$) to give back the original species as verified by the thin-layer spectroelectrochemical data in Figure 3-25 where the electrogenerated porphyrin product is characterized by an intense near-IR band at 872 nm ($NiPorCl_8$) and 868 nm ($NiPorBr_8$). This is not a typical porphyrin spectrum but reflects a spectrum where the *meso*-phenolate groups interact strongly with the porphyrin π-ring system as earlier described by Milgrom and coworkers[83] for the parent compound NiPor under the same solution conditions.

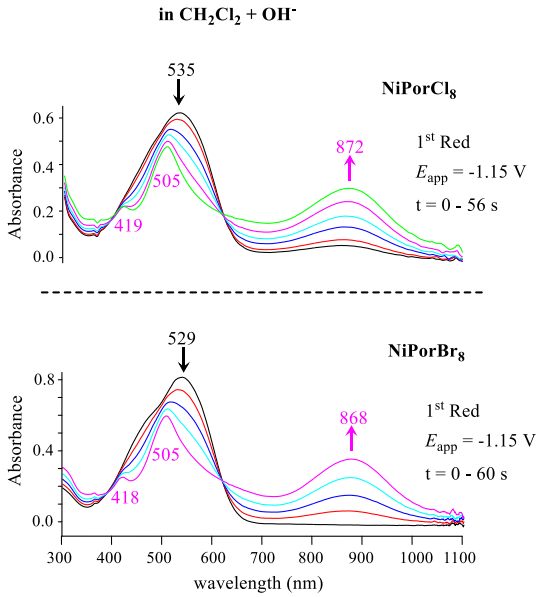

Figure 3-25. Spectral changes during the first reduction of chemically generated 5,15-bis-quinone methide from $NiPorCl_8$ and $NiPorBr_8$ in $CHCl_2$ containing excess TBA^+OH^-.

The same series of coupled electrochemical and chemical reactions also occur for NiPor as shown by the series of chemically and electrochemically generated spectral changes illustrated in

Figures 3-26 and 3-27, where the fully protonated porphyrin spectrum of the neutral compound in CH_2Cl_2 (Figure 3-26a, λ = 422 and 532 nm) is first converted to the fully deprotonated porphyrin spectrum having bands at 385, 479 and 738 nm (Figure 3-26b) and then slowly converts over time to the spectrum in Figure 3-26c. This spectrum has bands at 527, 664, and a shoulder at 805 nm and is assigned to the Ni(II) porpho-5,15-bis-paraquinone methide. The spectrum of the fully deprotonated NiPor derivative in Figure 3-26b is identical to a spectrum reported by Milgrom for the same compound in basic CH_2Cl_2. [83]

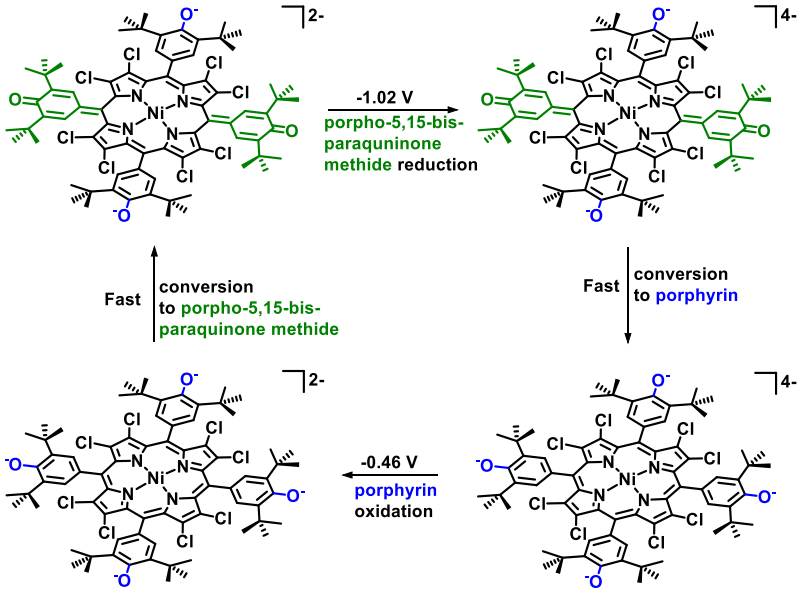

Scheme 3-5. Electrochemical EC mechanism for the conversion between the porphyrin and porpho-5,15-bis-paraquinone methide in CH_2Cl_2 containing 0.1 M TBA^+OH^-. The listed potentials are for $NiPorCl_8$ at a scan rate of 0.1 V/s.

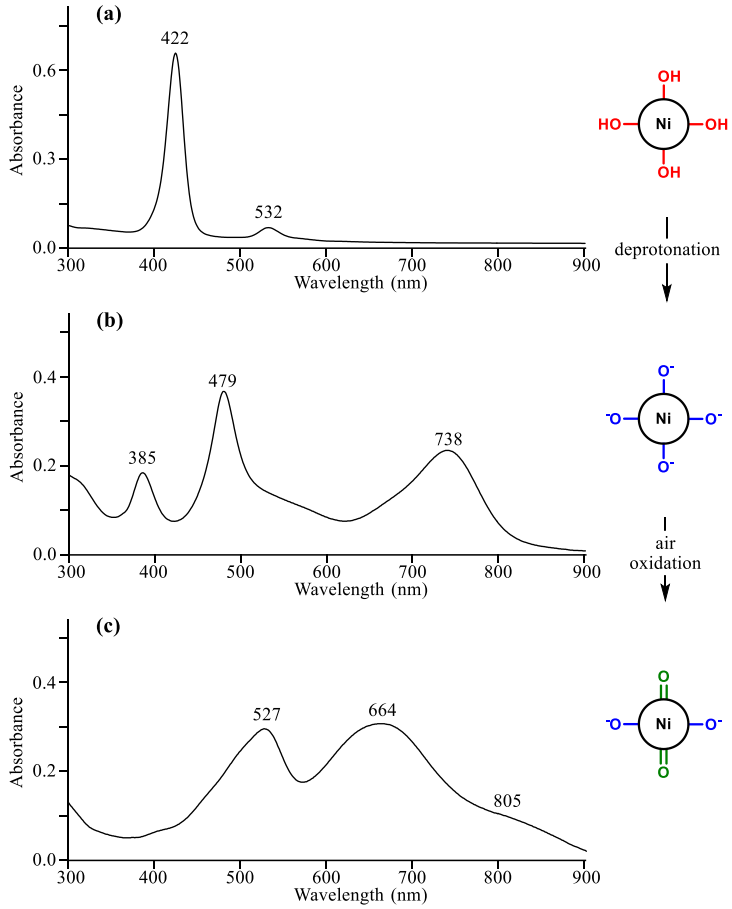

Figure 3-26. UV-vis spectra of NiPor (a) in neat CH_2Cl_2, (b) immediately after addition of excess OH^- in the form of TBA^+OH^- and (c) 40 minutes later.

A reversible conversion between the bis-paraquinone methide in Figure 3-26c and the fully deprotonated porphyrin in Figure 3-26b can also be carried out electrochemically under the application of a reducing or oxidizing potential. This is shown in Figure 3-27 where reduction of the chemically generated porpho-5,15-bis-paraquinone methide at -1.20 V generates the deprotonated porphyrin spectrum and reoxidation at 0.00 V gives back the bis-paraquinone methide species. Five isosbestic points can be seen in the figure indicating the lack of a spectrally detectable intermediate in this transition.

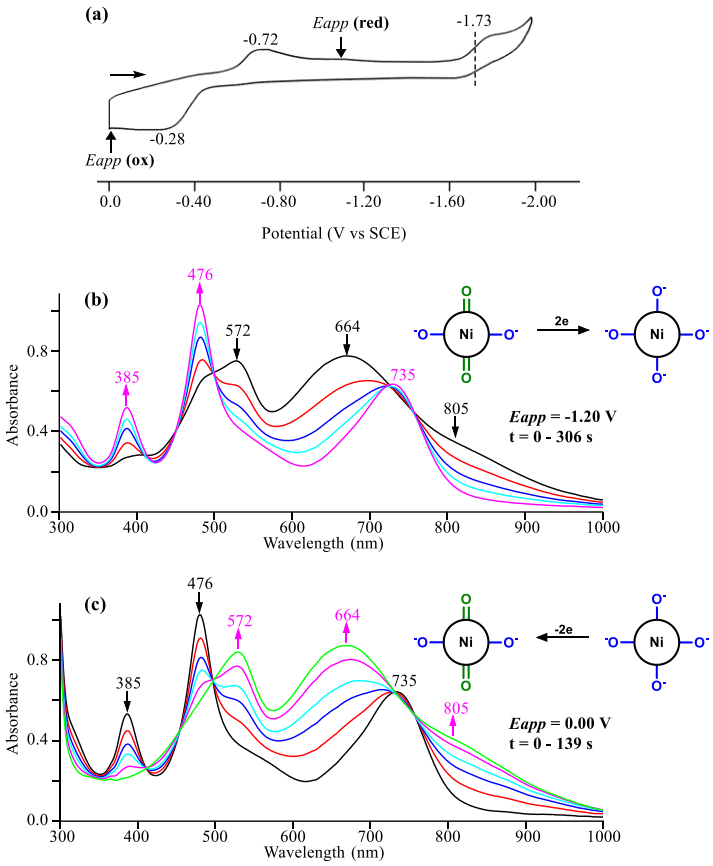

Figure 3-27. (a) Cyclic voltammogram of the porpho-5,15-bis-paraquinone methide generated from NiPor in CH_2Cl_2 containing 0.1 M TBAOH and spectral changes in a thin layer cell after (b) reduction at -1.20 V to generate the porphyrin followed by (c) the reoxidation at 0.00 V to give back the bis-paraquinone porphyrin-like product.

Finally, it should be noted that the tetranionic forms of $NiPorCl_8$ and $NiPorBr_8$ can be further reduced by two one electron transfer steps in basic CH_2Cl_2 solutions, these processes occurring at $E_{1/2}$ = -1.25 and ~ -1.60 V for $NiPorCl_8$ and $NiPorBr_8$ and -1.73 V for NiPor. The ~350 mV separation between these two reversible reductions of the octahalogenated tetranionic porphyrins $NiPorCl_8$ and $NiPorBr_8$ is virtually identical to the 320 mV separation between the two reversible reductions of the $NiPorCl_8$ in CH_2Cl_2 containing 0.1 M $TBAPF_6$ (-1.16 and -1.48 V). It is also identical to the $\Delta E_{1/2}$ between the two reversible one electron reductions in acidic CH_2Cl_2

containing 2 eq. of added TFA ($\Delta E_{1/2}$ = 330 mV, Figure 3-8) and that of $NiTPPCl_8$ in CH_2Cl_2, 0.1M TBAP (320 mV, Table 3-4). The reversible one electron reduction of the fully deprotonated NiPor at $E_{1/2}$ = -1.73 V (Figure 3-16a) in basic CH_2Cl_2 is cathodically shifted by 480 mV from the $E_{1/2}$ for the first one electron reduction of the fully deprotonated forms of $NiPorCl_8$ and $NiPorBr_8$ (Figure 3-13, $E_{1/2}$ = -1.25 V). This difference in reduction potentials is consistent with the lack of β-halogen substituents on the deprotonated parent compound NiPor which should shift the reduction anodically by ~60 mV per halogen substituent, or 480 mV total in the case of the deprotonated $NiPorX_8$ derivatives.

3.3 Conclusion

In summary, two structurally different porphyrin analogs can be obtained from octahalogenated nickel hydroxyphenylporphyrins by chemical or electrochemical methods. The current manuscript has focused on elucidating spectroscopic properties and electrochemistry of both the initial porphyrins and the porphyrin products in neutral, basic and acidic CH_2Cl_2 solutions and a mechanism is proposed for interconversion between these two forms of the tetrapyrrole. Studies of other metal derivatives of hydroxyphenyl porphyrins are in progress and should provide information as to how the central metal ion and the β-substituents of the compound affect this interconversion.

Chapter Four

Electrochemical Characterization of Acetylacetone (acac) and Ethyl Acetate (EA) Appended β-Trisubstituted Push-Pull Porphyrins. Formation of Electronically Communicating Porphyrin Dimers.

Reproduced in part with permission from [*Inorg. Chem.* **2018,** *57*, 13213-13224], American Chemical Society.

4.1 Introduction

Synthetic methods for the chemical modification of porphyrins are well established in the literature and enable access to a wide variety of derivatives which can be utilized for biological and material applications.[55, 58, 84, 85] Of recent special interest is the synthesis of 'push-pull' porphyrins[86-88] with multiple electrophilic substituents at the *β*-pyrrole positions which have been examined for use in nonlinear optics,[86] photodynamic therapy (PDT)[88, 89], and dye-sensitized solar cells (DSSC).[84, 85]

The aromatic electrophilic substitution of *meso*-tetraarylporphyrins with nitro, formyl, acyl, or bromo substituents is an important first synthetic step to expand the chemistry of a *β*-functionalized porphyrins.[89, 90] Menke's reaction conditions enables introduction of a single nitro group at the *β*-pyrrolic position[91] and is particularly useful for post modification of the porphyrin skeleton.[90, 92] Along these lines, a large number of *β*-functionalized 'push-pull' tetraphenylporphyrins have been synthesized and charaterized, examples of which are given by MTPP(NO_2)R_2, MTPP(NO_2)R_6, and MTPP(CHO)R_2 where R is a Me, Br, Ph, thienyl, or PE (phenylethynyl) substituent.[6, 93, 94] In all cases, we observed that the presence of a single nitro or formyl (CHO) group on the *β*-position on the porphyrin led to red shifted absorption spectra and tunable redox properties with reduced HOMO-LUMO gaps.

We wished to understand the behavior of push-pull porphyrins having a moderate electron-withdrawing acac or EAA substituents where acac = acetylacetone and EAA = ethyl acetoacetate at one *β*-position of the porphyrin with two bromo or two phenyl groups at the antipodal positions. However, none of the previous studies of acac and EAA porphyrins involved electrochemical characterization nor, to our knowledge, have any porphyrins been synthesized with a single acac

and EAA group and phenyl or bromo substituents at the antipodal positions. This is addressed in the current chapter which presents the synthesis, structural characterization, and electrochemistry of acac appended *β*-trisubstituted push-pull porphyrins. Attempts to make similar porphyrin with EAA were unsuccessful and led to the synthesis of ethyl acetate (EA) appended derivatives which are also spectroscopically, structurally, and electrochemically characterized in the present studies. Structures of the investigated compounds are shown in Chart 4-1.

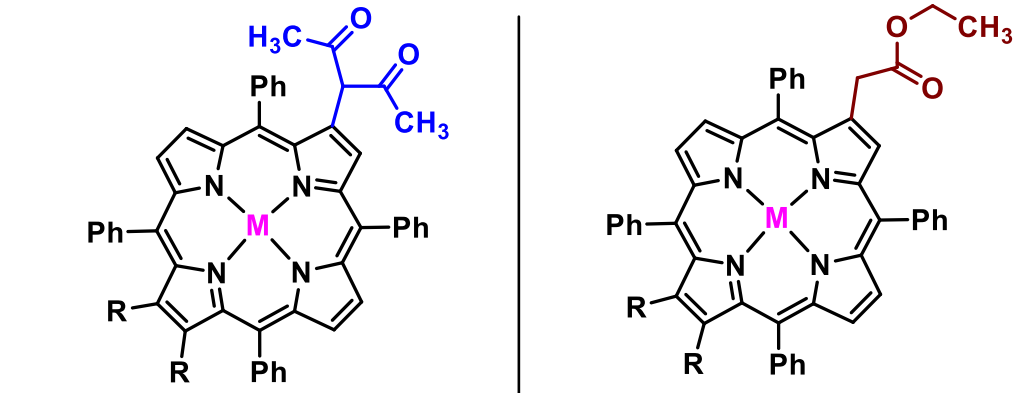

R = Br	R = Ph	R = Br	R = Ph
$MTPP(Br)_2acac$	$MTPP(Ph)_2acac$	$MTPP(Br)_2EA$	$MTPP(Ph)_2EA$
M = 2H	M = 2H	M = 2H	M = 2H
Co	Co	Co	Co
Ni	Ni	Ni	Ni
Cu	Cu	Cu	Cu
Zn	Zn	Zn	Zn

Chart 4-1. The molecular structures of the investigated pophyrins.

The two new families of examined push-pull tetraphenylporphyrins are represented as $MTPP(R)_2acac$ and $MTPP(R)_2EA$ where R = Br or Ph and M = H_2, Co, Ni, Cu, or Zn. $NiTPP(Br)_2acac$ exhibits an extremely nonplanar conformation while $H_2TPP(Br)_2EA$ and $ZnTPP(Ph)_2EA$ exhibit a quasi-planar conformation. Dimers were detected electrochemically for

the dibromo derivatives but not the diphenyl substituted porphyrins as shown in Scheme 4-1. A facile stepwise and reversible electrogeneration of the electronically communicating porphyrin dimers is observed for MTPP(Br)$_2$acac where M = Cu^{II}, Ni^{II}, or Zn^{II}.

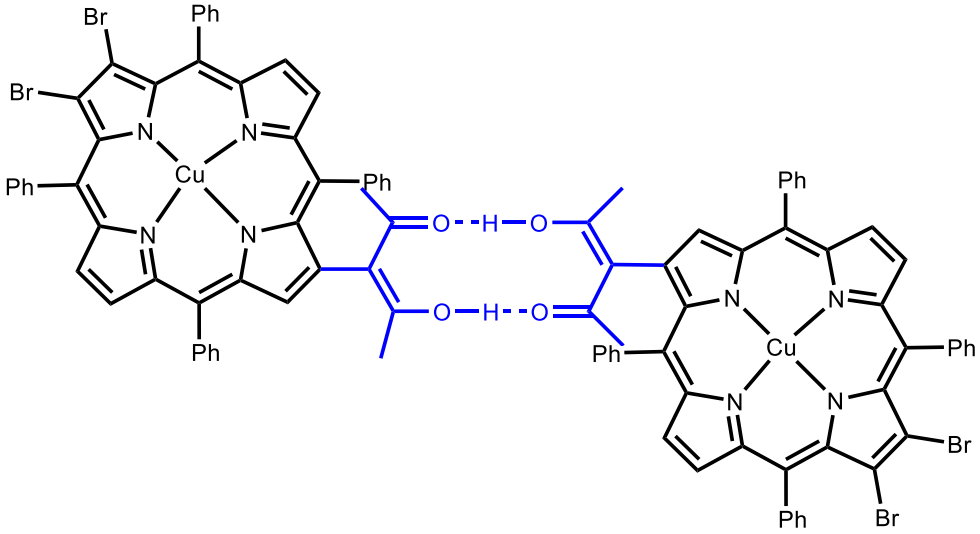

Scheme 4-1. Proposed structure of dimers formed in solution.

4.2 Results and Discussion

4.2.1 ^{1}H NMR and Mass Spectrometric Characterization.

The synthesised MTPP(R$_2$)X derivatives (where M = 2H, Ni(II), or Zn(II); X = acac or EA and R = Br or Ph) were characterized by ^{1}H NMR spectroscopy in $CDCl_3$ and MALDI-TOP mass spectra by our collaborator in Muniappan Sankar's lab from IIT Roorkee, india.[26] Figure 4-1 illustrates the ^{1}H NMR spectrum of H$_2$TPP(Br)$_2$acac Each porphyrin is characterized by proton signals arising from the *β*-substituents, the *β*-protons, the *meso*-phenyl groups, and the inner core nitrogens in the case of the free base porphyrins. The overall *β*-pyrrole resonances in MTPP(R$_2$)X (where M = 2H, Ni(II) or Zn(II); X = acac or EA; R = Br or Ph) are marginally upfield shifted as

compared to the $MTPP(NO_2)(R)_2$ precursors, due to a moderate electron-withdrawing nature of the diketone or ketoester groups. Larger shifts are seen for the nitro group appended porphyrins.

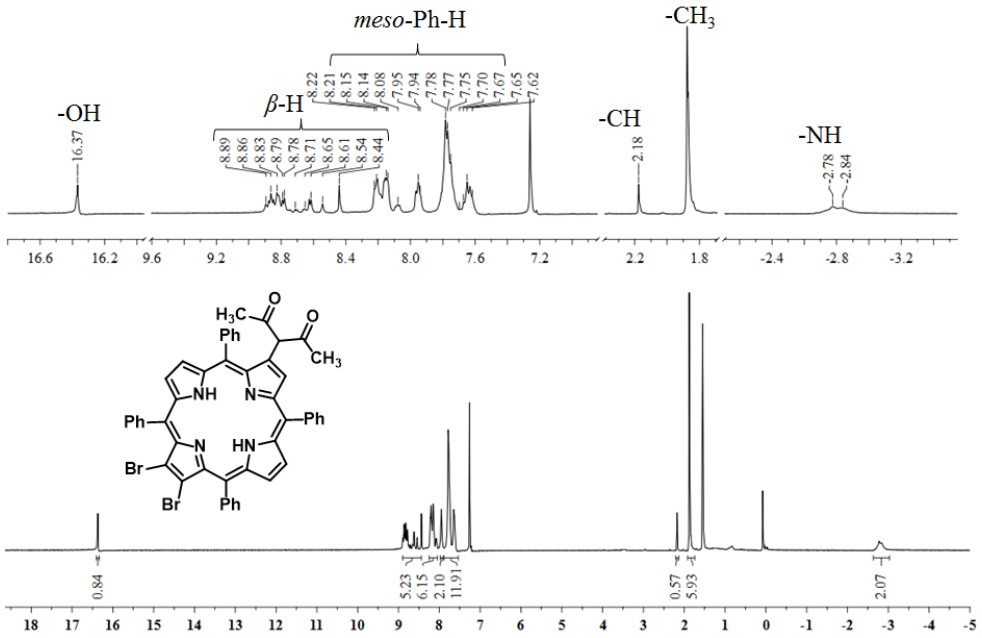

Figure 4-1. ^1H NMR spectrum of $H_2TPP(Br)_2acac$ in $CDCl_3$ at 298 K **(**reproduced with permission from [*Inorg. Chem.* **2018,** *57*, 13213-13224], American Chemical Society). [26]

The acetylacetone appended porphyrins exhibit a proton signals beyond 16 ppm corresponding to a single –OH, along with one signal at 2.18 ppm corresponding to –CH, thus indicating that these porphyrins exhibit a keto-enol tautomerism which can form a hydrogen bonded dimer discussed later in the manuscript as evidenced by data from the mass spectrometry and electrochemistry (*vide infra).* In the case of $H_2TPP(Br)_2EA$ porphyrin, the characteristic signals are observed for the $–CH_2$ and $–COOCH_2CH_3$ groups, confirming the presence of an EA substituent at the *β*-position.

Notably, resonances assigned to the inner core NH protons of $H_2TPP(Br)_2acac$ and $H_2TPP(Br)_2EA$ are observed as a split signal, which demonstrates that proton exchange involving the two inner core NH groups (NH tautomerism) is slow enough to be distinguished on the NMR time scale, even at room temperature as shown in the Figure 4-1. The inner core protons of phenyl-substituted porphyrins $H_2TPP(Ph)_2acac$ and $H_2TPP(Ph)_2EA$ are confirmed by a broad singlet indicating a fast exchange process for the two protons involved in NH tautomerism.

An example of MALDI-TOF mass spectra of the synthesized porphyrins is illustrated in Figure 4-2 and is recorded in the positive ion mode using HABA matrix. The acac appended porphyrins exhibit dimer formation as shown in Figure 4-2 for $H_2TPP(Ph)_2acac$ and it is the same as for the other acac derivatives with Br or Ph substituents. Dimers are not observed for EA porphyrins. The observed mass values match exactly with the proposed structures of both monomeric and dimeric acac porphyrins.

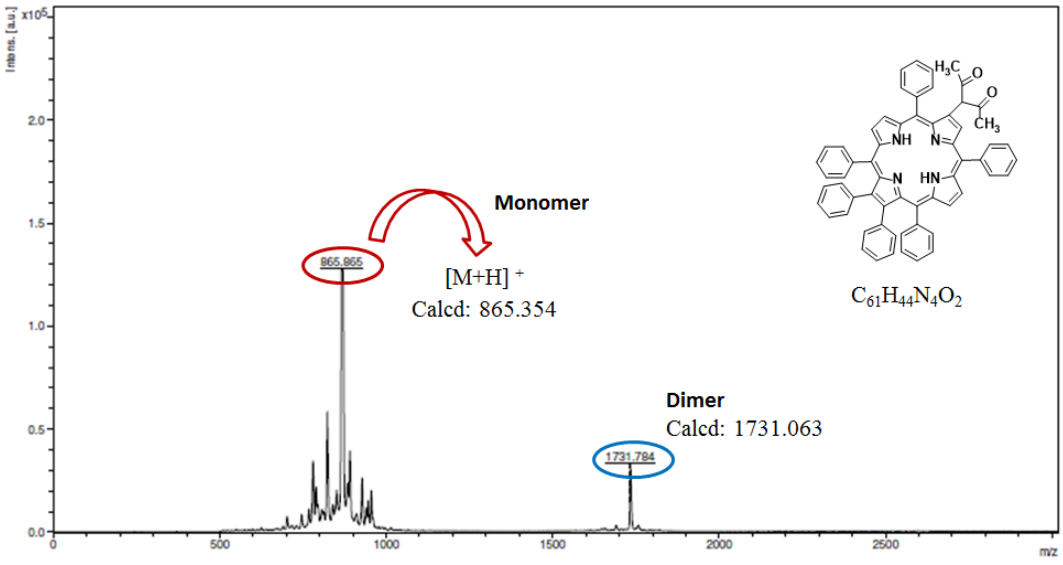

Figure 4-2. MALDI-TOF mass spectrum of $H_2TPP(Ph)_2acac$ in positive ion mode (reproduced with permission from [*Inorg. Chem.* **2018**, *57*, 13213-13224], American Chemical Society).[26]

4.2.2 Electrochemistry of MTPP(R)$_2$acac and MTPP(R)$_2$EA, M = Cu, Ni, Zn

The electrochemistry of each MTPP(R)$_2$acac and MTPP(R)$_2$EA derivative was investigated in CH_2Cl_2, pyridine or THF containing 0.1M TBAP. Most redox reactions of the tri-substituted porphyrins were reversible in the utilized electrochemical solvents at room temperature but an irreversible chemical reaction followed formation of the electrogenerated porphyrin dianion in some cases, leading to a new electroactive species in solution. We wished to minimize this side reaction in order to more accurately evaluate the true thermodynamic redox potentials of the newly synthesized porphyrins and this was accomplished by making measurements at low temperature where the rate of the chemical reaction was slowed down.

A summary of the measured potentials is given in Tables 4-1 and 4-2 and examples of cyclic voltammograms for the four tri-substituted Cu^{II} porphyrins and CuTPP in CH_2Cl_2 are shown in Figure 4-3. A comparison of the acac porphyrins with CuTPP is given in part (a) of the figure while part (b) shows the cyclic voltammograms of CuTPP and the EA derivatives.

All of the reactions in Figure 4-3 are assigned to electron transfers involving the porphyrin macrocycle. Under these conditions, redox behavior of the two EA derivatives in Figure 4-3b is as expected on the basis of what was earlier reported for tetraphenylporphyrins with phenyl or Br substituents at one or more β-pyrrole positions of the macrocycle,[1, 2] i.e., a shift of potentials towards easier reductions and harder oxidations for compounds with electron-donating substituents and an opposite effect for porphyrins with electron-withdrawing substituents.[1, 2] Nonplanarity of substituted tetraphenylporphyrin macrocycles will also lead to easier oxidations as compared to the unsubstituted parent TPP derivatives with the same central metal ion,[7] but this nonplanarity has little effect on reduction potentials of the metalloporphyrins.

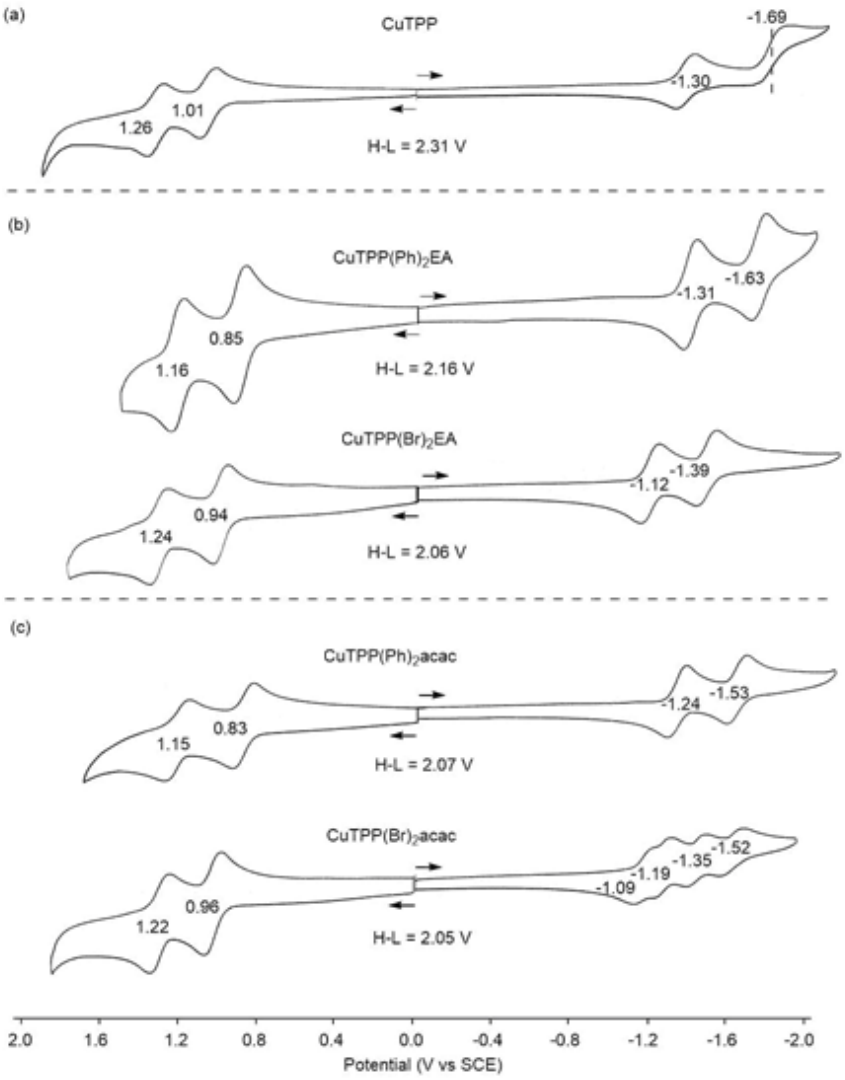

Figure 4-3. Cyclic voltammograms of (a) CuTPP, (b) CuTPP(Ph)$_2$EA, CuTPP(Br)$_2$EA and (c) CuTPP(Ph)$_2$acac, CuTPP(Br)$_2$acac in CH_2Cl_2, containing 0.1M TBAP. Scan rate = 100 mV/s. Measurements of the acac and EA complexes were carried out at -60 ^oC.

The effect of porphyrin nonplanarity in the current study is illustrated by the cyclic voltammograms for CuTPP(Ph)$_2$EA and CuTPP(Ph)$_2$acac in Figure 4-3, i.e., oxidations of the diphenyl derivatives are shifted negatively by 160-180 mV in the first step and by 100-110 mV in the second as compared to the same electrode reaction of CuTPP in CH_2Cl_2, while only a small difference is seen in $E_{1/2}$ for each reduction of the two compounds. The measured electrochemical

HOMO-LUMO gap is 2.31 V for CuTPP in CH_2Cl_2 but decreases to 2.16 V for CuTPP(Ph)$_2$EA and 2.07 V for CuTPP(Ph)$_2$acac, as seen in Figure 4-3.

The expected substituent effect of the electron-withdrawing Br groups is seen by a comparison of the voltammograms for CuTPP(Ph)$_2$EA and CuTPP(Br)$_2$EA, where a change from diphenyl to dibromo substitution is associated with a 190-240 mV positive shift in $E_{1/2}$ for the reductions and an 80-90 mV positive shift for the oxidations (see Table 4-1 and Figure 4-3). As previously demonstrated for related porphyrins, HOMO levels are less affected than the LUMOs by the electron-withdrawing Br groups.[93]

Table 4-1. Half-Wave potentials for the first two reductions and first two oxidations of MTPP(Br)$_2$EA and MTPP(Ph)$_2$EA in CH_2Cl_2, pyridine or THF containing 0.1M TBAP

Macrocycle	M	Solvent	Oxidation		Reduction		$\Delta E_{1/2}$
			Ox 2	Ox 1	Red 1	Red 2	|Red1-Ox1|
TPP(Br)$_2$EA	Cu	CH_2Cl_2	1.25	0.97	-1.16	-1.48[a]	2.13
		THF	1.11	1.11	-1.10	-1.38	2.21
	Ni	CH_2Cl_2	1.09	1.09	-1.11	-1.48[a]	2.20
		THF	1.18	1.03	-1.07	-1.46[a]	2.10
	Zn	CH_2Cl_2	1.08	0.83	-1.24	-1.50[a]	2.07
		THF	1.17	0.97	-1.17	-1.58[a]	2.14
TPP(Ph)$_2$EA	Cu	CH_2Cl_2	1.16	0.85	-1.31	-1.63	2.16
		THF	1.21	0.94	-1.22	-1.52	2.16
		Pyridine		0.80	-1.27	-1.60	2.07
	Ni	CH_2Cl_2	0.94	0.94	-1.23	-1.64	2.17
		THF	1.03	1.03	-1.24	-1.64	2.27
		Pyridine		0.57	-1.25	-1.60	1.82
	Zn	CH_2Cl_2	0.90	0.73	-1.34	-1.62	2.07
		THF	1.01	0.87	-1.34	-1.70	2.21
		Pyridine		0.78	-1.35	-1.71	2.13

[a]peak potential at a scan rate of 100 mV/s.

Table 4-2. Half-Wave Potentials for Redox Reactions of MTPP(Br)$_2$acaca and MTPP(Ph)$_2$acac Complexes in CH_2Cl_2 or Pyridine Containing 0.1M TBAP

Macrocycle	M	Solvent	Temp.	Oxidation		Reduction	
				Ox 2	Ox 1	Red 1	Red 2
TPP(Br)$_2$acac	Cu	CH_2Cl_2	-60 °C	1.22	0.96	-1.09, -1.19	-1.35, -1.52
		Pyridine	R.T.	1.02[b]	0.91[b]	-1.08, -1.17	-1.39, -1.55
	Ni	CH_2Cl_2	-60 °C			-1.06, -1.16	-1.38, -1.54
		Pyridine	R.T.		0.74	-1.12, -1.18	-1.37, -1.58
	Zn	CH_2Cl_2	-60 °C	1.09	0.82	-1.21, -1.31	-1.49, -1.70
		Pyridine	R.T.	0.92[b]	0.83[b]	-1.16, -1.26	-1.48, -1.67
TPP(Ph)$_2$acac	Cu	CH_2Cl_2	-60 °C	1.15	0.83	-1.24	-1.53
	Ni	CH_2Cl_2	-60 °C		0.91[b]	-1.21	-1.57
	Zn	CH_2Cl_2	-60 °C	0.87	0.74	-1.32	-1.59

[a]Reduction of the MTPP(Br)$_2$acac complexes involves a dimeric porphyrin where the first and third step generate the half reduced dimer. [b]Peak potential at scan rate of 100 mV/s.

A moderate substituent effect of the Br groups is seen on potentials for the oxidations of CuTPP(Br)$_2$acac, where the $E_{1/2}$ values are positively shifted by 70-130 mV as compared to CuTPP(Ph)$_2$acac. The measured half-wave potentials of CuTPP(Br)$_2$acac are located at 0.96 and 1.22 V (see Table 4-2), potentials almost identical to $E_{1/2}$ values for the two oxidations of CuTPP(Br)$_2$EA under the same solution conditions (see Table 4-1, 4-2 and Figure 4-3).

However, unlike what is seen for CuTPP(Br)$_2$EA (Figure 6b), the acac derivatives with two Br groups (Figure 4-3a) exhibit a splitting of the $E_{1/2}$ values for each one-electron reduction. This is consistent with electron addition to a dimeric porphyrin having two equivalent and interacting redox centers, in this case, the conjugated π systems of the macrocycle. MS characterization of the MTPP(Br)$_2$acac derivatives described earlier in the manuscript shows clearly the presence of dimers in the gas phase for the Cu^{II}, Ni^{II}, and Zn^{II} porphyrins, and hydrogen-bonded dimers were

assigned as existing in solution on the basis of the NMR data. Although the observation of split redox reactions for a dimeric porphyrin with interacting redox centers is well known in the literature,[95, 96] these processes have been in almost all cases limited to the oxidations and it is quite rare to see such an effect of interacting dimers on the reductions.

The first one electron addition to $[CuTPP(Br)_2acac]_2$ is assigned as generating a half reduced dimer where one π system of the porphyrin is in its π anion radical form and the other π system is intact. The second reduction then gives $[CuTPP(Br)_2acac]_2^{2-}$ where each porphyrin is in its π-anion radical form. This is then followed by the addition of two more electrons to give $[CuTPP(Br)_2acac]_2^{3-}$ and $[CuTPP(Br)_2acac]_2^{4-}$, the first containing a porphyrin π-anion radical linked with a porphyrin dianion and the second two linked porphyrin dianions. The peak current for each reduction of $CuTPP(Br)_2acac$ is approximately half the peak current for each oxidation, thus providing additional indirect evidence for the reactions given by eqs 5-8 where Por = $TPP(Br)_2acac$ and M = Cu^{II}.

$$[MPor]_2 + e^- \rightleftharpoons [MPor]_2^- \quad (4\text{-}1)$$

$$[MPor]_2^- + e^- \rightleftharpoons [MPor]_2^{2-} \quad (4\text{-}2)$$

$$[MPor]_2^{2-} + e^- \rightleftharpoons [MPor]_2^{3-} \quad (4\text{-}3)$$

$$[MPor]_2^{3-} + e^- \rightleftharpoons [MPor]_2^{4-} \quad (4\text{-}4)$$

The midpoint potential of the first two reversible reductions of $[CuTPP(Br)_2acac]_2$ (Equations 4-1 and 4-2) is located at 1.14 V and the last two (Equations 4-3 and 4-4) at 1.43 V (see Table 4-2). Both values are shifted positively by about 100 mV with respect to half-wave potentials associated with the corresponding one-electron reductions of monomeric $CuTPP(Ph)_2acac$ under the same solution conditions (Table 4-1).

A dimerization of the acac porphyrin with two Br groups is not limited to the copper derivative but also occurs for NiTPP(Br)$_2$acac and ZnTPP(Br)$_2$acac as shown in the cyclic voltammograms in Figure 4-4 which also includes voltammograms of the corresponding monomeric MTPP(Ph)$_2$acac species.

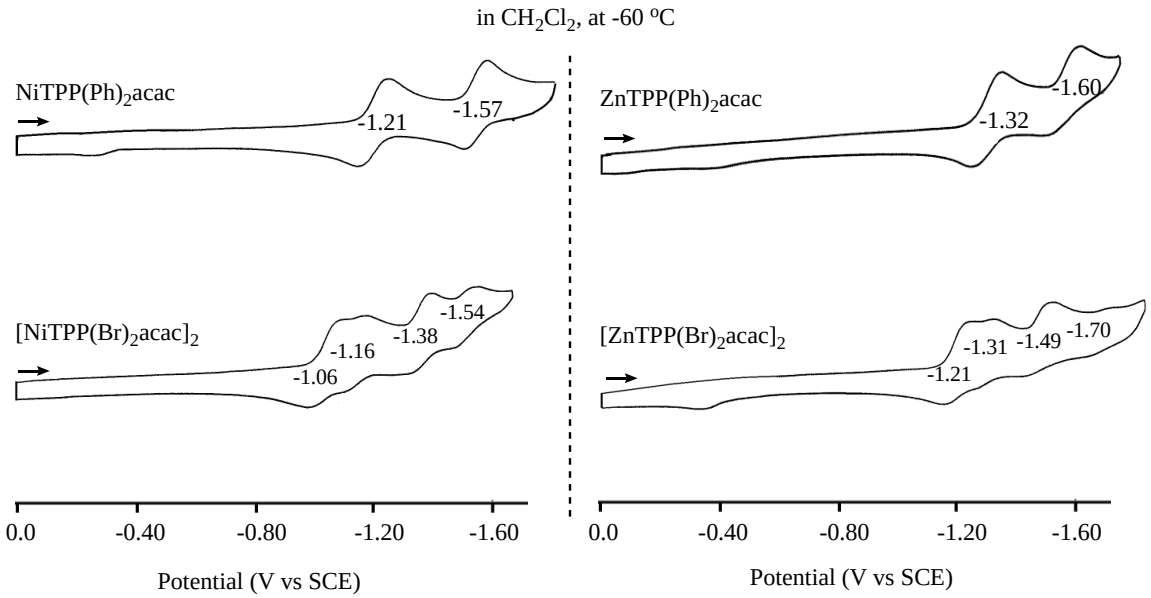

Figure 4-4. Cyclic voltammograms of [MTPP(Ph)$_2$acac]$_2$ and MTPP(Br)$_2$acac where M = Ni or Zn in CH_2Cl_2 at -60 °C, containing 0.1M TBAP. Scan rate = 100 mV/s.

The potential separation between Equations 4-3 and 4-4 is 100 mV for M = Cu^{II} and the same $\Delta E_{1/2}$ is seen for the Ni^{II} ($E_{1/2}$ = -1.06 and -1.16 V) and Zn^{II} ($E_{1/2}$ = -1.21 and -1.31 V) derivatives as seen in Figure 4-4 and Table 4-2. The $\Delta E_{1/2}$ between Equations 4-1 and 4-2 is 170 mV for M = Cu^{II} and this value can be compared to a $\Delta E_{1/2}$ of 160 mV for M = Ni^{II} (-1.38 and -1.54 V) and 210 mV for M = Zn^{II} (-1.49 and -1.70 V). Thus, for all three porphyrins, the degree of electronic interaction between the two units of the dimer is moderately strong.

Surprisingly, the dimerization is also not limited to the low dielectric constant solvent CH_2Cl_2 but also occurs in pyridine for the Cu, Zn and Ni derivatives, an example of which is given in Figure 4-5a. Dimerization is not electrochemically observed for the free base acac porphyrins nor is obtained for the Co^{II} porphyrins with Br substituents as discussed in a later section of the manuscript. This is consistant with the MS presented earlier in the thesis.

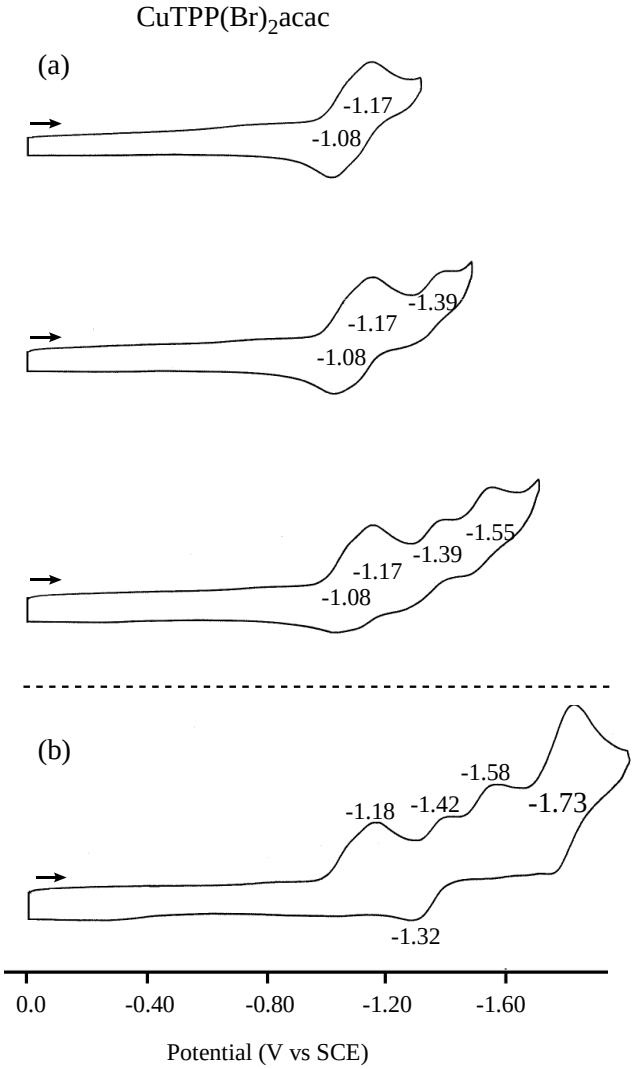

Figure 4-5. Cyclic voltammograms (CVs) illustrating the (a) the first four reductions of dimeric $[CuTPP(Br)_2acac]_2$ (b) the redox behavior after scanning beyond the first four processes in pyridine.

Chemical reaction of electrogenerated di-anions. Almost all of the investigated porphyrins undergo a chemical reaction following generation of the dianion in solution. This reaction occurs for both the MTPP(R)$_2$acac and MTPP(R)$_2$EA derivatives as illustrated in Figures 4-5b for CuTPP(Br)$_2$acac and Figure 4-6 for ZnTPP(Ph)$_2$acac

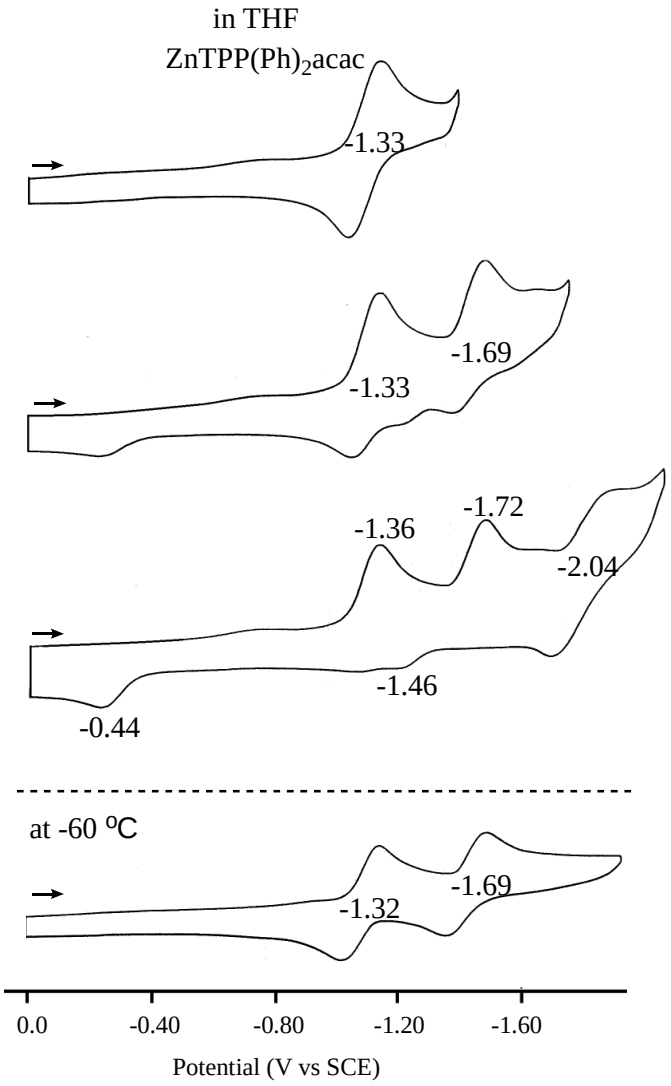

Figure 4-6. Cyclic voltammograms of ZnTPP(Ph)$_2$acac in THF where the chemical reaction following the formation of dianion is eliminated at -60 °C.

in pyridine and THF, respectively. The product generated in solution after formation of $[MTPP(Br)_2acac]_2^{4-}$ or $[MTPP(Ph)_2acac]^{2-}$ can then be reversibly reduced as seen in Figures 4-5 and 4-6. However, reversing the potential and then scanning back in a positive direction then shows the complete 'loss' of the original porphyrin at the electrode surface as evidenced by the lack of a reoxidation associated with original cathodic peaks. Similar chemical reactions occurred for the doubly reduced EA porphyrins with Br or Ph substituents. This reaction of the dianion may involve phlorin formation but this was not investigated as part of the current study.

4.2.3 Electrochemistry of $CoTPP(R)_2acac$ and $CoTPP(R)_2EA$

Cyclic voltammograms illustrating oxidation and reduction of the acac and EA derivatives of Co(II) are shown in Figure 4-7 along with a voltammogram of CoTPP under the same solution conditions. The most evident difference between the voltammograms in this figure and those in Figure 4-7 is the lack of an electrochemically observed dimerization for $CoTPP(Br)_2acac$, this process being well defined for the Cu(II), Ni(III), and Zn(II) analogues, not only in CH_2Cl_2 but also in pyridine, as shown in Figures 4-7 and 4-5. This lack of a dimerization is consistent with the MS data which shows only the presence of a monomeric $CoTPP(Br)_2acac$ species.

The redox behavior of the monomeric cobalt porphyrins can then be divided into two groups, one for the diphenylporphyrins $CoTPP(Ph)_2acac$ and $CoTPP(Ph)_2EA$ which are illustrated in Figure 4-7b along with CoTPP in Figure 4-7a, and the other, the dibromoporphyrins $CoTPP(Br)_2acac$ and $CoTPP(Br)_2EA$, for which CVs are shown in Figure 4-7c. All of the compounds are characterized by three reversible one-electron oxidations and two reductions in CH_2Cl_2, while the first reduction is less reversible as compared to $CoTPP(Br)_2acac$ and $CoTPP(Br)_2EA$ in the case of $CoTPP(Ph)_2acac$ and $CoTPP(Ph)_2EA$ (Figure 4-7c). Each one-

electron reduced species undergoes a fast chemical reaction with the CH_2Cl_2 solvent to give an electroactive carbon-based Co(III) product, which is then irreversibly reduced at E_p = -1.39 V (CoTPP), -1.40 V (CoTPP(Ph)$_2$EA) or -1.50 V (CoTPP(Ph)$_2$acac). This side reaction has earlier been described in the literature[12, 97] and is not observed when the voltammograms are recorded at low temperature in CH_2Cl_2.

The potentials for the reduction of CoTPP(Br)$_2$EA and CoTPP(Br)$_2$acac are almost identical to each other as seen in Figure 4-7c and the singly reduced forms of these two porphyrins are relatively stable on the cyclic voltammetry timescale. A similar stability was also recently reported for related tri-substituted CoTPP(R)$_2$NO$_2$ porphyrins with R = Ph, Br, PE, or CN. The electrogenerated Co(I) porphyrins in each case are then irreversibly reduced in a second step located at E_p = -1.16 to -1.29 V in the case of the NO_2 complexes or -1.68 V in the case of the currently examined EA or acac derivatives CoTPP(Br)$_2$EA and CoTPP(Br)$_2$acac.

4.3 Conclusion

In summary, two new series of asymmetrically β-trisubstituted porphyrins were synthesized and characterized. The EA substituted porphyrins H$_2$TPP(Br)$_2$EA and ZnTPP(Ph)$_2$EA have quasi-planar structures while the acac appended Ni porphyrin is saddle shaped with $\Delta 24$ = 0.44 Å and ΔC_β = 0.82 Å; to our knowledge, this is the most nonplanar mixed β-trisubstituted MTPP derivative reported to date. The MTPP(R)$_2$EA derivatives behave like MTPPs but the MTPP(R)$_2$acac porphyrins with Cu^{II} Ni^{II} or Zn^{II} central metal ions form strong hydrogen bonded dimers and exhibit mutiple reductions due to electronic communication between the two porphyrin π-ring systems. The first four reductions of MTPP(Br)$_2$acac generate dimers in four different oxidation

states, i.e., $[MTPP(Br)_2acac]_2^{n-}$ where n = 1, 2, 3, or 4. Remarkably, the dimers are stable not only in CH_2Cl_2 but also in pyridine containing 0.1M TBAP.

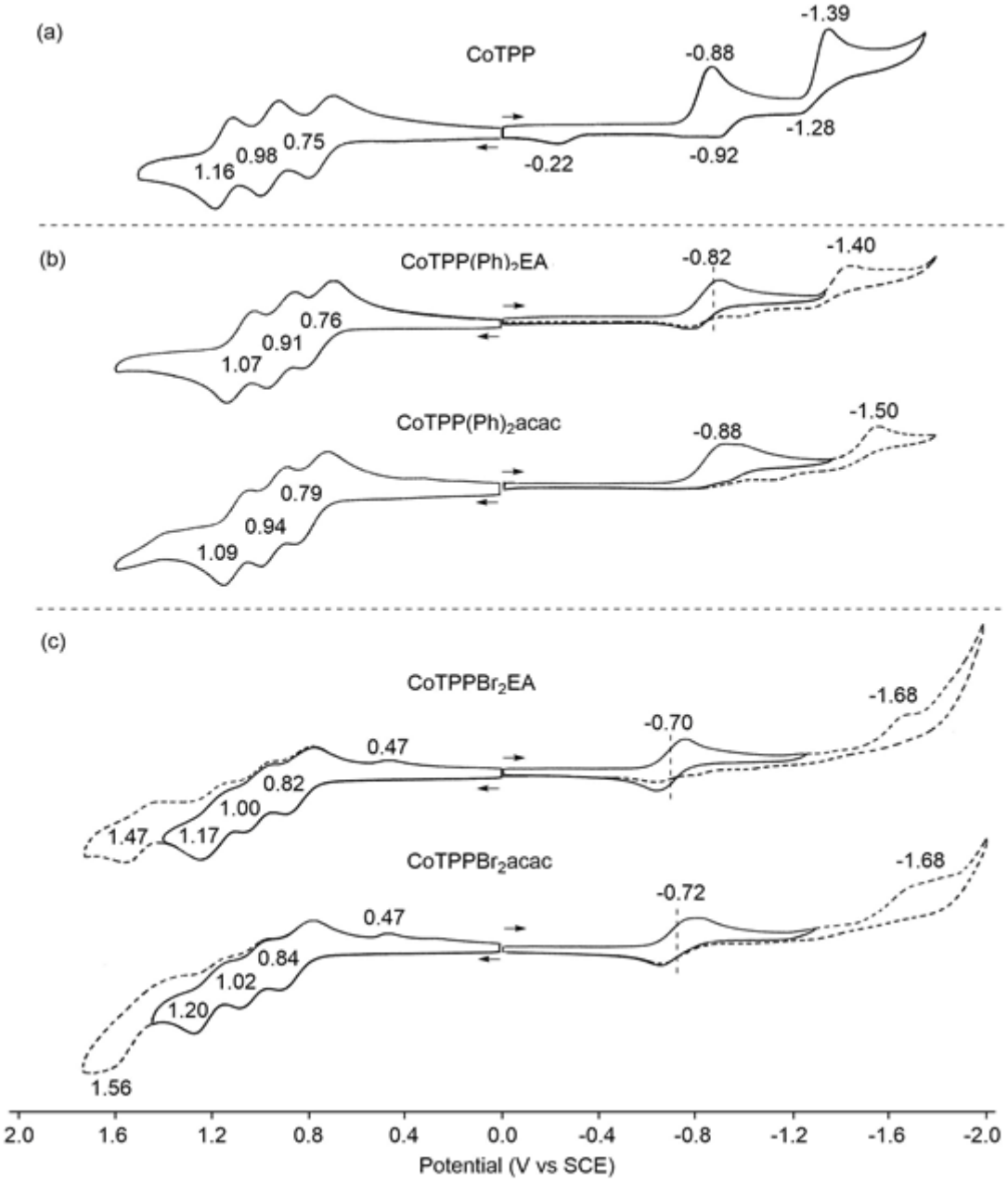

Figure 4-7. Cyclic voltammograms of a) CoTPP, $CoTPP(Ph)_2EA$, $CoTPP(Ph)_2acac$ and b) compounds $CoTPP(Br)_2EA$, $CoTPP(Br)_2acac$ in CH_2Cl_2 containing 0.1M TBAP. Scan rate = 100 mV/s.

Chapter Five

Electrochemical studies of porphyrazine derivatives

5.1 Introduction

The collaborator of our lab Dr. Maria Pia Donzello and Dr. Claudio Ercolani from the Sapienza University of Rome has long been devoted to studies involving the synthesis and characterization of new porphyrazine macrocycles and their metal derivatives having five, six or seven membered heterocyclic rings with S, Se or N atoms *o*-condensed on the external sites of the pyrrole groups, thus making these macrocycles more electron deficient than the related phthalocyanines, as systematically evidenced by their UV-visible and electrochemical behavior.[98] This includes the class of tetrakis(thiadiazole)porphyrazine complexes of the type [TTDPzM] (M = $Mg^{II}(H_2O)$, Zn^{II}) and [TTDPzMCl] (M = Al^{III}, Ga^{III}) compounds whose structure has been elucidated by single crystal X-ray work.[42, 99] Photoactivity for the generation of singlet oxygen, $^1O_2$, the key cytotoxic agent in the anticancer treatment known as photodynamic therapy (PDT),[88] was also previously monitored for these types of compounds in DMF or DMF/HCl solutions with the measured singlet oxygen quantum yield (Φ_Δ) in DMF/HCl increasing in the following order: Mg^{II} (0.30) < Al^{III} (0.35) < Zn^{II} (0.52) < Ga^{III} (0.69).[6] These results suggested the need to explore the photoactivity of complexes bearing trivalent metal ions of the octapyridinated tetrapyrazinoporphyrazine macrocycle, $Py_8TPyzPz$, their role in the area of PDT having previously been studied for this macrocycle only for complexes with the bivalent central metal ions $Mg^{II}(H_2O)$, Zn^{II} and Pd^{II} and the trivalent central metal ions Al^{III} and Ga^{III}. An example of these compounds is represented by derivatives having the formula [$Py_8TPyzPzM$] where $Py_8TPyzPz$ represents the tetrapyrazinoporphyrazine dianion and M is a metal ion.

In the present study details are given on synthetic procedures and general physicochemical and electrochemical properties of the mononuclear complexes having the formula

$[Py_8TPyzPzMX]\cdot xH_2O$ (M = Al^{III}, Ga^{III}; X = Cl^-, OH^-) and their related pentanuclear species $[(PdCl_2)_4Py_8TPyzPzMCl]\cdot xH_2O$ (M = Al^{III}, Ga^{III}). The ability of these compounds to generate singlet oxygen, $^1O_2$, for applications in PDT under appropriate experimental conditions will also be reported and discussed. The structures of the investigated porphyrazines are shown in Chart 5-1(a).

As part of our ongoing studies involving porphyrazines, we also wished to explore the influence of reducing or extending the central macrocyclic framework, with the aim of changing the size of the π-electron delocalized system. Accordingly, macrocycles having the formula $[Py_8PzM]$ were synthesized with the corresponding structures shown in Chart 5-1(b). The compounds can be formally thought of as being derived from $[Py_8TPyzPzM]$ by removing the pyrazine rings from the compounds. Template macrocyclization reactions enabled synthesis of the two new species as Mg^{II} derivatives, ie., $[Py_8PzMg(H_2O)]$ and $[Py_8QxPzMg(H_2O)]$,[100] and the examined UV-visible spectra of these compounds in dimethylformamide indicate that the Q band maximum moves systematically towards the red as the macrocycle π-system expands, ie. 635 → 658 for the sequence $[Py_8PzMg(H_2O)] \rightarrow [Py_8TPyzPzMg(H_2O)]$.

In an extension of our earlier work on tetrapyrazinoporphyrazines which are active as anticancer agents in PDT, it was thought interesting to open up additional perspectives on this class of macrocycles by virtue of their potential use as bimodal anticancer drugs in the area of boron neutron capture therapy (BNCT). Positive results for this kind of therapy have been reviewed for carboranylporphyrazines and carboranylphthalocyanines,[101] or reported using porphyrin macrocycles.[102, 103] To our knowledge, however, there have been only a few reports on the use of phthalocyanine derivatives positively tested.[104] The possibility of BNCT activity for a class of

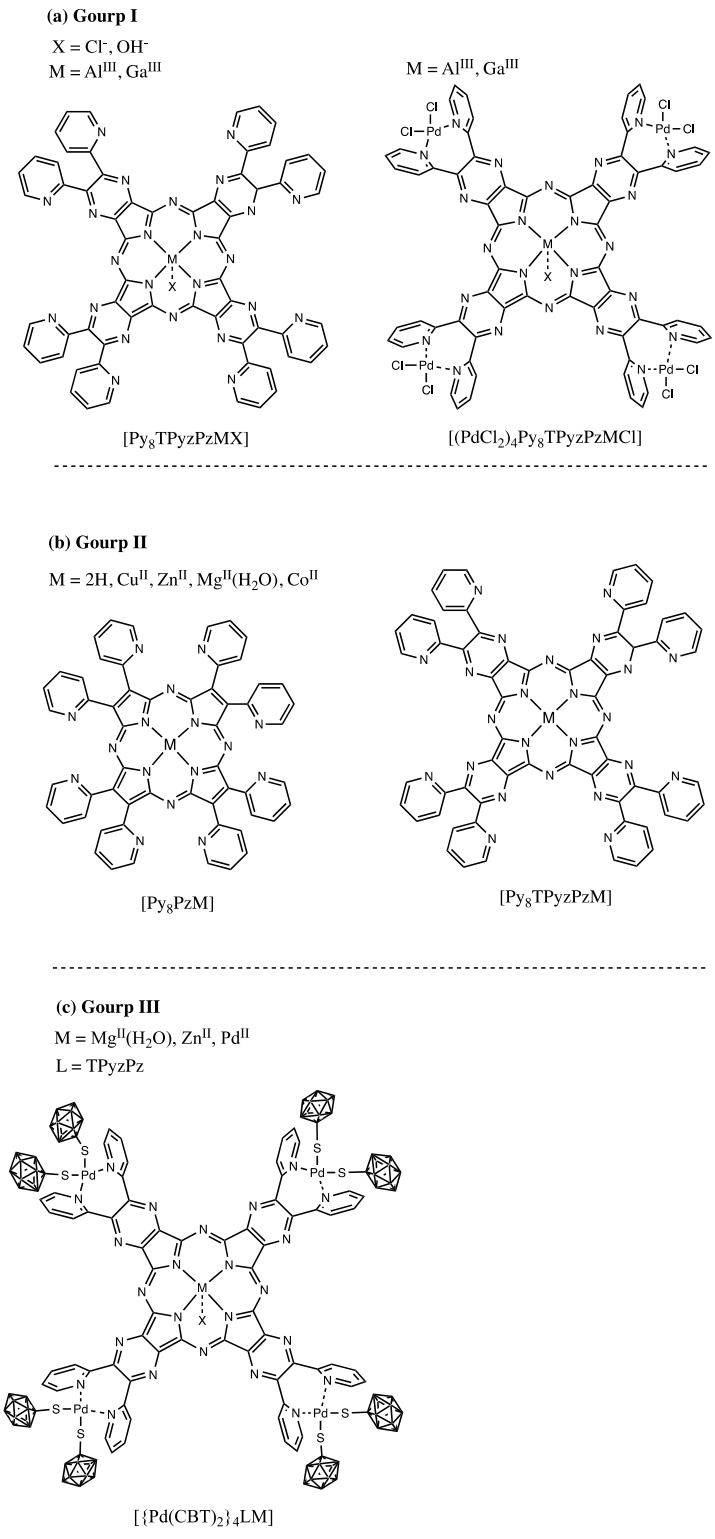

Chart 5-1. Structures of investigated porphyrazine derivatives.

octaanionic porphyrazines has also been reported.[105] In the present paper we describe the synthesis and physicochemical characterization of a new class of neutral m-carboran-1-thiolate (CBT) porphyrazine complexes. The structures of these newly synthesized compounds [[Pd(CBT)$_2$]$_4$LM] are shown in Chart 5-1(c). The behavior of these compounds as active species in PDT in DMF solution is a promising preliminary aspect which should lead to further combined exploration of PDT/BNCT using water solutions of this type of complexes incorporated in liposomes.

5.2 Results and Discussion

5.2.1 UV-visible Spectral Behavior of Group I Porphyrazine Derivatives

The currently investigated [Py$_8$TPyzPzMX] derivatives (M = Al^{III}, Ga^{III}; X = Cl^-, OH^-) are all insoluble in water and only very slightly soluble in THF, acetone or CH_2Cl_2. They are more soluble to about 10^{-4} M in the low-donor solvents DMSO, DMF and pyridine and their UV-vis spectral behavior in the latter solvents was examined by Dr. Maria Pia Donzello's laboratory from the Sapienza University of Rome using concentrations of the complexes on the order of 10^{-5}-10^{-6} M.

Depending upon the specific compound and the solvent, the spectra show in most cases low-intensity bands in the range 300-900 nm immediately after dissolution, with broad absorptions also appearing in the Soret (300-400 nm) and Q-band region (600-700 nm). In the case of the Al-Cl species the Soret and Q-band absorptions undergo with time (20-24 h) in DMSO and DMF (Figure 5-1) a progressive increase of intensity, ultimately giving a spectrum with peaks typical for a porphyrazine macrocycle, the final narrow Q-band peak clearly proving the presence of the complex exclusively in its monomeric form. Evolution of the spectra as a function of time shows well-defined isosbestic points, indicating the absence of spectrally detectable intermediates. On

this basis, it is reasonable to conclude that the observed spectral variation strongly suggests a conversion of the type dimer → monomer.

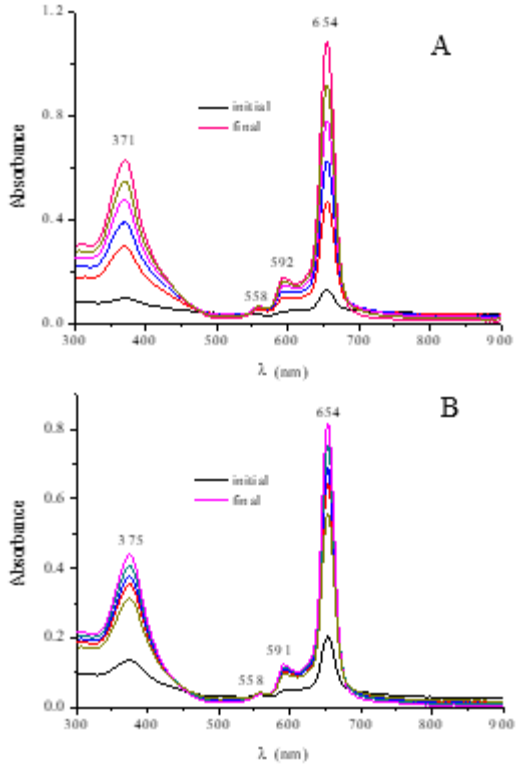

Figure 5-1. UV-visible spectral evolution with time of [Py_8TPyzPzAlCl] in A) DMSO (over 24 hrs) and B) DMF (over 19 hrs) (reproduced in part with permission from [*Inorg. Chem.* **2019**, *58*, 15269-15282], American Chemical Society).[45]

The spectral behavior of the Ga-Cl and Ga-OH species in DMSO as well as in pyridine parallels what is observed for the two Al^{III} species, i.e., a progressive spontaneous spectral evolution of a dimer → monomer conversion as exemplified in Figure 5-2A for the Ga-Cl complex in DMSO. The behavior of the Ga-Cl macrocycle in DMF (Figure 5-2B) requires special consideration in view of the fact that the spectrum observed immediately after dissolution is characterized by a Q band accompanied by a tail on the lower energy side, a small peak at 559 nm, and a broadening of the absorption with shoulders in the Soret region. These features closely recall

what is seen in the same solvent for the related mononuclear macrocycles [Py_8TPyzPzM] (M = $Mg^{II}(H_2O)$, Zn^{II}, Pd^{II}) upon reduction via electrochemistry to their -1 singly reduced forms.[38, 106]

For the currently examined Ga-Cl species, reduction is very likely caused by trace amounts of an impurity, presumably dimethylamine, formed from the hydrolysis of DMF, present in the solvent at a concentration on the same order of magnitude of the complex (10^{-5}-10^{-6} M) and acting as a reducing agent, a problematic aspect already considered in detail elsewhere.[39, 106] The observed facile reduction results from the fact that the first one-electron uptake takes place at a minimally negative $E_{1/2}$ value (see discussion below), similar to what was observed for some of the parent [Py_8TPyzPzM] species[39] and for the [TTDPzMX] (M = Al^{III}, Ga^{III}; X = Cl^-) analogs.[39, 42]

Addition of a slight excess of HCl ([HCl] ≅ $1x10^{-4}$ M) to the DMF solution is able to progressively reoxidize the complex to its neutral form with no further change of the Soret and Q-band peaks over time (Figure 5-2B), a process recalling findings for the mononuclear analogs carrying bivalent metal ions.[38, 106] It should be noted that HCl was also added to the DMSO solution of the compound (Figure 5-2A) to avoid the presence of even traces of the reduced species. The generated narrow Q-band absorptions, which are assigned as ligand-centered π-π* transitions, exhibit peak positions in the narrow range of 650-660 nm, no matter which the specific complex or the solvent, thus confirming that a change of the MX fragment does not significantly modify the electronic distribution within the macrocycle.

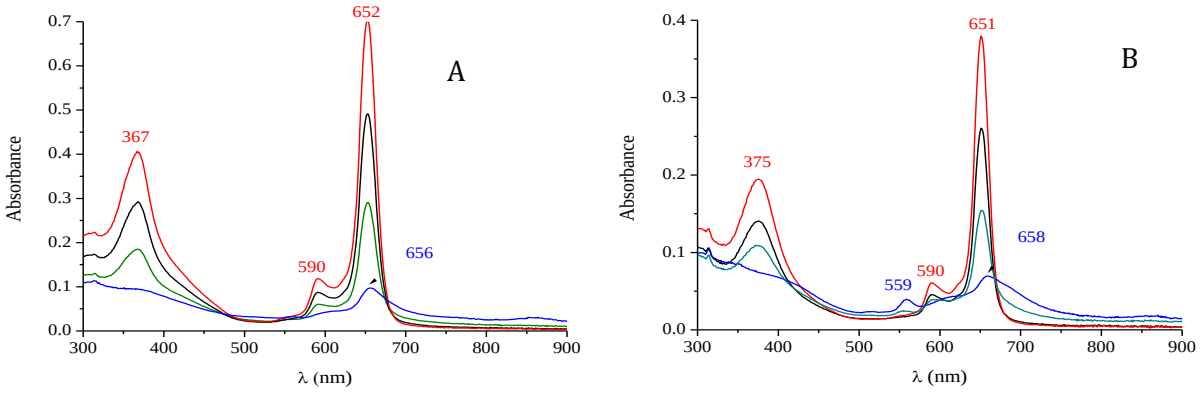

Figure 5-2. UV-visible spectra of [Py_8TPyzPzGaCl] in A) DMSO (blue line) and DMSO/HCl (from green to red; over 11 hrs) and B) in DMF (blue line) and DMF/HCl (from green to red; over 16 hrs) (reproduced in part with permission from [*Inorg. Chem.* **2019**, *58*, 15269-15282], American Chemical Society).[45]

The pentanuclear Al^{III} and Ga^{III} complexes have a relatively good solubility in DMSO and DMF comparable to that of the related mononuclear species. It should be noticed that dissolution in pyridine determines immediately the release of the external $PdCl_2$ units with formation of the respective monomeric species; this is strictly in line with the earlier observed behavior for the pentanuclear analogs carrying centrally bivalent metal centers.[38] The UV-visible spectrum of the [$(PdCl_2)_4Py_8$TPyzPzAlCl] complex in DMSO (Figure 5-3A) changes with time in a way suggesting formation of the monomeric species and this is consistent with a disaggregation process of the type dimer → monomer, as supported by the presence of isosbestic points. The spectrum in DMF (Figure 5-3B) provides evidence for formation of singly reduced species which is reversed to the neutral species upon addition of HCl HCl ([HCl] ≅ $1x10^{-4}$ M).

The initial spectrum of the pentanuclear Ga-Cl complex in solution of DMSO and DMF (Figure 5-4A,B) provides evidence for formation of the singly reduced species. The reduction is

definitively more evident in DMF and the features are totally consistent with those already observed for the related mononuclear species in the same solvent (Figure 5-2A,B). However, upon addition of HCl ([HCl] ≅ $1x10^{-4}$ M) to the solution, a reoxidation process immediately occurs, leading to a final spectrum which is as expected for a neutral macrocyclic species in its monomeric form.

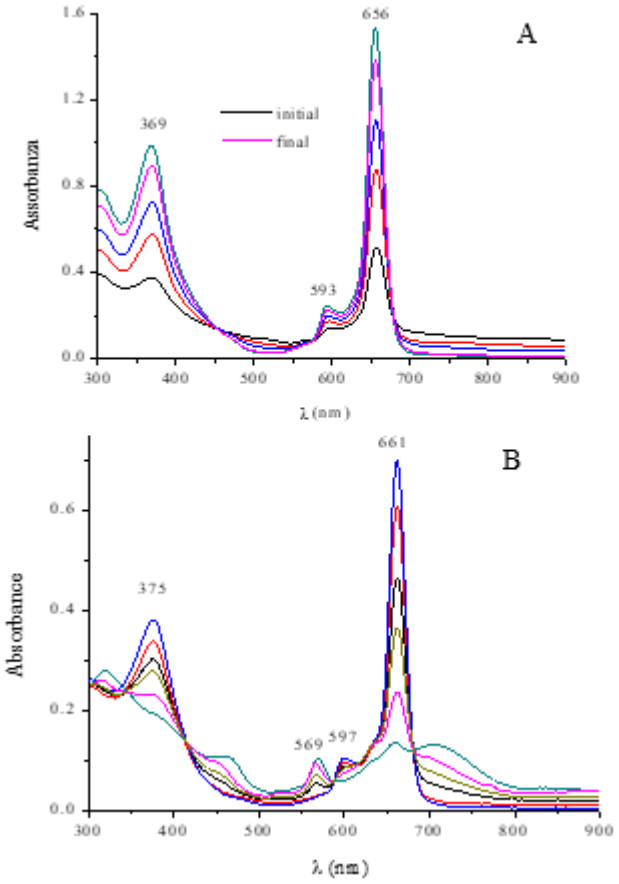

Figure 5-3. UV-visible spectral evolution with time of [$(PdCl_2)_4Py_8TPyzPzAlCl$] in (A) DMSO/HCl (over 72 hrs) and (B) DMF (green line) and DMF/HCl (from pink to blue; over 5 hrs) (reproduced in part with permission from [*Inorg. Chem.* **2019**, *58*, 15269-15282], American Chemical Society).[45]

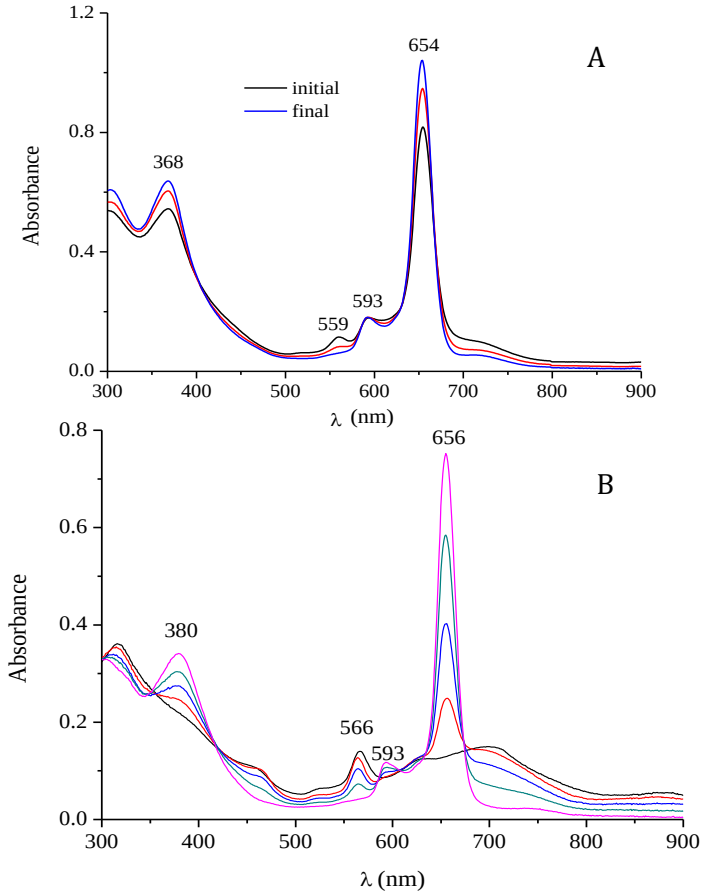

Figure 5-4. UV-visible spectral evolution with time of[$(PdCl_2)_4Py_8TPyzPzGaCl$] in A) DMSO/HCl (over 22 hrs) and B) DMF (black line) and DMF/HCl (from red to pink; over 4 hrs) (reproduced in part with permission from [*Inorg. Chem.* **2019**, *58*, 15269-15282], in press, American Chemical Society).[45]

A summary of the UV-visible spectral data for the present mono- and pentanuclear species is given in Table 5-1. As to the Ga^{III} complexes and the two Al^{III} and Ga^{III} pentanuclear complexes the values of molar absorptivities in DMSO and DMF were measured in the presence of HCl in order to compare the ε value for each single species in the complete absence of the related singly reduced form. For all of the species, the Soret and Q-band maxima are in the respective narrow ranges of 370-380 and 650-660 nm, the positions of both bands being bathochromically shifted in pyridine as compared to what is seen in DMSO or DMF. Furthermore, the position of the Q-band

for the two Al^{III} and Ga^{III} pentanuclear complexes is also bathochromically shifted by 2-5 nm with respect to that of the respective mononuclear species. This is in line with expectation, due to the more electron-deficient macrocycle resulting from the external coordination of $PdCl_2$.

Table 5-1. UV-visible spectra (λ, nm (log ε)) of the [Py_8TPyzPzMX] complexes, (M = Al^{III} or Ga^{III} and X = Cl^- or OH^-), [$(PdCl_2)_4Py_8$TPyzPzMCl] (M = Al^{III} or Ga^{III}) (reproduced in part with permission from [*Inorg. Chem.* **2019**, *58*, 15269-15282], American Chemical Society)[45]

Complex	Solvent	Soret region	Q-band region		
			λ, nm (log ε)		
[Py_8TPyzPzAlCl]	DMSO	371 (5.01)	558 (3.98)	592 (4.46)	654 (5.24)
	DMF	375 (5.11)	558 (4.05)	591 (4.56)	654 (5.38)
	Py	378 (4.48)	562 (3.49)	592 (3.97)	656 (4.77)
[Py_8TPyzPzAlOH]	DMSO	373 (5.01)	558 (4.06)	592 (4.49)	654 (5.26)
	DMF	374 (5.02)	558 (3.84)	592 (4.45)	654 (5.30)
	Py	378 (4.98)	563 (3.86)	592 (4.43)	655 (5.29)
[Py_8TPyzPzGaCl]	DMSO/HCl	367 (4.99)		590 (4.46)	652 (5.26)
	DMF/HCl	375 (4.97)		590 (4.43)	651 (5.26)
	Py	383		593	656
[Py_8TPyzPzGaOH]	DMSO/HCl	369 (4.92)		592 (4.39)	653 (5.17)
	DMF/HCl	375 (4.92)		590 (4.44)	652 (5.23)
	Py	381 (4.51)		592 (4.03)	655 (4.87)
[Py_8TPyzPzZn]	DMSO	372 (5.10)	592 (4.54)	629 (4.61)	655 (5.36)
	DMF	375 (4.90)	600 (4.38)	626sh (4.84)	657 (5.15)
	DMF/HCl	376 (4.98)	596 (4.45)	626 (4.50)	657 (5.27)
	Py	378 (4.90)	598 (4.31)	630 (4.35)	658 (5.18)
[$(PdCl_2)_4Py_8$TPyzPzAlCl]	DMSO/HCl	369 (5.02)		593 (4.42)	656 (5.21)
	DMF/HCl	375 (4.97)		597 (4.40)	661 (5.25)
[$(PdCl_2)_4Py_8$TPyzPzGaCl]	DMSO/HCl	368 (4.97)		593 (4.41)	654 (5.17)
	DMF/HCl	380 (4.88)		593 (4.41)	656 (5.23)
[$(PdCl_2)_4Py_8$TPyzPzZn]	DMSO	370 (5.03)	598 (4.47)		657 (5.23)
	DMF	377 (4.86)	600 (4.38)		662 (5.26)
	DMF/HCl	377 (4.86)	600 (4.40)		662 (5.28)

[a] Quantitative data refer to samples of the species in the precise hydrated form reported in the experimental section.

5.2.2 Electrochemistry of of Group I Porphyrazine Derivatives

The six newly synthesized monometallic and pentanuclear complexes were characterized by cyclic voltammetry in DMF and DMSO containing 0.1M TBAP. Examples of cyclic voltammograms for [Py_8TPyzPzMX] and [$(PdCl_2)_4Py_8$TPyzPzMCl] are given in Figures 5-5,5-7,5-8 and the measured half-wave or peak potentials are summarized in Table 5-2 along with data for related compounds.

Focusing first on the data obtained in DMF, the following comments can be made for the mononuclear [Py_8TPyzPzMX] derivatives:

1) The first and second one-electron reductions are reversible and well-defined for the AlCl and GaOH complexes, but are ill-defined for the AlOH and GaCl derivatives as seen in Figure 5-5. The GaCl derivative is poorly soluble in DMF while the AlOH compound shows evidence for an equilibrium between a neutral hydroxide bound AlOH species and a positively charged mono-DMF adduct, $Al(DMF)^+$ with a dissociated OH^- axial ligand, each of which is reduced at a different potential as shown in the figure, where the half wave potentials of -0.10 and -0.52 V can be assigned to the $Al(DMF)^+$ complex, and the $E_{1/2}$ values at -0.17 and -0. 58 V, reported in Table 5-2, are assigned to the neutral AlOH species. As expected, the $Al(DMF)^+$ species is easier to reduce by virtue of the positive charge on the complex. A similar equilibrium and similar findings have previously been reported for derivatives of TTDPz.[42] In this regard, it is appropriate here to report on the additional information obtained by measuring cyclic voltammograms of the AlOH species in DMF before and after addition of excess OH^- in the form of tetrabutylammomium hydroxide (TBAOH) (Figure 5-6). The figure shows that addition of OH^- ions shifts the equilibrium from the DMF bound charged Al(III) complex without a OH^- axial ligand to the uncharged AlOH species

which undergoes three clean reversible one-electron reductions, the first two shifted to slightly more negative values (-0.24 and -0.64 V).

2) The potentials for reduction of a given Al^{III} or Ga^{III} species are very similar to each other along the series of compounds, all electron additions being extremely facile and ranging from the $E_{1/2}$ = -0.04 V to -0.10 V for the first reduction. These potentials are almost identical to those reported earlier for related TTDzPz derivatives of Al^{III} and Ga^{III} (see Table 5-2) but are shifted by more than 500 mV from $E_{1/2}$ values for the first reduction of [PcAlCl] (compound **10**) in the same solvent. [42] These data thus provide clear evidence that a replacement of the four benzene rings in a phthalocyanine macrocycle by strongly electron-withdrawing dipyridinopyrazine fragments, confer to the porphyrazine core a general electron-deficient character, highly facilitating the electron uptake and associated charge redistribution within the macrocycle. This result is independent of the central metal ion and was earlier observed when comparing a related series of bivalent metal derivatives of the formula [Py_8TPyzPzM] with their phthalocyanine analogs [PcM]. [38-41]

A similar electron-deficient character was reported[42] for the [TTDPzMX] (compounds **6, 7**, **8** in Table 5-2), which show four distinct one-electron reductions at potentials less negative than the corresponding Pc analogs, and very close to the $E_{1/2}$ values for the presently studied octapyridinated species [Py_8TPyzPzMX] (the first reduction ranges from -0.07 to -0.12 V for compounds **6**, **7**, and **8**).

Table 5-2. Half-Wave Potentials (V vs SCE) of [Py_8TPyzPzMX] (M = Al^{III} or Ga^{III} and X = Cl^- or OH^-), [$(PdCl_2)_4Py_8$TPyzPzMCl] (M = Al^{III} or Ga^{III}) and related compounds in DMSO and DMF (0.1 M TBAP; scan rate = 100 mV/s)

Solvent	Cpd #	Macrocycle	Metal	Reductions (V vs SCE)				Ref.
				1st	2nd	3rd	4th	
DMF	**1**	Py_8TPyzPz	AlCl	-0.09	-0.47	-0.98[a]		tw
	2		AlOH[b]	-0.17	-0.58	-1.23	-1.46[a]	tw
	3		GaCl	-0.05	-0.40	-0.98	-1.41	tw
	4		GaOH	-0.10	-0.41	-1.22	-1.42	tw
	5		Zn	-0.39	-0.75	-1.41		39
	6	TTDPz	AlCl	-0.10	-0.54	-1.34	-1.78	42
	7		AlOH	-0.12	-0.56	-1.36	-1.80	42
	8		GaOH	-0.07	-0.47	-1.31	-1.82	42
	9		Zn	-0.44	-0.87	-1.65		42
	10	Pc	AlCl	-0.55	-1.00	-1.94		42
	11		Zn	-0.89	-1.33	-2.06	-2.68	41
	12	$(PdCl_2)_4Py_8$TPyzPz	AlCl	0.03	-0.34			tw
	13		GaCl	0.10	-0.20			tw
	14		Zn	-0.12	-0.52	-1.39	-1.62	41
DMSO	**1**	Py_8TPyzPz	AlCl	-0.04	-0.41	-1.02[a]	-1.34[a]	tw
	2		AlOH	-0.03	-0.42	-1.18	-1.45	tw
	3		GaCl	0.03	-0.35	-1.04	-1.60[a]	tw
	4		GaOH	0.04	-0.35	-1.12[a]	-1.47	tw
	5		Zn	-0.26	-0.67	-1.38	-1.64	106
	12	$(PdCl_2)_4Py_8$TPyzPz	AlCl[c]	0.02	-0.21			tw
	13		GaCl	0.15	-0.14			tw
	14		Zn	-0.13	-0.54	-1.39	-1.63	41

[a] irreversible process
[b] reductions assigned to $Al(DMF)^+$ species are also observed at E_{pc} = -0.10 and -0.52 V.
[c] reduction is also assigned to the $Al(DMSO)^+$ complex at $E_{1/2}$ = 0.15 V (see Figure 5-8).

1) It is interesting to note that $E_{1/2}$ values for the first and following reductions of the [Py_8TPyzPzMX] complexes (**1-4** in Table 5-2) are less negative than reduction potentials for the related M^{II} species [Py_8TPyzPzM] in the same solvent (see as an example the Zn^{II}

complex **5** shown in Table 5-2). These findings also parallel earlier results seen for the thiadiazole analogs [TTDPzMX] (compounds **6**, **7**, and **8** in Table 5-2), for which the out-of-plane displacement of the metal centers and their lower electronegativity with respect to that of the bivalent metal ions in the parent [TTDPzM] series (data for the Zn^{II} complex **9** in Table 5-2) favor the uptake of electrons by the porphyrazine macrocycle. A similar behavior is observed for the phthalocyanine analogs for which $E_{1/2}$ values are less negative than for reduction of the corresponding bivalent [PcM] complexes (-0.55 and -0.89 V in DMF for [PcAlCl] and [PcZn] respectively; see compounds **10** and **11** in Table 5-2).

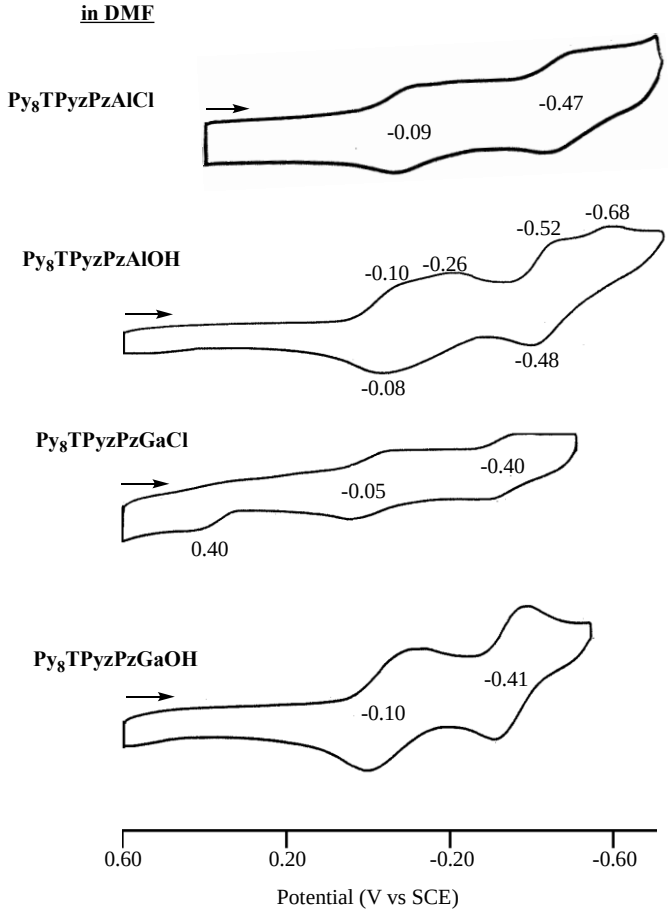

Figure 5-5. Cyclic voltammograms of first two reductions for [Py_8TPzPzMX] (M = Al^{III} or Ga^{III} and X = Cl^- or OH^-) in DMF, containing 0.1 M TBAP. Scan rate = 100 mV/s.

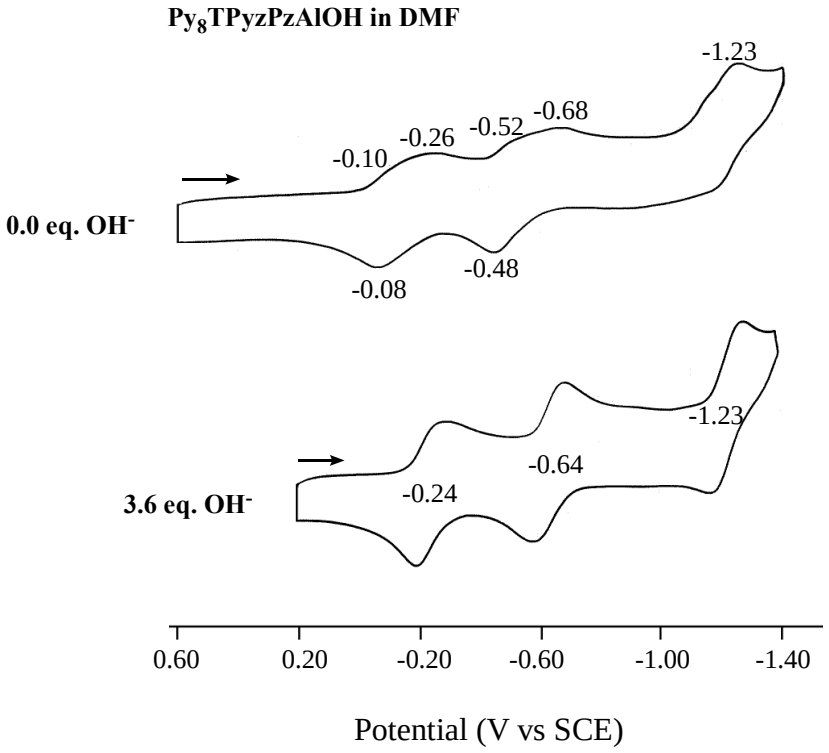

Figure 5-6. Cyclic voltammograms of [Py_8TPzPzAlOH] in DMF containing 0.0 eq. and 3.6 eq. TBAOH, 0.1 M TBAP. Scan rate = 100 mV/s.

In summary, closely similar observations and conclusive comments on the just illustrated electrochemical experiments conducted in DMF can be made for all the examined [Py_8TPyzPzMX] complexes in DMSO solution (see data in Table 5-2 for compounds **1-4** and CV reported in Figure 5-7**.**

The pentanuclear species, [$(PdCl_2)_4Py_8$TPyzPzMCl] (compounds **12** and **13**), were also characterized by cyclic voltammetry in both DMF and DMSO containing 0.1 M TBAP; the measured potentials are reported in Table 5-2 and examples of the cyclic voltammograms are shown in Figure 5-8. As can be seen from the figure and table, the first and second reductions of compounds **12** and **13** are positively shifted with respect to $E_{1/2}$ values for the related monometallic

species [Py_8TPyzPzMCl] having the same central metal ion and same axial ligand (compounds **1** and **3**). These findings parallel those of the corresponding species having a bivalent central metal ion (see data for **5, 14** in Table 5-2)[39, 40] and confirm that external coordination of the $PdCl_2$ units induces an easier acceptance of negative charge within the macrocyclic framework; this is in strict accordance with the enhanced electron-withdrawing properties of the external dipyridinopyrazine fragments once they are metalated.

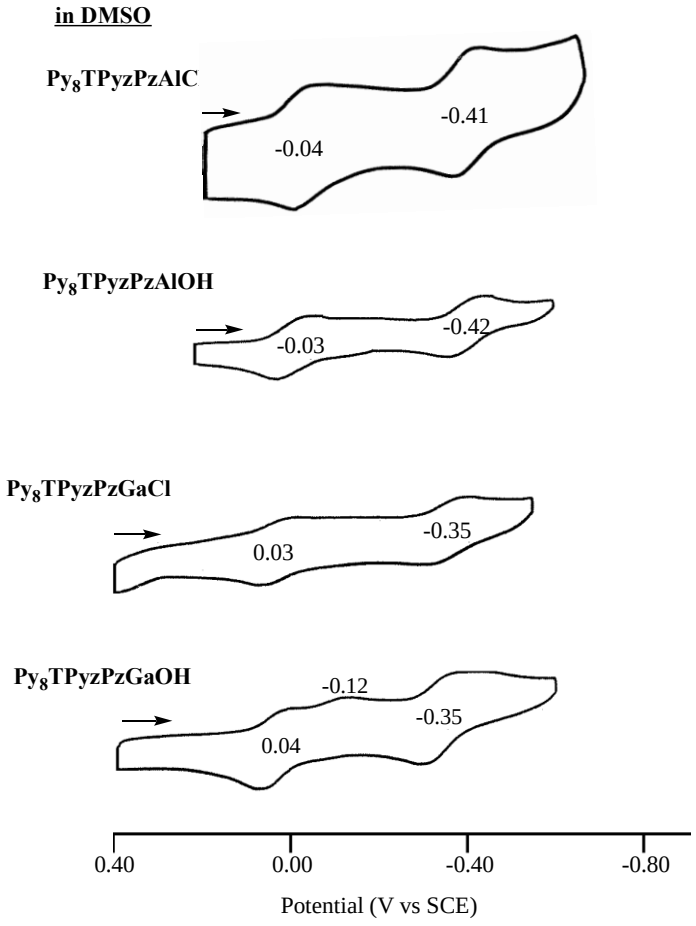

Figure 5-7. Cyclic voltammograms of first two reductions for [Py_8TPzPzMX] (M = Al^{III} or Ga^{III} and X = Cl^- or OH^-) in DMSO, containing 0.1 M TBAP. Scan rate = 100 mV/s.

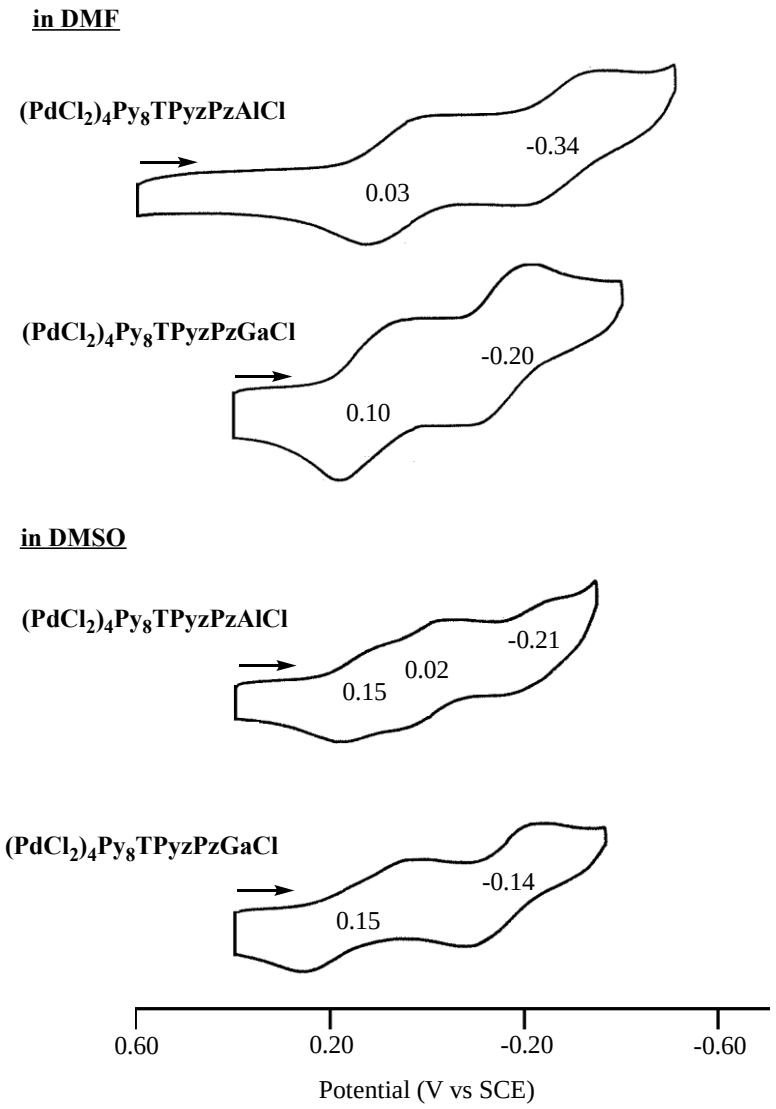

Figure 5-8. Cyclic voltammograms showing the first two reductions for $[(PdCl_2)_4Py_8TPzPzMCl]$ ($M = Al^{III}$ or Ga^{III}) in DMF and DMSO, containing 0.1 M TBAP. Scan rate = 100 mV/s.

Also worthy of note in the case of the pentanuclear species is the fact that compounds with the trivalent Al^{III} and Ga^{III} metal ions show less negative $E_{1/2}$ values than the corresponding M^{II} analogs $[(PdCl_2)_4Py_8TPyzPzM]$.

5.2.3 UV-Visible Spectral Behavior of Group II Porphyrazine Derivatives[44]

The examined [Py_8PzH_2] and its metal derivatives [Py_8PzM] possess good solubility in the polar non aqueous solvents pyridine, DMSO and DMF ($c \leq 10^{-3}$ M), and, as expected, higher than that of the related pyrazinoporphyrazine macrocycles [$Py_8TPyzPzM$]. Solubility of the [Py_8PzM] compounds was generally found to be lower in the non-donor solvents $CHCl_3$, CH_2Cl_2, exceptions being observed in the case of [Py_8PzH_2] and its Mg^{II} complex, for which solubility approached that observed in the low donor solvents.

Table 5-3. UV-visible Spectral Data (λ, nm (log ε)) of [Py_8PzH_2] and [Py_8PzM] (M = $Mg^{II}(H_2O)$, Co^{II}, Cu^{II}, Zn^{II}) in Different Solvents **(**reproduced in part with permission from [*Inorg. Chem.* **2017**, *56,* 5813-5826], American Chemical Society)[44]

		λ (nm) (logε)			
Compound	Solvent	Soret		Q-band	
[Py_8PzH_2]	DMF	370 (4.68)	551sh (4.04)	596 (4.45)	635 (4.46) 660 (4.64)
	DMSO	368 (4.67)	554sh (4.10)	598 (4.47)	633 (4.43) 661 (4.63)
	Py	375 (4.73)	557sh (4.11)	598 (4.53)	637 (4.36) 664 (4.71)
	$CHCl_3$	370 (4.87)	551sh (4.20)	594 (4.67)	637 (4.45) 663 (4.86)
	CH_2Cl_2	367 (4.67)	559sh (4.05)	594 (4.46)	637 (4.20) 662 (4.65)
[$Py_8PzMg(H_2O)$][a]	DMF	378 (5.05)	583 (4.46)		636 (5.18)
	DMSO	378 (4.52)	583 (3.95)		636 (4.63)
	py	381 (4.80)	583 (4.18)		638 (4.89)
	$CHCl_3$	378 (4.74)	583 (4.10)		637 (4.80)
[Py_8PzCo]	DMF	354 (4.52)	573sh (4.17)		613 (4.55)
	DMSO	357 (4.40)	572sh (3.06)		611 (4.50)
	py	356 (4.23)	571sh (3.88)		613 (4.29)
[Py_8PzCu]	DMF	371 (4.06)	578sh (3.62)		623 (4.24)
	DMSO	374 (4.54)	580sh (4.17)		627 (4.70)
	py	376 (4.71)	573 (4.27)		627 (5.01)
[Py_8PzZn]	DMF	380 (4.82)	585 (4.26)		637 (4.98)
	DMSO	380 (4.92)	584 (4.35)		636 (5.07)
	py	381 (4.85)	583 (4.27)		637 (4.97)

[a] See reference [100].

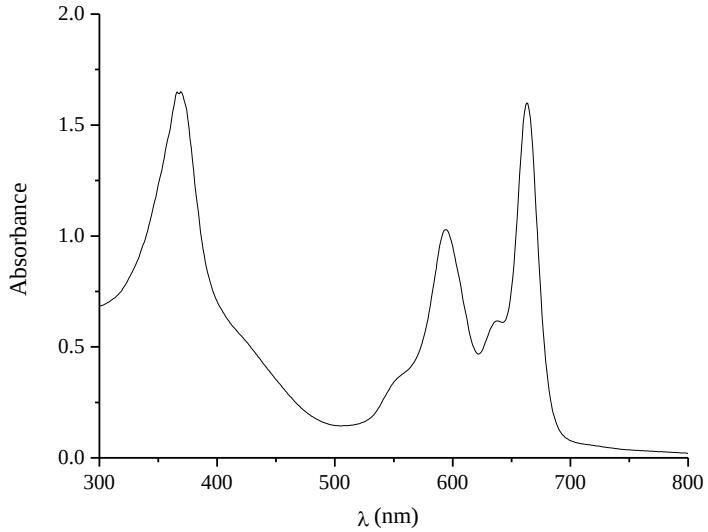

Figure 5-9. UV-visible spectrum of [Py_8PzH_2] in $CHCl_3$ solution **(**reproduced in part with permission from [*Inorg. Chem.* **2017**, *56*, 5813-5826], American Chemical Society).[44]

[Py_8PzH_2]. The spectrum of unmetalated macrocycle [Py_8PzH_2] is stable with time in solutions of $CHCl_3$ and is characterized by an intense absorption in the Soret region (370 nm) and a split Q band with peaks at 594 and 663 nm (Figure 5-9). This type of spectrum is as expected for D_{2h} symmetry and supports the presence of the macrocycle being in its monomeric form with two central N-H groups. A low intensity peak at 637 nm can be assigned to the presence of a small amount of the dianion $[Py_8Pz]^{2-}$ in equilibrium with the neutral form. Quite similar spectra were observed in CH_2Cl_2 (peaks at 594 and 662 nm) and pyridine (peaks at 598 and 664 nm) (data listed in Table 5-3). The two distinct absorptions in the Q-band region are assigned as the two components of the Q band, ie., Q_x and Q_y, due to the transitions $a_u \rightarrow b_{2g}$ and $a_u \rightarrow b_{3g}$, respectively. The presence of a stable split Q band for [Py_8PzH_2] at room temperature suggests a higher stability in its neutral form with respect to the related dianion $[Py_8Pz]^{2-}$ in $CHCl_3$, CH_2Cl_2 or in pyridine.

The absorption in the Soret region at 370-375 nm is assigned as the B band in all the solvents, DMSO and DMF included (Table 5-3).

It should be pointed out that the spectrum of the corresponding tetrapyrazinoporphyrazine compound [$Py_8TPyzPzH_2$], exhibits an unsplit Q band (667 nm) in pyridine.[107] This suggests a loss of the central protons and formation of the deprotonated dianion [$Py_8TPyzPz]^{2-}$ (D_{4h} symmetry). This result in pyridine solutions indicates that [$Py_8TPyzPzH_2$] is more acidic than [Py_8PzH_2]. An explanation for this result most likely resides in the fact that the pyrazine rings in the pyrazinoporphyrazine complex enhance the electron-deficiency of the macrocycle due to their electron-withdrawing properties, thus facilitating release of the central protons. A somewhat related spectral evolution was also observed for the octaphenyl substituted porphyrazine in pyridine solution.[108]

It should be noted that the observed 68-69 nm splitting of the Q bands for [Py_8PzH_2] in $CHCl_3$ and CH_2Cl_2 is much higher than the 33 nm splitting observed in the same solvents for the corresponding free-base pyrazinoporphyrazine, [$Py_8TPyzPzH_2$].[107] This seems to indicate that in going from [Py_8PzH_2] to [$Py_8TPyzPzH_2$], the splitting of the b_{2g} and b_{3g} HOMO energy levels decreases along with an extension of the π-delocalized system.

The examined spectral behavior of [Py_8PzH_2] in DMSO and DMF provides additional useful information about conversion of the neutral species to the corresponding dianion [$Py_8Pz]^{2-}$ in these solvents. Figure 5-10 shows the spectral changes observed for [Py_8PzH_2] in DMSO as a function of time, combined with heating of the solution (a parallel time dependent behavior is observed in DMF). As can be seen from the figure, the initial spectrum shows two peaks at 598 and 661 nm which are attributable to the split Q_x and Q_y absorptions in addition to a peak at 633 nm, a position

coincident with that of the low intensity peak also seen in the spectrum recorded in $CHCl_3$, CH_2Cl_2, and pyridine. This is clearly attributable to the presence of a small amount of the free-base macrocycle being in its dianionic $[Py_8Pz]^{2-}$ form (single Q band and D_{4h} symmetry). The combined double action of time and heating of the solution leads to an increase in intensity of the band at 633 nm and a concomitant decrease in intensity of peaks at 598 and 661 nm which are assigned to the neutral form of the compound. The final spectrum obtained after four days reveals exclusively the presence of the dianion (see Figure 5-11, red line). Noteworthy, differences do exist, as compared to the corresponding free-base pyrazinoporphyrazine $[Py_8TPyzPzH_2]$, which behaves the same in DMSO, DMF, and pyridine solutions, giving rise immediately after dissolution to formation of the deprotonated species $[Py_8TPyzPz]^{2-}$.[107]

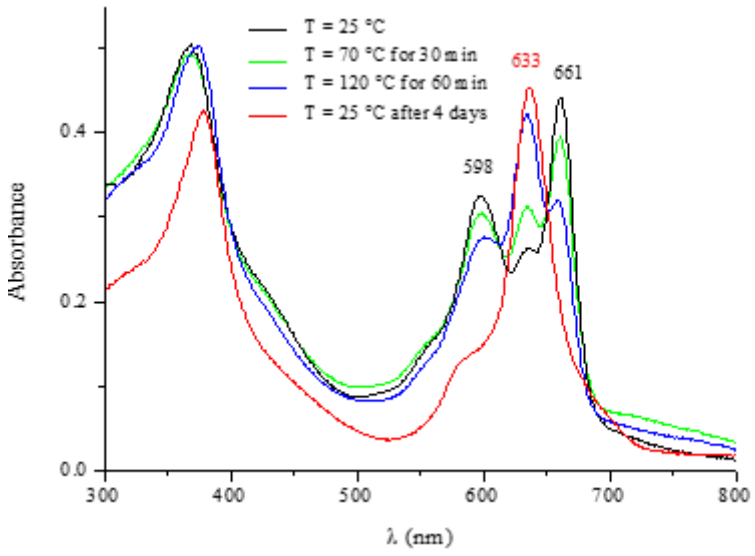

Figure 5-10. UV-visible spectral changes for $[Py_8PzH_2]$ in DMSO as a function of time and heating of the solution **(**reproduced in part with permission from [*Inorg. Chem.* **2017**, *56*, 5813-5826], American Chemical Society).[44]

In order to further support the formation of the dianion $[Py_8Pz]^{2-}$ in DMSO, a titration of $[Py_8PzH_2]$ was performed in this solvent with TBAOH. The observed UV-visible spectral changes are illustrated in Figure 5-11, where it can be seen that the spectrum of the neutral species changes towards that of the corresponding dianion, with the peak of this latter centered at 641 nm, only slightly batochromically shifted with respect to the position indicated in Figure 5-10. Accordingly, the concomitant disappearance of the absorptions of the neutral species at 597 and 661 nm is observed.

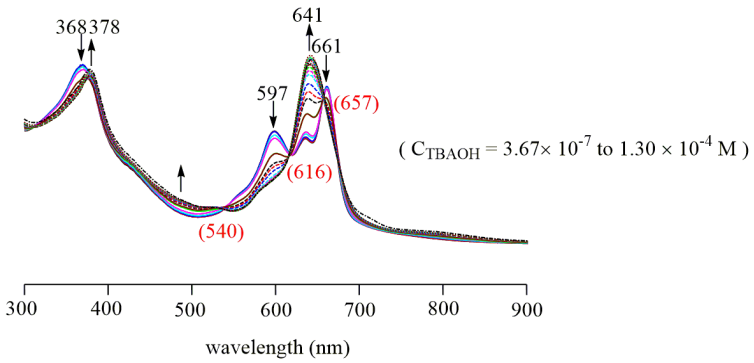

Figure 5-11. UV-visible spectral changes during the titration of $[Py_8PzH_2]$ with TBAOH in DMSO.

Spectral behaviour of the complexes [Py₈PzM] ($Mg^{II}(H_2O)$, Co^{II}, Cu^{II}, Zn^{II}). The UV-visible spectra of the metal complexes in pyridine, DMSO and DMF all show similar well-defined profiles (see example in Figure 5-12), with a single band in the Soret region of the spectrum (340-450 nm) and sharp unsplit Q bands in the region 610-640 nm which are attributable to ligand-centered $\pi \rightarrow \pi^*$ transitions in an approximate D_{4h} symmetry. The overall shape of the spectra indicate the presence of the almost exclusively monomeric species, even at the highest examined concentrations (ca. 10^{-3} M in DMF). The observed spectral features suggest a behavior which is in line with previous findings for M^{II} pyrazinoporphyrazines.

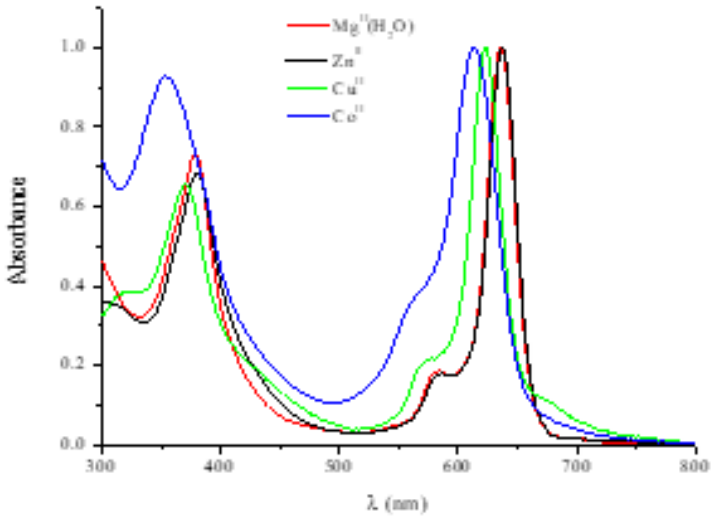

Figure 5-12. UV-visible spectra of the complexes [Py_8PzM] (M = $Mg^{II}(H_2O)$, Co^{II}, Cu^{II}, Zn^{II}) in DMF **(**reproduced in part with permission from [*Inorg. Chem.* **2017**, *56*, 5813-5826], American Chemical Society).[44]

In general, the Soret and Q bands exhibit only a small solvent effect, analogous to what is seen for the parallel series of pyrazinoporphyrazines. However, a marked change in the position of the Q-band maxima is seen with changes in the central metal ion, which increases in the sequence: Co^{II} (611-612 nm), Cu^{II} (623-627 nm), and Mg^{II} and Zn^{II} (636-638 nm). Interestingly, the same sequence of shifts occurs for the pyrazinoporphyrazine analogs: Co^{II} (634-635 nm), Cu^{II} (648-653 nm), and Mg^{II} and Zn^{II} (653-658 nm). From these data it clearly appears that moving from the [Py_8PzM] complexes to the corresponding pyrazinoporphyrazines [$Py_8TPyzPzM$] results in a 20-25 nm bathochromic shift of the Q-band maxima for each metal derivative. This bathochromic shift is determined by the increased extension of the π-electron delocalization consequent to incorporation of the pyrazine rings in going from [Py_8PzM] to [$Py_8TPyzPzM$].

5.2.4 Electrochemistry of Group II Porphyrazine Derivatives

[Py_8PzH_2] and the triad of complexes [Py_8PzM] (M = $Mg^{II}(H_2O)$, Zn^{II}, Cu^{II}) were electrochemically investigated in DMSO and pyridine, while [Py_8PzCo] was investigated in the same two solvents in addition to PhCN and CH_2Cl_2. Previous electrochemical studies on the related pyrazinoporphyrazine macrocycles derivatives [$Py_8TPyzPzH_2$][107] and [$Py_8TPyzPzM$],[40, 41, 106] and similar macrocycles bearing annulated diazepine[109] and thienyl rings,[110] have generally shown that each porphyrazine macrocyclic species can be reduced in four one-electron transfer steps and this is also the case for the currently investigated compounds, although the current-voltage curves were in many cases "complicated" by the presence of aggregation under some of the solution conditions. The electrochemical behavior of the present compounds is detailed here below.

[Py_8PzH_2]. Cyclic voltammograms of the metal-free [Py_8PzH_2] in pyridine are illustrated in Figure 5-13. The first two reductions are reversible and involve one electron additions to the macrocycle generating $[Py_8PzH_2]^-$ and $[Py_8PzH_2]^{2-}$, respectively. These processes occur at $E_{1/2}$ = -0.26 and -0.65 V vs. SCE and can be compared to $E_{1/2}$ values of -0.17 and -0.48 V for the corresponding reductions of [$Py_8TPyzPzH_2$] under the same solution conditions.[107] Two reversible one-electron reductions of [Py_8PzH_2] are also observed in DMSO (at $E_{1/2}$ = -0.17 and -0.57 V).

A third reversible reduction of [Py_8PzH_2] is observed at -0.93 V in pyridine (see Fig. 5-13) and this process corresponds to reduction of the deprotonated $[Py_8Pz]^{2-}$ macrocycle according to equation (5-1) as described earlier for [$Py_8TPyzPzH_2$].[107]

$$[Py_8Pz]^{2-} + e^- \rightleftharpoons [Py_8Pz]^{3-} \qquad (5\text{-}1)$$

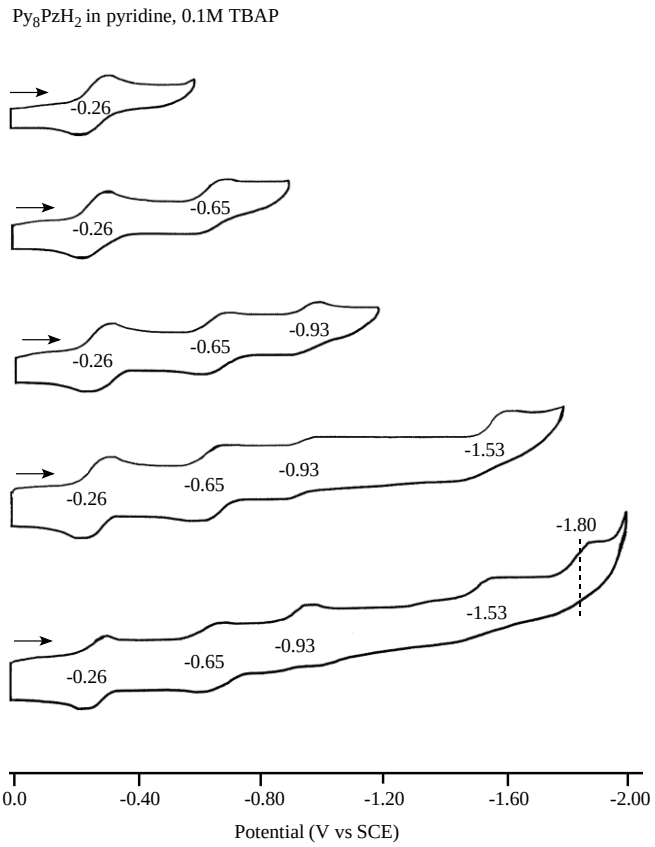

Figure 5-13. Cyclic voltammograms of [Py_8PzH_2] in pyridine, 0.1M TBAP. Scan rate = 0.1 V/s.

The first and second reductions of [Py_8PzH_2] are harder than the first and second reductions of [$Py_8TPyzPzH_2$], which is consistent with the smaller conjugated system in [Py_8PzH_2]. The same order in ease of reduction is also observed for the metal derivatives of these two macrocycles as described on the following pages. Surprisingly, the measured half wave potential for reduction of the deprotonated $[Py_8Pz]^{2-}$ in pyridine is exactly the same as $E_{1/2}$ for reduction of $[Py_8TPyzPz]^{2-}$ (-0.93 V) under the same solution conditions. Almost identical values in half-wave potentials are also seen for the same two macrocycles in DMSO where $[Py_8Pz]^{2-}$ is reduced at -0.87 V and $[Py_8TPyzPz]^{2-}$ at -0.89 V (see Table 5-4).

The last two reductions of [Py_8PzH_2] in pyridine are located at $E_{1/2}$ = -1.53 V and E_{pc} = -1.86 V as seen in Figure 5-13. Like the first two reductions, these processes are harder (occur at more negative potentials) than the third and fourth reductions of [$Py_8TPyzPzH_2$] in the same solvent, the magnitude of the potential difference between the relevant redox reactions being 290 and ~250 mV, respectively (see Table 5-4). The lack of well-defined reoxidation peaks for the reductions of [Py_8PzH_2] at -1.53 and -1.86 V are most likely related to equilibria involving the fully protonated porphyrazines and the deprotonated porphyrazine in its initial and/or singly reduced form, i.e. $[Py_8Pz]^{2-}$ and $[Py_8Pz]^{3-}$.

[Py_8PzM] where M = Cu^{II}, Zn^{II} and $Mg^{II}(H_2O)$. The first one-electron reduction of the Cu^{II}, Zn^{II} and $Mg^{II}(H_2O)$ porphyrazines is well defined in pyridine and located at -0.38, -0.46, and -0.54 V, respectively. These values can be compared to the first one-electron reduction of the analogous [$Py_8TPyzPzM$] derivatives which are reduced at -0.30, -0.34, and -0.40 V, respectively as seen in Table 3. Thus, like in the case of the free-base derivatives, more facile reductions are again seen for [$Py_8TPyzPzM$] than for [Py_8PzM], with the exact difference in potential varying with the type of central metal ion and following the order: Cu^{II} ($\Delta E_{1/2}$ = 80 mV) < Zn^{II} ($\Delta E_{1/2}$ = 120 mV) < $Mg^{II}(H_2O)$ ($\Delta E_{1/2}$ = 140 mV). The above separation in $E_{1/2}$ between the two related metallomacrocycles with the same metal ion can be compared with a $\Delta E_{1/2}$ of 90 mV between half-wave potentials for the first reduction of [Py_8PzH_2] and the first reduction of [$Py_8TPyzPzH_2$] (see above discussion and Table 5-4).

A second reversible one-electron reduction of [Py_8PzZn] is observed in pyridine and DMSO. These reductions occur at -0.91 and -0.85 V, respectively, and are shifted negatively by 180 to 190 mV

from $E_{1/2}$ values of [Py_8TPyzPzZn] in the same solutions, thus suggesting that the effect of the different π systems on $E_{1/2}$ values is greater for the second electron addition than for the first.

Table 5-4. Half-Wave Potentials ($E_{1/2}$, V vs SCE) of [Py_8PzM] and [Py_8PyzPzM] (M = 2H, Cu^{II}, Zn^{II}, $Mg(H_2O)$, Co^{II}) in Py and DMSO, containing 0.1M TBAP

		Reduction					
Solvent	Macrocycle	1st	2nd	$[Pz]^{2-}/[Pz]^{3-}$	3rd	4th	ref.
Py	[Py_8PzH_2]	-0.26	-0.65	-0.93	-1.53	-1.86[a]	tw.
	[Py_8TPyzPzH_2]	-0.17	-0.48	-0.93	-1.24	-1.61	107
	[Py_8PzCu]	-0.38					tw.
	[Py_8TPyzPzCu]	-0.30	-0.68		-1.28	-1.61	40
	[Py_8PzZn]	-0.46	-0.91		-1.66[a]	-1.92[a]	tw.
	[Py_8TPyzPzZn]	-0.34	-0.72		-1.38	-1.66	40
	[$Py_8PzMg(H_2O)$]	-0.54	-0.93		-1.49	-1.84[a]	tw.
	[Py_8TPyzPz$Mg(H_2O)$]	-0.40	-0.79		-1.43	-1.70	40
	[Py_8PzCo]	-0.33	-1.01		-1.60	-1.92[a]	tw.
	[Py_8TPyzPzCo]	-0.26	-0.87		-1.37	-1.83	40
DMSO	[Py_8PzH_2]	-0.17	-0.57	-0.87	-1.44	-1.80[a]	tw.
	[Py_8TPyzPzH_2][b]	-0.16	-0.40	-0.89	-1.21	-1.57	106
	[Py_8PzCu]	-0.34	-0.67				tw.
	[Py_8TPyzPzCu]	-0.33	-0.58		-1.22	-1.58	106
	[Py_8PzZn]	-0.43	-0.85		-1.57	-1.88	tw.
	[Py_8TPyzPzZn]	-0.26	-0.67		-1.38	-1.64	106
	[$Py_8PzMg(H_2O)$]	-0.44					tw.
	[Py_8TPyzPz$Mg(H_2O)$]	-0.33	-0.70		-1.39	-1.67	106
	[Py_8PzCo]	-0.19	-0.95		-1.53	-1.85	tw.
	[Py_8TPyzPzCo]	-0.06	-0.76		-1.31	-1.77	106

[a] Irreversible reduction reaction at scan rate = 100 mV/s. tw. = this work.

Unfortunately, all other electroreductions of the Cu^{II}, Zn^{II} and $Mg^{II}(H_2O)$ porphyrazines are ill-defined due to the presence of aggregation after electroreductions. This is seen by the cyclic voltammograms in Figure 5-14.

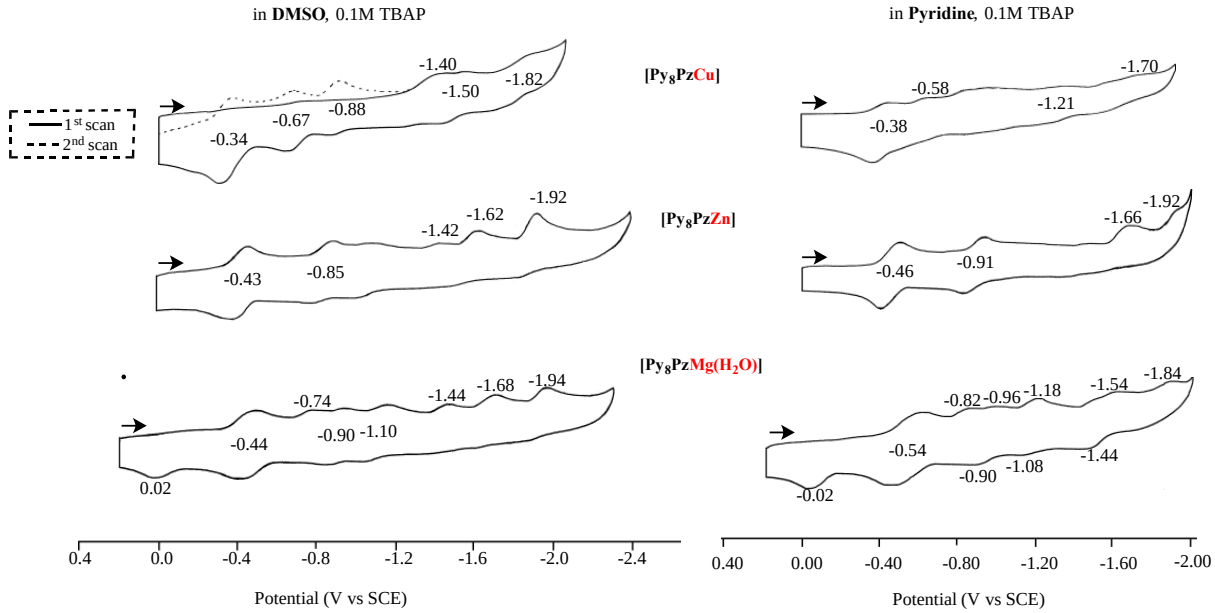

Figure 5-14. Cyclic voltammograms of [Py_8PzM] with M = Cu^{II}, Zn^{II} and $Mg^{II}(H_2O)$, in DMSO and Pyridine, 0.1M TBAP. Scan rate = 0.1 V/s.

[Py_8PzCo^{II}]. The Co^{II} complex is characterized by four one-electron reductions in pyridine and five in DMSO. A single oxidation is also observed at +0.25 V in pyridine. This process is quasi-reversible and corresponds to the reaction Co^{II}/Co^{III}. A similar Co^{II}/Co^{III} oxidation process has been reported for the pyrazinoporphyrazine complex [Py_8TPyzPzCo] in DMSO[106] as well as for Co^{II}-phthalocyanines.[36, 111-113]

The first one-electron reduction of [Py_8TPyzPzCo] to its Co^{I} form is reversible in DMSO[106] and this is also true for cobalt phthalocyanine [$PcCo^{II}$] in this solvent. Both of these processes occur at similar half wave potentials of -0.06 and -0.08 V (data in Figure 5-15), but this is not the case for [Py_8PzCo] where the reduction and reoxidation reactions are split into two separate

processes which are located at E_{pc} = -0.32 V and E_{pa} = -0.06 V for a scan rate of -0.1 V/s (see Figure 5-15).

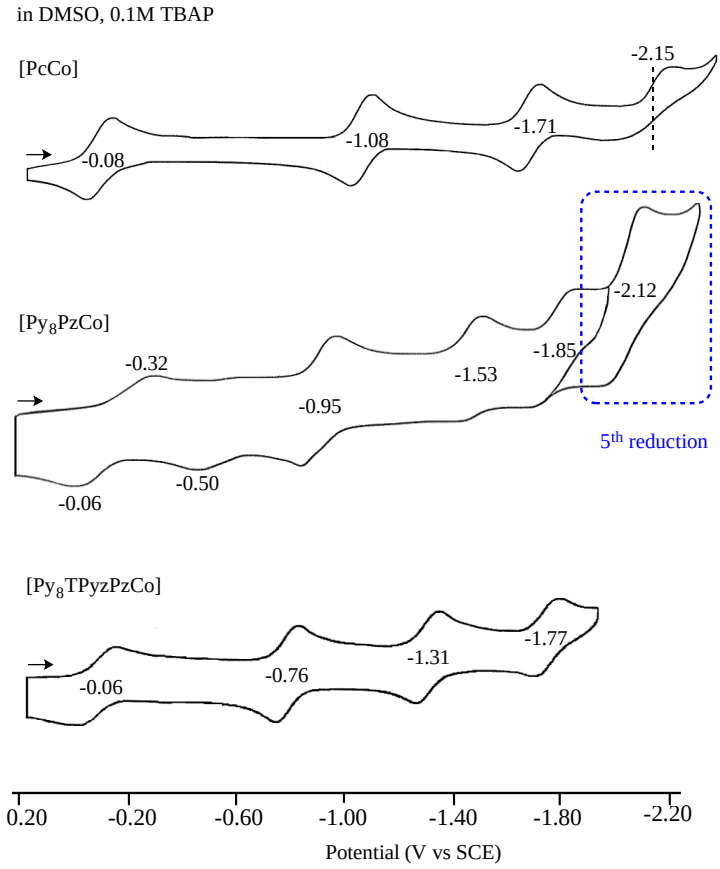

Figure 5-15. Cyclic voltammograms for [PcCo], [Py_8PzCo] and [Py_8TPyzPzCo] in DMSO, 0.1M TBAP. Scan rate = 0.1 V/s

This large separation of reduction and oxidation peaks for the Co^{II}/Co^{I} and reverse Co^{I}/Co^{II} reaction of [Py_8PzCo] can be accounted for by a well-known box mechanism[114, 115] of the type illustrated in Scheme 5-1. The reduction at E_{pc} = -0.32 V involves electron addition to a six coordinate Co^{II} porphyrazine while the reoxidation at E_{pa} = -0.06 V involves electron abstraction from an unsolvated four-coordinate Co^{I} form of the compound.

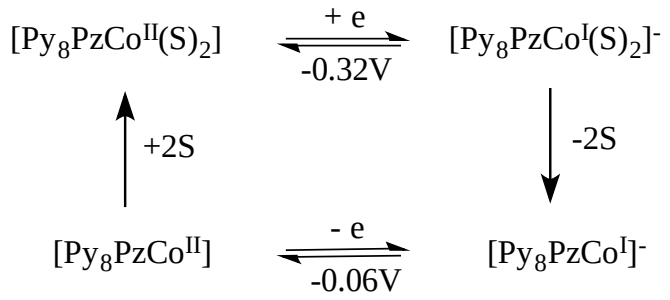

Scheme 5-1. Mechanism for the reduction and reoxidation of [Py_8PzCo] in DMSO, 0.1M TBAP.

The almost identical $E_{1/2}$ values for the first reduction of [PcCo] (-0.08 V) and [Py_8TPyzPzCo] (-0.06 V) indicates a negligible difference in how these two macrocycles effect the Co^{II}/Co^{I} process of the compounds. However, this is not the case for the second, third and fourth reductions of the three related species, where the ease of electron addition follows the order: [Py_8TPyzPzCo] > [Py_8PzCo] > [PcCo] for each redox process beyond the first. The absolute difference between the measured reduction potential of [Py_8PzCo] and [Py_8TPyzPzCo] amounts to 190 mV for the second electron addition, 210 mV for the third, and 80 mV for the fourth. A fifth, never before seen reduction of [Py_8PzCo] is also present in DMSO and this may be related to the fact that four ring-centered reductions and one metal-centered Co^{II}/Co^{I} process are expected to occur for this compound.

In this regard, it should be pointed out that the reversible third and fourth reductions of [Py_8TPyzPzCo] were earlier proposed to generate a Co^{II} porphyrazine with a triply and quadruply reduced macrocycle and this may also be the case for [Py_8PzCo] where $E_{1/2}$ values for addition of the third and fourth electrons are quite similar to measured potentials for reduction of the [Py_8PzZn] derivative under similar solution conditions (see Table 5-4).

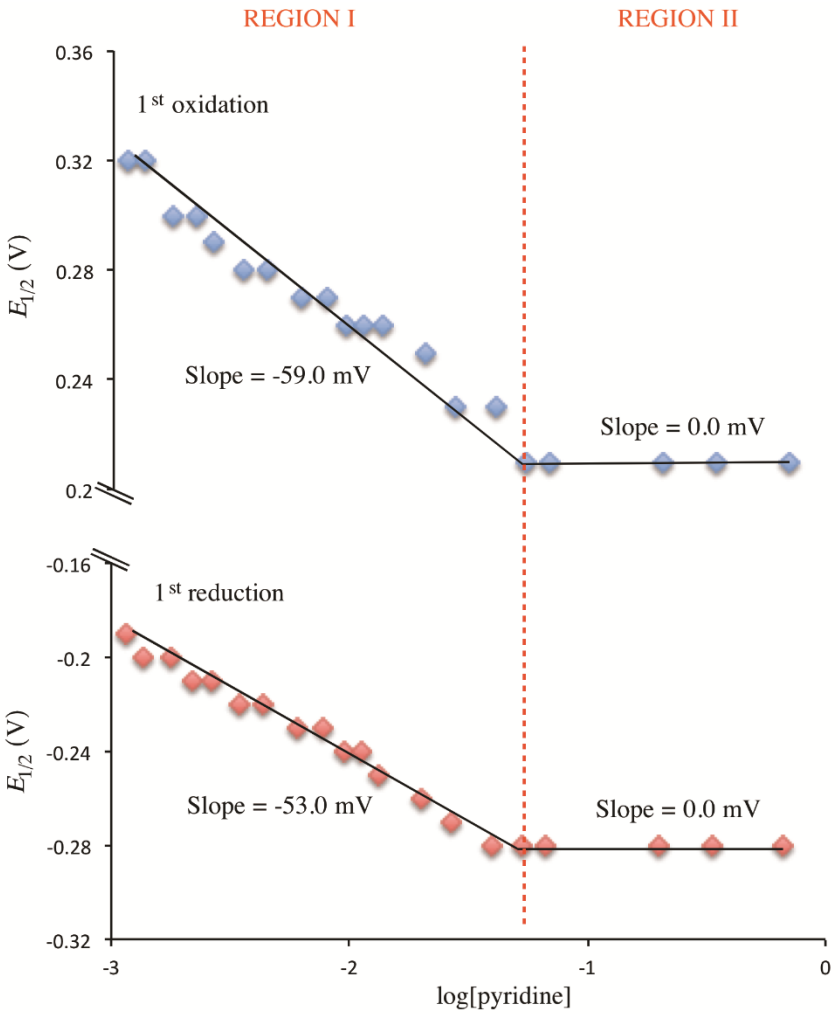

REGION I

$[(Py)_8PzCo^{III}(S)_2]^+ + e \rightleftharpoons [(Py)_8PzCo^{II}(S)] + S$

$[(Py)_8PzCo^{II}(S)] + e \rightleftharpoons [(Py)_8PzCo^{I}]^- + S$

Where S = pyridine

REGION II

$[(Py)_8PzCo^{III}(S)_2]^+ + e \rightleftharpoons [(Py)_8PzCo^{II}(S)_2]$

$[(Py)_8PzCo^{II}(S)_2] + e \rightleftharpoons [(Py)_8PzCo^{II}(S)_2]^{2-}$

Figure 5-16. Plot of $E_{1/2}$ for the first oxidation and first reduction of [Py_8PzCo] in CH_2Cl_2 vs log of the pyridine concentration added to solution.

Finally, the axial coordination of pyridine to the Co^{III} and Co^{II} forms of [Py_8PzCo] in CH_2Cl_2 and neat pyridine was investigated. Aggregation of [Py_8PzCo] is present in CH_2Cl_2 solutions and, under these conditions, neither the first metal-centered reduction nor first metal-centered oxidation

can be observed in initial scans by cyclic voltammetry. However, the extent of aggregation decreases upon addition of pyridine to solution and in CH_2Cl_2/pyridine mixtures, three well-defined reductions and one oxidation can be easily detected. The potentials for the second and third reductions are almost invariant with changes in the CH_2Cl_2/pyridine ratio but this is not the case for the first oxidation and first reduction where the half-wave potentials vary systematically with the concentration of pyridine as shown by the data in Figure 5-16.

The measured $E_{1/2}$ for the Co^{II}/Co^{III} and Co^{II}/Co^{I} processes of [Py_8PzCo] initally shifts by 53-59 mV per ten-fold change in the log[py] concentration (Region I of Figure) but as more pyridine is added to solution, the half-wave potentials for these two reactions stop shifting, as shown in Region I of the figure. The magnitude of the shift follows classical behavior for the loss or gain of axial ligands upon oxidation or reduction[115] and the overall mechanism for the first electron addition and first electron abstraction of [Py_8PzCo] is as described in the figure. In CH_2Cl_2 solutions with low concentrations of pyridine, the prevailing electrode reactions involve $[Py_8PzCo^{III}(Py)_2]^+$, $[Py_8PzCo^{II}(Py)]$ and $[Py_8PzCo^{I}]^-$ species, while in solutions with higher concentrations the reactive species are all six-coordinate on the timescale of the electron transfer, i.e. $[Py_8PzCo^{III}(Py)_2]^+$, $[Py_8PzCo^{II}(Py)_2]$ and $[Py_8PzCo^{I}(Py)_2]^-$.

5.2.5 UV-Visible Spectral Behavior of Group III Porphyrazine Derivatives[43]

The [[Pd(CBT)$_2$]$_4$LM] complexes (M = $Mg^{II}(H_2O)$, Zn^{II}, Pd^{II}) are completely insoluble in water and nearly insoluble in nonaqueous non-donor solvents (acetone, THF, CH_2Cl_2). They are fairly soluble in DMSO, DMF and pyridine (c ~ 10^{-4} M) and the UV-visible spectra taken immediately after dissolving the compounds in these solvents at concentrations of 10^{-4}-10^{-5} M show a profile closely resembling that of monomeric porphyrazines, ie., the spectra are

characterized by well defined peaks in the Soret (300-400 nm) and Q-band regions (600-700 nm; see Figure 5-17 for the Zn^{II} complex), with the bands assigned to π-π* ligand-centered transitions and clearly indicative of the exclusive presence of the complexes in their monomeric form. Noteworthy, a broad intense absorption is present for all three CBT complexes in the range 400-500 nm; this point is addressed in further details below.

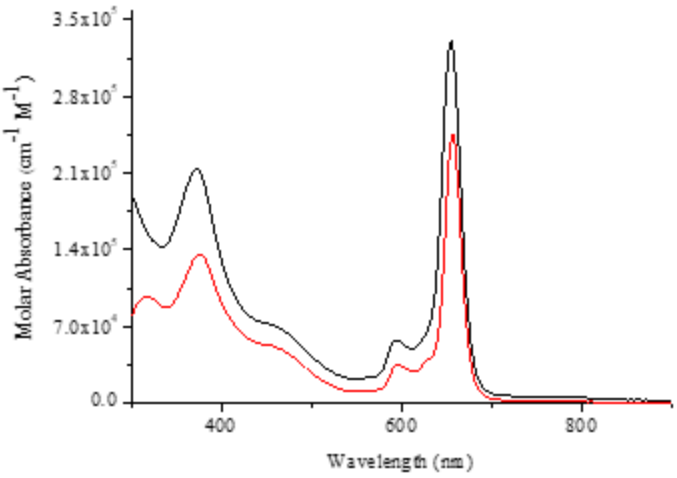

Figure 5-17. UV-visible spectra of [[Pd(CBT)$_2$]$_4$LZn] in DMSO (black line) and DMF (red line) **(**reproduced in part with permission from [*Inorg. Chem.* **2019**, *58*, 1120-1133], American Chemical Society).[43]

The stability of the three CBT derivatives in DMSO, DMF and pyridine is shown by the spectra in Figure 5-18 where the measurements were first taken immediately after dissolving the compounds and again after 24 h. In the case of the Mg^{II} and Zn^{II} complexes (top and center of Figure 5-18), the spectra in DMSO (A,D) and DMF (B,E) indicate stability over 24h, with only a slight decrease of the broad band in the 400-500 nm region for the Mg^{II} species. It is worth noting here that this broad absorption is completely absent in the spectra of the pentanuclear analogs [(PdCl$_2$)$_4$LM] (M = Mg^{II} and Zn^{II}),[41] from which the complexes are generated, and it is also not

seen in spectra of the respective mononuclear [LM] species,[40] the overall spectra in the Soret and Q-band regions for both types of species closely resembling those of the CBT derivatives. These findings strongly suggest that the occurrence of the 400-500 nm band for the latter species is strictly related to the presence of the CBT external moieties.

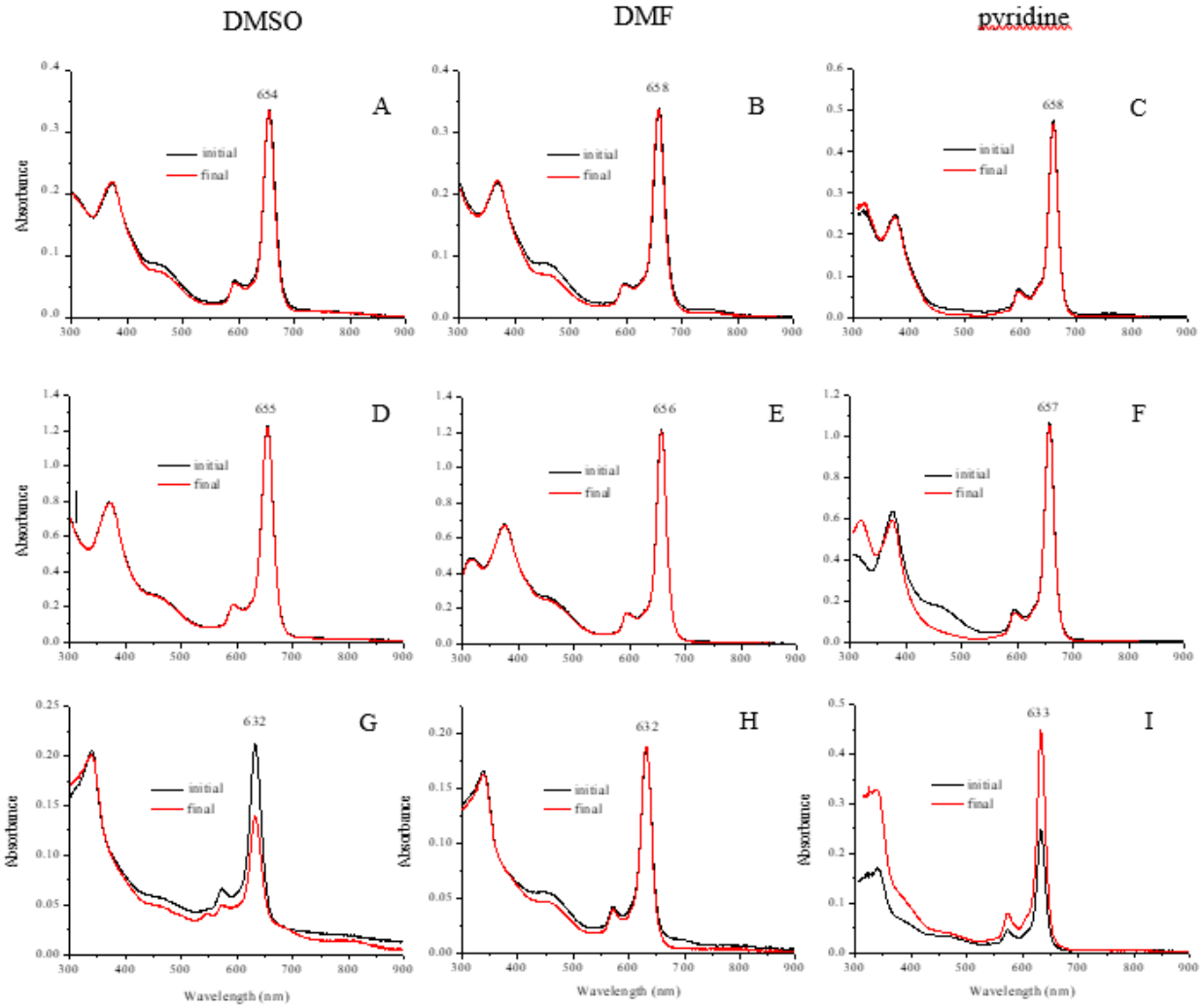

Figure 5-18. UV-visible spectra (c ~ 10^{-5} M) (each one run immediately and after ca. 24 h) in the range 300-900 nm of the complexes [[Pd(CBT)$_2$]$_4$LMg(H$_2$O)] (A, B, C), [[Pd(CBT)$_2$]$_4$LZn] (D, E, F) and [[Pd(CBT)$_2$]$_4$LPd)] (G, H, I) in DMSO (left side), DMF (centre) and pyridine (right side) (reproduced in part with permission from [*Inorg. Chem.* **2019**, *58*, 1120-1133], American Chemical Society).[43]

It is interesting to note that the Mg^{II} complex in pyridine (Figure 5-18C) shows a complete absence of the 400-500 nm band in the initial and final spectrum, the full spectral pattern maintaining identical features in terms of relative intensities and positions of the Soret and Q-band absorptions, features perfectly adherent to those found for the previously reported corresponding mononuclear complex $[LMg(H_2O)]$.[40] As to the Zn^{II} complex, the spectrum in pyridine solution shows well evident the band at 400-500 nm immediately after dissolution, although this decreases with time and practically disappears after 24 h. The spectral changes of the homopentanuclear Pd^{II} complex $[[Pd(CBT)_2]_4LPd]$ with time in DMSO (Figure 5-18G) and pyridine solutions (Figure 5-18I) offers a more complex picture, since, the 400-500 nm absorption is almost absent since the beginning of the spectral evolution, and a decrease of the intensity of the Q band occurs in both solvents perhaps due to precipitation. This contrasts with the spectral behavior of the same Pd^{II} complex in DMF, the initial spectrum of which shows the presence of the 400-500 nm band and the changes observed after 24 h closely resembling what is seen for the Mg^{II} complex in the same solvent (Figure 5-18B).

It is relevant to point out that the spectral evolution of the Mg^{II} and Zn^{II} complexes in pyridine, whilst determining complete disappearance of the 400-500 nm absorption, leads to final spectra which nicely coincide, with those of the parent mononuclear species [LM]. Thus, the observed spectral behavior for the two CBT complexes in pyridine solution provides clear support for the irreversible progressive detachment of the peripheral $Pd(CBT)_2$ moieties from the vicinal 2-pyridyl rings and concomitant formation of the related mononuclear species [LM] in the process $[[Pd(CBT)_2]_4LM] \rightarrow [LM] + 4Pd(CBT)_2$, this latter CBT derivative supposedly converted in solution into its bis-pyridine derivative py_2-Pd-$(CBT)_2$. Moreover, the observed spectral behavior

also indicates that the broad band at 400-500 nm is intimately connected with the presence of the peripheral coordination sites "py_2-Pd-$(CBT)_2$" (py intended as the 2-pyridyl ring) in the initial intact porphyrazine macrocycle. Definitely deserving mention, the finally formed bis-pyridine derivative py_2-Pd-$(CBT)_2$ could be isolated as stable to air yellow needles (procedure in the Experimental Section for the Zn^{II} complex) and its structure crystallographically elucidated, as described later in the manuscript. In this complex the coordination site for Pd^{II} of the type N_2PdS_2, closely recalling its analog present in the CBT porphyrazine macrocycles. The UV-visible spectrum in CH_3CN of the new species, precisely formulated as *trans*-[$py_2(CBT)_2Pd$], shows only absorptions confined in the UV region 200-350 nm, in the complete absence of absorptions in the region above 400 nm. On the basis of these findings, the absence for the complex of broad absorptions in the region 400-500 nm of the type shown instead in the spectra of the carboranthiolate complexes seems to call for a role of the Pd^{II} coordination site and its S-functionalities only when involved within the entire porphyrazine macrocycle. Presently the spectrum of *trans*-[$py_2(CBT)_2Pd$] is being examined by DFT calculations. Indeed, required theoretical calculations will be in due course extended to the CBT macrocycles in the context of further work being presently conducted on their photoactivity, partly already exposed in the present work, and related applicative aspects.

5.2.6 Electrochemistry of Group III Porphyrazine Derivatives

The electrochemical investigation on the new octacarboranthiolate [[$Pd(CBT)_2]_4LM$] complexes (M = $Mg^{II}(H_2O)$, Zn^{II}, or Pd^{II}) was directed to have additional information on the effect of perturbation brought by the externally coordinated $Pd(CBT)_2$ units on the electronic distribution of the π-delocalized pyrazinoporphyrazine core, and evaluate whether in line or not with the

findings from the above reported NMR and UV-visible spectral data. Attempts of cyclic voltammetric experiments performed for all three complexes at concentrations of 10^{-3}-10^{-4} M in pyridine solutions in the presence of TBAP (0.1 M) indicated, based on UV-visible spectra and confirming the above findings, the immediate loss of the $Pd(CBT)_2$ units and formation of the corresponding mononuclear species; the same occurrence with a more moderate evolution was verified also in DMSO. Under similar cyclic voltammetric experimental conditions, the Mg^{II} complex $[[Pd(CBT)_2]_4LMg(H_2O)]$ showed little to no change in the absorption in the range 400-500 nm^{-1}. As shown in Figure 5-9, of the four expected one-electron reductions on the conjugated macrocycle, only the first two reductions are reversible and located at $E_{1/2}$ = -0.38 and -0.71 V vs SCE (Table 5-5), when the negative potential sweep is reversed at -0.80 V, and these processes remain reversible when reversing the scan at more negative potentials, despite the fact that all further reductions after the second one (Figure 5-19) were ill-defined on the cyclic voltammetry timescale.

Table 5-5. Half-Wave or Peak Potentials ($E_{1/2}$ or E_p, V vs SCE) for $[[Pd(CBT)_2]_4LMg(H_2O)]$, $[LMg(H_2O)]$ and $[(PdCl_2)_4LMg(H_2O)]$ in DMF containing 0.1M TBAP

	Reductions					
Macrocycle	1st	2nd	3rd	4th	5th	Ref.
$[Pd[CBT_2]_4LMg(H_2O)]$	-0.38	-0.71	-0.94	-1.30[a]	-1.52	tw
$[LMg(H_2O)]$	-0.42	-0.80	-1.43			39
$[(PdCl_2)_4LMg(H_2O)]$	-0.15	*b*	*b*	*b*		41

[a] E_p (V vs SCE). Scan rate = 100 mV/s.
[b] Badly resolved peaks because of the presence of the transmetalation contaminant $[(PdCl_2)_4LPd]$

The potential value of the first reduction (-0.38 V) is practically coincident with that measured for the corresponding mononuclear species $[LMg(H_2O)]$ in the same solvent (-0.42 V).[39] These data are important because they indicate that the external attachment to $[LMg(H_2O)]$ of the

$Pd(CBT)_2$ units does not modify the π-conjugation within the macrocyclic core, in perfect agreement with the conclusions drawn on the basis of the NMR and UV-visible spectral data. This is different from what has been observed for the related pentanuclear analog carrying externally $PdCl_2$ units, ie. $[(PdCl_2)_4LMg(H_2O)]$, which is easier to reduce than the monometallic derivative $[LMg(H_2O)]$, with the first one-electron reduction in DMF solution (0.1 M TBAP) found at at $E_{1/2}$ = -0.15 V.[41] The fact that the external coordination of the $PdCl_2$ units induces an easier acceptance of excess negative charge within the macrocyclic framework, is in strict accordance with the enhanced electron-withdrawing properties of the external dipyridinopyrazine fragments, once they are metalated.

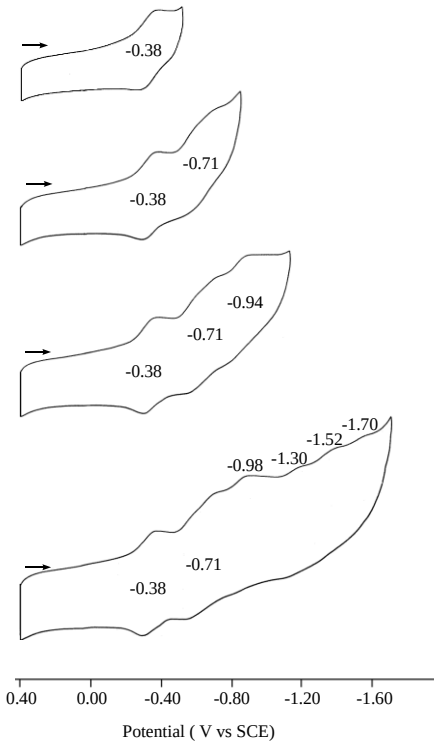

Figure 5-19. Cyclic voltammograms of $[Pd(CBT_2)_4LMg(H_2O)]$ in DMF containing 0.1M TBAP.

5.3 Conclusion

New mononuclear complexes having the formula $[Py_8TPyzPzMX]\cdot xH_2O$ ($M = Al^{III}$, Ga^{III}; $X = Cl^-$, OH^-) and their related pentanuclear species $[(PdCl_2)_4Py_8TPyzPzMCl]\cdot xH_2O$ ($M = Al^{III}$, Ga^{III}) are reported. The UV-vis spectral behavior in these solvents for all the species show Soret and Q-band maxima in the respective narrow ranges of 370-380 and 650-660 nm. Furthermore, the position of the Q-band for the two Al^{III} and Ga^{III} pentanuclear complexes is bathochromically shifted by 2-5 nm with respect to that of the corresponding mononuclear species. This is in line with expectation, due to the more electron-deficient character of the macrocycle resulting from the external coordination of $PdCl_2$, an effect also observed for the structurally related mono- and pentanuclear analogs having centrally bivalent metal ions. The six newly synthesized monometallic and pentanuclear complexes have been characterized by cyclic voltammetry in DMF and DMSO containing 0.1M TBAP. The potentials for reduction of a given Al^{III} or Ga^{III} species are very similar to each other along the series of compounds, all electron additions being extremely facile and ranging from the $E_{1/2}$ = -0.04 V to -0.10 V for the first reduction. These potentials are almost identical to those reported earlier for related TTDzPz derivatives of Al^{III} and Ga^{III} but are shifted by more than 500 mV from $E_{1/2}$ values for the first reduction of [PcAlCl] in the same solvent. These data thus provide clear evidence that a replacement of the four benzene rings in a phthalocyanine macrocycle by strongly electron-withdrawing dipyridinopyrazine fragments, confer to the porphyrazine core a general electron-deficient character, highly facilitating the electron uptake and associated charge redistribution within the macrocycle. This result is independent of the central metal ion and was earlier observed when comparing a related series of bivalent metal derivatives of the formula $[Py_8TPyzPzM]$ with their phthalocyanine analogs [PcM].

Worth of notice, the $E_{1/2}$ values for the first and following reductions of the [Py_8TPyzPzMX] complexes are less negative than reduction potentials for the related M^{II} species [Py_8TPyzPzM] in the same solvent. These findings also parallel earlier results seen for the thiadiazole analogs [TTDPzMX], for which the out-of-plane displacement of the metal centers and their lower electronegativity with respect to that of the bivalent metal ions in the parent [TTDPzM] series, favor the uptake of electrons by the porphyrazine macrocycle. For the pentanuclear species, [$(PdCl_2)_4Py_8$TPyzPzMCl], the first and second reductions are positively shifted with respect to $E_{1/2}$ values for the related monometallic species [Py_8TPyzPzMCl] having the same central metal ion and same axial ligand. These findings confirm that external coordination of the $PdCl_2$ units induces an easier acceptance of negative charge within the macrocyclic framework; this is in strict accordance with the enhanced electron-withdrawing properties of the external dipyridinopyrazine fragments once they are metalated.

As part of our continuing studies on porphyrazine compounds, which included extensive work conducted on the recently partly reviewed tetrapirazinoporphyrazines of formula [Py_8TPyzPzM] (M = bivalent metal ion), it was found of great interest to explore the effect of reducing or extending the size of the central pyrazinoporphyrazine macrocyclic framework, thus modifying the level of the π-electron delocalization.

UV-visible spectra of [Py_8PzH_2] in solution of non-donor solvents (CH_2Cl_2, $CHCl_3$) and in pyridine are indicative of D_{2h} symmetry, as suggested by the observed large splitting of the Q band peaks (ca. 65 nm). Spectral changes in solution of DMSO and DMF show that [Py_8PzH_2] irreversibly results along with the time in the formation to its corresponding dianion $[Py_8Pz]^{2-}$. The overall spectral data suggest lower acidity for the smaller macrocycle [Py_8PzH_2] with respect to

that of [$Py_8TPyzPzH_2$], the findings being in strict relationship with the different extension of the π-electron delocalized system for the two species. UV-visible spectra of the complexes [Py_8PzM] (M = Co^{II}, Cu^{II}, Zn^{II}), similarly to what previously reported for the Mg^{II} analog, show clean UV-visible spectral profiles in pyridine, DMSO and DMF, typical of monomeric species, with the Q band hypsochromically shifted by 20-25 nm with respect to the corresponding values of the parallel series of [$Py_8TPyzPzM$] compounds, this confirming for the two series of compounds the dependence of the UV-visible spectral behaviour by the different size of the macrocycle and level of π-electron distribution. Cyclic voltammetric studies of [Py_8PzH_2] show that the observed reversible first and second one-electron reductions in pyridine solution generating $[Py_8PzH_2]^-$ and $[Py_8PzH_2]^{2-}$ are found at more negative $E_{½}$ values (similar values in DMSO) than those for [$Py_8TPyzPzH_2$], data proving that harder reductions are occurring for [Py_8PzH_2], in keeping with its smaller π-conjugated system. The third and the fourth reductions for [Py_8PzH_2] follow the same trend. Well defined first one-electron reductions occur in pyridine for the Cu^{II}, Zn^{II} and Mg^{II} complexes at slightly more negative $E_{½}$ values than those of the [$Py_8TPyzPzM$] systems, paralleling the results for the unmetalated species. A second reversible one-electron reduction is observed for the Zn^{II} complex in pyridine and DMSO, but all other reductions of the Zn^{II}, Cu^{II}, and Mg(H_2O) complexes are ill defined due mainly to aggregation, among other possible reasons (demetalization). Four one-electron nicely reversible steps of reduction are observed for the Co^{II} complex [Py_8PzCo] in pyridine (five in DMSO). The Co^{II}/Co^{III} oxidation process occurs in pyridine, recalling similar processes in DMSO for [$Py_8TPyzPzCo$] and Co^{II}-phthalocyanines. The first one-electron uptake and release for [Py_8PzCo] in DMSO has been interpreted as metal centered, ie. Co^{II}/Co^{I} and reverse Co^{I}/Co^{II} processes, involving the "box-mechanism", details of

which are given in the text; this is in line with the findings for [Py_8TPyzPzCo] and [PcCo] in the same solvent, the difference being that for [Py_8PzCo] the process is split into two separate processes, characterized by E_{pc} and E_{pa} values different by 0.24 V vs SCE.

The chemistry and electrochemistry of a third group of new pentanuclear porphyrazine complexes of formula [[Pd(CBT)$_2$]$_4$LM]·xH_2O (M = $Mg^{II}(H_2O)$, Zn^{II}, and Pd^{II}), characterized by the presence of eight external *m*-carboran-1-thiolate groups, are also described in this chapter. The UV-visible spectral behavior of the macrocycles in these solvents indicates different stability over 24 hours, an effect caused by the tendency of the compounds to undergo progressive detachment of the Pd(CBT)$_2$ units, leading finally to formation of the corresponding mononuclear species [LM]. Detailed information from electrochemical solution studies of the new CBT complexes indicates that coordination of the external Pd(CBT)$_2$ units does not significantly perturb the π-conjugated electronic distribution of the internal macrocyclic LM core. Attempts are now being carried out for delivering of the new carboranthiolate complexes in water solutions and further developments of the research work are expected in this direction.

Chapter Six

Chemical and Electrochemical Properties of Doubly Fused Porphyrins and Related Fused-Chlorins

6.1 Introduction

π-Conjugated porphyrinic systems have long been a topic of research interest due to their unique photophysical,[75, 116-119] electrochemical,[120, 121] optical, and magnetic properties[122-124] as well as their potential applications in the areas of non-linear optics, two-photon absorption and photoacoustic agents.[125-128] π-Extended fused porphyrins have also shown promise in dye-sensitizing solar cell (DSSC) applications[129, 130] and have been proven to be good photosensitizers for high performance dye-sensitized solar cells with remarkable power conversion efficiencies of 8.78%–10.7%.[130] The specific electronic features of these compounds might also be useful in biological and material applications.[131-133]

One of the best ways to obtain extended π-conjugation of a porphyrin is *via* intramolecular fusion of the porphyrin's π-system with *β*-substituents. The introduction of an exocyclic fused ring into the periphery of a porphyrin macrocycle has attracted much attention because of the resulting compound's unique photophysical properties, one of which is a reduced HOMO-LUMO gap.[134-137] Having a long wavelength absorption window is also a prerequisite for good sensitizers in photodynamic therapy (PDT) because the light penetration in tissue is optimum at longer wavelengths.[22, 31, 138, 139]

Several synthetic strategies have been followed to obtain π-extended porphyrins,[140-143] with early synthetic procedures involving intramolecular fusion where at least one *β*-pyrrolic carbon was linked to a *meso*-aryl substituent. Among the ring-fused porphyrins reported in the literature, those containing a six membered exocyclic fused ring without a heteroatom at the junction have emerged as a new important class of porphyrin derivatives.

Our collaborators' research group has reported synthetic methods for obtaining cyclopropyl and *trans*-chlorins using a size-dependent approach of the active methylene groups.[33, 144] The obtained cyclopropyl chlorins could then be converted into mono- and tri-substituted porphyrins by an acid catalyzed ring opening reaction[32] while the *trans*-chlorins could be converted into mono-fused porphyrins through a metal induced skeletal rearrangement.[26]

Di-fused chlorins (DFC) and di-fused porphyrins (DFP) could also be obtained *via* an oxidative fusion reaction and using this method we recently reported the synthesis of di-fused Ni(II) porphyrins from Ni(II) *trans*-chlorins in a single step, giving a porphyrin product whose two *meso*-phenyl groups were connected to the β-substituents through direct C-C bond formation.[26] The work in this chapter is to characterize the spectral, electronic properties, and redox behavior of the newly synthesized Cu(II), Zn(II), Co(II), Ni(II), and free-base di-fused porphyrin derivatives in solutions of CH_2Cl_2. The effect of macrocycle, β-substituent, metal center, solvent, and temperature on the electrochemical behavior of these porphyrin derivatives will be discussed in detail in this chapter. The di-fused free-base chlorins formed as intermediates during the synthesis were also isolated by our collaborators and characterized in Houston as to their redox properties under similar conditions. As described below, these free-base chlorins undergo four well-defined one-electron reductions. The stuctures of the investigated di-fused porphyrins and chlorins are shown in Charts 6-1 and 6-2 (IND = indanedione group, MN = malononitrile group).

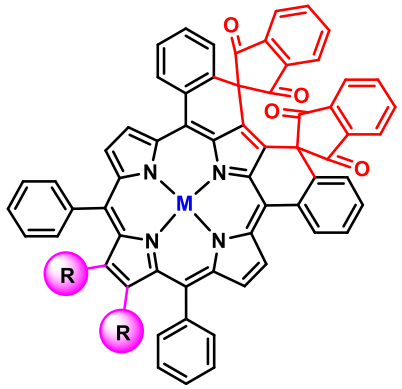

R = H	R = Br	R = Ph
$MDFP(IND)_2$	$MDFP(IND)_2Br_2$	$MDFP(IND)_2Ph_2$
M = 2H **$1H_2$**	M = 2H **$2H_2$**	M = 2H **$3H_2$**
Co **1Co**	Co **2Co**	Co **3Co**
Ni **1Ni**	Ni **2Ni**	Ni **3Ni**
Cu **1Cu**	Cu **2Cu**	Cu **3Cu**
Zn **1Zn**	Zn **2Zn**	Zn **3Zn**

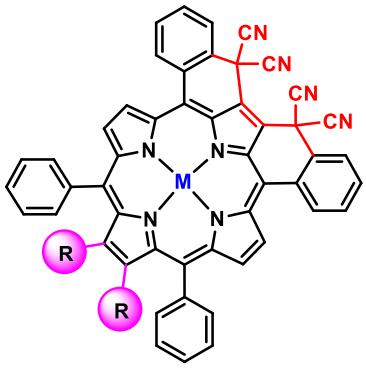

R = H	R = Br	R = Ph
$MDFP(MN)_2$	$MDFP(MN)_2Br_2$	$MDFP(MN)_2Ph_2$
M = 2H **$4H_2$**	M = 2H **$5H_2$**	M = 2H **$6H_2$**
Co **4Co**	Co **5Co**	Co **6Co**
Ni **4Ni**	Ni **5Ni**	Ni **6Ni**
Cu **4Cu**	Cu **5Cu**	Cu **6Cu**
Zn **4Zn**	Zn **5Zn**	Zn **6Zn**

Chart 6-1. Structures of synthesized di-fused metalloporphyrins (DFPs) where IND = indanedione group, MN = malononitrile group.

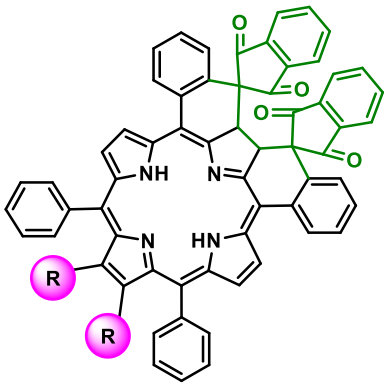

R = H	$H_2DFC(IND)_2$	**$7H_2$**
R = Br	$H_2DFC(IND)_2Br_2$	**$8H_2$**
R = Ph	$H_2DFC(IND)_2Ph_2$	**$9H_2$**

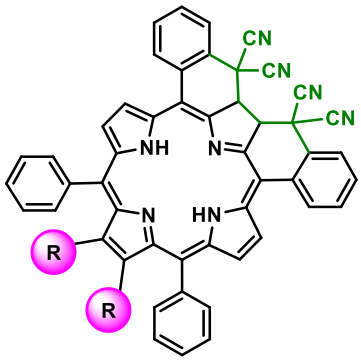

R = H	$H_2DFC(MN)_2$	**$10H_2$**
R = Br	$H_2DFC(MN)_2Br_2$	**$11H_2$**
R = Ph	$H_2DFC(MN)_2Ph_2$	**$12H_2$**

Chart 6-2. Structures of examined di-fused chlorins (DFCs), where IND = indanedione group, MN = malononitrile group.

6.2 Results and discussion

6.2.1 Mass Spectrometric Analysis

The MALDI-TOF spectra of the newly synthesized porphyrins recorded in the positive ion mode measured by our collaborator Dr. Muniappan Sankar's laboratory in IIT Roorkee, india.

The observed mass values match exactly the calculated mass values. A rich fragmentation pattern is observed due to the labile nature of the bromo and cyano groups in the malononitrile appended dibromo porphyrins. The MN-appended porphyrins (MN = malononitrile group) have mass values indicating a loss of one or two cyano groups. Similarly, the dibromo derivatives of the di-fused MN compounds have intense mass peaks in their spectra consistent with the loss of one or two bromo groups. An example of the recorded MALDI-TOF mass spectrum of compound **5H₂** is shown in Figure 6-1 (the unlabelled peak located at ≈713 could be assigned to $[M+H]^+$-2Br,CN^-).

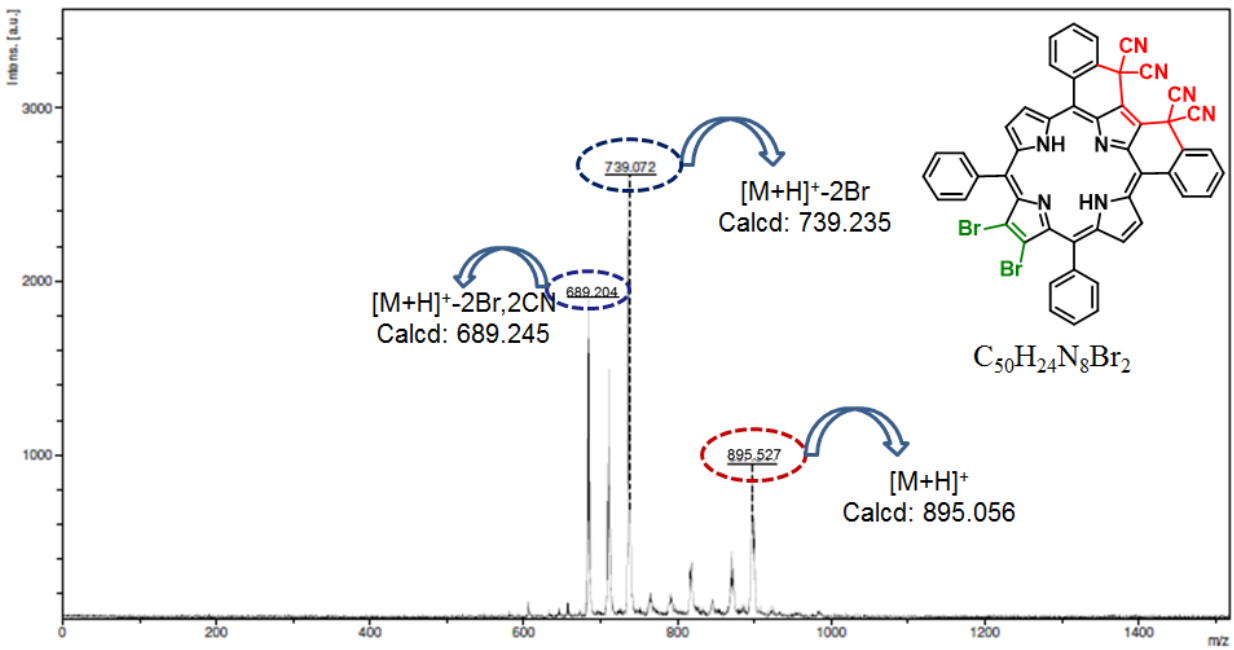

Figure 6-1. MALDI-TOF mass spectrum of $H_2DFP(MN)_2Br_2$ (**5H₂**) (reproduced with permission from *Inorganic Chemistry*, unpublished work, American Chemical Society).

As described below, this lability is reflected in the electrochemistry of compounds in this series. The indanedione di-fused porphyrins also have mass peak values indicating an association with sodium and potassium ion adducts.

6.2.2 Electrochemistry

The six sets of di-fused porphyrins and chlorins in Charts 6-1 and 6-2 were characterized by cyclic voltammetry in CH_2Cl_2 containing 0.1 M TBAP. The redox behavior is described below and was analyzed as a function of the following parameters: i) type of macrocycle (chlorin or porphyrin), ii) type of group in the fused ring (IND or MN), iii) specific R group (H, Br or Ph) and iv) reactivity or stability of electrogenerated species.

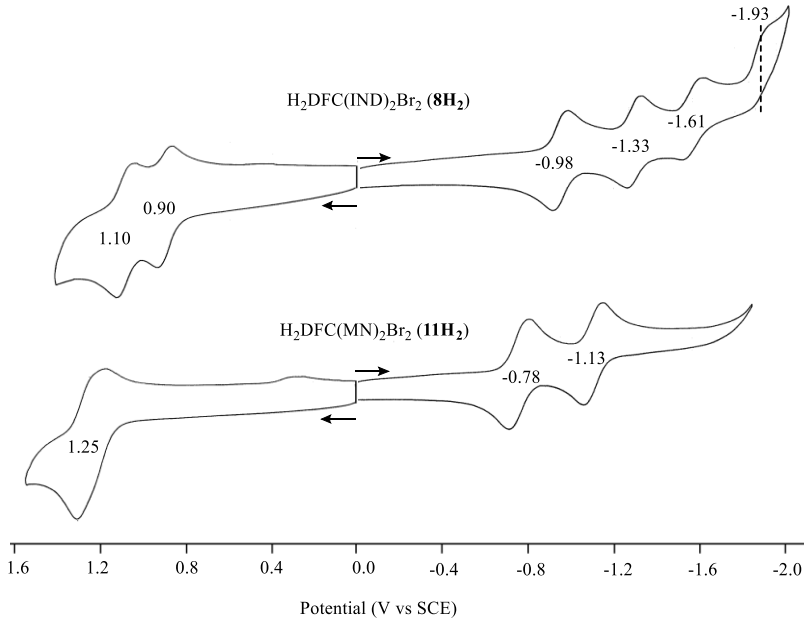

Figure 6-2. Cyclic voltammograms of di-fused chlorins **$8H_2$** and **$11H_2$** in CH_2Cl_2, containing 0.1 M TBAP. Scan rate = 0.1 V/s.

Chlorins. All of the synthesized di-fused chlorins with indanedione (IND) or malononitrile (MN) groups (**$7H_2$-$12H_2$**) exhibit well defined and mainly reversible redox behavior in CH_2Cl_2

containing 0.1 M TBAP, an example of which is illustrated by the cyclic voltammograms in Figure 6-2 for the dibromoderivatives **8H₂** and **11H₂**. The di-fused IND chlorin **8H₂** is characterized by four reversible one-electron reductions and two reversible one-electron oxidations within the range of the electrochemical solvent while the corresponding di-fused MN chlorin **11H₂** exhibits two one-electron reductions and two one-electron oxidations, the latter of which are overlapped in potential at 1.25 V.

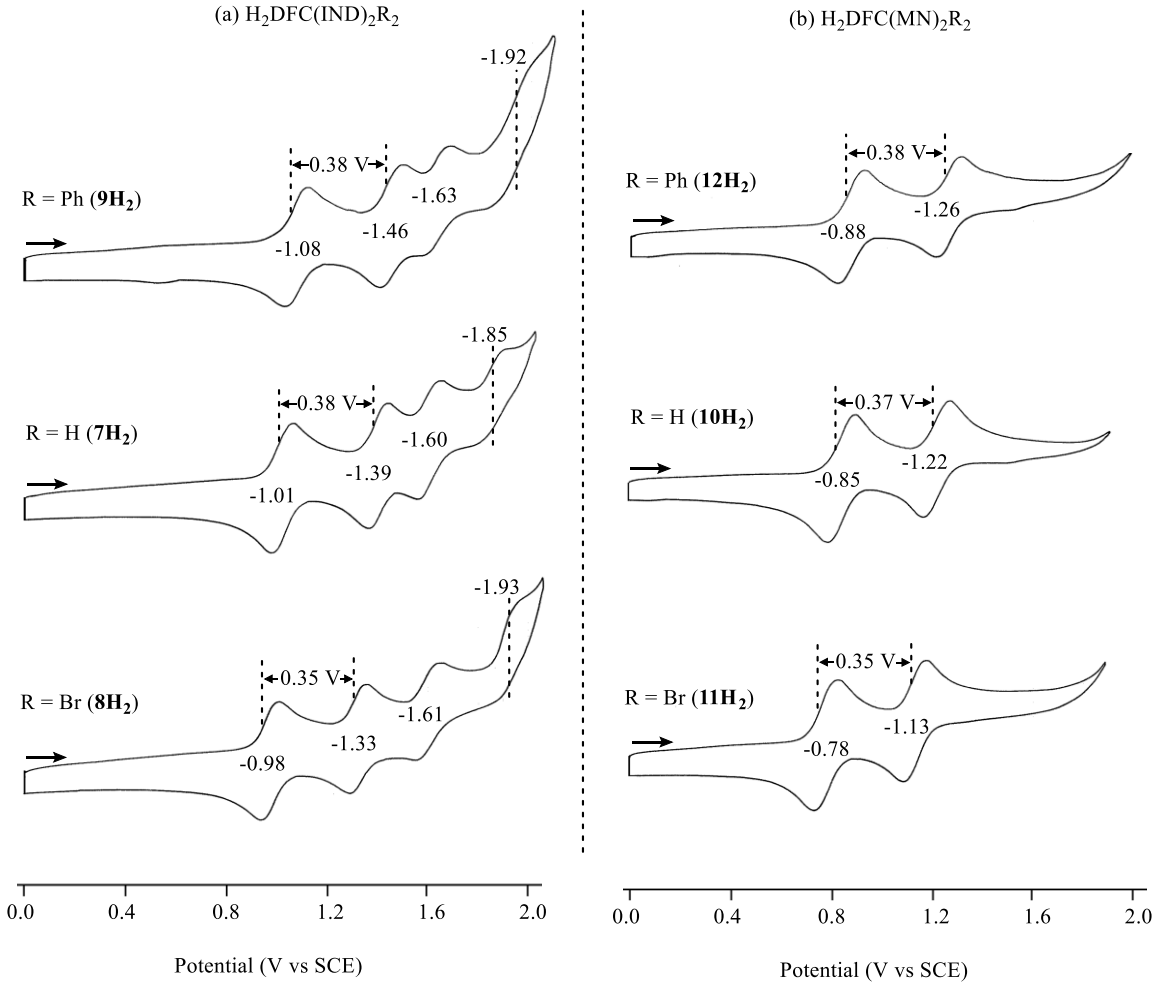

Figure 6-3. Cyclic voltammograms illustrating the reduction of free-base chlorins with a) di-fused indanedione (IND) (**7H₂-9H₂**) and b) di-fused malononitrile (MN) (**10H₂-12H₂**) in CH_2Cl_2, containing 0.1 M TBAP. Scan rate = 0.1 V/s.

Similar redox behavior is seen for all of the chlorins which also undergo two one-electron oxidations and two or four one-electron reductions as shown in Figure 6-3 for **$8H_2$** and **$11H_2$**. Each di-fused malononitrile chlorin is easier to reduce than the corresponding di-fused indanedione derivative, consistent with the stronger electron withdrawing properties of the cyano-containing MN groups.

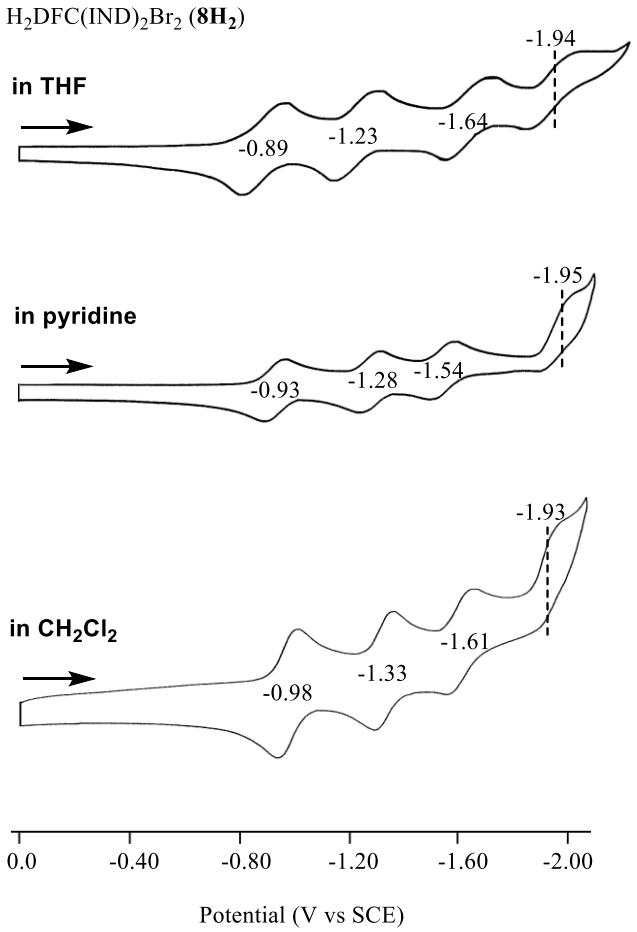

Figure 6-4. Cyclic voltammograms illustrating the reduction of $8H_2$ in THF, pyridine and CH_2Cl_2, containing 0.1 M TBAP. Scan rate = 0.1 V/s.

In addition, the chlorins in the $H_2DFC(IND)_2R_2$ or $H_2DFC(MN)_2R_2$ series with R = Br are easier to reduce by 100-130 mV than those with R = Ph and this is consistent with the electron-

withdrawing or donating properties of the trans β-substituents, namely the easiest ring-centered reductions occur for the dibromo chlorins and the hardest for the diphenyl derivatives (see Figure 6-3 and Table 6-1). However, what might not have been predicted is that each chlorin in the indanedione series **$7H_2$-$9H_2$** exhibits a third and fourth well-defined reduction which is not seen for the related di-fused MN chlorins **$10H_2$-$12H_2$**, despite the fact that the malononitrile derivatives are easier to reduce by more than 200 mV.

Table 6-1. Half-wave ($E_{1/2}$ vs SCE) or peak potentials E_p of free-base di-fused chlorins and porphyrins in CH_2Cl_2, containing 0.1M TBAP

Cpd #	Macrocycle	Temp.[a]	R	Oxidations		Reductions				H-L[b]
				2nd	1st	1st	2nd	3rd	4th	
$7H_2$	H_2DFC(IND)$_2$	RT	H	1.17	0.87	-1.01	-1.39	-1.60	-1.85	1.88
$8H_2$			Br	1.10	0.90	-0.98	-1.33	-1.61	-1.93	1.88
$9H_2$			Ph	0.99	0.76	-1.08	-1.46	-1.63	-1.92	1.84
$10H_2$	H_2DFC(MN)$_2$	RT	H	1.35	1.18	-0.85	-1.22			2.03
$11H_2$			Br	1.25[e]	1.25[e]	-0.78	-1.13			2.03
$12H_2$			Ph	1.19	1.09	-0.88	-1.26			1.97
$1H_2$	H_2DFP(IND)$_2$	RT	H	1.30[c]	0.92	-0.95	-1.29	irr.[d]		1.87
$2H_2$			Br		0.98[c]	-0.85	-1.10	-1.57		
$3H_2$			Ph	1.08	0.88	-0.96	-1.34[b]	irr.[d]		1.84
$4H_2$	H_2DFP(MN)$_2$	-60 °C	H	1.39	1.18	-0.63	-0.96[b]	irr.[d]		1.81
$5H_2$			Br	1.33	1.22	-0.52	-0.78[b]	irr.[d]		1.74
$6H_2$			Ph	1.23	1.10	-0.64	-0.96[b]	irr.[d]		1.74

[a.] RT = room temperature (~22 °C)
[b.] H-L = Difference in potentials between reversible first reduction and first oxidation (the HOMO-LUMO gap)
[c.] Peak potential at scan rate of 100mV/s.
[d.] irr. = redox process involves product of chemical reaction and not the original compound added to solution.
[e] overlapping oxidations at same $E_{1/2}$

Half wave potentials for the third reduction of H_2DFC(IND)$_2R_2$ are located between -1.60 (**$7H_2$**) and -1.63 V (**$9H_2$**) and are virtually independent of the specific R group on the compound. The fourth reduction of each chlorin is close the CH_2Cl_2 solvent limit of about -2.1 V, but this

process also occurs at a potential which is relatively independent of the R group substituents, the measured $E_{1/2}$ values being -1.85 V for R = H, -1.93 V for R = Br and -1.92 V for R = Ph (see Figure 6-3 and Table 6-1). Finally, it should be noted that the last two reductions of **$7H_2$-$9H_2$** in Figure 6-3a are not limited to CH_2Cl_2 solvent as illustrated by cyclic voltammograms of **$8H_2$** in THF and pyridine (Figure 6-4), two commonly used electrochemical solvents which possess an extended negative potential window, thus allowing for a facile measurement of $E_{1/2}$ values for addition of a fourth electron to these compounds.

Porphyrins. Unlike the chlorins which are stable in their electroreduced forms, the electrogenerated anionic forms of the free-base di-fused porphyrins are all highly reactive, thus leading to cyclic voltammograms having reduction peaks not only of the synthesized compound added to solution but also of one or more new redox active species formed at the electrode surface in a homogenous chemical reaction following electron transfer. Despite this reactivity, a comparison between potentials for the reversible addition or abstraction of electrons to the related di-fused chlorins and di-fused porphyrins in the IND or MN series is still possible and such a comparison is shown by the voltammograms in Figure 6-5.

Based on earlier studies of structurally similar chlorins and porphyrins,[29] it was expected that the di-fused chlorins and porphyrins of IND with the same R group substituents (H, Br or Ph) would exhibit similar reduction potentials for the reversible formation of π-anion radicals and dianions and this is indeed the case as shown in Figure 6-5 for **$7H_2$** and **$1H_2$** which are reduced in the first step at $E_{1/2}$ = -1.01 and -0.95 V, respectively, in CH_2Cl_2 at room temperature (Figure 6-5). The halfwave potential for oxidation of the porphyrin is 50 mV more difficult than for the chlorin and thus the HOMO-LUMO gaps of the two free-base macrocycles are essentially identical.

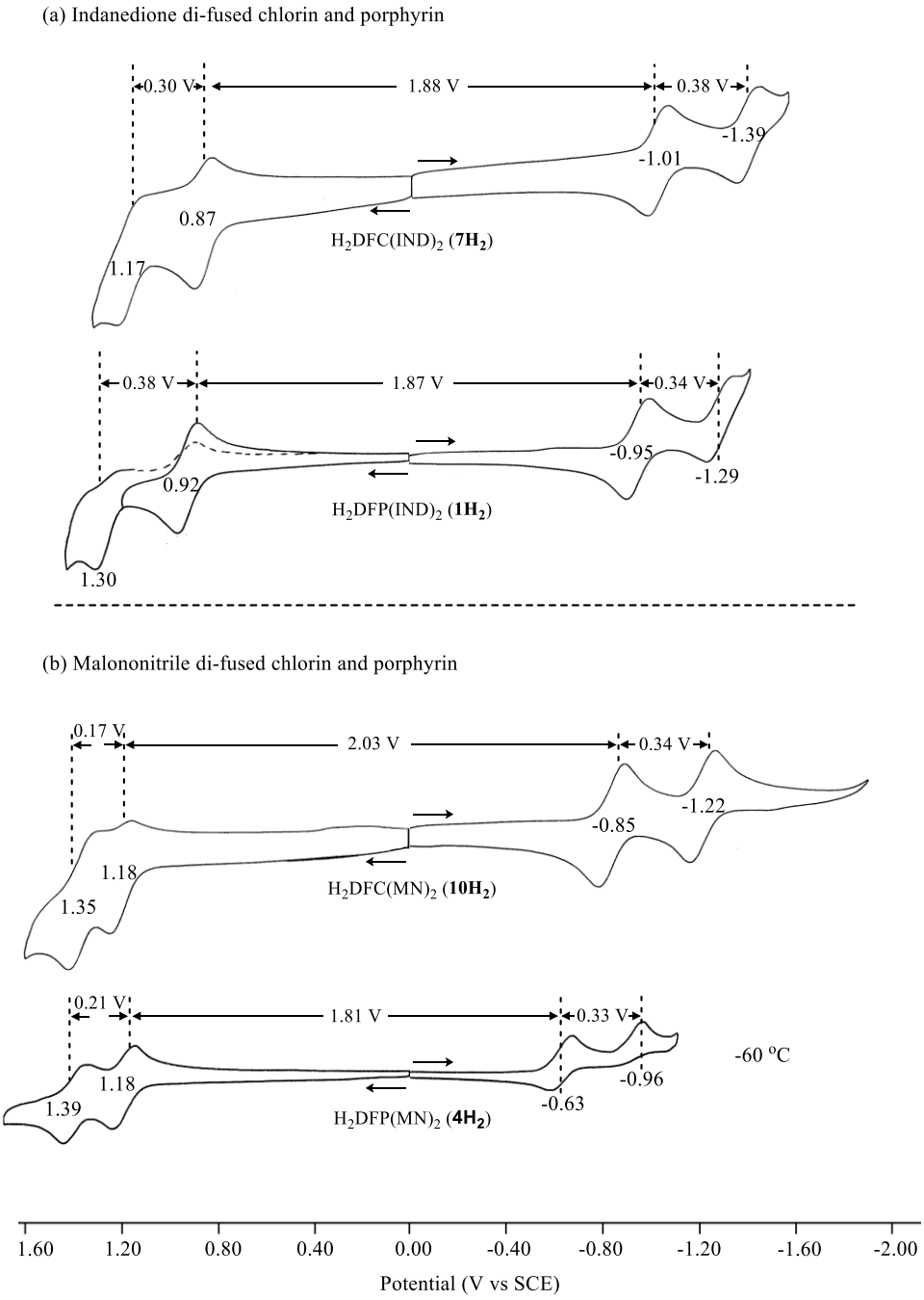

Figure 6-5. Cyclic voltammograms of a) di-fused indanedione porphyrins and chlorins and b) related malononitrile fused derivatives in CH_2Cl_2, containing 0.1M TBAP. Scan rate = 0.1 V/s.

It was also expected that similar reduction potentials would be exhibited by the di-fused MN chlorins and porphyrins with the same R substituents, but this is not the case as shown in Figure

6-5b for **10H₂** and **4H₂** and also in Table 6-1 which summarizes the measured half-wave or peak potentials for each free-base compound in CH_2Cl_2. Although the listed potentials for the di-fused MN porphyrins were obtained at -60 °C and those for the chlorins at room temperature, it is clearly evident that all three porphyrins in the malononitrile series (**4H₂**-**6H₂**) are 240-260 mV easier to reduce than the related chlorin compounds (**10H₂**-**12H₂**). This significantly larger substituent effect of the di-fused MN groups on the porphyrin reduction potentials provides strong indirect evidence that the first two added electrons are located in large part on, or close to, the pyrrole ring having the fused MN groups and a saturated double bond in the case of the chlorin, the latter of which decreases the electron-withdrawing effect of the four CN groups of the malononitrile.

A good example of the chemical reactions following electroreduction of the malononitrile porphyrins is given by the voltammograms in Figure 6-6 for **6H₂** in CH_2Cl_2. At room temperature, three major cathodic reduction peaks are observed at -0.70, -0.90, and -1.22 V on the forward negative potential sweep between 0.0 and -1.8 V and three peaks are also seen on the reverse anodic scan (E_{pa} = -1.10, -0.80, and -0.46 V), but the anodic oxidation peaks are not coupled to the cathodic reductions as seen in Figure 6-6A.

The first two reductions of **6H₂** can be assigned to formation of an initial porphyrin π-anion radical and dianion, and both processes are followed by a homogeneous chemical reaction, the product of which is associated with the irreversible reduction at E_{pc} = -1.22 V on the forward potential sweep and three oxidations of equal current height on the return sweep. The positively shifted potentials of $E_{1/2}$ = -0.50, -0.83 (dashed line in Figure 6-6a) and E_{pa} = -1.10 V for the final *in situ* electrogenerated product of reduction and reoxidation at room temperature suggests formation of a porphyrin having one or more cyano substituents at the β-pyrrole position of the

macrocycle. The instability of the singly and doubly reduced free base porphyrins in CH_2Cl_2 and the proposed formation of a β-CN substituted porphyrin product is consistent with the mass spectral data of these compounds which indicates a loss of one or two CN^- groups from the synthesized compound in the gas phase (see Figure 6-1).

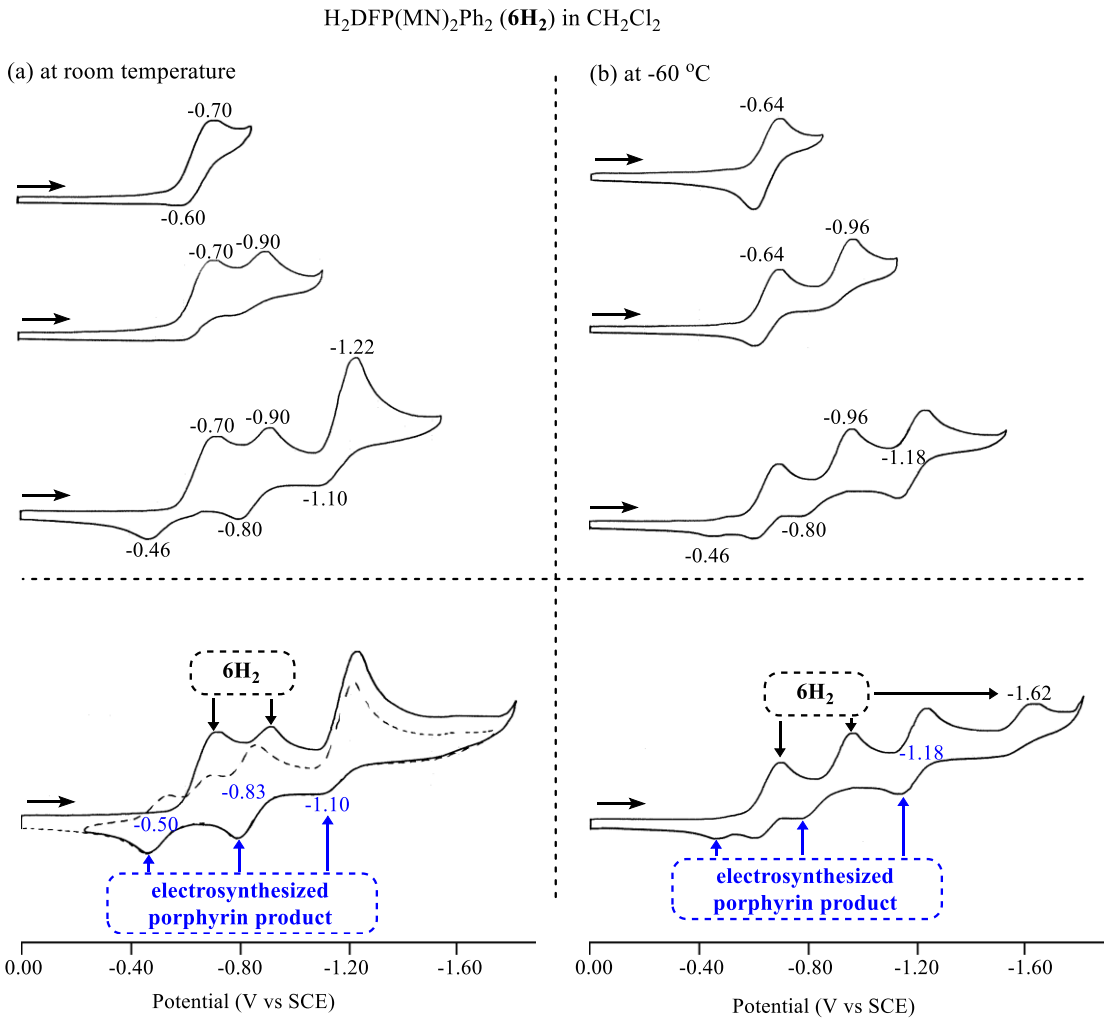

Figure 6-6. Cyclic voltammograms showing reduction of the di-fused malononitrile porphyrin $6H_2$ in CH_2Cl_2, containing 0.1 M TBAP at a) room temperature and b) -60 °C. Scan rate = 0.1 V/s.

A similar electrochemistry is observed for $H_2DFP(MN)_2Ph_2$ **$6H_2$** when the reduction was carried out at -60 °C in CH_2Cl_2. The voltammograms under these solution conditions are illustrated

in Figure 6-6b and are consistent with the same electrosynthesized β-CN product but with a decreased rate of the chemical reaction following electron transfer. Evidence for the decreased chemical reaction rate at low temperature is given by the reduced anodic currents of the electrosynthesized product on the reverse potential sweep and the presence of a fourth reduction process at E_{pc} = -1.62 V which is not observed at room temperature. This latter irreversible process is assigned as a third reduction of the initial unreacted porphyrin to its trianionic form.

As mentioned above, one or more homogeneous chemical reactions follow the addition of electrons to the free-base di-fused MN porphyrin and the prevailing redox behavior is almost identical to what is observed for the metal complexes containing Cu^{II}, Ni^{II}, Zn^{II} and in part Co^{II}. This point is illustrated in Figure 6-7 where a new redox active species is *in-situ* generated in each case after an initial one- or two-electron addition, with almost identical current-voltage curves being obtained on the return potential sweep and on all subsequent potential sweeps.

The first reduction of the *in-situ* generated redox active product from $H_2DFP(MN)_2$ is located at $E_{1/2}$ = -0.46 V while the electrosynthesized Cu^{II}, Ni^{II}, and Zn^{II} derivatives have $E_{1/2}$ values of -0.55, -0.54 and -0.69 V (Figure 6-3, 6-4). Again, the final porphyrin reduction product is assigned to a porphyrin with β-CN groups on the basis of its facile reduction and the mass spectral data showing the loss of one or two CN groups in the gas phase (Figure 6-1). A charaterization of the in-situ generated reduction product is needed and is not part of this dissertation.

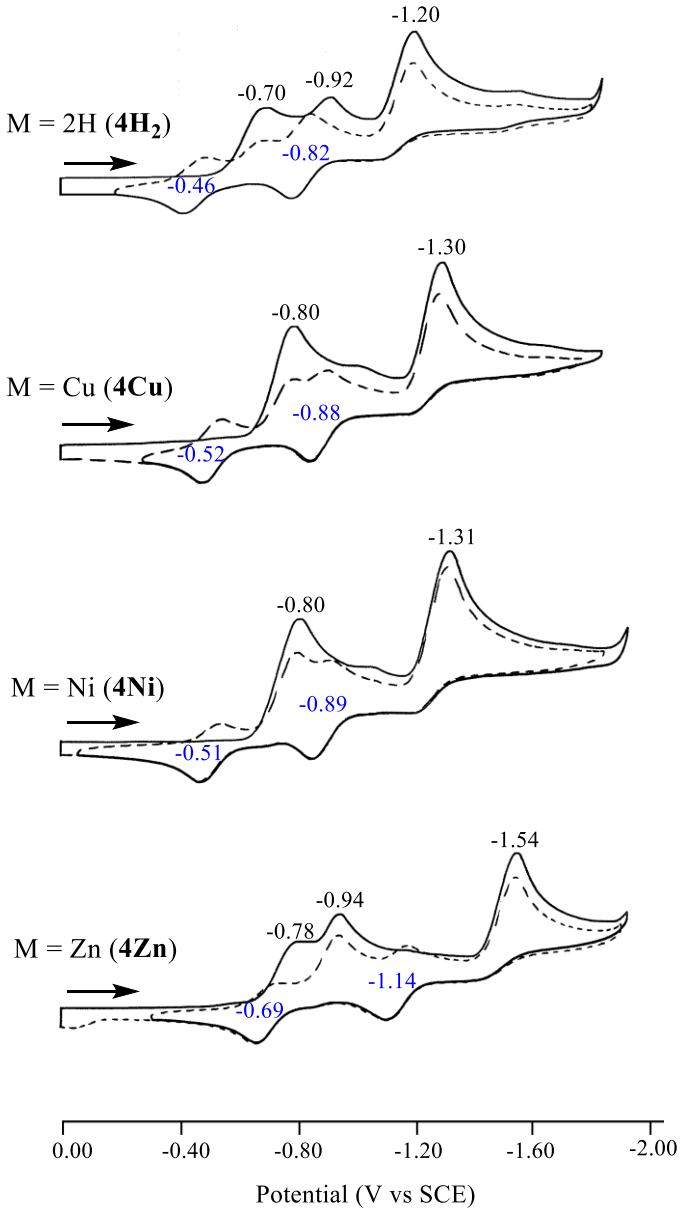

Figure 6-7. Cyclic voltammograms showing reduction of the di-fused malononitrile porphyrins 4M (where M = 2H, Cu^{II}, Ni^{II} or Zn^{II}) in CH_2Cl_2, containing 0.1 M TBAP at room temperature. Scan rate = 0.1 V/s.

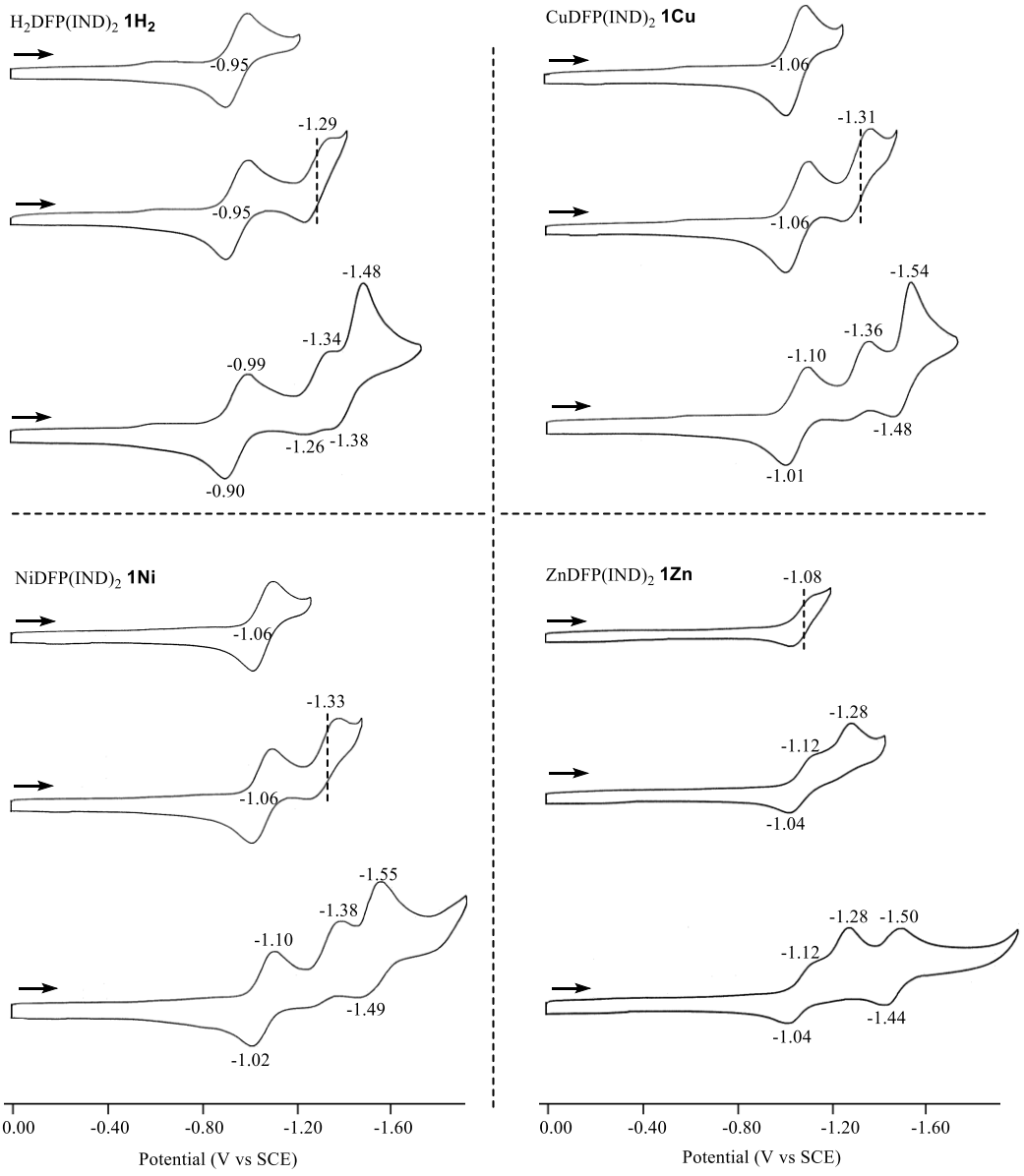

Figure 6-8. Cyclic voltammograms for MDFP(IND)$_2$, M = Cu, Ni, 2H, Zn in CH_2Cl_2, containing 0.1M TBAP. Scan rate = 0.1 V/s.

Similar current voltage curves are also seen for reduction and reoxidation of each porphyrin in the indanedione series, with examples given in Figure 6-8 for MDFP(IND)$_2$R$_2$, where M = 2H, Cu^{II}, Ni^{II} or Zn^{II}. The singly reduced forms of MDFP(IND)$_2$R$_2$ are stable on the cyclic voltammetry timescale, but the doubly and triply reduced forms of the porphyrin rapidly react to give new *in-situ* generated products with two reversible reductions, the second of which is negatively shifted by about 150 mV as compared to the second reduction of the originally synthesized compound added to solution.

Again, like in the use of the DFP(MN)$_2$R derivatives, a charaterization of the in-situ generated reduction product is needed and is not part of this dissertation.

Substituent effects of R group and number of fused IND rings on redox potentials, site or electron transfer and stability of electroreduced compounds. The effect of adding one or more halogens to the β-pyrrole position of a porphyrin or chlorin macrocycle has been examined for a large number of compounds[19, 66, 94, 145] and it is generally accepted that the brominated porphyrins will be easier to reduce to their anionic and dianionic forms by 50-60 mV per each added Br substituent. This positive shift of potential towards an easier reduction is also seen in the redox behavior of the investigated chlorins as described earlier in the dissertation (pp131-135) and also illustrated in Figure 6-3 and Table 6-1 for the di-fused chlorins of IND and MN.

A similar substituent effect on the electron-withdrawing Br groups is also observed for the first one-electron reduction of the DFP(IND)$_2$R$_2$ derivatives as graphically shown in Figure 6-9 for CuDFP(IND)$_2$R$_2$ and also in Table 6-2 for other porphyrins in the bis-fused IND series of compounds. However, also seen in Figure 6-9, measured $E_{1/2}$ values for the second reversible reduction of the three CuDFP(IND)$_2$R$_2$ complexes are invariant with changes in the R group from

Ph to H to Br, with all three porphyrins being reduced to their dianionic form at an $E_{1/2}$ value close to -1.30 V vs. SCE. A similar $E_{1/2}$ value was also measured for most of the other di-fused IND metalloporphyrins as well as for $H_2DFP(IND)_2R_2$, thus providing strong evidence that the second electron is primarily added to a site on the molecule sufficiently removed from the electron-withdrawing Br substituents so as not to be affected by their presence. This would suggest a location very close to the two fused IND rings.

Table 6-2. Redox potentials of di-fused metalloporphyrins $MDFP(IND)_2R_2$ and $MDFP(IND)_2R_2$ in CH_2Cl_2, containing 0.1M TBAP. Scan rate = 100 mV/s

Cpd #	Mac	R	Metal	Ox			Red			H-L[a]
				3rd	2nd	1st	1st	2nd	3rd	
1Co	$DFP(IND)_2$	H	Co	1.32[b]	0.92	0.72	-0.74	-1.30	-1.62[b]	1.46
1Ni		H	Ni		1.38[b]	0.95	-1.06	-1.33	-1.55[b]	2.01
1Cu		H	Cu		1.30[b]	0.89	-1.06	-1.31	-1.54[b]	1.95
1Zn		H	Zn		1.04	0.70	-1.08	-1.28[b]	irr.[c]	1.78
2Co		Br	Co		0.97	0.78	-0.68	-1.31	-1.80[b]	1.46
2Ni		Br	Ni		1.36[b]	1.03	-0.97	-1.33	-1.73[b]	2.00
2Cu		Br	Cu		1.20[b]	0.95	-0.96	-1.30	-1.66[b]	1.91
2Zn		Br	Zn		1.12[b]	0.74	-1.08	-1.40[b]	irr.[c]	1.82
3Co		Ph	Co	1.28[b]	0.91	0.73	-0.77	-1.31	-1.66[b]	1.50
3Ni		Ph	Ni		1.32[b]	0.91	-1.10	-1.36	-1.68[b]	2.01
3Cu		Ph	Cu		1.16	0.87	-1.06	-1.30	-1.57[b]	1.93
3Zn		Ph	Zn		0.91	0.64	-1.11	-1.34[b]	irr.[c]	1.75
4Co	$DFP(MN)_2$	H	Co	1.45	1.11	0.90[b]	-0.53	-1.24[b]	irr.[c]	
4Ni		H	Ni		1.40	1.27	-0.72	-1.08[b]	irr.[c]	1.99
4Cu		H	Cu		1.41	1.27	-0.73	-1.08[b]	irr.[c]	2.00
4Zn		H	Zn		1.24	0.92	-0.79	-0.98[b]	irr.[c]	1.71
5Co		Br	Co	1.32	1.20	1.07	-0.47	-1.08[b]	irr.[c]	1.54
5Ni		Br	Ni		1.33	1.33	-0.64	-0.94[b]	irr.[c]	1.97
5Cu		Br	Cu		1.41	1.21	-0.63	-0.94[b]	irr.[c]	1.84
5Zn		Br	Zn		1.22	0.97	-0.70	-0.92[b]	irr.[c]	1.67
6Co		Ph	Co	1.35	1.05	0.90[b]	-0.54	-1.22[b]	irr.[c]	
6Ni		Ph	Ni							
6Cu		Ph	Cu		1.30	1.09	-0.74	-1.06[b]	irr.[c]	1.83
6Zn		Ph	Zn		1.13	0.88	-0.81	-1.04[b]	irr.[c]	1.69

[a.] H-L = Difference in potentials between reversible first reduction and first oxidation (the HOMO-LUMO gap)
[b.] Peak potential at scan rate of 100mV/s.
[c.] irr. = redox process involves product of chemical reaction and not the original compound added to solution.

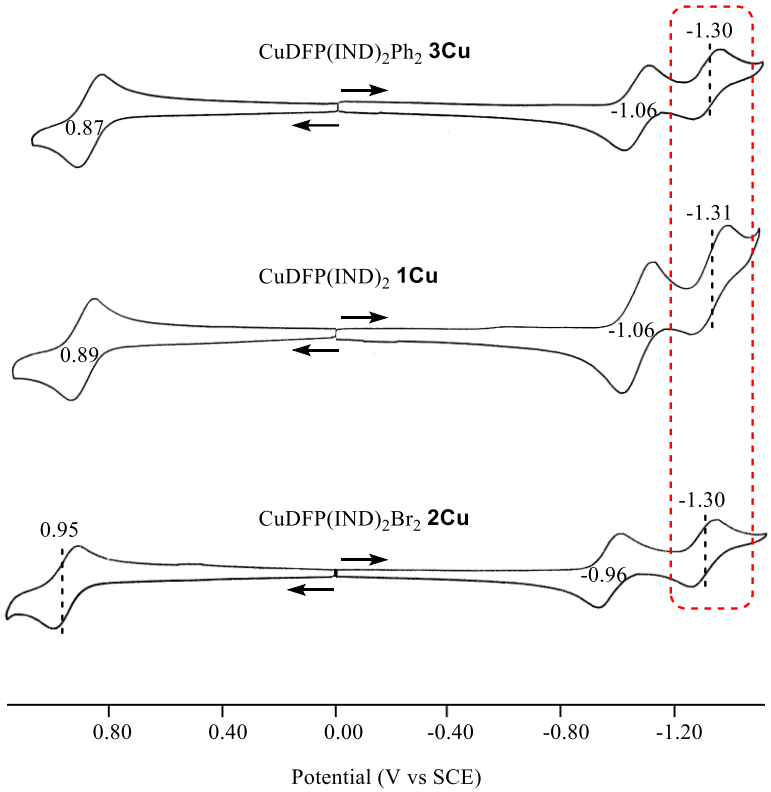

Figure 6-9. Cyclic voltammograms for CuDFP(IND)$_2$R$_2$, R = Ph, H and Br in CH_2Cl_2, containing 0.1M TBAP. Scan rate = 0.1 V/s. The reductions boxed in red are independent of R substituent.

Additional indirect evidence for this assignment is given by the measured substituent effect of the IND groups on the first and second reduction potentials upon changing the examined molecule from MTPP to the previously reported mono-fused indanedione porphyrin, MFP(IND), and then to DFP(IND)$_2$.

Cyclic voltammograms for these three compounds containing Cu(II) central metal ions are given in Figure 6-10. As seen in the figure, the addition of one fused IND group to CuTPP shifts the $E_{1/2}$ values for the first and second reduction negatively by 160 and 250 mV, respectively. The IND substituent effect is increased even further upon going to CuDFP(IND)$_2$ where the observed overall negative shift in $E_{1/2}$ from CuTPP amounts to 260 and 410 mV for the first and second one-

electron addtions, respectively. The larger substituent effect for the second one-electron addition is consistent with the location of the second added electron being close to the electron-withdrawing (and fused) IND groups and this is also consistent with the lack of a measurable substituent effect by the trans Br groups on the molecule. Again, this result is only observed for the porphyrins and not the chlorins where the expected R group substituent effects are observed. (all chlorins have the same third reduction potential (~ -1.60 V) as seen in Figure 6-3.

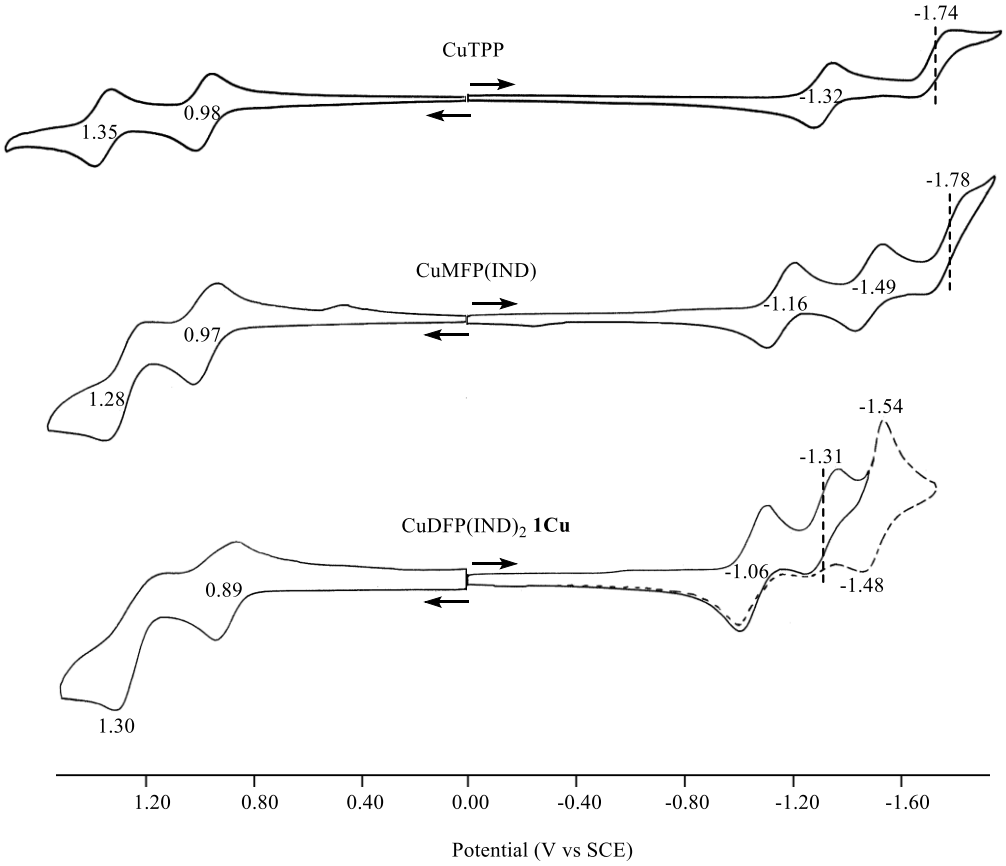

Figure 6-10. Cyclic voltammograms comparing CuTPP, with the copper mono-fused and di-fused indanedione porphyrins in CH_2Cl_2, containing 0.1 M TBAP. Scan rate = 0.1 V/s.

Electrochemistry of Co centered di-fused porphyrins. The six di-fused Co porphyrins in Chart 6-1 were characterized by cyclic voltammetry in CH_2Cl_2 containing 0.1 M TBAP. An example of the cyclic voltammograms for CoDFP$(MN)_2$ is shown in Figure 6-11.

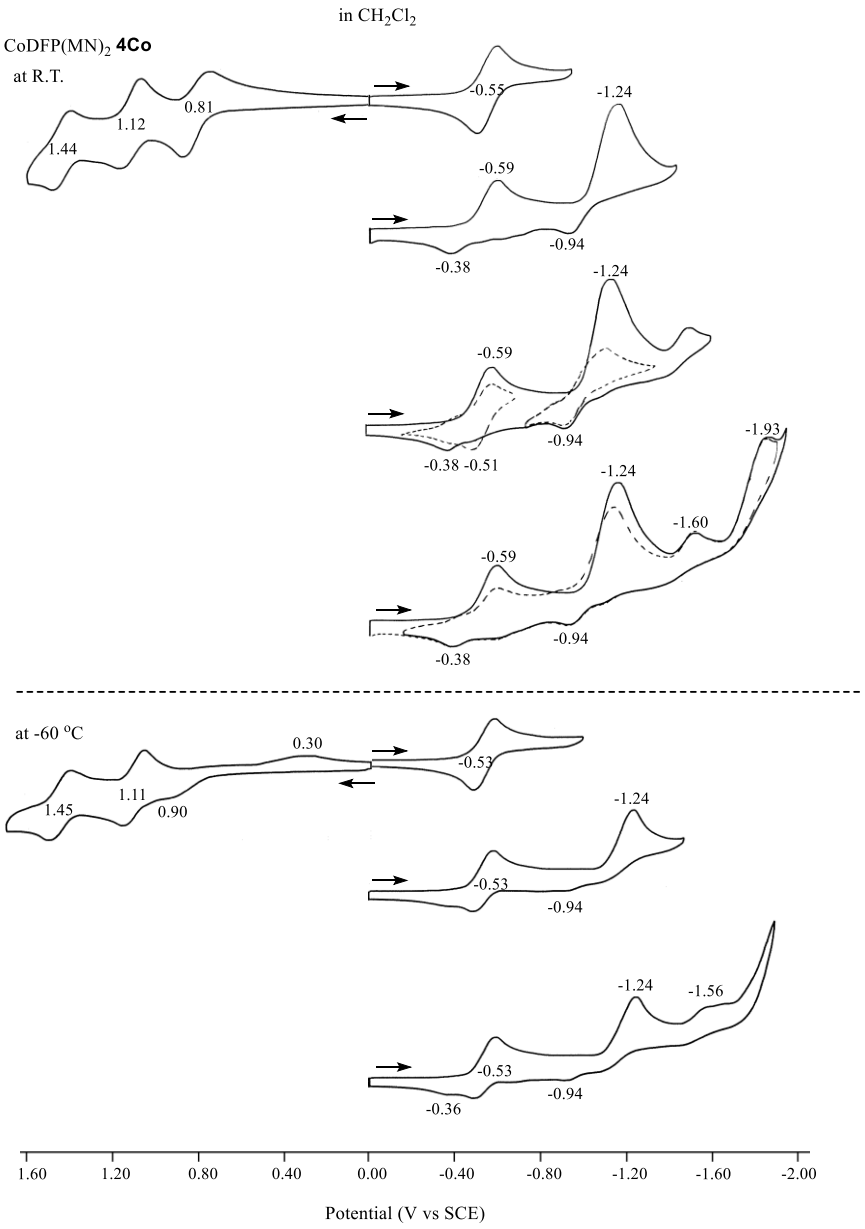

Figure 6-11. Cyclic voltammograms of CoDFP$(MN)_2$ in CH_2Cl_2, containing 0.1 M TBAP at room temperature and -60ºC. Scan rate = 0.1 V/s.

As seen in Figure 6-11, three well-defined reversible oxidations located at $E_{1/2}$ = 0.81, 1.12 and 1.44 V are observed for compound **4Co** at room temperature which is assigned to be one Co^{II}/Co^{III} metal-centered oxidation followed by two ring centered oxidations. The first reversible reduction of $CoDFP(MN)_2$ located at $E_{1/2}$ = -0.55 V is positively shifted by around 200 mV as compared to the first reversible reduction of $MDFP(MN)_2$ where M = Ni, Cu, Zn and 2H which suggests that the first reversible reduction of $CoDFP(MN)_2$ is assigned to be a metal centered Co^{II}/Co^{I} reduction as often reported. This reversible metal-centered reduction is then followed by a homogeneous chemical reaction, the product of which is associated with the irreversible reduction at E_{pc} = -1.24 V on the forward potential sweep and two oxidations of equal current height on the return sweep (E_{pa} = -0.94 and -0.38 V). The positive shift of the reoxidation peak also suggests the formation of a porphyrin having one or more cyano substituents at the β-pyrrole position of the macrocycle which is consistent with the loss of one or two CN^- groups from the synthesized compound in the gas phase as shown in the mass spec.

The chemical reaction following generation of $[Co^{I}DFP(MN)_2]^-$ is not eliminated at low temperature as shown in Figure 6-11 while the oxidation behavior changes. The first reversible oxidation at room temperature becomes irrversible with peak potential E_{pa} = 0.90 V. This is probably due to the presence of water which coordinates to the Co center at low temperature. A similar temperature dependent change in the redox behavior is observed for $CoDFP(MN)_2Ph_2$ as shown in Figure 6-12.

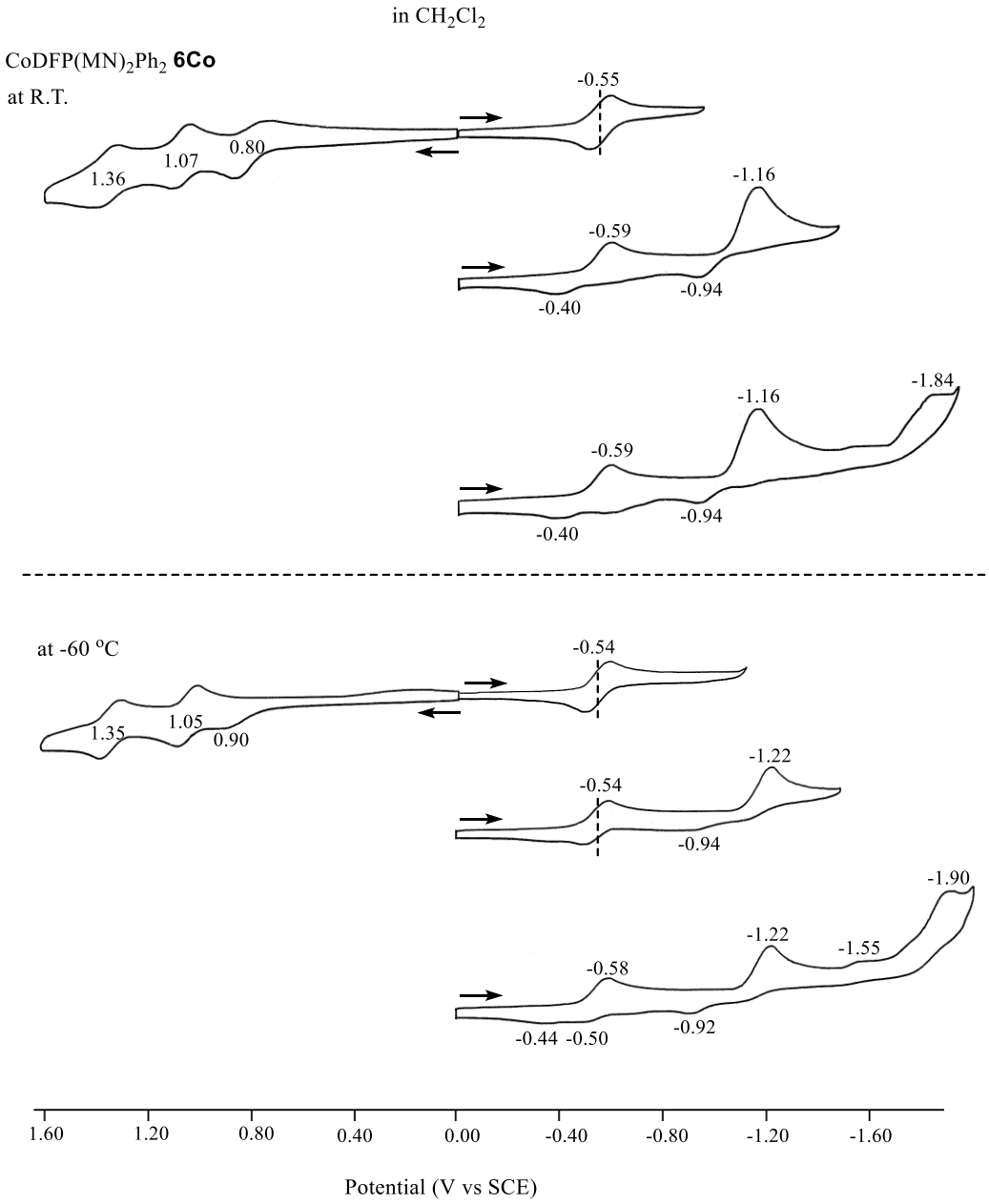

Figure 6-12. Cyclic voltammograms of $CoDFP(MN)_2Ph_2$ in CH_2Cl_2, containing 0.1 M TBAP at room temperature and -60°C. Scan rate = 0.1 V/s.

Cyclic voltammograms of each cobalt porphyrin in the indanedione series were also obtained in CH_2Cl_2 containing 0.1M TBAP at room temperatue and -60 ^oC. An example is given in Figure 6-13 for CoDFP(IND)$_2$ **1Co**.

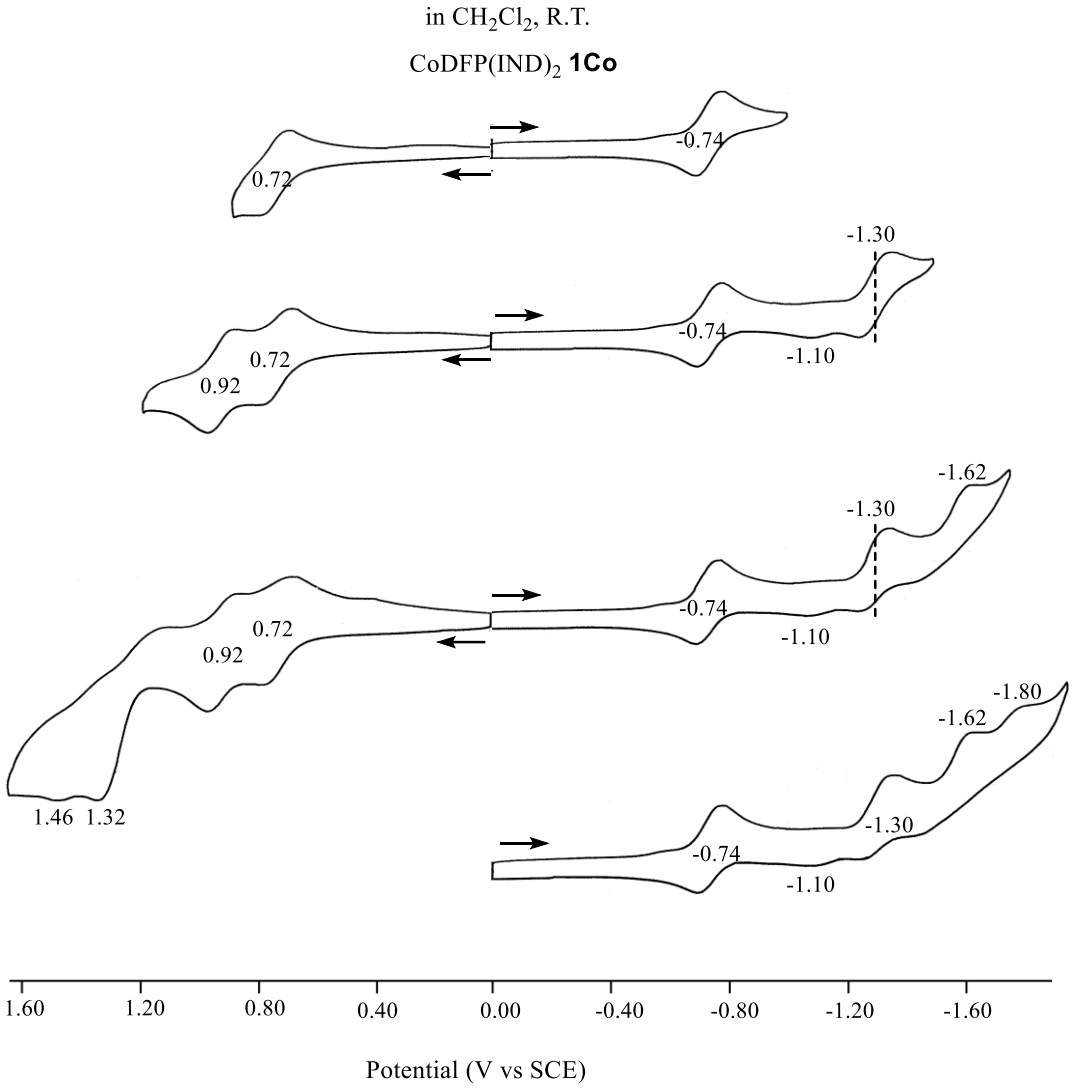

Figure 6-13. Cyclic voltammograms of CoDFP(IND)$_2$ in CH_2Cl_2, containing 0.1 M TBAP. Scan rate = 0.1 V/s.

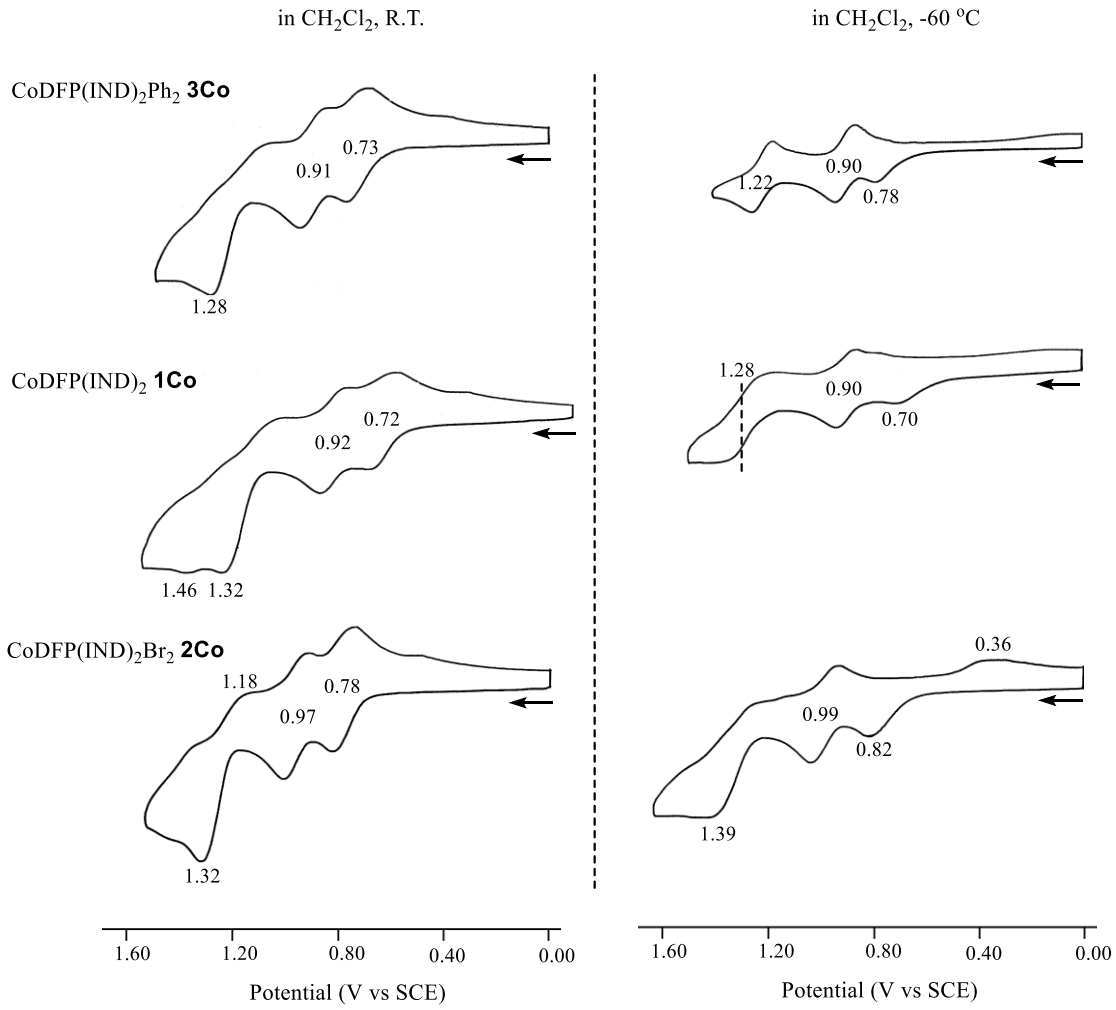

Figure 6-14. Cyclic voltammograms of oxidations for $CoDFP(IND)_2R_2$ in CH_2Cl_2, containing 0.1 M TBAP at room temperature and -60 °C. Scan rate = 0.1 V/s.

As seen in Figure 6-13, the singly and doubly reduced forms of $CoDFP(IND)_2$ are more stable than $CoDFP(MN)_2$. Two reversible reductions are observed for compound **1Co** with half-wave potentials $E_{1/2}$ = -0.74 and -1.30 V. One or more chemical reactions are observed after the second reversible reduction. The lack of reoxidation peaks (only a small peak located at E_{pa} = -1.10 V) on the reverse scan shows that no obvious electrogeneration of product is observed. Two

reversible oxidations located at $E_{1/2}$ = 0.72 and 0.92 V are observed for compound **1Co**, followed by an irreversible third oxidation which becomes reversible or quasireversible at low temperature. Examples illustrating the oxidations and reductions of CoDFP(IND)$_2$R$_2$ are given in Figures 6-14 and 6-15.

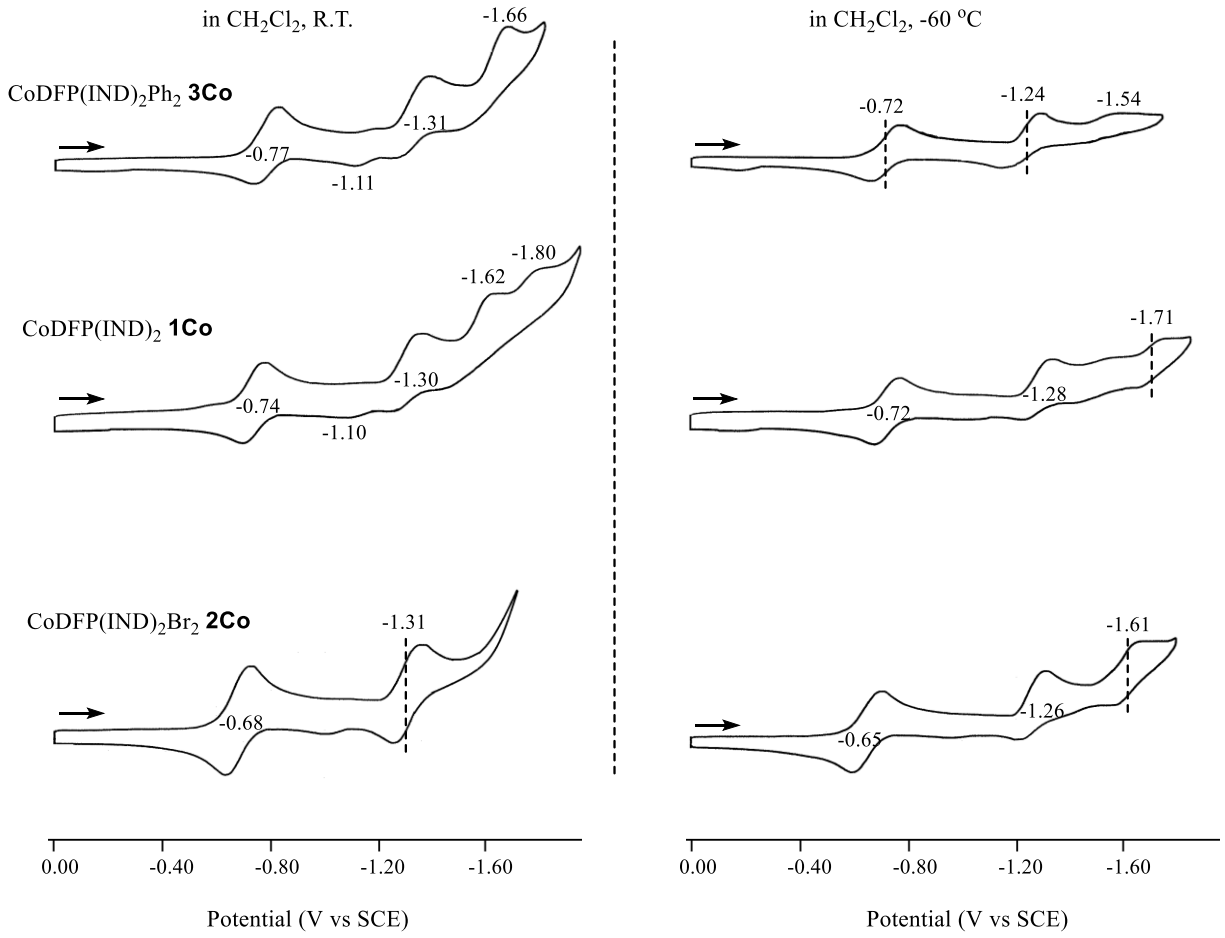

Figure 6-15. Cyclic voltammograms of reductions for CoDFP(IND)$_2$R$_2$ in CH_2Cl_2, containing 0.1 M TBAP at room temperature and -60 ºC. Scan rate = 0.1 V/s.

As seen in Figure 6-14, the third oxidation becomes reversible at -60 ºC for CoDFP(IND)$_2$Ph$_2$ ($E_{1/2}$ = 1.22 V) and CoDFP(IND)$_2$H$_2$ ($E_{1/2}$ = 1.28 V) while it stays irreversible for CoDFP(IND)$_2$Br$_2$. The first oxidation becomes irreversible or quasireversible at -60 ºC due to the coordination of a water molecule with the Co center as described above.

Figure 6-15 shows the reduction behavior of the CoDFP(IND)$_2$R$_2$ compounds in CH_2Cl_2 at both room temperature and at -60 ºC. Two almost reversible reductions followed by one or two irreversible reductions at more negative potentials are seen for all of the three compounds at room temperature. Chemical reactions which occur after the second reduction are virtually eliminated at low temperature, leading to three reversible reductions for compounds **1Co** and **2Co**. They are located at $E_{1/2}$ = -0.72, -1.28 amd -1.71 V and -0.65, -1.26 and -1.61 V, respectively. Due to the potential limit of the solvent, two reversible reductions located at $E_{1/2}$ = -0.72 V and -1.24 V are observed for compound **3Co**.

6.3 Conclusion

Di-fused chlorins and two sets of di-fused porphyrins are discussed in this chapter. Chlorins are known to undergo two reversible reductions and two reversible oxidations.[29, 33] With the fusion of two indanedione groups (IND) to the chlorin macrocyle, two extra reductions are observed while the fusion of two malononitrile groups (MN) does not result in extra reductions. The fusion of two IND or MN groups to the porphyrin macrocycle also has an effect on the electrochemical behavior. Electrosynthesized products are observed after the generation of an anion or dianion. The proposed formation of a β-CN substituted porphyrin product is consistent with the mass spectral data of these compounds which indicates a loss of one or two CN^- groups from the synthesized compound in the gas phase. The malononitrile series of Co di-fused porphyrins shows a similar in-situ

generated electrosynthesized product after formation of $[Co^{I}DFP(MN)_2R_2]^-$ while the indanedione series of Co di-fused porphyrins are more stable on the cyclic voltammogram time scale.

Chapter Seven

Spectral and Electrochemical Properties of differently substituted porphyrins

7.1 Introduction

The electrochemistry of metalloporphyrins has attracted considerable attention over many decades due in part to the biological relevance of these compounds and in part to their use in a number of applications in the field of material science.[1, 20, 23] Metalloporphyrins have attracted considerable attention for use in a broad range of applications due to their versatile properties, related in part to the conjugated π ring system and in part to the coordination ability of the central metal ion which can exist in a variety of different oxidation states, from M^{I} to M^{VI}.[1, 3]

Numerous transition metal porphyrins have been studied by our laboratory which shows that the electrochemical properties could be 'tuned' by modifying substituents on the meso- or β-pyrrole positions of the macrocycle.[3, 4, 7, 66, 93, 94] We have recently turned our attention to characterizing several new series of synthetic porphyrins and related macrocycles containing tetraphenylporphyrin skeletal structures with high electron withdrawing and/or π-extending substituents.

These porphyrin compounds were synthesized by our collaborators at the IIT in Roorkee, India[67, 146] and sent to us for carrying out electrochemical and spectroelectrochemical measurements. We have obtained numerous complexes of Ni, Co, Cu, and free-base porphyrins to characterize in the past years. The porphyrin structures discussed in this chapter are shown in Chart 7-1. The first group labeled as Group I, (3,5-di-tert-butyl-4-hydroxyphenyl)porphyrin includes porphyrin with four meso-*t*-butyl-phenoxide substituents NiPor (Group IA) and porphyrins with four meso-*t*-butyl-phenoxide substituents in addition to –CHO (Group IB) and $–CH=C(CN)_2$ (Group IC) substituents at β-position and the second includes porphyrins with a single β-pyrrole-dicyanovinyl substituent $NiTPP(CN)_2$, $H_2TPP(CN)_2$ (Group IID), and $NiOPP(CN)_2$, $H_2OPP(CN)_2$

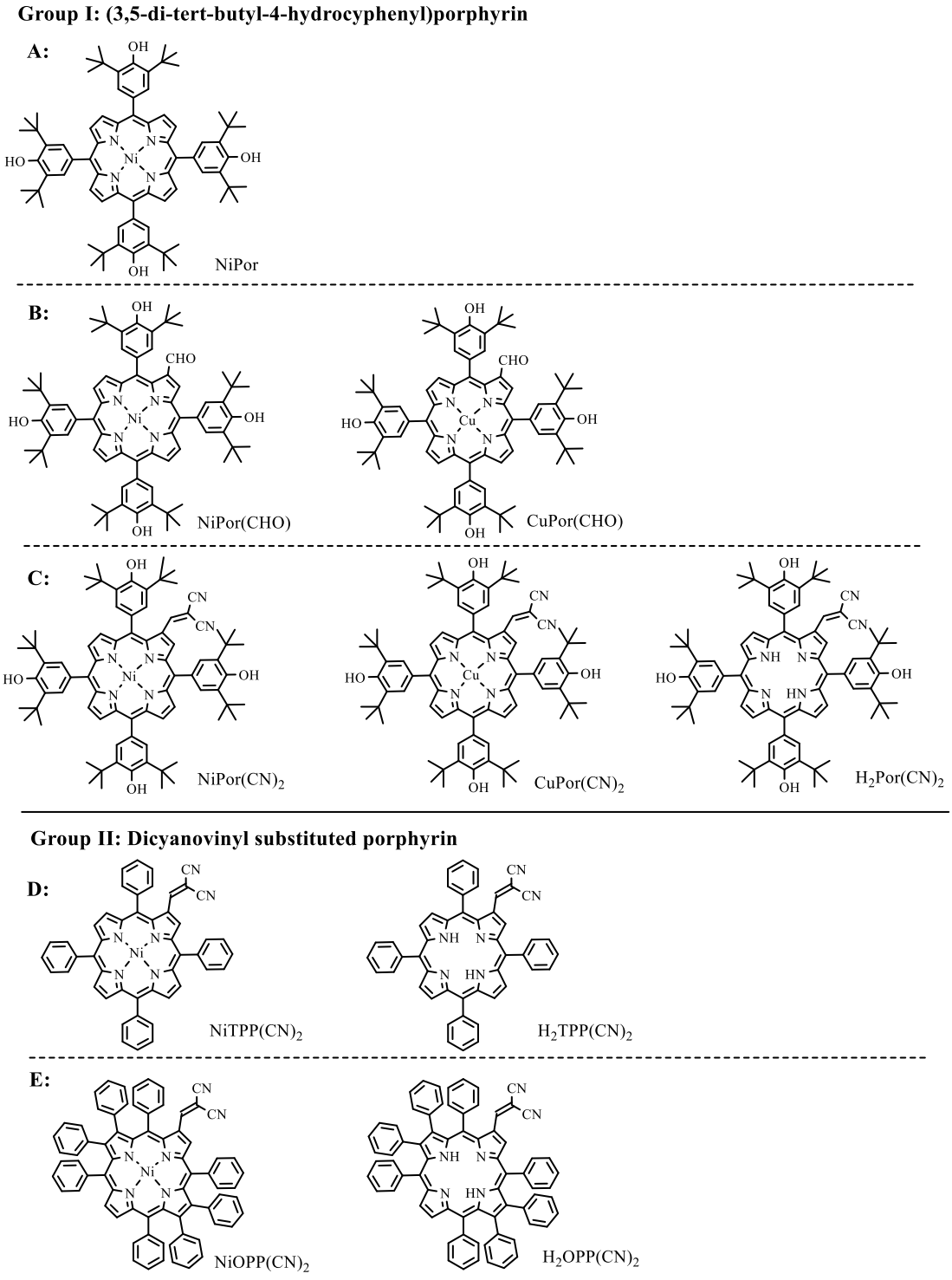

Chart 7-1. Structures of two groups of investigated porphyrins.

(Group IIE). These compounds were previously electrochemically studied in CH_2Cl_2.[67, 146] Table 7-1 provides a summary for the redox potentials of these compounds. These compounds were sent to us for further detailed electrochemical investigation as well as spectroelectrochemistry characterization.

7.2 Results and Discussion

7.2.1 Electrochemistry of Group I (3,5-di-tert-Butyl-4-Hydroxyphenyl)Porphyrins

The effect of meso and *β*-pyrrole substituents on the electrochemistry was investigated by cyclic voltammetry and spectroelectrochemistry under different solution conditions. Examples of cyclic voltammograms for the first group of investigated nickel porphyrins as compared to NiTPP in CH_2Cl_2 containing 0.1M TBAP or $TBAPF_6$ are given in Figure 7-1.

As shown in Figure 7-1, all of the nickel porphyrins undergo two reductions which are assigned to be ring-centered reductions. The dianion generated after the second reduction may react fast with some species in the solvent leading to an irreversible second reduction. The reduction behavior of NiPor is very similar to the parent compound NiTPP with the reversible first ring-centered reduction located at $E_{1/2}$ = -1.34 V and the irreversible second reduction located at E_{pc} = -1.94 V. With the addition of β-pyrrole electron-withdrawing substituents, the first reduction is positively shifted by 200 mV for NiPor(CHO) and 420 mV for NiPor$(CN)_2$ which is reduced at -0.92 V to -1.14 V. This is in accordance with the stonger electron-withdrawing ability of dicyanovinyl group as compared to –CHO group. As a result, the potential for the second reduction of NiPor$(CN)_2$ is positively shifted by 300 mV as compared to compound NiPor(CHO).

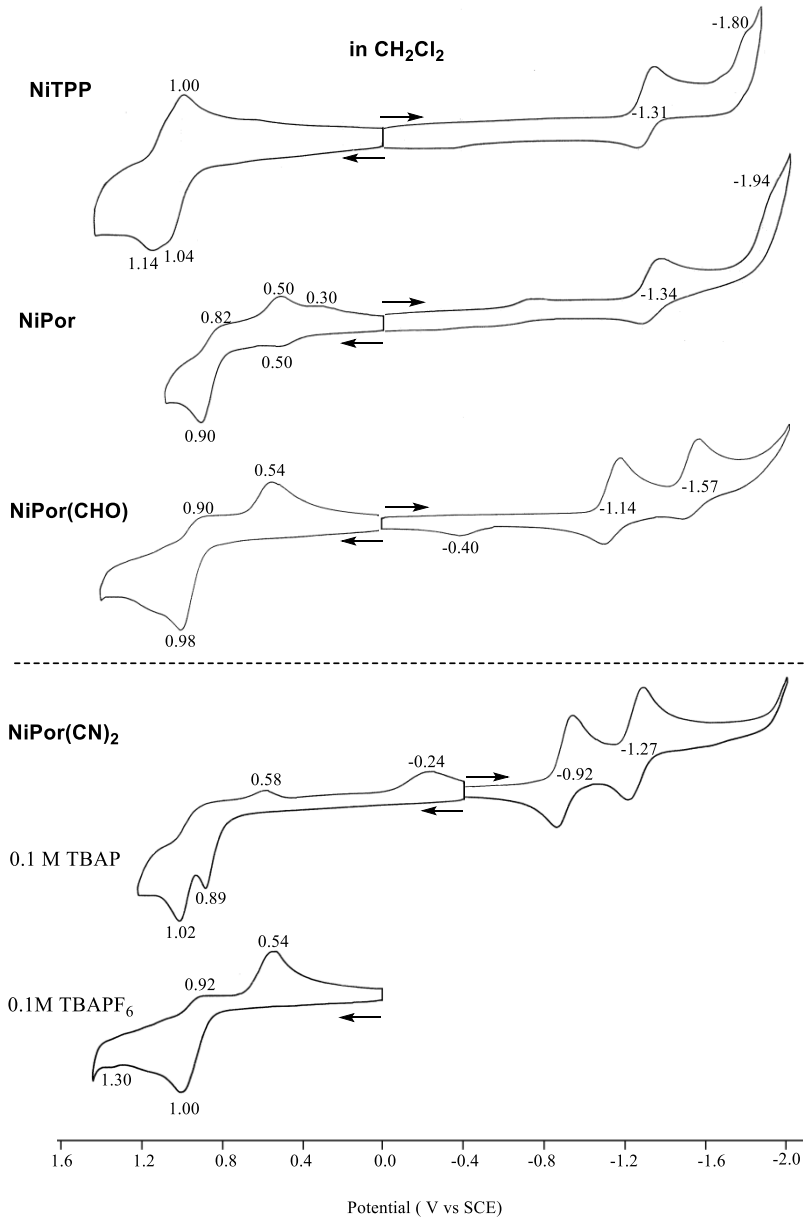

Figure 7-1. Cyclic voltammograms of NiTPP, NiPor, NiPor(CHO), and $NiPor(CN)_2$ in CH_2Cl_2, containing 0.1M TBAP or $TBAPF_6$. Scan rate = 100 mV/s.

For the oxidation, NiTPP is known to undergo two partially overlapped oxidations as shown in Figure 7-1. However, after addition of four *t*-butyl-phenylhydroxide groups at meso positions of the macrocycle, one irreversible process is observed for NiPor, NiPor(CHO), $NiPor(CN)_2$. This oxidation is located at E_{pa} = 0.90, 0.98 and 0.89, 1.02 V respectively. The irreversibility of the

oxidation is consistent with a chemical reaction happens after the electron transfer step which may relate to to chemical reaction of the four meso-phenoxide groups or the generation of the isoporphyrin. A possible mechanism of the chemical reaction of phenoxide groups is shown in Scheme 7-1.[147] The existence of water in CH_2Cl_2 may react with the generated phenoxide cation in solution which results in the irreversibility as observed in Figure 7-1.

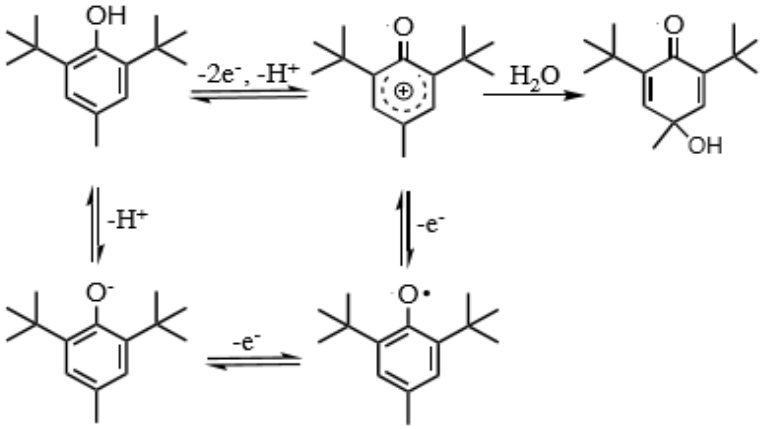

Scheme 7-1. Proposed mechanism for the chemical reaction of phenoxide groups.[147]

Another possibility for the observed irreversibility of oxidations is the generation of isoporphyrin (a tautomer of porphyrin with a saturated meso carbon). The diagnostic UV-visible low-energy bands of isoporphyrin are reported to locate at around 850 and 950 nm[148] which are seen in spectroelectrochemistry for $NiPor(CN)_2$ after the first oxidation. More spectroelectrochemistry studies should be done to further prove this possibility. Also, a charaterization of the in-situ generated oxidation product is needed and is not part of this dissertation.

A similar comparison is made for the copper centered porphyrins as shown in Figure 7-2.

As shown in Figure 7-2, all of the three Cu porphyrins, CuTPP, CuPor(CHO), and $CuPor(CN)_2$ undergo two reversible reductions located at $E_{1/2}$ = -1.31, -1.17 and -0.96 V in the first step and $E_{1/2}$ = -1.73, -1.54 and -1.30 V in the second. By looking at the positive potential shift of the first and second reversible reductions, it is clear that both the dicyanovinyl and –CHO groups have an electron-withdrawing effect while the dicyanovinyl group has a stronger electron-withdrawing effect that the –CHO group which is also the case for the nickel porphyrins as mentioned above.

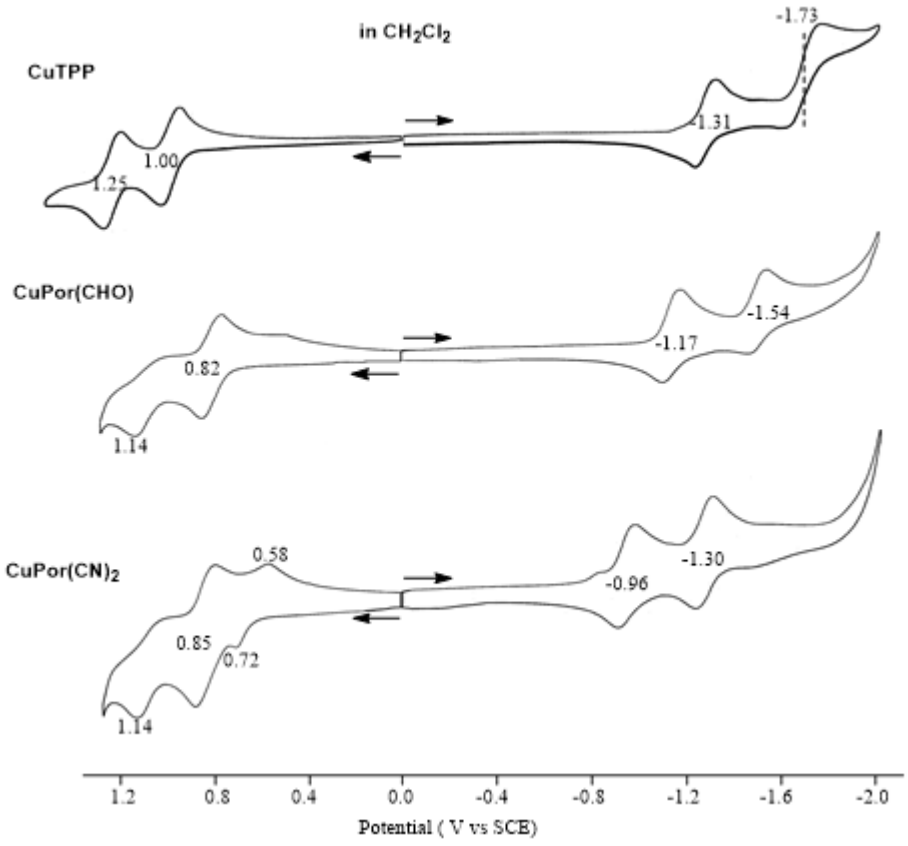

Figure 7-2. Cyclic voltammograms of CuTPP, CuPor(CHO)**,** and $NiPor(CN)_2$ in CH_2Cl_2, containing 0.1M TBAP. Scan rate = 100 mV/s.

Slightly easier oxidations are observed for CuPor(CHO) and NiPor$(CN)_2$ as compared to CuTPP which may be due to the presence of four *t*-butyl-phenoxide groups on the *meso* positions of the macrocycle. The second oxidations of CuPor(CHO) and NiPor$(CN)_2$ are irreversible as seen in Figure 7-2 and this may be due to a chemical reaction of the four *meso*-phenoxide groups or the generation of the isoporphyrin after the first oxidation. Similar differences exist between the free-base compounds H_2TPP and H_2Por$(CN)_2$ as seen in Figure 7-3.

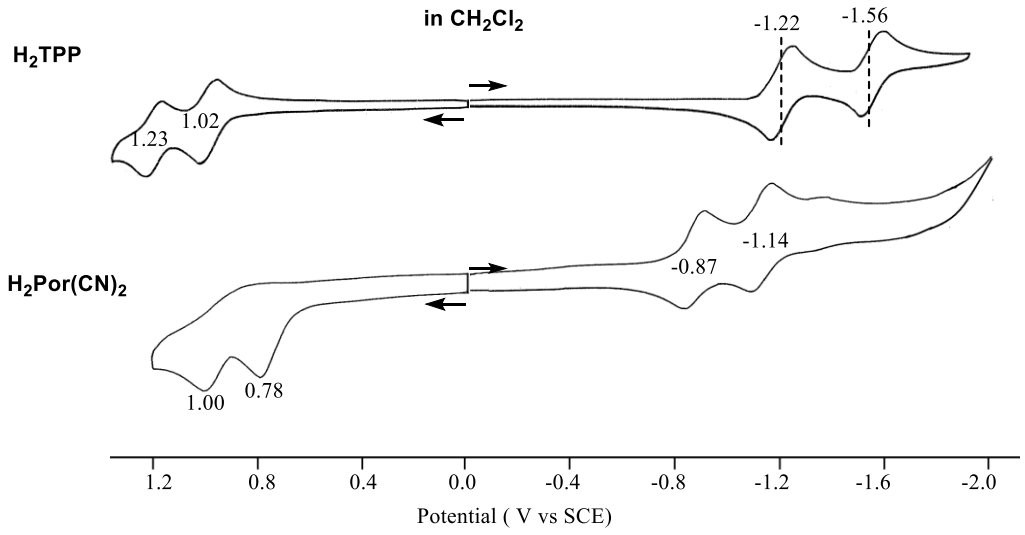

Figure 7-3. Cyclic voltammograms of H_2TPP and H_2Por$(CN)_2$ in CH_2Cl_2, containing 0.1M TBAP. Scan rate = 100 mV/s.

7.2.2 Electrochemistry of Group II Dicyanovinyl Substituted Porphyrin

The electrochemistry of the four β-dicyanovinyl substituted nickel and free base porphyrins were characterized by cyclic voltammetry. An example of the reductions for NiTPP$(CN)_2$ and NiOPP$(CN)_2$ as compared to their parent compounds NiTPP and NiOPP in CH_2Cl_2 containing 0.1M TBAP is shown in Figure 7-4.

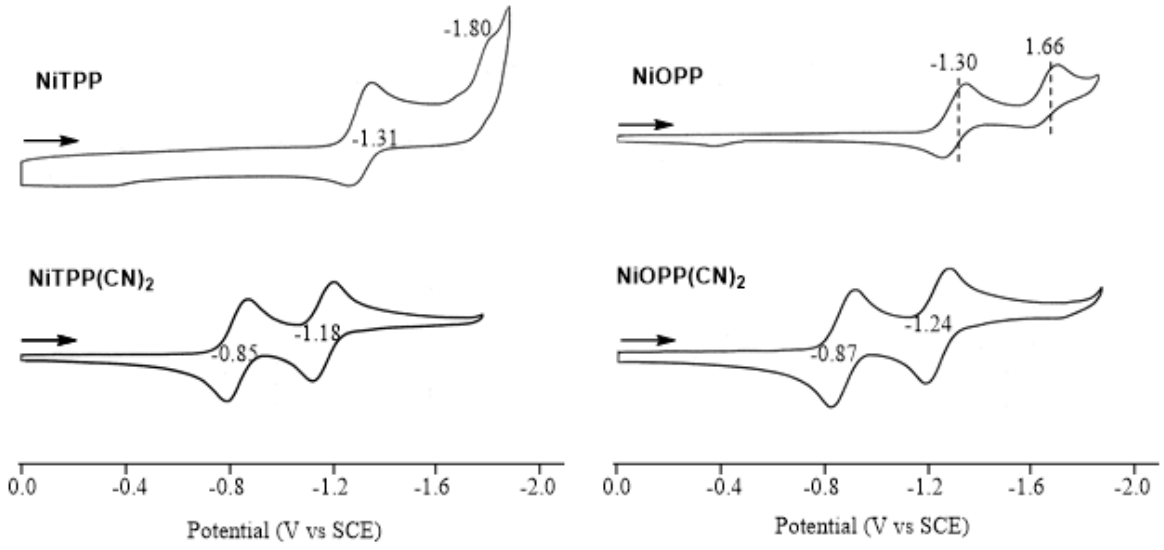

Figure 7-4. Comparison of cyclic voltammograms for $NiTPP(CN)_2$, $NiOPP(CN)_2$ with NiTPP and NiOPP in CH_2Cl_2, containing 0.1M TBAP. Scan rate = 100 mV/s.

As shown in Figure 7-4, by adding electron-withdrawing dicyanovinyl substituent on the β-position of the macrocycle, a positive shift of 460 mV are observed for the first reduction of $NiTPP(CN)_2$ as compared to NiTPP. An even bigger positive shift of aound 600 mV is observed for the second reduction for $NiTPP(CN)_2$. This is also the case for NiOPP and $NiOPP(CN)_2$ where a positive shift of 430 mV and 420 mV is observed for the first and second reduction, respectively. The two reduction potentials for $NiTPP(CN)_2$ ($E_{1/2}$ = -0.85 and -1.18 V) are very similar to those for $NiPor(CN)_2$ ($E_{1/2}$ = -0.92 and -1.27 V) with a slightly positive shift of 70-90 mV which also proves that the four t-butyl-phenoxide groups do not effect the reduction potentials significantly (as shown in Figure 7-5). This is also the case for the free base porphyrins. Examples of cyclic voltammograms for NiPor(CHO), $NiPor(CN)_2$, $NiTPP(CN)_2$, and $NiOPP(CN)_2$ and a comparison of electrochemical behavior for compounds $H_2Por(CN)_2$, $H_2TPP(CN)_2$, and $H_2OPP(CN)_2$ in

CH_2Cl_2 is shown Figure 7-5 and Figure 7-6). The measured and literature reported half-wave or peak potentials for investigated compounds in CH_2Cl_2 are summarized in Table 7-1. The literature reported potentials are measured in CH_2Cl_2 containing 0.1M $TBAPF_6$ versus Ag/AgCl and has been converted to SCE as listed in Table 7-1.

Table 7-1. Measured and reported half-wave potentials or peak potentials (V vs SCE) of investigated compounds in CH_2Cl_2 containing 0.1 M TBAP/$TBAPF_6$. Scan rate = 100 mV/s

Compounds	**Ox (V vs SCE)**			**Red (V vs SCE)**		**Ref**
	3rd	2nd	1st	1st	2nd	
NiPor(CHO)			0.98[b]	-1.14	-1.57	tw.
			0.98	-1.14	-1.28	[67]
CuPor(CHO)		1.14[b]	0.82	-1.17	-1.54	tw.
		1.20	0.87	-1.18	-1.55	[67]
$NiPor(CN)_2$		1.02[b]	0.89[b]	-0.92	-1.27	tw.
			1.02	-0.93	-1.12	[67]
$CuPor(CN)_2$		1.14[b]	0.85	-0.96	-1.30	tw.
		1.29	0.91	-0.94	-1.26	[67]
$H_2Por(CN)_2$		1.00[b]	0.78[b]	-0.87	-1.14	tw.
			1.03	-0.84		[67]
$NiTPP(CN)_2$	1.82	1.18	1.18	-0.87	-1.21	tw.
	1.94	1.37	1.20	-0.84	-1.18	[146]
$H_2TPP(CN)_2$		1.27	1.13	-0.78	-1.06	tw.
		1.44	1.20	-0.73	-1.00	[146]
$NiOPP(CN)_2$	1.73	1.06	1.06	-0.86	-1.22	tw.
	1.85	1.26	1.08	-0.84	-1.21	[146]
$H_2OPP(CN)_2$	1.50[b]		0.94[b]	-0.83	-1.07	tw.
			1.07	-0.79	-1.04	[146]

[a.] Overlapped process
[b.] Irreversible process

The difference in the supporting electrolyte will have an influence on the redox behavior. Changing from TBAP to $TBAPF_6$ typically results in the more separated two ring-centered oxidations of Ni porphyrins which parallels to what we observed compared to the literature reported potentials as listed in Table 7-1. Two split oxidations of $NiTPP(CN)_2$ ($E_{1/2}$ = 1.20 and 1.37 V) and $NiOPP(CN)_2$ ($E_{1/2}$ = 1.08 and 1.26 V) are observed with the supporting electrolyte of

$TBAPF_6$ while with the supporting electrolyte of TBAP, two overlapped oxidations are observed at $E_{1/2}$ = 1.18, 1.06 V, respectively. The third metal centered reversible oxidations of $NiTPP(CN)_2$ and $NiOPP(CN)_2$ measured by us ($E_{1/2}$ = 1.82, 1.73 V) are both 120 mV easier compared to the ones reported by Dr. Sankar's laboratory ($E_{1/2}$ = 1.94, 1.85 V) while almost identical reduction potentials are seen by us as compared to the reported ones. This is the also the case for $H_2TPP(CN)_2$ and $H_2OPP(CN)_2$. However, it is worthy of notice that the oxidation behavior for $H_2OPP(CN)_2$ observed by us is different with what was reported before. Two irreversible oxidations located at E_{pa} = 0.94 and 1.50 V are observed while a reversible oxidation located at $E_{1/2}$ = 1.07 V is reported in the literature. The irreversibility of the oxidations for $H_2OPP(CN)_2$ seen by us is the result of the chemical reactions following the generation of $H_2OPP(CN)_2$ cation in solution.

In the case of Group I porphyrins, almost identical first reduction behavior is observed by us as compared to what has been reported with small potential differences of up to 30 mV which is within the error range since the electrochemical measurements are carried out under different solution conditions utilizing different instruments. However, the second reduction for NiPor(CHO) and $NiPor(CN)_2$ reported by us ($E_{1/2}$ = -1.57, -1.27 V) is 290 and 150 mV negatively shifted as compared to the literature reported ones ($E_{1/2}$ = -1.28, -1.12 V). This is not the case for CuPor(CHO) and $CuPor(CN)_2$. The second ring-centered reduction of $H_2Por(CN)_2$ is observed by us located at $E_{1/2}$ = -1.14 V which was not reported in the literature as seen in Table 7-1. The reversibility and potentials of oxidations for Group I compounds measured by us is different from what was reported. For example, the oxidation of NiPor(CHO) measured by us is irreversible (E_{pa} = 0.98 V) while a reversible oxidation located at $E_{1/2}$ = 0.98 V is reported. The difference in the reversibility and potentials for oxidations of Group I compounds may due to the different solution conditions used

by two different labs. Chemical reactions may take place between the generated cations or dications and reagents in solution.

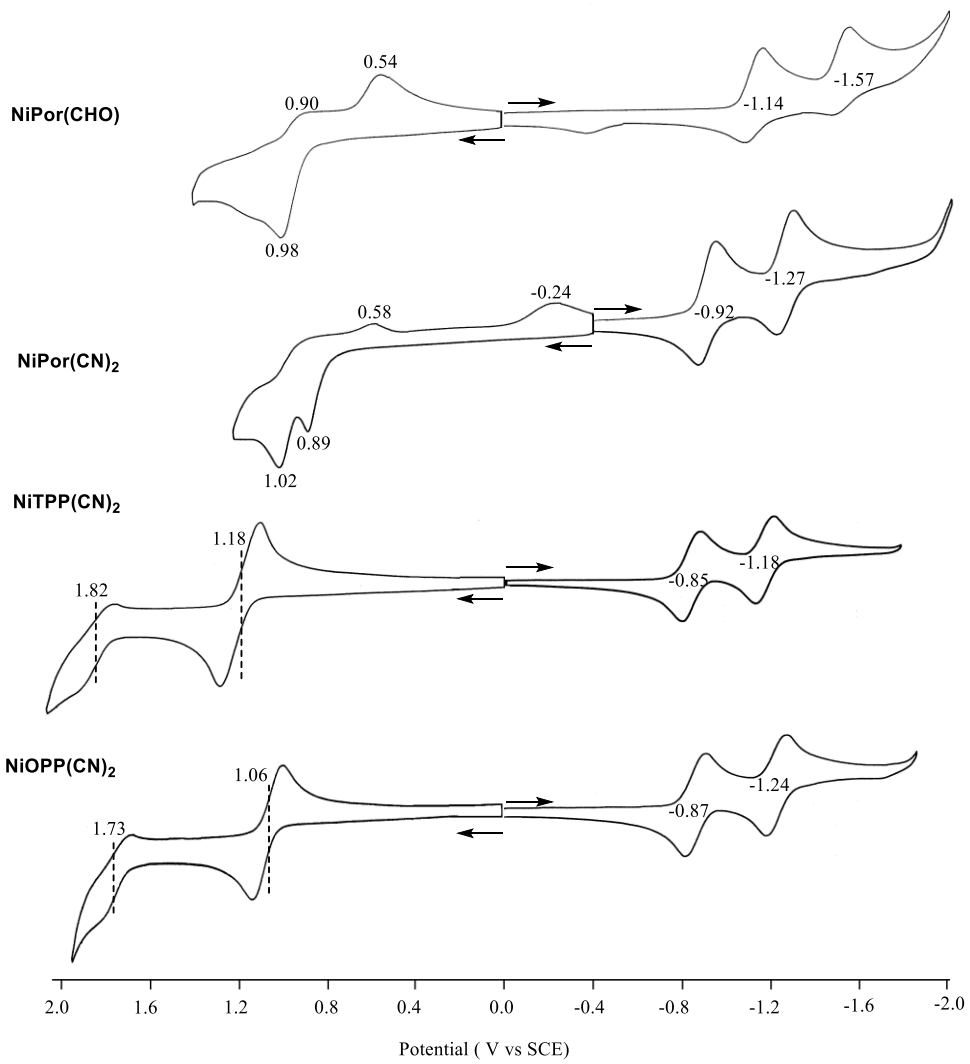

Figure 7-5. Cyclic voltammograms of NiPor(CHO), NiPor(CN)$_2$, NiTPP(CN)$_2$, and NiOPP(CN)$_2$ in CH_2Cl_2, containing 0.1M TBAP. Scan rate = 100 mV/s.

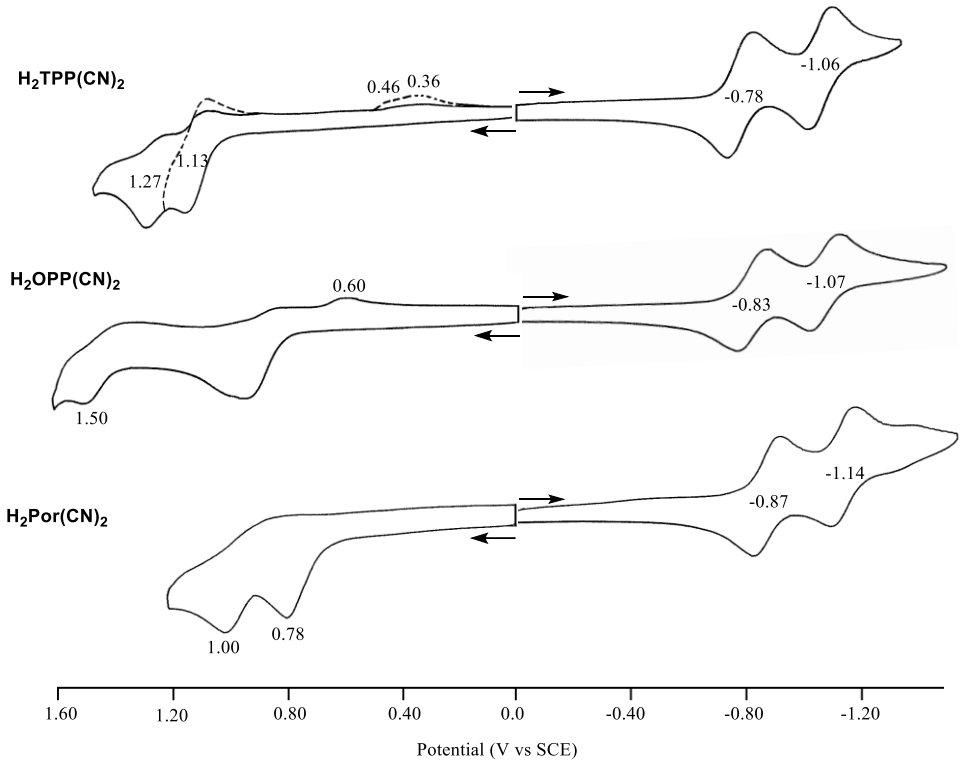

Figure 7-6. Cyclic voltammograms for $H_2TPP(CN)_2$, $H_2OPP(CN)_2$ and $H_2Por(CN)_2$ in CH_2Cl_2, containing 0.1M TBAP. Scan rate = 100 mV/s.

The electrochemical properties of each porphyrin in Group II were not only examined in CH_2Cl_2 but also in PhCN and THF containing 0.1M TBAP. A summary of the half-wave and peak potentials for $NiTPP(CN)_2$ and $NiOPP(CN)_2$ are shown in Table 7-2. The donor number of three solvents is also listed as seen in the table.

The first two reductions and three oxidations of $NiTPP(CN)_2$ and $NiOPP(CN)_2$ are reversible or quasireversible in the three solvents as seen in Table 7-2. The first reductions are located at almost identical half-wave potentials in PhCN and THF except for $H_2TPP(CN)_2$ ($E_{1/2}$ = -0.69 V in THF, $E_{1/2}$ = -0.77 V in PhCN) but are shifted positively from the $E_{1/2}$ values in CH_2Cl_2 which is related to the smaller donor number of CH_2Cl_2 as compared to PhCN and THF. Very little

difference is seen in potential for the second reduction where $E_{1/2}$ varies no more than 30 mV for $NiTPP(CN)_2$, $NiOPP(CN)_2$ and $H_2TPP(CN)_2$ with change of solvents. However, for $H_2OPP(CN)_2$, the second reduction is negatively shifted by 80 mV for PhCN ($E_{1/2}$ = -1.08 V) as compared to THF ($E_{1/2}$ = -1.00 V). The first two oxidations of $NiTPP(CN)_2$ and $NiOPP(CN)_2$ are totally overlapped in CH_2Cl_2 and PhCN but not in THF where separate one-electron transfers are seen which may due to the less polarity of THF as compared to PhCN and CH_2Cl_2.

Half-wave potentials of compounds $NiTPP(CN)_2$, $NiOPP(CN)_2$, $H_2TPP(CN)_2$, and $H_2OPP(CN)_2$ are plotted versus Gutman donor number in order to see the solvent effect on the electrochemical behavior. A linear relationship is seen for the first, second reductions as well as the first oxidation of $NiTPP(CN)_2$ as shown in Figure 7-6. No such linear relationships are seen for $NiOPP(CN)_2$, $H_2TPP(CN)_2$, and $H_2OPP(CN)_2$.

Table 7-2. Half-Wave Potentials or peak potentials (V vs SCE) of $MTPP(CN)_2$ and $MOPP(CN)_2$, M = 2H, Ni in CH_2Cl_2, THF, PhCN containing 0.1 M TBAP. Scan rate = 100 mV/s

Solvent	DN[c]	Compounds	Ox (V vs SCE)			Red (V vs SCE)		
			3rd	2nd	1st	1st	2nd	3rd
DCM	1.0	$NiTPP(CN)_2$	1.82	1.18	1.18	-0.87	-1.21	
		$NiOPP(CN)_2$	1.73	1.06	1.06	-0.86	-1.22	
		$H_2TPP(CN)_2$		1.27	1.13	-0.78	-1.06	
		$H_2OPP(CN)_2$		1.50[a]	0.94[a]	-0.83	-1.07	
PhCN	11.9	$NiTPP(CN)_2$	1.74	1.02	1.02	-0.80	-1.20	
		$NiOPP(CN)_2$	1.85	1.19	1.19	-0.78	-1.20	
		$H_2TPP(CN)_2$		1.42[a]	0.94[a]	-0.77	-1.06	
		$H_2OPP(CN)_2$		1.30	1.13	-0.73	-1.08	
THF	20.0	$NiTPP(CN)_2$		1.04	0.91	-0.77	-1.18	-2.02[a]
		$NiOPP(CN)_2$		1.11	1.11	-0.79	-1.23	-2.00[a]
		$H_2TPP(CN)_2$		1.52[a]	1.30[a]	-0.69	-1.03	-1.92
		$H_2OPP(CN)_2$		1.44[a]	1.00[a]	-0.73	-1.00	-1.86[a]

[a]. Irreversible process
[c]. Gutman donor number[71]

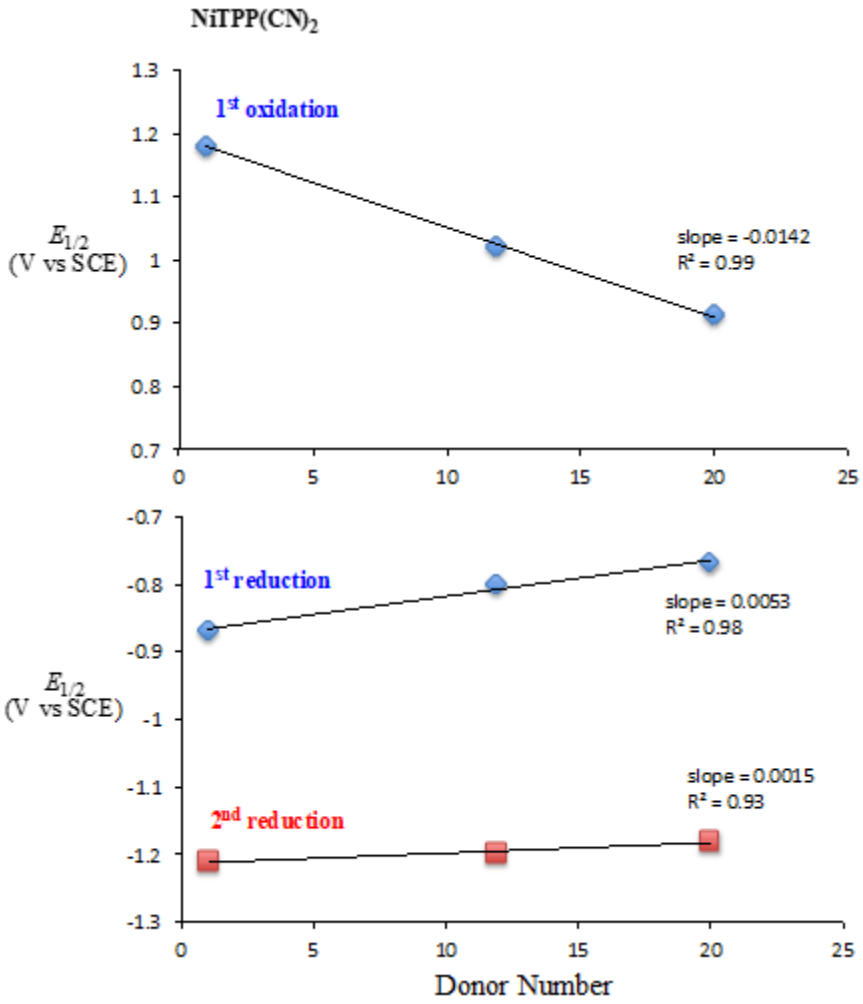

Figure 7-7. Plot of half-wave potentials for $NiTPP(CN)_2$ vs. gutman donor number.

7.2.3 Spectroelectrochemistry of Investigated Compounds

In order to investigate the site of electron transfer in the first reduction of Group II compounds, the same electrode reactions were carried out in the thin-layer cell and the spectral changes obtained during electron addition were recorded as shown in Figure 7-8.

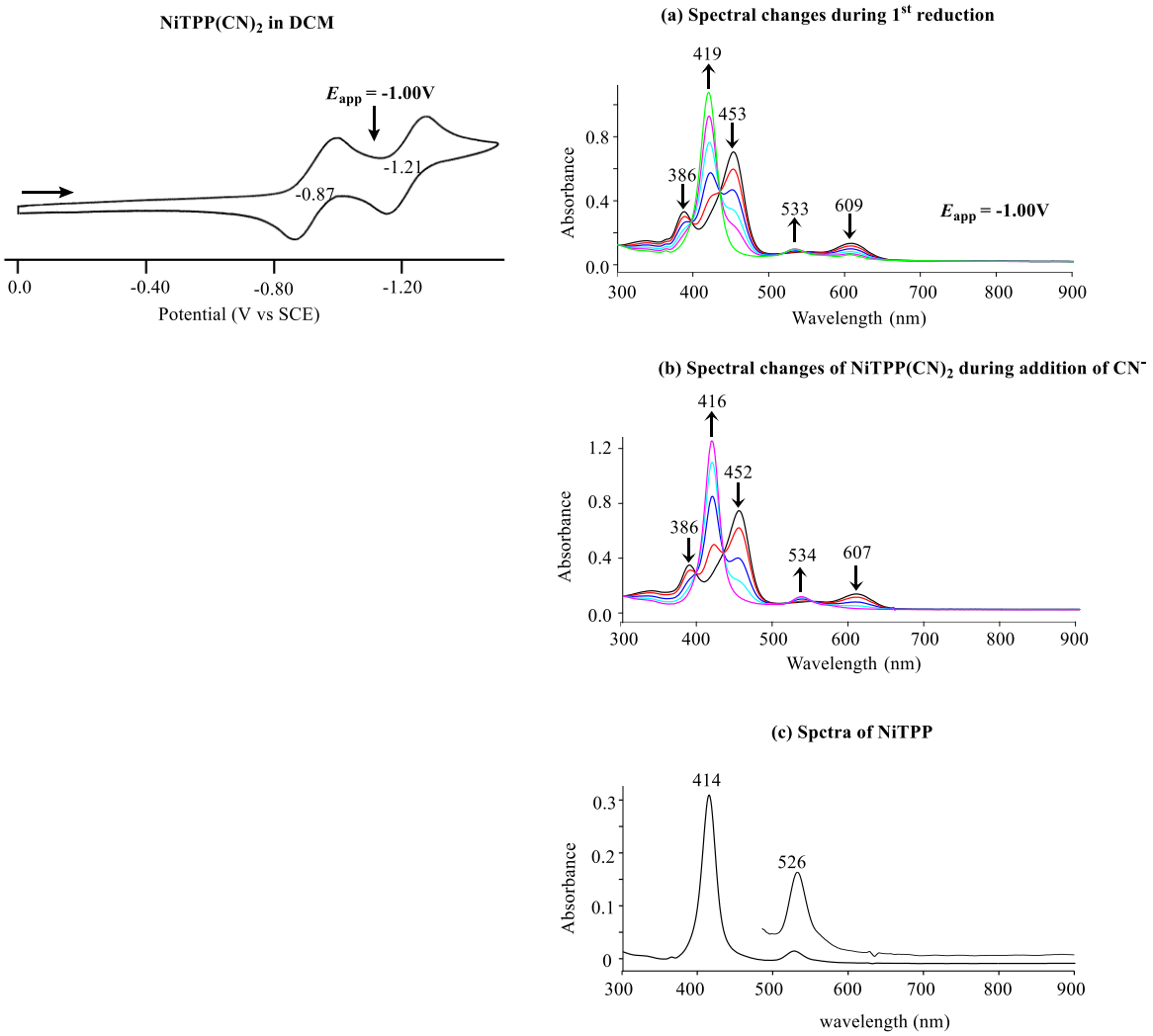

Figure 7-8. Spectral changes during (a) the first reduction of $NiTPP(CN)_2$ and (b) the spectral titration of $NiTPP(CN)_2$ with CN^- (c) the spectra of NiTPP in CH_2Cl_2 containing 0.1M TBAP.

As seen in the figure, after applying a reduced potential at -1.00V, a strong and new soret band at 419 nm appears while the original 453 nm Soret band disappears. This type of changes is not typically observed for ring-centered reductions but looks more like a metal-centered electro-reduction. However, a Ni^{II}/Ni^{I} reaction has never been reported or suggested for these types of nickel porphyrins with TPP skeletal structures and thus, we might consider the possibility that the

first reduction might occur at the dicyanovinyl group. If this were the case, the spectra of the porphyrins species generated after the first reduction might resemble spectrally and electrochemically the neutral reference compounds NiTPP and NiOPP and this seems to be the case as shown by the data in Figure 7-4. For example, the half-wave potential for the second reduction of $NiTPP(CN)_2$ at -1.18 V in CH_2Cl_2 is not so different from the $E_{1/2}$ for the first reduction of NiTPP in the same solvent (-1.31 V).

Spectral changes during the titration of $NiTPP(CN)_2$ with TBACN in CH_2Cl_2 are also monitered as shown in Figure 7-8(b). With the addition of CN^- group to the double bond[149] in the dicyanovinyl substituent, a new and intense Soret band located at 416 nm appears while the original soret band located at 452nm disappears. Almost identical spectral changes are observed during the titration with CN^- as compared to the spectral changes seen during the first reduction which further proves that the first electron addition takes place on the double bond in the β-dicyanovinyl group. The final spectra after the first electron addition step and the CN^- addition step are very similar to the NiTPP which further proves that the first reduction might occur at the dicyanovinyl group. Similar behavior is observed for $NiOPP(CN)_2$, $H_2TPP(CN)_2$, and $H_2OPP(CN)_2$. An example of the spectral changes for $NiOPP(CN)_2$ during the first reduction and the CN^- titration is shown in Figure 7-9.

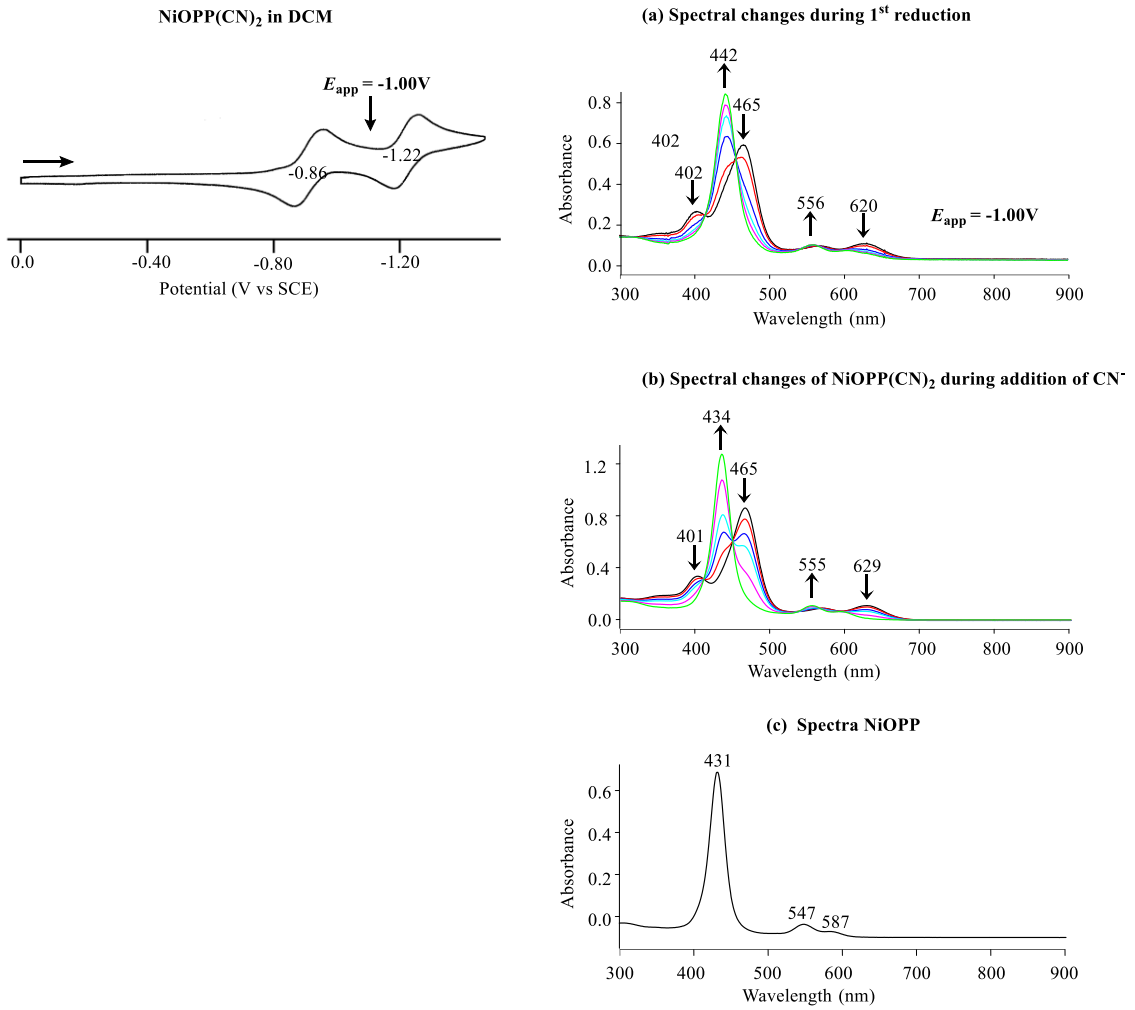

Figure 7-9. Spectral changes during (a) the first reduction of $NiOPP(CN)_2$ and (b) the spectral titration of $NiOPP(CN)_2$ with CN^- (c) UV-visible spectra of NiOPP in CH_2Cl_2 containing 0.1M TBAP.

7.2.4 Porpho-5,15-bis-Paraquinone Methide Generation in Basic Solutions

As described ealier in Chapter three, porphyrins with *meso*-*t*-butyl-hydroxyphenyl groups are known to react with base and generate porpho-5,15-bis-paraquinone methide compounds. Cyclic voltammograms of the first and second reductions of $NiPor(CN)_2$ titrated with up to 4.0 eq. TBAOH in CH_2Cl_2, containing 0.1M $TBAPF_6$ are shown in Figure 7-10.

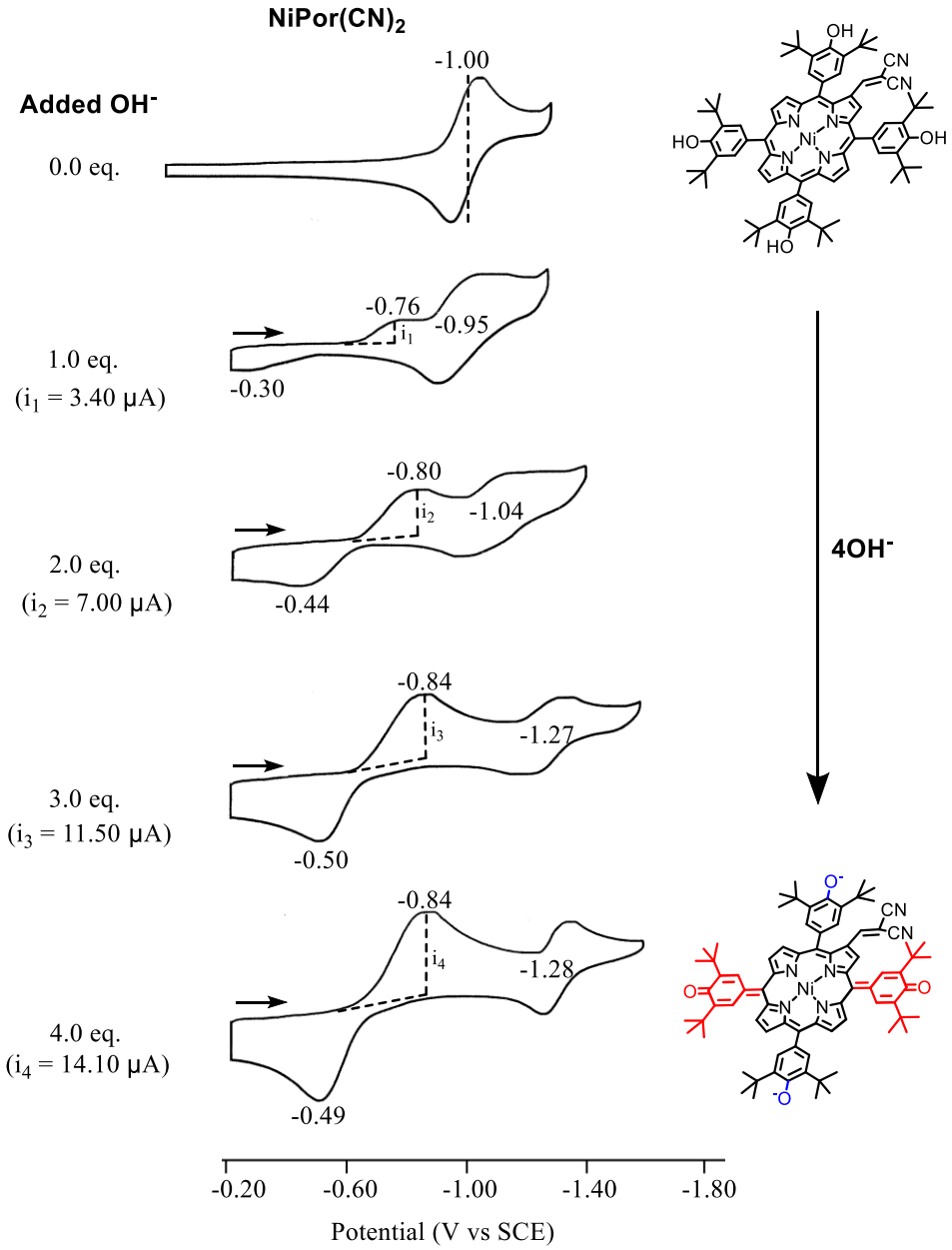

Figure 7-10. Cyclic voltammograms of the first and second reductions of $NiPor(CN)_2$ titrated with up to 4.0 eq. TBAOH in CH_2Cl_2, containing 0.1M $TBAPF_6$. Scan rate = 100 mV/s.

As seen in Figure 7-10, by adding 1.0 eq. of OH^- to solution, a new reduction peak starts to appear at E_{pc} = -0.80 V . The shape and position of this reduction peak resembles what was ealier observed for NiPor. $NiPorCl_8$ and $NiPorBr_8$ when titrated with TBAOH. As a result, porpho-5,15-

bis-paraquinone methide is also generated for NiPor$(CN)_2$ compound with added base. The reduction process located at E_{pc} = -0.84 V and the reoxidation process located at E_{pa} = -0.50 V with 4.0 eq. of added base corresponds to the electrochemical interconversion between the generated porpho-5,15-bis-paraquinone methide and reduced porphyrin. With more and more OH^- added to solution, the peak current for this reaction gets higher. By measuring the peak current height for the first reduction process, it is clear that the current height for the NiPor$(CN)_2$ with 4.0 eq. of OH^- is four times of the NiPor$(CN)_2$ with 1.0 eq. of OH^- which proves that with more and more OH^- added to the solution, the amount of generated porpho-5,15-bis-paraquinone methide increases.

Figure 7-11 shows the cyclic voltammograms of NiPor$(CN)_2$ titrated with more than 4 eq. of TBAOH in CH_2Cl_2, containing 0.1M $TBAPF_6$. Two examples of cyclic voltammograms are shown in this figure. With 20 eq. of added OH^-, the peak potential for the first quasireversible reduction process is positively shifted by 20 mV while the second reversible reduction potential is positively shifted by 40 mV as compared to 4.0 eq. of added base. When 300 eq. of OH^- is added to the solution, the peak potential for the first quasireversible reduction process is further positively shifted by 150 mV while the second reversible reduction potential is positively shifted by 100 mV which indicate that the excess base in solution attacks the double bond in the dicyanovinyl substituent. The proposed product structure is shown in Figure 7-11. With the halfly reduced double bond in the dicyanovinyl group for NiPor$(CN)_2$, easier electron additions are observed.

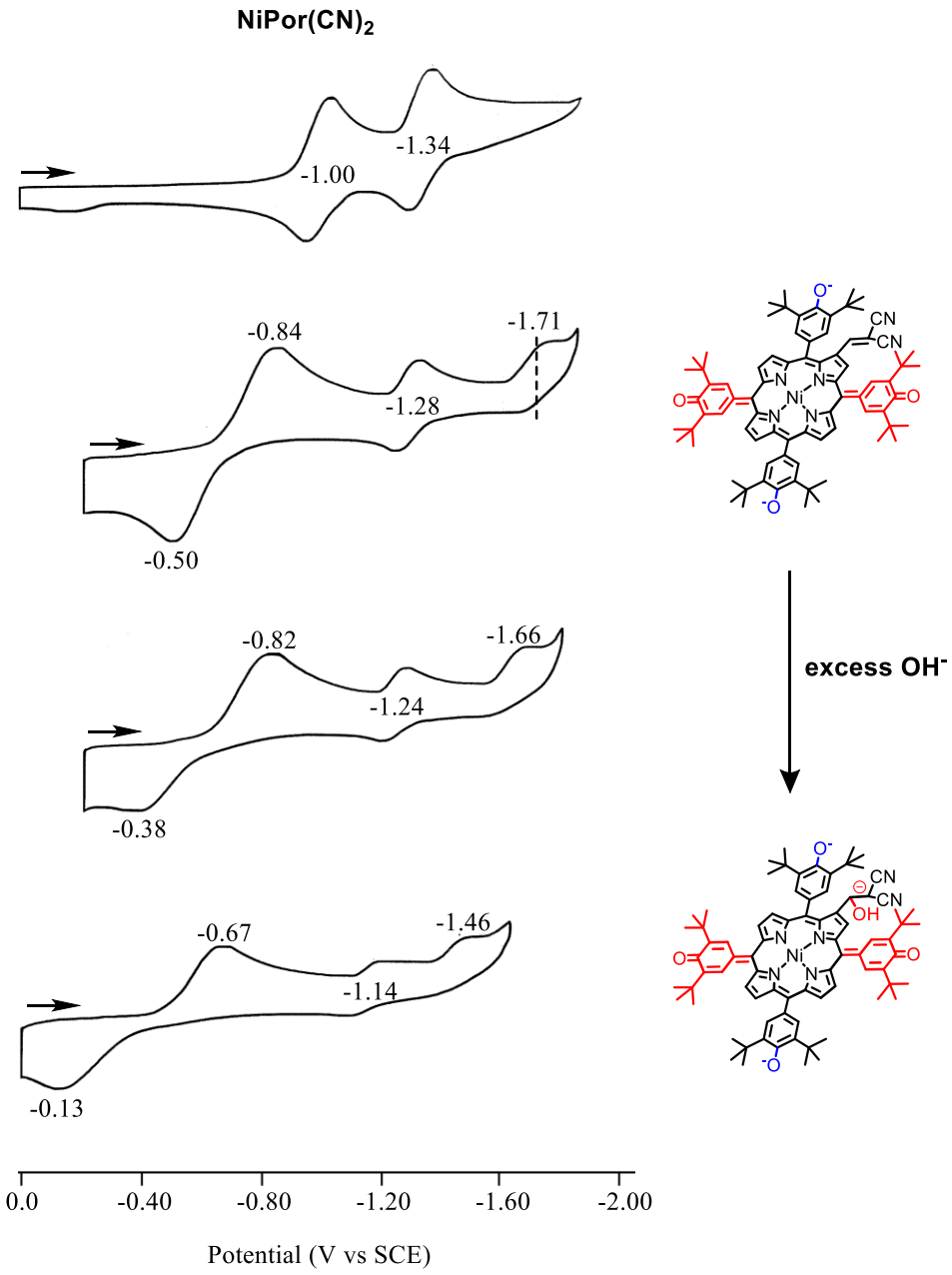

Figure 7-11. Cyclic voltammograms of NiPor(CN)$_2$ titrated with TBAOH in CH_2Cl_2, containing 0.1M $TBAPF_6$. Scan rate = 100 mV/s.

7.3 Conclusions

In summary, the electrochemistry, spectroelectrochemistry of two groups of differently substituted porphyrins are discussed in this chapter. The redox potentials for porphyrins were 'tuned' by adding different electron-withdrawing or donating groups to the meso- or β-position of the porphyrin macrocycle. With electron-withdrawing substituents such as –CHO, -CH=$(CN)_2$, the reduction potentials are positively shifted by ~160 mV and ~400 mV respectively. Solvent effect on the electrochemical behavior was also investigated. The site of electron-transfer of the reduction process can also be changed with the addition of substituent. The first electron addition of NiTPP$(CN)_2$, NiOPP$(CN)_2$ as well as H_2TPP$(CN)_2$, H_2OPP$(CN)_2$ takes place on the double bond in the β-dicyanovinyl substituent or takes place on the ring and then transferred to the β-dicyanovinyl substituent which is proved both electrochemically and spectroelectrochemically. The generation of porpho-5,15-bis-paraquinone methide is also observed for NiPor$(CN)_2$ compound with added base as ealier described in Chapter Three. The reduction process located at E_{pc} = -0.84 V and the reoxidation process located at E_{pa} = -0.50 V with 4.0 eq. of added base corresponds to the electrochemical interconversion between the chemically generated porpho-5,15-bis-paraquinone methide and reduced porphyrin.

Bibliography

1. Kadish, K. M.; Van Caemelbecke, E.; Royal, G., Electrochemistry of metalloporphyrins in non-aqueous media. In *The Porphyrin Handbook*, Kadish, K. M.; Smith, K. M.; Guilard, R., Eds. Academic Press: New York, 2000; Vol. 8, pp 1-144.

2. Kadish, K. M., The electrochemistry of metalloporphyrins in nonaquaous media. In *The Electrochemistry of Metalloporphyrins in Nonaquaous Media*, John Wiley & Sons, Inc.: 1986; Vol. 34, pp 435-605.

3. Kadish, K. M.; Morrison, M. M., Substituent effects on the redox reactions of tetraphenylporphyrins. *Bioinorg. Chem.* **1977,** *7*, 107-15.

4. Ke, X.; Yadav, P.; Cong, L.; Kumar, R.; Sankar, M.; Kadish, K. M., Facile and reversible electrogeneration of porphyrin trianions and tetraanions in nonaqueous media. *Inorg. Chem.* **2017,** *56*, 8527-8537.

5. Kadish, K. M.; Van Caemelbecke, E.; Boulas, P.; D'Souza, F.; Vogel, E.; Kisters, M.; Medforth, C. J.; Smith, K. M., First reversible electrogeneration of triply oxidized nickel porphyrins and porphycenes. Formation of nickel(III) π dications. *Inorg. Chem.* **1993,** *32*, 4177-8.

6. Bhyrappa, P.; Sankar, M.; Varghese, B., Mixed substituted porphyrins: structural and electrochemical redox properties. *Inorg. Chem.* **2006,** *45*, 4136-4149.

7. Kadish, K. M.; Lin, M.; Van Caemelbecke, E.; De Stefano, G.; Medforth, C. J.; Nurco, D. J.; Nelson, N. Y.; Krattinger, B.; Muzzi, C. M.; Jaquinod, L.; Xu, Y.; Shyr, D. C.; Smith, K. M.; Shelnutt, J. A., Influence of electronic and structural effects on the oxidative behavior of nickel porphyrins. *Inorg. Chem.* **2002,** *41*, 6673-6687.

8. Ye, L.; Fang, Y.; Ou, Z.; Xue, S.; Kadish, K. M., Cobalt tetrabutano- and tetrabenzotetraarylporphyrin complexes: effect of substituents on the electrochemical properties and catalytic activity of oxygen reduction reactions. *Inorg. Chem* **2017,** *56*, 13613-13626.

9. Ye, L.; Fang, Y.; Ou, Z.; Xue, S.; Wang, L.; Kadish, K. M., Electrochemistry of N-confused inner amino-substituted free-base tetraarylporphyrins in nonaqueous media. *J. Porphyrins Phthalocyanines* **2018,** *22*, 908-917.

10. Xue, S.; Ou, Z.; Ye, L.; Lu, G.; Fang, Y.; Jiang, X.; Kadish, K. M., Effect of solvent and protonation/deprotonation on electrochemistry, spectroelectrochemistry and electron-transfer mechanisms of N-confused tetraarylporphyrins in nonaqueous media. *Chem. - Eur. J.* **2015,** *21*, 2651-2661.

11. Cong, L.; Chahal, M. K.; Osterloh, R.; Sankar, M.; Kadish, K. M., Synthesis, electrochemistry, and reversible interconversion among perhalogenated hydroxyphenyl Ni(II) porphyrins, porphodimethenes, and porpho-5,15-bis-paraquinone methide. *Inorganic Chemistry* **2019,** *58*, 14361-14376.

12. Ke, X.; Kumar, R.; Sankar, M.; Kadish, K. M., Electrochemistry and spectroelectrochemistry of cobalt porphyrins with π-extending and/or highly electron-withdrawing pyrrole substituents. In situ electrogeneration of σ-bonded complexes. *Inorg. Chem.* **2018,** *57*, 1490-1503.

13. D'Souza, F.; Villard, A.; Van Caemelbecke, E.; Franzen, M.; Boschi, T.; Tagliatesta, P.; Kadish, K. M., Electrochemical and spectroelectrochemical behavior of cobalt(III), cobalt(II), and cobalt(I) complexes of meso-tetraphenylporphyrinate bearing bromides on the β-pyrrole positions. *Inorg. Chem.* **1993,** *32*, 4042-8.

14. Kadish, K. M.; Tabard, A.; Lee, W.; Liu, Y. H.; Ratti, C.; Guilard, R., Effect of pyridine binding and spin state on spectroscopic and electrochemical properties of phenyl- and (perfluorophenyl)iron(III) porphyrins. *Inorg. Chem.* **1991,** *30*, 1542-9.

15. Kadish, K. M.; Morrison, M. M.; Constant, L. A.; Dickens, L.; Davis, D. G., A study of solvent and substituent effects on the redox potentials and electron-transfer rate constants of substituted iron meso-tetraphenylporphyrins. *J. Am. Chem. Soc.* **1976,** *98*, 8387-90.

16. Fang, Y.; Wang, L.; Xu, W.; Ou, Z.; Chen, M.; Cong, L.; Shan, W.; Ke, X.; Kadish, K. M., Spectral, electrochemical, and ESR characterization of manganese tetraarylporphyrins containing four *β*,*β*'-pyrrole fused butano and benzo groups in nonaqueous media. *Inorg. Chem.* **2019,** *58*, 2576-2587.

17. Bottomley, L. A.; Kadish, K. M., Solvent and ligation effects on the electroreduction of chromium porphyrins. *Inorg. Chem.* **1983,** *22*, 342-9.

18. Kadish, K. M.; Mu, X., Spectroelectrochemistry of metalloporphyrins. *Pure Appl. Chem.* **1990,** *62*, 1051-1054.

19. Fang, Y.; Bhyrappa, P.; Ou, Z.; Kadish, K. M., Planar and nonplanar free-base tetraarylporphyrins: *β*-pyrrole substituents and geometric effects on electrochemistry, spectroelectrochemistry, and protonation/deprotonation reactions in nonaqueous media. *Chem. Eur. J.* **2014,** *20*, 524-532.

20. Meunier, B. R., A.; Pratviel, G.; Bernadou, J., Metalloporphyrins in catalytic oxidations and oxidative DNA cleavage. In *The Porphyrin Handbook*, Kadish, K. M., Smith, K. M., Guilard, R., Ed. Academic Press: 2000; Vol. 4, pp 119-187.

21. Mansuy, D.; Battioni, P., Diversity of reactions catalyzed by heme-thiolate proteins. In *The Porphyrin Handbook*, Kadish, K. M., Smith, K. M., Guilard, R., Ed. Academic Press: 2000; Vol. 4, pp 1-15.

22. Pandey, R.; Zheng, G., Applications: past, present and future. In *The Porphyrin Handbook*, Kadish, K. M.; Smith, K. M.; Guilard, R., Eds. Academic Press: San Diego, 2000; Vol. 6, pp 158-225.

23. Pandey, R. K.; Zheng, G., Porphyrins as photosensitizers in photodynamic therapy. In *The Porphyrin Handbook*, Kadish, K. M., Smith, K. M., Guilard, R., Ed. Academic Press: 2000; Vol. 6, pp 154-230.

24. Webb, L. E.; Fleischer, E. B., Structure of porphine. *J. Am. Chem. Soc.* **1965,** *87*, 667-669.

25. Gouterman, M., Spectra of porphyrins. *J. Mol. Spectrosc* **1961,** *6*, 138-163.

26. Chaudhri, N.; Cong, L.; Grover, N.; Shan, W.; Anshul, K.; Sankar, M.; Kadish, K. M., Synthesis and electrochemical characterization of acetylacetone (acac) and ethyl acetate (EA) appended *β*-trisubstituted push-pull porphyrins: formation of electronically communicating porphyrin dimers. *Inorg. Chem.* **2018,** *57*, 13213-13224.

27. de Oliveira, K. T.; Momo, P. B.; de Assis, F. F.; Ferreira, M. A. B.; Brocksom, T. J., Chlorins: Natural Sources, Synthetic Developments and Main Applications. *Curr. Org. Synth.* **2014,** *11*, 42-58.

28. Taniguchi, M.; Lindsey, J. S., Synthetic chlorins, possible surrogates for chlorophylls, prepared by derivatization of porphyrins. *Chem. Rev.* **2017,** *117*, 344-535.

29. Chang, D.; Malinski, T.; Ulman, A.; Kadish, K. M., Electrochemistry of nickel(II) porphyrins and chlorins. *Inorg. Chem.* **1984,** *23*, 817-824.

30. Chaudhri, N.; Grover, N.; Sankar, M., Selective conversion of planar trans-chlorins into highly twisted doubly fused porphyrins or chlorins via oxidative fusion. *Inorg. Chem.* **2018,** *57*, 6658-6668.

31. Boyle, R. W.; Dolphin, D., 5,15-Diphenyl-7-oxobenzochlorins. Novel long-wavelength absorbing photosensitizers for photodynamic therapy. *J. Chem. Soc., Chem. Commun.* **1994**, 2463-2464.

32. Grover, N.; Chaudhri, N.; Sankar, M., Facile conversion of Ni(II) cyclopropylchlorins into novel *β*-substituted porphyrins through acid-catalyzed ring-opening reaction. *Inorg. Chem.* **2017,** *56*, 424-437.

33. Chaudhri, N.; Grover, N.; Sankar, M., Versatile synthetic route for *β*-functionalized chlorins and porphyrins by varying the size of michael donors: syntheses, photophysical, and electrochemical redox properties. *Inorg. Chem.* **2017,** *56*, 11532-11545.

34. Fukuzumi, S.; Ohkubo, K.; Imahori, H.; Shao, J.; Ou, Z.; Zheng, G.; Chen, Y.; Pandey, R. K.; Fujitsuka, M.; Ito, O.; Kadish, K. M., Photochemical and electrochemical properties of zinc chlorin−C_{60} dyad as compared to corresponding free-base chlorin−C_{60}, free-base porphyrin−C_{60}, and zinc porphyrin−C_{60} dyads. *J. Am. Chem. Soc.* **2001,** *123*, 10676-10683.

35. Novakova, V.; Donzello, M. P.; Ercolani, C.; Zimcik, P.; Stuzhin, P. A., Tetrapyrazinoporphyrazines and their metal derivatives. Part II: Electronic structure, electrochemical, spectral, photophysical and other application related properties. *Coord. Chem. Rev.* **2018,** *361,* 1-73.

36. Shao, J.; Commodore, J.; Han, B.; Pruente, C.; Hansen, C. A., Electrochemical, spectroelectrochemical and ESR spectroscopic characterization of 2,3- and 3,4-cobalt tetrapyridoporphyrazine isomers in non-aqueous media. *J. Porphyrins Phthalocyanines* **2009,** *13,* 876-887.

37. Lever, A. B. P.; Milaeva, E. R.; Speier, G.; Zimcik, P.; Stuzhin, P. A., Phthalocyanines: properties and applications. Leznoff, C. C.; Lever, A. B. P., Eds. New York, 1993; Vol. 3, pp 1-70.

38. Donzello, M. P.; Viola, E.; Cai, X.; Mannina, L.; Rizzoli, C.; Ricciardi, G.; Ercolani, C.; Kadish, K. M.; Rosa, A., Tetra-2,3-pyrazinoporphyrazines with externally appended pyridine rings. 5. Synthesis, physicochemical and theoretical studies of a novel pentanuclear palladium(II) complex and related mononuclear species. *Inorg. Chem.* **2008,** *47,* 3903-3919.

39. Donzello, M. P.; Viola, E.; Ercolani, C.; Fu, Z.; Futur, D.; Kadish, K. M., Tetra-2,3-pyrazinoporphyrazines with externally appended pyridine rings. 12. New heteropentanuclear complexes carrying four exocyclic cis-platin-like functionalities as potential bimodal (PDT/cis-platin) anticancer agents. *Inorg. Chem.* **2012,** *51,* 12548-12559.

40. Donzello, M. P.; Ou, Z.; Dini, D.; Meneghetti, M.; Ercolani, C.; Kadish, K. M., Tetra-2,3-pyrazinoporphyrazines with externally appended pyridine rings. 2. Metal complexes of ttrakis-2,3-[5,6-di(2-pyridyl)pyrazino]porphyrazine: Linear and nonlinear optical properties and electrochemical behavior. *Inorg. Chem.* **2004,** *43,* 8637-8648.

41. Donzello, M. P.; Viola, E.; Cai, X.; Mannina, L.; Ercolani, C.; Kadish, K. M., Tetra-2,3-pyrazinoporphyrazines with externally appended pyridine rings. 8. Central (Zn^{II}, Cu^{II}, $Mg^{II}(H_2O)$, Cd^{II}) and exocyclic (Pd^{II}) metal ion binding in heteropentametallic complexes from tetrakis-2,3-[5,6-di(2-pyridyl)pyrazino]porphyrazine. *Inorg. Chem.* **2010,** *49,* 2447-2456.

42. Donzello, M. P.; Agostinetto, R.; Ivanova, S. S.; Fujimori, M.; Suzuki, Y.; Yoshikawa, H.; Shen, J.; Awaga, K.; Ercolani, C.; Kadish, K. M.; Stuzhin, P. A., Tetrakis(thiadiazole)porphyrazines. 4. Direct template synthesis, structure, general physicochemical behavior, and redox properties of Al^{III}, Ga^{III}, and In^{III} complexes. *Inorg. Chem.* **2005,** *44*, 8539-8551.

43. Viola, E.; Donzello, M. P.; Testani, S.; Luccisano, G.; Astolfi, M. L.; Rizzoli, C.; Cong, L.; Mannina, L.; Ercolani, C.; Kadish, K. M., Tetra-2,3-pyrazinoporphyrazines with peripherally appended pyridine rings. 19. Pentanuclear octa(2-pyridyl)tetrapyrazinoporphyrazines carrying externally carboranthiolate groups: Physicochemical properties and potentialities as anticancer drugs. *Inorg. Chem.* **2019,** *58*, 1120-1133.

44. Sciscione, F.; Cong, L.; Donzello, M. P.; Viola, E.; Ercolani, C.; Kadish, K. M., Octakis(2-pyridyl)porphyrazine and its neutral metal derivatives: UV-visible spectral, electrochemical, and potoactivity sudies. *Inorg. Chem.* **2017,** *56*, 5813-5826.

45. Saltini, G.; Cong, L.; Donzello, M. P.; Ercolani, C.; Viola, E.; Pettiti, I.; Stuzhin, P. A.; Kadish, K. M., Tetra-2,3-pyrazinoporphyrazines with peripherally appended pyridine rings. 20. Mono- and pentanuclear Al^{III} and Ga^{III} complexes: synthesis and physicochemical and photoactivity studies. *Inorg. Chem* **2019,** 58, 15269-15282.

46. Headridge, J. B., Cyclic voltammetry, chronopotentiometry and other techniques for verifying reversibility. In *Electrochemical techniques for inorganic chemistry*, Academic Press Inc.: New York, 1969; pp 44-45.

47. Chang, R., The Hill Equation. In *Physical Chemistry for the Chemical and Biological Sciences*, University Science Books: Sausalito, 2000; pp 538-539.

48. Skoog, D. A.; West, D. M.; Holler, F. J., Chemical equilibria. In *Fundamentals of Analytical Chemistry. 9th Ed*, Cengage Learning: Belmont, 2014; pp 203-204.

49. Chang, R., The Beer-Lambert Law. In *Physical Chemistry for the Chemical and Biological Sciences*, University Science Books: Sausalito, 2000; pp 710-711.

50. Wilbraham, A. C.; Staley, D. D.; Simpson, C. J.; Matta, M. S., Conservation of mass. In *Analytical Chemistry*, Addison-Wesley Publishing Company Inc.: Canada, 1993; pp 15-16.

51. Ellis, P. E., Jr.; Linard, J. E.; Szymanski, T.; Jones, R. D.; Budge, J. R.; Basolo, F., Axial ligation constants of iron(II) and cobalt(II) "capped" porphyrins. *J. Am. Chem. Soc.* **1980,** *102*, 1889-96.

52. Skoog, D. A.; West, D. M.; Holler, F. J., Introduction to electrochemistry. In *Fundamentals of Analytical Chemistry. 9th Ed*, Cengage Learning: Belmont 2014; pp 460-461.

53. Kadish, K. M., The electrochemistry of iron porphyrins in nonaqueous media. In *Physical Bioinorganic Chemistry Series: Iron Porphyrins, Part II*, Lever, A. B. P.; Gray, H. B., Eds. Addison-Wesley Publ. Co.: Massachusetts, 1983; pp 195-196.

54. Kadish, K. M., The electrochemistry of iron porphyrins in nonaqueous media. In *Physical Bioinorganic Chemistry Series: Iron Porphyrins, Part II*, Lever, A. B. P.; Gray, H. B., Eds. Addison-Wesley Publ. Co.: Massachusetts, 1983; p 203.

55. Senge, M. O., Highly substituted porphyrins. In *The Porphyrin Handbook*, Kadish, K. M. S., K. M.; Guilard, R., Ed. Academic Press: San Diego, 2000; Vol. 1, pp 239-347.

56. Medforth, C. J.; Haddad, R. E.; Muzzi, C. M.; Dooley, N. R.; Jaquinod, L.; Shyr, D. C.; Nurco, D. J.; Olmstead, M. M.; Smith, K. M.; Ma, J.-G.; Shelnutt, J. A., Unusual aryl-porphyrin rotational barriers in peripherally crowded porphyrins. *Inorg. Chem.* **2003,** *42*, 2227-2241.

57. Bhyrappa, P., Recent advances in mixed *β*-pyrrole substituted *meso*-tetraphenylporphyrins. *Tetrahedron Lett.* **2016,** *57*, 5150-5167.

58. Senge, M. O., Exercises in molecular gymnastics-bending, stretching and twisting porphyrins. *Chem. Commun.* **2006**, 243-256.

59. Haddad, R. E.; Gazeau, S.; Pécaut, J.; Marchon, J.-C.; Medforth, C. J.; Shelnutt, J. A., Origin of the red shifts in the optical absorption bands of nonplanar tetraalkylporphyrins. *J. Am. Chem. Soc.* **2003,** *125*, 1253-1268.

60. Nguyen, K. A.; Day, P. N.; Pachter, R.; Tretiak, S.; Chernyak, V.; Mukamel, S., Analysis of absorption spectra of zinc porphyrin, zinc *meso*-tetraphenylporphyrin, and halogenated derivatives. *J. Phys. Chem. A* **2002,** *106*, 10285-10293.

61. Bhyrappa, P.; Purushothaman, B., Perbrominated 2-nitrotetraphenylporphyrins: electrochemical and axial ligation properties. *J. Chem. Soc., Perkin Trans.* **2001**, 238-242.

62. Autret, M.; Ou, Z.; Antonini, A.; Boschi, T.; Tagliatesta, P.; Kadish, K. M., Synthesis and electrochemistry of 2,3,7,8,12,13,17,18-octachloro-5,10,15,20-tetrakis(3,5-dichloro-2,6-dimethoxyphenyl)porphyrin (H_2tdcdmpp), [Co^{II}(tdcdmpp)] and [M(tdcdmpp)Cl] (M = Fe^{III} or Mn^{III}). *Dalton Trans.* **1996**, 2793-2797.

63. Baciocchi, E.; Boschi, T.; Cassioli, L.; Galli, C.; Jaquinod, L.; Lapi, A.; Paolesse, R.; Smith, K. M.; Tagliatesta, P., Electronic effects on the stereoselectivity of epoxidation reactions catalyzed by manganese porphyrins. *Eur. J. Org. Chem.* **1999**, 3281-3286.

64. Wasbotten, I. H.; Conradie, J.; Ghosh, A., Electronic absorption and resonance raman signatures of hyperporphyrins and nonplanar porphyrins. *J. Phys. Chem. B* **2003,** *107*, 3613-3623.

65. Hodge, J. A.; Hill, M. G.; Gray, H. B., Electrochemistry of nonplanar zinc(II) tetrakis(pentafluorophenyl)porphyrins. *Inorg. Chem.* **1995,** *34*, 809-812.

66. Tagliatesta, P.; Li, J.; Autret, M.; Van Caemelbecke, E.; Villard, A.; D'Souza, F.; Kadish, K. M., Electrochemistry and spectral characterization of oxidized and reduced (TPPBrx)FeCl where TPPBrx is the dianion of β-brominated-pyrrole tetraphenylporphyrin and x varies from 0 to 8. *Inorg. Chem.* **1996,** *35*, 5570-5576.

67. Chahal, M. K.; Sankar, M., Switching between porphyrin, porphodimethene and porphyrinogen using cyanide and fluoride ions mimicking volatile molecular memory and the 'NOR' logic gate. *Dalton Trans.* **2016,** *45*, 16404-16412.

68. Chahal, M. K.; Sankar, M.; Butcher, R. J., An insight into the communication between *β*-olefin/phenyl olefin-mediated acceptors and porphyrin π-system: a way to establish porphyrin based chemodosimeters and chemosensors. *Phys. Chem. Chem. Phys.* **2017,** *19*, 4530-4540.

69. Golder, A. J.; Nolan, K. B.; Povey, D. C.; Traylor, T. G., Metal complexes of sterically hindered porphyrins. Crystal and molecular structure of meso-tetrakis(3,5-di-*tert*-butyl-4-hydroxyphenyl)porphyrin-nickel(II). *Inorg. Chim. Acta* **1988,** *143*, 71-75.

70. Spyroulias, G. A.; Despotopoulos, A. P.; Raptopoulou, C. P.; Terzis, A.; de Montauzon, D.; Poilblanc, R.; Coutsolelos, A. G., Comparative study of structure-properties relationship for novel *β*-halogenated lanthanide porphyrins and their nickel and free bases precursors, as a function of number and nature of halogens atoms. *Inorg. Chem.* **2002,** *41*, 2648-2659.

71. Gutmann, V., Solvent effects on the reactivities of organometallic compounds. *Coord. Chem. Rev.* **1976,** *18*, 225-55.

72. Thies, S.; Sell, H.; Bornholdt, C.; Schütt, C.; Köhler, F.; Tuczek, F.; Herges, R., Light-driven coordination-induced spin-state switching: rational design of photodissociable ligands. *Chem. Eur. J.* **2012,** *18*, 16358-16368.

73. Dommaschk, M.; Thoms, V.; Schütt, C.; Näther, C.; Puttreddy, R.; Rissanen, K.; Herges, R., Coordination-induced spin-state switching with nickel chlorin and nickel isobacteriochlorin. *Inorg. Chem.* **2015,** *54*, 9390-9392.

74. Loliger, J.; Scheffold, R., Paramagnetic moment measurements by NMR. A micro technique. *J. Chem. Educ.* **1972,** *49*, 646.

75. Richeter, S. J., C.; Kyritsakas, N.; Ruppert, R.; Callot, H. J., Preparation of six isomeric bis-acylporphyrins with chromophores reaching the near-infrared via intramolecular friedel−crafts reaction. *J. Org. Chem.* **2003,** *68*, 9200-9208.

76. Ghosh, A.; Halvorsen, I.; Nilsen, H. J.; Steene, E.; Wondimagegn, T.; Lie, R.; van Caemelbecke, E.; Guo, N.; Ou, Z.; Kadish, K. M., Electrochemistry of nickel and copper *β*-octahalogeno-*meso*-tetraarylporphyrins. Evidence for important role played by saddling-induced metal(dx_2-y_2)-porphyrin("a_2u") orbital interactions. *J. Phys. Chem. B* **2001,** *105*, 8120-8124.

77. Bard, A. J.; Faulkner, L. R., *Electrochemical Methods: fundamentals and applications*. Wiley: New York, 2001.

78. Kojima, T.; Hanabusa, K.; Ohkubo, K.; Shiro, M.; Fukuzumi, S., Formation of dodecaphenylporphodimethene via facile protonation of saddle-distorted dodecaphenylporphyrin. *Chem. Commun.* **2008**, 6513-6515.

79. Renner, M. W.; Buchler, J. W., Cation and anion radicals of (5,15-dimethyl-2,3,7,8,12,13,17,18-octaethyl-5H,15H- porphinato)nickel(II): Comparison of the nickel complexes of porphodimethene and chlorin chromophores. *J. Phys. Chem.* **1995,** *99*, 8045-8049.

80. Ishihara, S.; Hill, J. P.; Shundo, A.; Richards, G. J.; Labuta, J.; Ohkubo, K.; Fukuzumi, S.; Sato, A.; Elsegood, M. R. J.; Teat, S. J.; Ariga, K., Reversible photoredox switching of porphyrin-bridged bis-2,6-di-*tert*-butylphenols. *J. Am. Chem. Soc.* **2011,** *133*, 16119-16126.

81. Ishihara, S.; Hill, J. P.; Shundo, A.; Richards, G. J.; Labuta, J.; Ohkubo, K.; Fukuzumi, S.-I.; Sato, A.; Elsegood, M. R. J.; Teat, S. J.; Ariga, K., Reversible photoredox switching of porphyrin-bridged bis-2,6-di-*tert*-butylphenols. *J. Am. Chem. Soc.* **2011,** *133*, 16119-16126.

82. Harmjanz, M.; Gill, H. S.; Scott, M. J., Porphodimethene-porphyrin interconversion: a tetrapyrrolic redox-switchable macrocycle. *J. Am. Chem. Soc.* **2000,** *122*, 10476-10477.

83. Milgrom, L. R.; Jones, C. C.; Harriman, A., Facile aerial oxidation of a porphyrin. Part 3. Some metal complexes of meso-tetrakis(3,5-di-tert-butyl-4-hydroxyphenyl)porphyrin. *J. Chem. Soc., Perkin Trans. 2* **1988**, 71-9.

84. Higashino, T.; Imahori, H., Porphyrins as excellent dyes for dye-sensitized solar cells: recent developments and insights. *Dalton Trans.* **2015,** *44*, 448-463.

85. Urbani, M.; Gratzel, M.; Nazeeruddin, M. K.; Torres, T., *Meso*-substituted porphyrins for dye-sensitized solar cells. *Chem. Rev.* **2014,** *114*, 12330-12396.

86. Senge, M. O.; Fazekas, M.; Pintea, M.; Zawadzka, M.; Blau, W. J., 5,15-A_2B_2- and 5,15-A_2BC-Type porphyrins with donor and acceptor groups for use in nonlinear optics and photodynamic therapy. *Eur. J. Org. Chem.* **2011,** *29*, 5797-5816.

87. Wang, H.; Jinadasa, R. G. W.; Kumar, S., Push-pull porphyrins: synthesis, properties and applications. In *Handbook of Porphyrin Science*, World Scientific Publishing Company: 2016; Vol. 40, pp 105-200.

88. Ethirajan, M.; Chen, Y.; Joshi, P.; Pandey, R. K., The role of porphyrin chemistry in tumor imaging and photodynamic therapy. *Chem. Soc. Rev.* **2011,** *40*, 340-362.

89. Moura, N. M. M.; Faustino, M. A. F.; Neves, M. G. P. M. S.; Duarte, A. C.; Cavaleiro, J. A. S., Vilsmeier-haack formylation of Cu(II) and Ni(II) porphyrin complexes under microwaves irradiation. *J. Porphyrins Phthalocyanines* **2011,** *15*, 652-658.

90. Jaquinod, L.; Gros, C.; Khoury, R. G.; Smith, K. M., A convenient synthesis of functionalized tetraphenylchlorins. *Chem. Commun.* **1996**, 2581-2582.

91. Giraudeau, A.; Callot, H. J.; Jordan, J.; Ezhar, I.; Gross, M., Substituent effects in the electroreduction of porphyrins and metalloporphyrins. *J. Am. Chem. Soc.* **1979,** *101*, 3857-3862.

92. Crossley, M. J.; King, L. G., Reaction of metallo-2-nitro-5,10,15,20-tetraphenylporphyrins with oxyanions. temperature-dependent competition between nucleophilic addition and single-electron transfer processes. *J. Chem. Soc., Perkin Trans.* **1996**, 1251-1260.

93. Kumar, R.; Sankar, M., Synthesis, spectral, and electrochemical studies of electronically tunable β-substituted porphyrins with mixed substituent pattern. *Inorg. Chem.* **2014,** *53*, 12706-12719.

94. Grover, N.; Sankar, M.; Song, Y.; Kadish, K. M., Asymmetrically crowded "Push-Pull" octaphenylporphyrins with modulated frontier orbitals: Syntheses, photophysical, and electrochemical redox properties. *Inorg. Chem.* **2016,** *55*, 584-597.

95. Kadish, K. M.; Adamian, V. A.; Van Caemelbecke, E.; Gueletii, E.; Will, S.; Erben, C.; Vogel, E., Electrogeneration of oxidized corrole dimers. Electrochemistry of (OEC)M Where M = Mn, Co, Ni, or Cu and OEC is the trianion of 2,3,7,8,12,13,17,18-octaethylcorrole. *J. Am. Chem. Soc.* **1998,** *120*, 11986-11993.

96. Kadish, K. M.; Shao, J.; Ou, Z.; Gros, C. P.; Bolze, F.; Barbe, J.-M.; Guilard, R., Alkyl- and Aryl-Substituted Corroles. 4. Solvent effects on the electrochemical and spectral properties of cobalt corroles. *Inorg. Chem.* **2003,** *42*, 4062-4070.

97. Kadish, K. M.; Lin, X. Q.; Han, B. C., Chloride-binding reactions and electrochemistry of (tetraphenylporphyrinato)cobalt and chloro(tetraphenylporphyrinato)cobalt in dichloromethane. *Inorg. Chem.* **1987,** *26*, 4161-4167.

98. Donzello, M. P.; Ercolani, C.; Novakova, V.; Zimcik, P.; Stuzhin, P. A., Tetrapyrazinoporphyrazines and their metal derivatives. Part I: Synthesis and basic structural information. *Coord. Chem. Rev.* **2016,** *309*, 107-179.

99. Suzuki, Y.; Fujimori, M.; Yoshikawa, H.; Awaga, K., Packing motifs and magneto-structural correlations in crystal structures of metallo-tetrakis(1,2,5-thiadiazole)porphyrazine series, MTTDPz (M=H_2, Fe, Co, Ni, Cu, Zn). *Chem. Eur. J.* **2004,** *10*, 5158-5164.

100. Donzello, M. P.; De Mori, G.; Viola, E.; Ercolani, C.; Ricciardi, G.; Rosa, A., Tetra-2,3-pyrazinoporphyrazines with externally appended pyridine rings. 15. Effects of the pyridyl substituents and fused exocyclic rings on the UV–Visible spectroscopic properties of Mg(II)–porphyrazines: a combined experimental and DFT/TDDFT study. *Inorg. Chem.* **2014,** *53*, 8009-8019.

101. Pietrangeli, D.; Rosa, A.; Ristori, S.; Salvati, A.; Altieri, S.; Ricciardi, G., Carboranyl-porphyrazines and derivatives for boron neutron capture therapy: From synthesis to in vitro tests. *Coord. Chem. Rev.* **2013,** *257*, 2213-2231.

102. Ongayi, O.; Gottumukkala, V.; Fronczek, F. R.; Vicente, M. G. H., Synthesis and characterization of a carboranyl-tetrabenzoporphyrin. *Bioorg. Med. Chem. Lett.* **2005,** *15*, 1665-1668.

103. Gottumukkala, V.; Luguya, R.; Fronczek, F. R.; Vicente, M. G. H., Synthesis and cellular studies of an octa-anionic 5,10,15,20-tetra[3,5-(nido-carboranylmethyl)phenyl]porphyrin (H_2OCP) for application in BNCT. *Bioorg. Med. Chem. Lett.* **2005,** *13*, 1633-1640.

104. Kahl, S. B.; Li, J., Synthesis and characterization of a boronated metallophthalocyanine for boron neutron capture therapy. *Inorg. Chem.* **1996,** *35*, 3878-3880.

105. Pietrangeli, D.; Rosa, A.; Pepe, A.; Altieri, S.; Bortolussi, S.; Postuma, I.; Protti, N.; Ferrari, C.; Cansolino, L.; Clerici, A. M.; Viola, E.; Donzello, M. P.; Ricciardi, G., Water-soluble carboranyl-phthalocyanines for BNCT. Synthesis, characterization, and in vitro tests of the Zn(II)-nido-carboranyl-hexylthiophthalocyanine. *Dalton Trans.* **2015,** *44*, 11021-11028.

106. Bergami, C.; Donzello, M. P.; Monacelli, F.; Ercolani, C.; Kadish, K. M., Tetra-2,3-pyrazinoporphyrazines with externally appended pyridine rings. 4. UV-Visible spectral and electrochemical evidence of the remarkable electron-deficient properties of the new tetrakis-2,3-[5,6-di{2-(N-methyl)pyridiniumyl}pyrazino]porphyrazinatometal octacations, [(2-Mepy)8TPyzPzM]8^+ (M = $Mg^{II}(H_2O)$, Co^{II}, Cu^{II}, Zn^{II}). *Inorg. Chem.* **2005,** *44*, 9862-9873.

107. Donzello, M. P.; Ou, Z.; Monacelli, F.; Ricciardi, G.; Rizzoli, C.; Ercolani, C.; Kadish, K. M., Tetra-2,3-pyrazinoporphyrazines with externally appended pyridine rings. 1. Tetrakis-2,3-[5,6-di(2-pyridyl)pyrazino]porphyrazine: A new macrocycle with remarkable electron-deficient properties. *Inorg. Chem.* **2004,** *43*, 8626-8636.

108. Berezina, B. D.; Khelevina, O. G.; Gerasimova, N. D.; Stuzhin, P. A., Kinetics of formation of octaphenyltetrazaporphine complexes in a pyridine solution. *Zh. Fiz. Khim.* **1982,** *56*, 2768-2772.

109. Donzello, M. P.; Dini, D.; D'Arcangelo, G.; Ercolani, C.; Zhan, R.; Ou, Z.; Stuzhin, P. A.; Kadish, K. M., Porphyrazines with annulated diazepine rings. 2. Alternative synthetic route to Tetrakis-2,3-(5,7-diphenyl-1,4-diazepino)porphyrazines: New metal complexes, general physicochemical data, ultraviolet-visible linear and optical limiting behavior, and electrochemical and spectroelectrochemical properties. *J. Am. Chem. Soc.* **2003,** *125*, 14190-14204.

110. De Mori, G.; Fu, Z.; Viola, E.; Cai, X.; Ercolani, C.; Pia Donzello, M.; Kadish, K. M., Tetra-2,3-pyrazinoporphyrazines with externally appended thienyl rings: synthesis, UV-visible spectra, electrochemical behavior, and photoactivity for the generation of singlet oxygen. *Inorg. Chem.* **2011,** *50*, 8225-8237.

111. Lever, A. B. P.; Wilshire, J. P., Redox potentials of metal phthalocyanines in nonaqueous media. *Can. J. Chem.* **1976,** *54*, 2514-2516.

112. Giraudeau, A.; Fan, F.-R. F.; Bard, A. J., Semiconductor electrodes. 30. Spectral sensitization of the semiconductors titanium oxide (n-TiO_2) and tungsten oxide (n-WO_3) with metal phthalocyanines. *J. Am. Chem. Soc.* **1980,** *102*, 5137-5142.

113. Mashazi, P.; Antunes, E.; Nyokong, T., Probing electrochemical and electrocatalytic properties of cobalt(II) and manganese(III) octakis(hexylthio)phthalocyanine as self-assembled monolayers. *J. Porphyrins Phthalocyanines* **2010,** *14*, 932-947.

114. Truxillo, L. A.; Davis, D. G., Electrochemistry of cobalt tetraphenylporphyrin in aprotic media. *Anal. Chem.* **1975,** *47*, 2260-7.

115. Walker, F. A.; Beroiz, D.; Kadish, K. M., Electronic effects in transition metal porphyrins. 2. The sensitivity of redox and ligand addition reactions in para-substituted tetraphenylporphyrin complexes of cobalt(II). *J. Am. Chem. Soc.* **1976,** *98*, 3484-3489.

116. Davis, N. K. S.; Thompson, A. L.; Anderson, H. L., A porphyrin fused to four anthracenes. *J. Am. Chem. Soc.* **2011,** *133*, 30-31.

117. Zeng, W.; Lee, S.; Son, M.; Ishida, M.; Furukawa, K.; Hu, P.; Sun, Z.; Kim, D.; Wu, J., Phenalenyl-fused porphyrins with different ground states. *Chem. Sci.* **2015,** *6*, 2427-2433.

118. Fujimoto, K.; Kasuga, Y.; Fukui, N.; Osuka, A., Diphenylphosphine-oxide-fused and diphenylphosphine-fused porphyrins: Synthesis, tunable electronic properties, and formation of cofacial dimers. *Chem. Eur. J.* **2017,** *23*, 6741-6745.

119. Wu, L.; Li, F.; Rao, Y.; Wen, B.; Xu, L.; Zhou, M.; Tanaka, T.; Osuka, A.; Song, J., Synthesis, structures, and near-IR absorption of heterole-fused earring porphyrins. *Angew. Chem.* **2019,** *58*, 8124-8128.

120. Richeter, S.; Jeandon, C.; Gisselbrecht, J.-P.; Ruppert, R.; Callot, H. J., Syntheses and optical and electrochemical properties of porphyrin dimers linked by metal ions. *J. Am. Chem. Soc.* **2002,** *124*, 6168-6179.

121. Richeter, S.; Jeandon, C.; Gisselbrecht, J.-P.; Ruppert, R.; Callot, H. J., Synthesis, structural characterization, and electrochemical studies of nickel porphyrins bearing two peripheral conjugated chelating groups. *Inorg. Chem.* **2007,** *46*, 10241-10251.

122. Kiran, B.; Nguyen, M. T., Density functional studies on N-fused porphyrin. Electronic, magnetic and metal binding properties. *J. Organomet. Chem.* **2002,** *643*, 265-271.

123. Fukui, N.; Cha, W.; Shimizu, D.; Oh, J.; Furukawa, K.; Yorimitsu, H.; Kim, D.; Osuka, A., Highly planar diarylamine-fused porphyrins and their remarkably stable radical cations. *Chem. Sci.* **2017,** *8*, 189-199.

124. Kato, K.; Osuka, A., *Meta*- and *para*-Phenylenediamine-fused porphyrin dimers: Synthesis and magnetic interactions of their dication diradicals. *Angew. Chem.* **2019,** *58*, 8546-8550.

125. Rath, H.; Sankar, J.; PrabhuRaja, V.; Chandrashekar, T. K.; Nag, A.; Goswami, D., Core-modified expanded porphyrins with large third-order nonlinear optical response. *J. Am. Chem. Soc.* **2005,** *127*, 11608-11609.

126. Aratani, N.; Kim, D.; Osuka, A., π-Conjugation enlargement toward the creation of multi-porphyrinic systems with large two-photon absorption properties. *Chem. Asian J.* **2009,** *4*, 1172-1182.

127. Banala, S.; Fokong, S.; Brand, C.; Andreou, C.; Kraeutler, B.; Rueping, M.; Kiessling, F., Quinone-fused porphyrins as contrast agents for photoacoustic imaging. *Chem. Sci.* **2017,** *8*, 6176-6181.

128. Li, J.; Merino-Diez, N.; Carbonell-Sanroma, E.; Vilas-Varela, M.; de Oteyza, D. G.; Pena, D.; Corso, M.; Pascual, J. I., Survival of spin state in magnetic porphyrins contacted by graphene nanoribbons. *Sci. Adv.* **2018,** *4*, eaaq0582/1-eaaq0582/6.

129. Jiao, C.; Zu, N.; Huang, K.-W.; Wang, P.; Wu, J., Perylene anhydride fused porphyrins as near-infrared sensitizers for dye-sensitized solar cells. *Org. Lett.* **2011,** *13*, 3652-3655.

130. Kurumisawa, Y.; Higashino, T.; Nimura, S.; Tsuji, Y.; Iiyama, H.; Imahori, H., Renaissance of fused porphyrins: Substituted methylene-bridged thiophene-fused strategy for high-performance dye-sensitized solar cells. *J. Am. Chem. Soc.* **2019,** *141*, 9910-9919.

131. Mori, H.; Tanaka, T.; Osuka, A., Fused porphyrinoids as promising near-infrared absorbing dyes. *J. Mater. Chem. C* **2013,** *1*, 2500-2519.

132. Zhong, Q.; Diev, V. V.; Roberts, S. T.; Antunez, P. D.; Brutchey, R. L.; Bradforth, S. E.; Thompson, M. E., Fused porphyrin-single-walled carbon nanotube hybrids: Efficient formation and photophysical characterization. *ACS Nano* **2013,** *7*, 3466-3475.

133. Baba, K.; Bengasi, G.; El Assad, D.; Grysan, P.; Lentzen, E.; Heinze, K.; Frache, G.; Boscher, N. D., Conductive directly fused poly(porphyrin) coatings by oxidative chemical vapor deposition - from single- to triple-fused. *Eur. J. Org. Chem.* **2019**, 2368-2375.

134. Lewtak, J. P.; Gryko, D. T., Synthesis of π-extended porphyrins via intramolecular oxidative coupling. *Chem. Comm.* **2012,** *48*, 10069-10086.

135. Ishizuka, T.; Saegusa, Y.; Shiota, Y.; Ohtake, K.; Yoshizawa, K.; Kojima, T., Multiply-fused porphyrins—effects of extended π-conjugation on the optical and electrochemical properties. *Chem. Commun.* **2013,** *49*, 5939-5941.

136. Saegusa, Y. I., T.; Komamura, K.; Shimizu, S.; Kotani, H.; Kobayashi, N.; Kojima, T., Ring-fused porphyrins: extension of π-conjugation significantly affects the aromaticity and optical properties of the porphyrin π-systems and the Lewis acidity of the central metal ions. *Phys. Chem. Chem. Phys.* **2015,** *17*, 15001-15011.

137. Fujimoto, K.; Osuka, A., A 1,5-naphthyridine-fused porphyrin dimer: Intense NIR absorption and facile redox interconversion with its reduced congener. *Chem. Eur. J.* **2018,** *24*, 6530-6533.

138. Pandey, R. K.; Bellnier, D. A.; Smith, K. M.; Dougherty, T. J., Chlroins and porphyrin derivatives as potential photosensitizers in photodynamic therapy. *Photochem. Photobiol.* **1991,** *53*, 65-72.

139. Sternberg, E. D.; Dolphin, D.; Brückner, C., Porphyrin-based photosensitizers for use in photodynamic therapy. *Tetrahedron* **1998,** *54*, 4151-4202.

140. Jasat, A.; Dolphin, D., Expanded Porphyrins and Their Heterologs. *Chem. Rev.* **1997,** *97*, 2267-2340.

141. Roznyatovskiy, V. V.; Lee, C.-H.; Sessler, J. L., π-Extended isomeric and expanded porphyrins. *Chem. Soc. Rev.* **2013,** *42*, 1921-1933.

142. Sarma, T. P., P. K., Annulated isomeric, expanded, and contracted porphyrins. *Chem. Rev.* **2017,** *117*, 2785-2838.

143. Tanaka, T. O., A., Chemistry of meso-Aryl-Substituted Expanded Porphyrins: Aromaticity and Molecular Twist. . *Chem. Rev.* **2017**, 2584-2640.

144. Chaudhri, N.; Grover, N.; Sankar, M., Asymmetrically *β*-substituted porphyrins and chlorins: synthesis, spectroscopic, and electrochemical redox properties. *ECS Trans.* **2015,** *66*, 11-20.

145. Takeuchi, T.; Gray, H. B.; Goddard, W. A., III, Electronic structures of halogenated porphyrins: Spectroscopic properties of $ZnTFPPX_8$ ($TFPPX_8$ = Octa-*β*-halotetrakis(pentafluorophenyl)porphyrin; X = Cl, Br). *J. Am. Chem. Soc.* **1994,** *116*, 9730-9732.

146. Chahal, M. K.; Sankar, M., Porphyrin chemodosimeters: synthesis, electrochemical redox properties and selective 'naked-eye' detection of cyanide ions. *RSC Adv.* **2015,** *5*, 99028-99036.

147. Richards, J. A.; Whitson, P. E.; Evans, D. H., Electrochemical oxidation of 2,4,6-tri-tert-butylphenol. *J. Electroanal. Chem.* **1975,** *63*, 311-327.

148. Cong, Z.; Kurahashi, T.; Fujii, H., Formation of iron(III) *meso*-chloro-isoporphyrin as a reactive chlorinating agent from oxoiron(IV) porphyrin π-cation radical. *J. Am. Chem. Soc.* **2012,** *134*, 4469-4472.

149. Chahal, M. K.; Sankar, M., *β*-Dicyanovinyl substituted porphyrinogen: synthesis, a reversible sensor for picric acid among explosives and a unique sensor for cyanide and fluoride ions by switching between various porphyrinoid states. *Dalton Trans.* **2017,** *46*, 11669-11678.